UNIVERSIDAD
DE GRANADA

Production and measurement of low-energy neutrons using accelerator-based neutron sources for applications in medicine

TESIS DOCTORAL

Antònia Verdera Garau

PROGRAMA DE DOCTORADO EN FÍSICA Y CIENCIAS DEL ESPACIO

Granada, 2025

Production and measurement of low-energy neutrons using accelerator-based neutron sources for applications in medicine

REALIZADA POR:
Antònia Verdera Garau

DIRIGIDA POR:
Antonio Javier Praena Rodríguez

DEPARTAMENTO:
Departamento de Física Atómica, Molecular y Nuclear

UNIVERSIDAD DE GRANADA

PROGRAMA DE DOCTORADO EN FÍSICA Y CIENCIAS DEL ESPACIO

Granada, 2025

Editor: Universidad de Granada. Tesis Doctorales
Autor: Antònia Verdera Grau
ISBN: 978-84-1195-829-5
URI: https://hdl.handle.net/10481/105388

Abstract

Accelerator-based neutron sources are currently in the spotlight due to the wide range of uses, particularly in medical applications, such as Boron Neutron Capture Therapy (BNCT). Conventional BNCT facilities, either based on nuclear reactors or on accelerators, require a moderation system or a Beam Shaping Assembly (BSA) to tailor the neutron spectrum, adding complexity, important maintenance and operation and avoiding flexibility in the neutron field.

To overcome these challenges, this work proposes a novel approach leveraging the ^{51}V(p,n) and ^{45}Sc(p,n) reactions near their thresholds, eliminating the need for moderation and fulfilling the quality factors established by the International Atomic Energy Agency (IAEA) for BNCT.

Neutron time-of-flight measurements were conducted at the accelerator-based neutron facility MONNET at the Joint Research Centre in Geel, Belgium. First, experiments were performed using as a reference the well-known ^{7}Li(p,n) near-threshold reaction. Subsequently, angle-dependent measurements were carried out for the ^{51}V(p,n) reaction near its threshold, including the integrated neutron spectrum produced by this reaction.

The results of the experiments with the ^{51}V(p,n) reaction and the studies on ^{45}Sc(p,n) reaction using available data, demonstrate that the proposed neutron sources achieve the IAEA quality factors with comparable figures of merit to existing BNCT facilities. In particular, the ^{45}Sc(p,n) reaction can be used with available accelerators, meanwhile ^{51}V(p,n) would need higher proton currents than existing accelerators. This approach not only simplifies the design of accelerator-based BNCT facilities but also enables fine-tuning of neutron penetration depth into the human body through small adjustments in proton energy, opening new possibilities for treatment optimization.

This thesis makes significant contributions to the field of accelerator-based neutron sources by providing high-precision experimental data and proposing an innovative approach to neutron generation for BNCT. This new proposal has been submitted as a patent.

Resumen

Las fuentes de neutrones basadas en aceleradores están actualmente en el punto de mira, debido a su amplia gama de aplicaciones, especialmente en el ámbito médico, como la Terapia por Captura de Neutrones en Boro (BNCT). Las instalaciones convencionales de BNCT, ya sean basadas en reactores nucleares o en aceleradores, requieren un sistema de moderación o un Ensamblaje de Modelado del Espectro (BSA) para ajustar el espectro de neutrones, lo que añade complejidad, requiere un mantenimiento importante y limita la flexibilidad del campo de neutrones.

Para superar estos desafíos, este trabajo propone un enfoque novedoso que aprovecha las reacciones ^{51}V(p,n) y ^{45}Sc(p,n) cerca de sus umbrales, eliminando la necesidad de moderación mientras se cumplen los factores de calidad de neutrones establecidos por la Agencia Internacional de Energía Atómica (IAEA) para BNCT.

Las mediciones de tiempo de vuelo de neutrones se llevaron a cabo en la instalación de neutrones basada en aceleradores MONNET, en el Joint Research Centre en Geel, Bélgica. En primer lugar, se realizaron experimentos utilizando como referencia la bien conocida reacción ^{7}Li(p,n) cerca de su umbral. Posteriormente, se llevaron a cabo mediciones dependientes del ángulo para la reacción ^{51}V(p,n) cerca de su umbral, incluyendo el espectro de neutrones integrado producido por esta reacción.

Los experimentos realizados con la reacción ^{51}V(p,n), junto con estudios sobre ^{45}Sc(p,n) basados en datos disponibles, demuestran que las fuentes de neutrones propuestas logran los factores de calidad de la IAEA con figuras de mérito comparables a las de las instalaciones existentes de BNCT. En particular, la reacción ^{45}Sc(p,n) puede utilizarse con los aceleradores disponibles, mientras que la reacción ^{51}V(p,n) requeriría corrientes de protones más altas que las de los aceleradores actuales. Este enfoque no solo simplifica el diseño de las instalaciones de BNCT basadas en aceleradores, sino que también permite un ajuste preciso de la profundidad de penetración de los neutrones en el cuerpo humano mediante pequeñas modificaciones en la energía de los protones, abriendo nuevas posibilidades para la optimización del tratamiento. Se espera que el enfoque propuesto simplifique las instalaciones de BNCT basadas en aceleradores.

Esta tesis ha realizado contribuciones significativas en el campo de las fuentes de neutrones basadas en aceleradores, proporcionando datos experimentales de alta precisión y proponiendo un enfoque innovador para la generación de neutrones en BNCT. Esta nueva propuesta ha sido presentada como una patente.

Acknowledgements

Quiero agradecer a todas las personas que me han acompañado para poder llegar hasta aquí. Esta tesis no sería posible sin vosotros. Han sido años de desafíos, de cambios y de mucho trabajo, pero también han sido unos años muy bonitos.

Para empezar, me gustaría agradecer a mi director de tesis, Javier, por haber confiado en mí. Muchas gracias por tu generosidad, por todas las ideas que has decidido compartir conmigo, por todas las cosas que me has enseñado y, sobre todo, por haber valorado siempre mi esfuerzo.

A todos los miembros del grupo de Física de Neutrones de la UGR. Ignacio, me contagiaste tu pasión por este mundo y, si no te hubiese encontrado en el máster, hoy no estaría aquí. Pablo, me enseñaste muchísimo en muy poco tiempo; estoy segura de que tu capacidad de trabajo te llevará muy lejos. Elena, gracias por haberme ayudado tanto en el inicio de la tesis, por darme siempre tu punto de vista y por echarme una mano siempre que has podido. Ahora terminamos este camino a la vez. Matilde, gracias por las miles de preguntas que nos hemos hecho juntas y por todos los planes fuera del trabajo. A las dos, gracias por nuestros paseos por Granada.

A todos mis compañeros del departamento, o mejor dicho, del FAMN. Sabéis que me habéis alegrado el día a día, y espero que yo a vosotros un poco también. Dani, por ser siempre la cohesión del grupo. Alejandro, por tu espíritu de "sí a todo". Joaquín, por dejarme conocerte mejor. Fran, por las risas aseguradas. Pablo F., por todas las horas juntos en ese despacho y las dudas existenciales que me has aclarado. Laura, por ser siempre una mirada cómplice. Juan, por ser tan impredecible. Pedro, por compartir tanto de tí. Álvaro, por sumar siempre. Pablo C., por entenderme tan bien. A todos los que habéis pasado por aquí, por todos los buenos ratos que hemos pasado. Os espero en Mallorca.

To the MONNET team at the Joint Research Centre in Geel, Belgium, I express my sincere gratitude. Special thanks to my supervisor, Miguel, for his invaluable guidance and support, and to Cristiano, Cedric, Wouter, and Stephan for their collaboration and insightful discussions that enriched my research. Thank you to everyone for the cakes and coffees shared.

To my Boeretang family, for the moments in the dorms and the countless unforgettable experiences. From playing thousands of board games to going on bike rides and traveling across Belgium and the Netherlands, every moment was unique thanks to you. Fatima, Alba, Alessandro, Alessio, Martas, Karolina, Nar-

cis, Bernat, Lucas, and many others, thank you for making Boeretang feel like home.

A mis chicas del piso, Fernanda, Carmen, Paula y Natalia, con vosotras empecé esta aventura y, aunque no me entendíais, siempre me animabais a seguir. Hemos aprendido mucho juntas y sé que seguiremos haciéndolo.

A mi Pilar, por ser siempre mi apoyo y por todas las risas, viajes y ratos que hemos pasado juntas estos años. Has sido mi familia en Granada.

No estaria aquí si no fos pels meus companys de la carrera. Les hores infinites de biblioteca amb vosaltres, les festes i tots els plans que vàrem fer junts em varen fer enganxar a sa física, però també a vosaltres. Lluc, vàrem començar aquest camí juntes i ara estam acabant el doctorat les dues de sa mà. Moltes gràcies per ser sempre un referent i, sobretot, una tan bona amiga. Juan, ens vàrem trobar més tard, però des que ens vàrem unir ja no hi ha qui ens separi. Hem estat anys junts i anys a distància, i sempre heu estat allà per jo.

A les meves nines. Cadascuna diferent, sempre ens hem donat suport i ens hem alegrat la vida les unes a ses altres, i sé que serà així sempre. Carme, Júlia, Magda i Mercè, gràcies per ensenyar-me tant, per totes les visites a Granada, a Bèlgica i per tots els viatges que hem fet juntes aquests anys. Gràcies per ser sempre casa per jo.

També m'agradaria donar les gràcies a tota la meva família. Als meus padrins, que ja no hi són. A les meves padrines, sou dues dones valentes i fortes que m'heu ensenyat a no rendir-me mai. Als meus cosins i tios, per ser una gran part de qui soc. A tu Claus, per esforçar-te a entendre un poc més que és allò que he fet i per ser un més.

Per acabar, a la meva família més propera. Als meus pares. Mama, gràcies per escoltar-me sempre, encara que no m'entenguis, i ser una amiga per jo. Papa, gràcies per ensenyar-me què és l'esforç. Gràcies a tots dos per sentir-vos tan orgullosos de jo, jo també ho estic de vosaltres. Maria, ets el meu referent, així que sense tu res seria possible. Gràcies per donar-me tan de suport sempre. A na Marieta, per qualque dia contar-li històries de tot el que he escrit aquí.

Carles, aquesta tesi també és teva. M'has fet costat, sostingut i ajudat a no rendir-me durant tots aquests anys. Gràcies per ser sempre tot el que he necessitat.

Contents

List of Figures

List of Tables

Acronyms

AB-BNCT Accelerator-based Boron Neutron Capture Therapy.

ABNS Accelerator-based Neutron Sources.

AD Advantage Depth.

BGRR Brookhaven Graphite Research Reactor.

BMRR Brookhaven Medical Research Reactor.

BNCT Boron Neutron Capture Therapy.

BPA Boronophenylalanine.

BSA Beam Shaping Assembly.

BSA-free Beam Shaping Assembly-Free.

BSH Sodium Borocaptate.

C-BENS Cyclotron-based Epithermal Neutron Source.

CANS Compact Accelerator-Driven Neutron Source.

CBE Clinical Biological Effectiveness.

DAQ Data Acquisition System.

DDD Double Dose Depth.

DTL Drift Tube Linacs.

EM Expectation-Maximization.

ENDF Evaluated Nuclear Data File.

ESQ Electrostatic Quadrupole.

ESS European Spallation Source.

FOMs Figures of Merit.

FWHM Full Width at Half Maximum.

IAEA International Atomic Energy Agency.

ICRP International Commission on Radiological Protection.

ICRU International Commission on Radiological Units and Measurements.

JRC Joint Research Centre.

JRC-Geel Joint Research Centre in Geel.

KURRI Kyoto University Research Reactor Institute.

LC Long Counter.

LET Linear Energy Transfer.

LINACs Linear Accelerators.

MACS Maxwellian-Averaged Cross Sections.

MC Monte Carlo.

MCNP Monte Carlo N-Particle.

MONNET Mono-Energetic Neutron Tower.

MTR Maximum Therapeutic Ratio.

NCT Neutron Capture Therapy.

NeMeSis Neutrons for Medicine and Scientific applications.

nTOF neutron Time-Of-Flight.

NUPECC Nuclear Physics European Collaboration Committee.

OTRI Oficina de Transferencia de Resultados de Investigación.

PLC De Pangher precision Long Counter.

PSD Pulse Shape Discrimination.

R&K Ratynski & Käppeler.

RBE Relative Biological Effectiveness.

RFQ Radiofrequency Quadrupole.

RM Response Matrix.

SI International System of Units.

SNS Spallation Neutron Source.

SRIM Stopping power and Range of Ions in Matter.

T/N Ratio Tumor/Normal Tissue Ratio.

TDD Triple Dose Depth.

TENDL TALYS-based Evaluated Nuclear Data Library.

THR Threshold.

TOF Time-Of-Flight.

TR Therapeutic Range.

UGR Universidad de Granada.

VITA Vacuum-Insulated Tandem Accelerator.

Outline

- Chapter 1 provides an introduction to low-energy neutron sources, focusing specifically on Accelerator-based Neutron Sources. It also introduces Boron Neutron Capture Therapy as a key medical application of these sources. The chapter concludes with an explanation of the objectives of this thesis.
- Chapter 2 reviews the state of the art in proton-induced neutron (p,n) production reactions relevant to low-energy neutron generation. The chapter focuses on four key (p,n) reactions: ^{7}Li(p,n)^{7}Be, ^{9}Be(p,n)^{9}B, ^{45}Sc(p,n)^{45}Ti, and ^{51}V(p,n)^{51}Cr, reviewing the literature and the kinematics of these reactions.
- Chapter 3 details the experimental method used to measure the neutron spectra from the ^{7}Li(p,n)^{7}Be and ^{51}V(p,n)^{51}Cr reactions. This includes a description of the experimental setup, instruments, and techniques employed to accurately characterize the neutron spectra resulting from these reactions, which were conducted at the MONNET facility at Joint Research Centre in Geel, Belgium.
- Chapter 4 focuses on the measurement of the ^{7}Li(p,n)^{7}Be reaction near the threshold. The chapter presents experimental data, methodology, and a comparison between experimental results and theoretical predictions to assess the energy spectrum. This reaction is useful for testing the experimental method.
- Chapter 5 examines the ^{51}V(p,n)^{51}Cr reaction near its threshold energy. This chapter includes a neutron-vanadium transmission measurement and provides a detailed analysis of the angle-dependent and integrated neutron spectra.
- Chapter 6 presents a new Accelerator-based Neutron Sources for Boron Neutron Capture Therapy: Beam Shaping Assembly-Free Approach. The potential use of two reactions near threshold, ^{45}Sc(p,n)^{45}Ti and ^{51}V(p,n)^{51}Cr, to produce neutrons is discussed, utilizing the measured data for the vanadium case.
- Chapter 7 presents the final conclusions and summarizes the key findings of the thesis.

Chapter 1

Introduction

Neutrons are neutral subatomic particles that are stable within atomic nuclei but become unstable and decay with a half-life of just over 10 minutes when they are free [1]. Unlike charged particles, neutrons do not interact with electromagnetic forces, allowing them to penetrate deeply into matter without significant deflection or slowing. This property makes them particles that require unique methods to be produced, measured, and stopped.

Neutrons are typically divided into three groups according to their kinetic energy: slow neutrons, intermediate-energy neutrons, and fast neutrons [2]. However, in this thesis, four different groups will be considered: fast neutrons ($\geq$ 10 keV), epithermal neutrons (0.5 eV to 10 keV), thermal neutrons (0.025 eV to 0.5 eV) and cold neutrons ($\leq$ 0.025 eV). Low-energy neutrons, 0.025 eV $\leq$ E_n $\leq$ 10 keV, epithermal and thermal, are particularly useful in scientific and medical applications due to their specific interaction properties with matter. The neutrons in this energy range will be the focus in this thesis.

The energy of the produced neutron depends on the nuclear reaction involved and the energy of the initiating particle. Neutrons can be produced through processes like nuclear fission, spallation, or fusion. In addition, the Accelerator-based Neutron Sources (ABNS) have recently gained prominence for their capability to generate high neutron fluxes in a controlled manner.

Traditionally, nuclear reactors have been the primary sources of neutrons. These reactors generate a significant number of neutrons through nuclear fission, which can be utilized for a wide range of applications, such as material testing and scientific research. Research reactors, in particular, are designed to provide a high neutron flux environment, enabling the irradiation of material samples to study their properties under neutron exposure. In addition to nuclear reactors, certain isotopes, like californium-252, have historically been used as neutron sources due to their ability to undergo spontaneous fission. This natural process releases neutrons without external triggers, offering a reliable and portable option for industrial, medical, and research applications.

Recent advancements have positioned Accelerator-based Neutron Sources (ABNS) as promising alternatives to research reactors and spontaneous fission sources. Ac-

cording to the International Atomic Energy Agency (IAEA), ABNS are categorized into three types: Compact Accelerator-Driven Neutron Source (CANS), Neutron Generators, and Spallation Sources. CANS encompass low-energy proton-, deuteron-, and electron-accelerators, designed in linear or circular configurations with moderate beam power ($\leq$ 30 kW). Neutron Generators create neutron beams through nuclear fusion, using compact linear accelerators to fuse hydrogen isotopes such as deuterium (D) or tritium (T), and are referred to as D-D or D-T generators based on the target isotope. Spallation Sources, in contrast, are high-flux neutron sources where high-energy protons ($\geq$ 0.5 GeV) strike a heavy metal target, emitting neutrons as a result. In this thesis, we will focus on neutrons produced by the ABNS. Therefore, they will be explained in greater detail below.

1.1 Neutron Sources Based on Accelerators

Accelerator-based Neutron Sources have emerged as a versatile and precise method for neutron production, offering significant advantages over the aforementioned traditional neutron sources. As stated, these sources operate by accelerating charged particles, such as protons, deuterons, or heavy ions, and directing them onto target materials like lithium, beryllium, or deuterium. The collision of these accelerated particles with the target nuclei induces nuclear reactions that release neutrons. The ability to control the neutron production parameters, including flux, energy, and direction, makes accelerators a valuable tool for applications requiring specific neutron characteristics.

Neutrons can be produced in accelerators through various methods. Each of these technologies presents unique characteristics that make them suitable for different applications. The most powerful established method for neutron production is spallation, which involves accelerating high-energy protons and colliding them with a heavy target material, causing the emission of neutrons. Spallation sources have become the most powerful neutron sources available, surpassing high-flux fission reactors, which have a natural upper limit on neutron production. In 2022 the Spallation Neutron Source (SNS) in Oak Ridge, Tennessee, was recognized as the most powerful neutron source in the world [3]. Meanwhile, the European Spallation Source (ESS) in Lund, Sweden, which is currently under construction, aims to become the world's leading facility for intermediate-duration pulsed neutron production [4].

In the case of Neutron Generators or CANS, the neutron production rate is comparatively lower [5]. CANS typically produce one neutron per nuclear reaction, in contrast to the 20–30 neutrons generated during spallation [6]. To produce low-energy neutrons, CANS primarily utilize technologies such as Linear Accelerators (LINACs), cyclotrons, and electrostatic accelerators [7], while Neutron Generators rely on sealed tubes [8], [9].

Sealed tube Neutron Generators are typically low-energy particle accelerators that direct deuteron beams onto deuterium or tritium targets. Known for their

operational simplicity, these devices are user-friendly and designed for long operational lifetimes. Their high gas efficiency, along with their ability to produce high-density plasmas, allows them to generate significant yields of monatomic species, making them reliable and effective for both research and practical uses.

Electrostatic accelerators, on the other hand, drive charged particles to high energies using a static high-voltage potential. Although primarily effective at lower energy levels, they are still valuable for certain applications requiring modest energy outputs. Notable examples include the Electrostatic Quadrupole (ESQ) accelerator, the Vacuum-Insulated Tandem Accelerator (VITA), and the Single Ended or Dynamitron accelerators.

Cyclotrons, by contrast, accelerate charged particles outward from the center of a cylindrical vacuum chamber along a spiral path. They are notable for their ability to handle fairly high currents, making them well-suited for applications that require more substantial energy outputs.

Finally, linear accelerators or LINACs, particularly Radio-frequency Quadrupole (RFQ) linacs or Drift Tube Linacs (DTL), or a combination of both, offer an excellent solution for delivering large beam currents at energies in the range of a few MeV. This makes them highly efficient for applications where high currents and moderate energies are required.

The Neutron Generation sources and the CANS offer several notable advantages. First, they provide exceptional versatility by allowing the production of neutrons with a wide range of energies through the use of different charged particles and target materials, which is crucial for precise applications like neutron scattering and nuclear data measurements. Secondly, these sources ensure controlled and safe operation, as they can be turned on and off easily, reducing the risk of radioactive contamination and enabling on-demand neutron production, which minimizes waste and simplifies maintenance. Finally, Compact Accelerator-Driven Neutron Source are more compact and adaptable than traditional reactors, making them suitable for various environments, including hospitals and research laboratories, where space and safety are important considerations [10], [11].

Together, these technologies provide precise control over neutron production conditions, which is crucial for applications such as astrophysics, fundamental physics, nuclear technologies and through the different techniques of neutron scattering in condensed matter, biology, biotechnology or electronics. In medicine their importance are centered in radioisotope production and an experimental therapy for cancer known as Boron Neutron Capture Therapy (BNCT). In summary, the use of accelerators for low-energy neutron production offers a versatile and controlled alternative to traditional sources, driving significant advances across multiple scientific and technological disciplines.

1.2 Boron Neutron Capture Therapy of Cancer

One of applications of neutrons in health is called Boron Neutron Capture Therapy [12]. This experimental form of radiotherapy is opening up a new field of research. BNCT stands out from other forms of radiotherapy because of it is ability to selectively target malignant cells while preserving normal tissue. This selective treatment is achieved through the interaction of low-energy thermal neutrons with boron-10, a stable, non-radioactive isotope that is administered to tumor cells prior to irradiation. A key advantage of BNCT is that treatment is usually completed in a single session on the same day. The application lasts only about 30 minutes. This is a major benefit compared to conventional therapies, which require multiple sessions over several weeks.

The therapeutic mechanism of BNCT involves nuclear capture and fission reactions. When boron-10, which is a non-radioactive component of natural boron, is irradiated with low-energy thermal neutrons, it produces high Linear Energy Transfer (LET) to α-particles (helium-4) and lithium-7 recoil nuclei. The reaction can be summarized as follows:

$$^{10}B \ + \ n \ \rightarrow \ [^{11}B] \ \begin{cases} \quad ^{4}He \ + \ ^{7}Li \ + \ 2.79 \text{ MeV} \quad (6\%) \\ ^{4}He \ + \ ^{7}Li \ + \ \gamma \ (0.48 \text{ MeV}) \ + \ 2.31 \text{ MeV} \quad (94\%) \end{cases}$$

For BNCT to be effective, it is crucial to achieve a sufficient concentration of boron-10 in the tumor and ensure that an adequate number of thermal neutrons are absorbed to facilitate capture reactions. The primary nuclear reaction releases gamma rays (denoted as γ), α-particles (denoted as ^{4}He), and lithium-7 ions (denoted as ^{7}Li) with energies of 0.478 MeV, 1.47 MeV, and 0.84 MeV, respectively. Importantly, this decay pathway occurs in about 94% of interactions, with the remaining 6% resulting in the production of only alpha particles and lithium ions without gamma ray emission [13].

Boron-10 is chosen for this therapy due to its high neutron capture cross-section of approximately 3800 barns for thermal neutrons, indicating a strong likelihood of reaction occurrence. Additionally, most of the energy from the reaction is carried by the short-range lithium and alpha particles, ensuring that the damage remains confined to the boron-containing malignant cells. This localized effect helps minimize collateral damage to the surrounding healthy tissue, making boron-10 an effective choice for targeting cancer cells while sparing healthy tissue.

BNCT is especially advantageous for treating tumors located in radiosensitive organs, such as brain tumors and spinal cord cancers. The short range of the isotopes, ^{7}Li and ^{4}He, ensures that the destructive effects of these high-energy particles are confined to the targeted cancer cells, as long as boron is sufficiently localized within the tumor cells. Therefore, clinical interest in BNCT is mainly focused on high-grade gliomas and brain metastases, cancers that have a poor prognosis with other forms of radiotherapy.

1.2.1 The History of BNCT

The history of BNCT began with the discovery of the neutron. An early proposal suggested that if a boron compound could concentrate within a tumor and then be irradiated with neutrons, the resulting boron capture reaction could destroy the tumor cells. This concept was developed by Gordon L. Locher in his 1936 article, "Biological Effects and Therapeutic Possibilities of Neutrons" [14].

In 1950, BNCT was first tested in the United States under neurologist William Herbert Sweet [15], using the Brookhaven Graphite Research Reactor (BGRR). Later, the Brookhaven Medical Research Reactor (BMRR) was built for medical use. Despite numerous trials in the 1960s, results were disappointing due to insufficient neutron penetration of thermal neutrons.

United States experiments led to BNCT research moving to Japan, where Hiroshi Hatanaka initiated a BNCT program. He conducted several clinical trials using a new boron compound, Sodium Borocaptate (BSH or $Na2B12H_{11}SH$), to treat patients with malignant brain tumors across different reactors throughout the country. Hatanaka concluded that the low penetrability of thermal neutrons made a craniotomy, a surgical procedure in which part of the skull is removed to access the brain, necessary. He thus termed his approach "intraoperative BNCT." In 1990, he published promising results on his treatment [16], which showed that the effectiveness of the therapy and patient survival rates improved over time.

The craniotomy is invasive and dangerous for the patient; therefore, alternative methods were explored. The best option found is the use of an epithermal neutron beam. The neutrons produced by these beams penetrate without directly irradiating the brain. During this time, a new boron compound, Boronophenylalanine (BPA), was developed [17]. BPA is a boronated amino acid designed to be more selective for malignant cells and used in BNCT [17].

Starting in the 1990s, efforts were made to modify nuclear reactors to produce a neutron beam suitable for BNCT after moderation. This led to new clinical trials of "modern BNCT" [18], [19], specifically targeting cancers with poor prognoses. BNCT was particularly developed for recurrent head and neck cancers and high-grade gliomas.

Overall, clinical results have been positive and promising. A 2014 report from the Nuclear Physics European Collaboration Committee (NUPECC) [20] indicated that BNCT offers a higher survival rate compared to conventional therapies, especially for head and neck cancers. Most cases show only mild adverse effects, while disease symptoms are significantly reduced.

1.2.2 Current Neutron Sources for BNCT

In recent years, there has been growing interest in Accelerator-based Boron Neutron Capture Therapy (AB-BNCT). As mentioned, advancements in accelerator technology and neutron generation have enabled the production of neutron beams

that, after moderation, can be used for BNCT. These compact systems are expected to be installed in hospitals.

Facility	Accelerator	Beam energy (MeV)	Target reaction	Current designed /status (mA)	Present status
		Cyclotrons			
C-BENS Kyoto University, Japan [21], [22]	Cyclotron	30	^{9}Be(p,n)	1 / 1	Clinical trial
Southern Tohoku Hospital, Japan [23]	Cyclotron	30	^{9}Be(p,n)	1 / 1	Treatments*
Kansai BNCT Research Center, Japan	Cyclotron	30	^{9}Be(p,n)	1 / 1	Treatments*
Pengbo Hainan BNCT Center, China	Cyclotron	30	^{9}Be(p,n)	1 / -	Project planning
		Linac			
A-BNCT, Dawon Medax, Rep. Korea	RFQ-DTL	10	^{9}Be(p,n)	8 / -	Preclinical
Tsukaba University, Japan [24], [25]	RFQ-DTL	8	^{9}Be(p,n)	5 / >2	Preclinical
SARAF, Soreq, Israel [26]	RFQ-DTL	2.5	Liq-Li(p,n)	20 / 1-2	Developing
Legnaro INFN, Italia [27]	RFQ	5	^{9}Be(p,n)	30 / -	Developing
IHEP, BNCT-01, Dongguan, China [28]	RFQ	3.5	^{7}Li(p,n)	5 / 5	Operational
IHEP, BNCT-02, Dongguan, China [28]	RFQ	2.8	^{7}Li(p,n)	20 / -	Under construction
National Cancer Center, Tokyo, Japan [29]–[32]	RFQ	2.5	^{7}Li(p,n)	20 / 12	Clinical trial
Edogawa Hospital BNCT Center, Japan	RFQ	2.5	^{7}Li(p,n)	20 / -	Commissioning
		Electrostatic			
Budker Institute, Novosibirsk, Russia [33]	VITA	2.0-2.3	^{7}Li(p,n)	10 / 3	Operational

Continues on the next page.

Facility	Accelerator	Beam energy (MeV)	Target reaction	Current designed /status (mA)	Present status
Blokhin Cancer Center, Moscow, Russia [34]	VITA	2.3	^{7}Li(p,n)	7 / -	Under construction
Xiamen Humanity Hospital, Neuboron BNCT Center, China [35], [36]	VITA	2.5	^{7}Li(p,n)	10 / 10	Clinical study
CNAO, Pavia, Italy [37], [38]	VITA	2.5	^{7}Li(p,n)	10 / -	Under construction
Nagoya University, Japan [39], [40]	Dynamitron	2.8	^{7}Li(p,n)	15 / -	Commissioning
University of Birmingham, UK	Single ended	2.6	^{7}Li(p,n)	30 / -	Under installation
Helsinki University Central Hospital, Finland [41]	Single ended	2.6	^{7}Li(p,n)	30 / 20	Commissioning
Shonan Kamukara Hospital, Japan	Single ended	2.6	^{7}Li(p,n)	30 / -	Under installation
University Hospital of Brussels, Belgium [42]	Single ended	2.6	^{7}Li(p,n)	30 / -	Project planning
NeMeSis, University of Granada, Spain [43], [44]	Single ended	2.1	^{7}Li(p,n)	30 / -	Under development
CNEA, Argentina [45], [46]	ESQ	1.45	^{9}Be(d,n) Thin 8 μm ^{13}C(d,n)	30 / <1	Under development
KIRAMS, Rep. Korea	ESQ	1.45	^{9}Be(d,n) Thin 8 μm ^{13}C(d,n)	30 / <1	Under development

Table 1.1. List of AB-BNCT current facilities [47], [48]. All targets are thick except those specified. *Treatments covered by public insurance in Japan.

A variety of accelerators are used for BNCT facilities [47], [48], ranging from low-energy electrostatic machines to RFQs, DTLs, and higher-energy cyclotrons. In Table 1.1, a list of the current Accelerator-based Boron Neutron Capture Therapy projects worldwide is presented. The type of accelerator, the energy beam, the target material used for neutron production, the current status, and the details of

each project are indicated.

The table is divided into three sections based on the type of accelerator used: Cyclotrons, Linacs, and Electrostatic Machines. For each facility, detailed information is provided about the specific accelerator type and its corresponding parameters. The beam energy ranges from 1.45 MeV for electrostatic machines to 30 MeV for the cyclotrons. The targets used for neutron production vary, with most facilities utilizing beryllium (Be) or lithium (Li) targets, while a few projects explore other options like carbon-13.

Additionally, the table offers insights into the different stages of these projects, from clinical trials and ongoing treatments to projects under development or construction. Some facilities, like the C-BENS (Cyclotron-based Epithermal Neutron Source) facility at Kyoto University in Japan, are already in clinical use, while others, such as the NeMeSis (Neutrons for Medicine and Scientific applications) at the University of Granada (UGR) in Spain, are still under development. All these projects are designed to follow the guidelines and recommendations outlined in the Technical Document from the International Atomic Energy Agency [48].

It is important to mention NeuCure, an Accelerator-based Boron Neutron Capture Therapy device developed by Sumitomo Heavy Industries, Ltd., which was registered as a medical device for radiation therapy in Japan in 2020. Consequently, BNCT covered by public insurance has been initiated using this device, and numerous patients have already undergone treatment at two hospitals in Japan. As of 2023, clinical studies are ongoing in Japan, China, and Korea, utilizing AB-BNCT devices from various manufacturers, demonstrating the growing global interest and progress in this innovative cancer treatment modality.

All the projects mentioned are based on the conventional approach for BNCT, where neutron moderation is mandatory. This thesis proposes a new approach in which neutron moderation will not be needed.

1.3 Objectives

This thesis aims to explore in detail the processes and methods involved in the production of low-energy neutrons using accelerators, specifically neutron sources based on proton-induced neutron reactions. We will address the measurement techniques needed to accurately characterize and evaluate these neutrons by including the angle-energy spectra of two reactions: the ^{7}Li(p,n) reaction as a reference reaction and the ^{51}V(p,n) reaction as a new measurement. Additionally, the ^{45}Sc(p,n) reaction will be reviewed since data are available in the literature. Finally, based on all this data, we will study the use of the ^{51}V(p,n) and ^{45}Sc(p,n) reactions for BNCT without neutron moderation. We will find that the ^{45}Sc(p,n) reaction would be suitable with existing accelerators, while the ^{51}V(p,n) reaction would require a higher current than that of existing accelerators.

Chapter 2

Overview of (p,n) Reactions as Sources of Low-Energy Neutrons

Proton-induced nuclear reactions, commonly referred to as (p,n) reactions, are recognized as one of the most efficient techniques for neutron production [49]. In these reactions, a proton beam generated by an accelerator is directed onto a suitable target material. When the protons collide with the nuclei of the atoms of the target, neutrons are released as result of the nuclear interaction. The versatility of (p,n) reactions makes them a preferred choice for generating neutrons across a broad energy spectrum. By carefully selecting the target material, it is possible to produce neutrons with energies tailored to specific applications, from fast neutrons to thermal and epithermal neutrons.

This thesis focuses on the study of low-energy, epithermal and thermal, neutrons which are essential for various research and medical applications. To obtain these neutrons, it is critical to select (p,n) reactions capable of generating neutrons within these energy ranges. The most commonly studied reactions for producing these neutrons are ^{7}Li(p,n)^{7}Be and ^{9}Be(p,n)^{9}B [50], known for producing high-energy neutrons that require subsequent moderation to reach lower energies. However, this thesis also investigates alternative reactions, specifically ^{45}Sc(p,n)^{45}Ti and ^{51}V(p,n)^{51}Cr, which offer the potential to directly generate neutrons within the desired energy range, eliminating the need for moderation. The selection of reactions was based on kinematic calculations and previous studies.

2.1 Kinematics of the (p,n) Reactions

The (p,n) reaction is a nuclear process in which an incoming proton is converted into a neutron through interaction with a target nucleus. This type of charge-exchange reaction can be expressed by the following equation:

$$\mathrm{p} + {}^{A}_{Z}X \rightarrow {}^{A}_{Z+1}Y + \mathrm{n} + Q, \tag{2.1}$$

where ${}^{A}_{Z}X$ represents the target nucleus with Z protons and $N = A-Z$ neutrons, A is the mass number, and ${}^{A}_{Z+1}Y$ is the residual nucleus after the proton is exchanged for a neutron. The produced neutron is represented by n and the incident proton by p. Q is the Q-value of the reaction, representing the energy balance, which can be either positive or negative. A positive Q-value signifies energy release, classifying the reaction as exothermic, while a negative Q-value indicates energy absorption, classifying the reaction as endothermic.

Analyzing the kinematics of this type of reaction is crucial for determining the energy and angular distributions of the emitted particles, particularly neutrons, as well as for designing experiments and interpreting results. By applying conservation laws of energy and momentum, one can effectively predict the behavior of the resulting particles [2], [51].

For a (p,n) reaction, it is essential that the total energy before the reaction equals the total energy after the reaction, reflecting the conservation of energy. This total energy includes the kinetic energy of the incident proton, the rest mass energy of the target nucleus, and the kinetic and rest mass energies of the reaction products. We use E_{p} as the proton's kinetic energy, E_{n} as the neutron's kinetic energy, and E_{res} as the kinetic energy of the remaining nucleus. The energy conservation equation can be expressed as:

$$E_{\mathrm{p}} + M({}^{A}_{Z}X)c^2 = E_{\mathrm{n}} + E_{\mathrm{res}} + M({}^{A}_{Z+1}Y)c^2 + Q, \tag{2.2}$$

where $M({}^{A}_{Z}X)$ and $M({}^{A}_{Z+1}Y)$ represent the masses of the target and residual nuclei, respectively, and Q is, again, the Q-value of the reaction. In many nuclear reactions, although the Q-value is small compared to the kinetic energies of the particles, it can still influence the reaction threshold and energy distribution, meaning it cannot be disregarded.

In addition to energy conservation, momentum must also be conserved in the reaction. Before the reaction, the momentum is derived from the incoming proton, while the target nucleus remains at rest. After the reaction, the momentum is shared between the produced neutron and the residual nucleus. The magnitude of the momentum can be related to the kinetic energies, E, by $p = \sqrt{2mE}$. Therefore, momentum conservation can be expressed as:

$$\sqrt{2m_{\mathrm{p}}E_{\mathrm{p}}} = \sqrt{2m_{\mathrm{n}}E_{\mathrm{n}}} + \sqrt{2M({}^{A}_{Z+1}Y)E_{\mathrm{res}}}, \tag{2.3}$$

where m_{p}, m_{n}, and $M({}^{A}_{Z+1}Y)$ are the masses of the proton, neutron, and residual nucleus, respectively. In literature, the mass of the residual nucleus can also be denoted as M_{res}.

The (p,n) reaction often has a threshold energy, defined as the minimum kinetic energy that the incident proton must possess for the reaction to occur. This threshold depends directly on the Q-value of the reaction and the masses of the particles involved. The threshold energy, denoted as E_{th}, can be derived from

energy and momentum conservation considerations and is expressed by:

$$E_{\mathrm{th}} = \frac{(M(^{A}_{Z+1}Y) + m_{\mathrm{n}} - M(^{A}_{Z}X))^2 - (m_{\mathrm{p}} + m_{\mathrm{n}})^2}{2M(^{A}_{Z}X)/c^2}. \tag{2.4}$$

This equation can be rewritten in terms of the Q-value as:

$$E_{\mathrm{th}} = \frac{|Q| \left(m_{\mathrm{p}} + M(^{A}_{Z}X)\right)}{M(^{A}_{Z}X)}. \tag{2.5}$$

This threshold energy is crucial for selecting the appropriate reactions for different applications. For instance, lower threshold energies allow for the use of less energetic proton beams, which enhances treatment accuracy and reduces damage to surrounding healthy tissue in medical applications. In nuclear research, knowing the threshold energy aids in selecting suitable target materials and optimizing experimental setups, making it a key factor in the study of (p,n) reactions.

By knowing the threshold energy for protons, we can compute the corresponding neutron energy, denoted as $E_{\mathrm{n}}(E_{\mathrm{th}})$:

$$E_{\mathrm{n}}(E_{\mathrm{th}}) = \frac{E_{\mathrm{th}} m_{\mathrm{p}} m_{\mathrm{n}}}{(m_{\mathrm{n}} + M(^{A}_{Z+1}Y))^2}. \tag{2.6}$$

Moreover, the angle at which the neutron is emitted, θ_{n}, relative to the direction of the incident proton, is crucial in this kinematic study. The neutron's energy and scattering angle are interrelated and can be predicted using the principles of kinematics. The θ_{n_0} scattering angle, refers to the maximum angle at which the neutron can be emitted as a result of the reaction, and it can be expressed as:

$$\theta_{\mathrm{n}_0}(E_{\mathrm{p}}) = \arccos \left| \sqrt{\frac{M(^{A}_{Z+1}Y) \left(m_{\mathrm{n}} + M(^{A}_{Z+1}Y)\right)}{m_{\mathrm{p}} m_{\mathrm{n}}} \left(\frac{|Q|}{E_{\mathrm{p}}} + \frac{m_{\mathrm{p}}}{M(^{A}_{Z+1}Y)} - 1 \right)} \right| \tag{2.7}$$

In the laboratory frame, the neutron's kinetic energy as a function of its scattering angle can be determined from the conservation of energy and momentum. The general relation for the energy of the neutron as a function of the scattering angle is expressed as:

$$\begin{aligned} E_{\mathrm{n}}(\theta_{\mathrm{n}}) = {} & \frac{E_{\mathrm{p}} m_{\mathrm{p}} m_{\mathrm{n}}}{\left(m_{\mathrm{n}} + M(^{A}_{Z+1}Y)\right)^2} \\ & \times \left[2\cos^2\theta_{\mathrm{n}} + \frac{m_{\mathrm{n}} + M(^{A}_{Z+1}Y)}{m_{\mathrm{n}}} \left(\frac{M(^{A}_{Z+1}Y)}{m_{\mathrm{p}}} \left(\frac{Q}{E_{\mathrm{p}}} + 1 \right) - 1 \right) \right. \\ & \left. \pm 2\cos\theta_{\mathrm{n}} \sqrt{\cos^2\theta_{\mathrm{n}} + \frac{m_{\mathrm{n}} + M(^{A}_{Z+1}Y)}{m_{\mathrm{n}}} \left(\frac{M(^{A}_{Z+1}Y)}{m_{\mathrm{p}}} \left(\frac{Q}{E_{\mathrm{p}}} + 1 \right) - 1 \right)} \right] \end{aligned} \tag{2.8}$$

The angular distribution of the emitted neutrons depends on the nuclear structure and the dynamics of the reaction, often exhibiting anisotropy.

Understanding the kinematics of (p,n) reactions is essential for studying charge-exchange processes and the energy and momentum of the reaction products. By applying conservation laws and utilizing known nuclear masses along with the Q-value, we can predict the energy required for the reaction, the scattering angles of the particles, and the energy distributions of the emitted neutrons and residual nuclei.

2.2 Conventional Low-Energy Neutron Sources Based on (p,n) Reactions

The relatively low-energy neutron spectrum produced by the ^{9}Be(p,n)^{9}B and ^{7}Li(p,n)^{7}Be reactions has motivated their use in various applications. These reactions are particularly significant in the fields of nuclear physics and medicine, where the production of neutrons is critical for various applications, including BNCT for cancer treatment. Both proton reactions are endothermic, with energy thresholds of 1.88 MeV for ^{9}Be(p,n)^{9}B and 2.06 MeV for ^{7}Li(p,n)^{7}Be. This characteristic makes them particularly suitable for applications requiring controlled neutron production, as the reactions can be finely tuned by adjusting the proton beam energy.

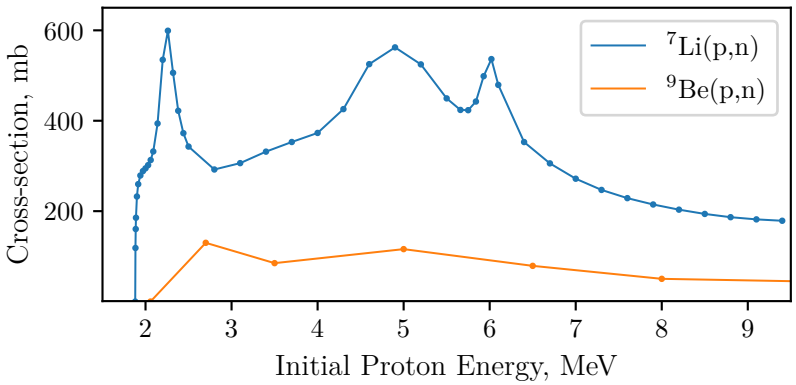

Figure 2.1. Evaluated data from TENDL 2021 [52] for the cross-section data of the ^{9}Be(p,n)^{9}B and ^{7}Li(p,n)^{7}Be reactions.

Figure 2.1 illustrates the cross-sections for both reactions, enabling a direct comparison. Extensive data is available for these two reactions, and for this study, we present the evaluated cross-section data from TALYS-based Evaluated Nuclear Data Library (TENDL) [52]. Since neutron yields are directly determined by the cross-sections of the reactions, this comparison provides valuable insights into their efficiency as neutron sources. The ^{7}Li(p,n)^{7}Be reaction produces a significantly

higher neutron yield at lower proton energies compared to the ^{9}Be(p,n)^{9}B reaction. As illustrated in Fig. 2.1, the cross-section of the ^{7}Li reaction displays distinct resonances, with the first and most pronounced peak occurring at approximately 2.4 MeV.

2.2.1 ^{7}Li(p,n)^{7}Be Reaction as a Neutron Source

The ^{7}Li(p,n)^{7}Be reaction plays an important role in the production of neutrons within the keV energy range. In astrophysics, this reaction is particularly significant because it serves as a reference for a neutron source that replicates neutron fluxes characteristic of certain stellar environments. Specifically, the neutron flux generated through this reaction near the threshold is akin to that of a Maxwellian distribution at a temperature of $kT \approx 25$ keV [53]–[56]. In medical physics, the reaction is crucial, especially in the context of BNCT, as mentioned in Chapter 1, as it is a suitable candidate for producing the needed neutrons for BNCT if they are moderated [48]. Beyond these fields, the ^{7}Li(p,n)^{7}Be reaction is widely utilized in significant research facilities, serving as a reliable and well-understood neutron source across various experimental settings [57].

The lithium reaction exhibits a strong angular dependence when it is produced at energies close to the threshold. When the incident proton energy is 1.912 MeV (the reaction threshold is 1.88 MeV), neutrons are generated within a 60° forward emission cone with energies below 100 keV. In certain applications, this directional emission enhances efficiency compared to isotropic sources by directing more neutrons in the direction of the target. The forward-directed neutron beam also minimizes back-angle radiation, potentially reducing the need of extensive shielding.

The energy spectrum of the neutrons generated by this reaction becomes more complex when the initial proton energy exceeds 2.37 MeV, as it can leave the ^{7}Be nucleus in an excited state, producing lower-energy neutrons. Further complications arise above 3.69 MeV with the opening of the ^{7}Li(p,n^{3}He)^{4}He reaction channel and above 7.11 MeV with another excitation of ^{7}Be. Typically, this complicated region is avoided when producing neutrons, as the goal is to maximize yield. For this reason, neutrons are usually generated through a resonance reaction at a proton energy of approximately 2.25 MeV.

When lithium is used as the target material, the properties of this metal must be considered. Lithium has a melting point of around 180°C and a thermal conductivity of 71 W/(m°C). Due to proton beam irradiation of about 25-75 kW, a significant amount of heat (tens of kW/m^2) is transferred to the lithium target. As a result, advanced cooling techniques are required for the target material system in lithium-based neutron sources. An engineering challenge is designing a lithium target that can handle the high power of the proton beam without damage [58]. To address this challenge, some groups have proposed using liquid lithium as a target material [59]. If liquid lithium is used, the target system should be designed to

ensure safe handling. Additionally, it is important to consider that when lithium reacts with protons to produce neutrons, it transforms into beryllium-7, which has a half-life of approximately 53 days. Due to its relatively long half-life, careful management of the radioisotope is required.

However, lithium offers the advantage of requiring a relatively low proton energy (around 2.5 MeV) for neutron production, allowing the use of a smaller accelerator compared to what is needed for a beryllium-based neutron source. Furthermore, the maximum energy of neutrons emitted from lithium is only a few hundred kilo-electronvolts, which enables the use of smaller moderators for producing epithermal neutrons and reduces the required size of shielding walls. This can result in a more compact building to house the device, potentially lowering the initial cost of the facility. The majority of the AB-BNCT current facilities, presented in Table 1.1, are using a solid lithium target. It is worth mentioning that all these AB-BNCT systems require neutron moderation.

2.2.2 ^{9}Be(p,n)^{9}B Reaction as a Neutron Source

The ^{9}Be(p,n)^{9}B reaction is extensively used to produce neutrons for a variety of industrial and scientific applications, including neutron radiography, non-destructive testing, and neutron scattering experiments. This reaction is commonly employed in particle accelerators and compact neutron generators due to its ability to produce a high flux of neutrons. As mentioned in Chapter 1, one potential application of this reaction is as a neutron source for BNCT [48]. Many of the AB-BNCT facilities listed in Table 1.1 utilize a beryllium target.

The ^{9}Be(p,n)^{9}B reaction occurs just above the threshold energy of 2.057 MeV and is characterized by the emission of neutrons predominantly in the forward direction. Many detailed measurements have been performed to obtain the angle-dependent spectra at different proton energies for this reaction [60]. To achieve optimal neutron yields, slightly higher proton energies or larger beam currents are typically required compared to those used with the lithium reaction. Beryllium offers a higher neutron yield due to its favorable physical properties.

Beryllium has a higher melting point (approximately 1287°C) and better thermal conductivity than lithium, making it more suitable for designing and maintaining neutron target systems. However, the efficiency and safety of using beryllium as a target depend largely on the energy of the incident protons. Higher proton energies increase neutron yield and allow for a thicker target, but they also result in higher energy neutrons, which, in turn, increase the risk of radioactivation. To address this, the proton energy must be carefully optimized to minimize radioactivation while maintaining high neutron production and enabling compact system designs. It is important to note that all these AB-BNCT systems require neutron moderation.

2.3 ^{45}Sc(p,n)^{45}Ti Reaction as a Neutron Source

Turning to reactions that produce low-energy neutrons directly, the scandium (p,n) reaction or ^{45}Sc(p,n)^{45}Ti reaction stands out as a well-studied and promising candidate. This reaction is characterized by threshold energy of 2908.58 ± 0.52 keV and a negative Q-value of -2845.40 ± 0.52 keV, as is measured and reported in Refs. [61]–[63]. As mentioned, this reaction produces neutrons in the keV region, making it significant in various applications.

Figure 2.2 illustrates the kinematics of the reaction, derived from the equations discussed in Section 2.1. This figure presents the dependency between the maximum neutron energy and the incident proton energy across a range of emission angles (0, 15, 30, 45, 60, 75, 90, and 180 degrees). As shown, there is a pronounced angular dependence near the reaction threshold (marked by the grey dashed line), where neutron energies vary significantly depending on emission angle. However, once the proton energy surpasses this threshold, the angular dependence diminishes rapidly, transitioning to a more linear and predictable relationship between proton energy and neutron energy.

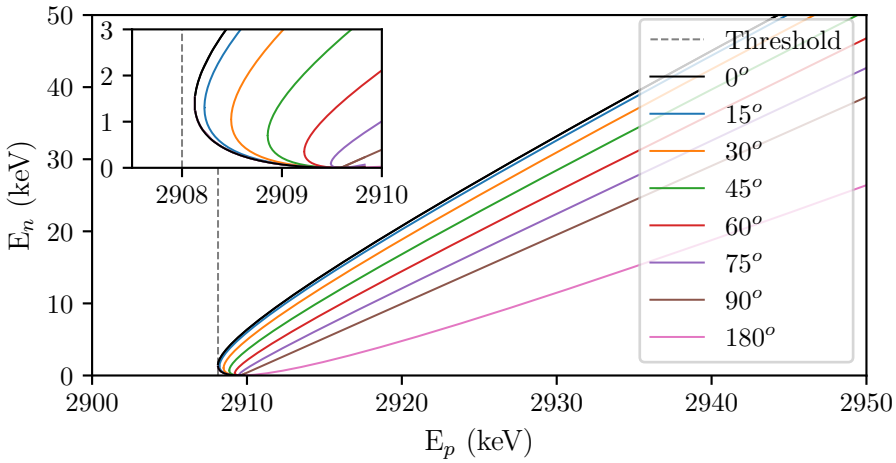

Figure 2.2. Kinematics of ^{45}Sc(p,n)^{45}Ti reaction near-threshold. Maximum neutron energy versus the initial proton energy across a range of emission angles (0, 15, 30, 45, 60, 75, 90, and 180 degrees). The energy threshold is shown by a grey dashed line.

One key feature near the threshold is a small bi-valued region, meaning that at each emission angle, θ_n, neutrons may be produced at two different energies. At the precise threshold energy, a single group of neutrons is emitted at 0° with a unique, monoenergetic energy level, resulting in a distinct energy point. Once the energy surpasses this threshold, two neutron groups with different energy levels are emitted, confined to an expanding forward cone. As the neutron energy continues to increase, this emission cone broadens to eventually cover the entire solid angle.

Meanwhile, the energy of the first neutron group increases, while the energy of the second group gradually approaches zero [64]. This bi-valued characteristic arises due to the nature of the reaction mechanics close to the threshold, resulting in a non-linear behavior that smooths out as the proton energy increases.

The properties of ^{45}Sc(p,n)^{45}Ti reaction make it an attractive substitute for the ^{7}Li(p,n) reaction to generate low-energy monoenergetic neutron fields, as is shown in Ref. [61]. However, the neutron yield is ten times lower than that of the lithium reaction for generating, for instance, 8 keV neutron fields. This deficit could be compensated by allowing higher beam currents and reduced distances. According to Rogers [62], monoenergetic neutrons are produced up to the energy threshold for the 37 keV level in ^{45}Ti, which is reached at an incident energy of 2946 keV. At this threshold, neutrons with an energy of 53 keV are generated.

Moreover, this reaction is a good option for certain detector calibration processes [65], [66]. The ISO standard 8529 [67] recommends ^{7}Li(p,n) and ^{45}Sc(p,n) reactions to calibrate detectors for neutrons with energies below 100 keV. Therefore, the production of the neutrons with energies between 5.6 and 53 keV in the ion beam direction allows for the avoidance of using high emission angles to calibrate neutron devices in this energy range [64]. As studied in Ref. [68], it is a good candidate compared to other reactions, as it presents a high yield at the resonances of 8 and 27 keV.

Referring to the scandium target, it is important to point out that natural scandium consists of one stable isotope, ^{45}Sc, which greatly simplifies the target preparation process. Moreover, solid metallic scandium has a melting point of approximately 1541 °C and a thermal conductivity of 16 W/(m°C), offering better properties compared to beryllium or lithium. A key characteristic shared by all (p,n) reactions for neutron production is that the required target thickness depends on the desired monoenergeticity. As target thickness increases, so do both yield and energy width. Therefore, target thickness should be selected based on specific needs and adjusted according to the stopping power of the reactive layer.

Likewise when the scandium is used as a target, a backing is usually required. In 2010, Lamirand, Thomas, Gressier, *et al.* [69] studied the best backing for this reaction. They compared silver, molybdenum, aluminium, tantalum, tungsten and platinum backings using high beam current irradiation. This study revealed that silver and molybdenum backings significantly contributed to neutron production with a 2.9 MeV proton incident ion beam, rendering them unsuitable for this reaction. Aluminum, while possessing inadequate thermal and mechanical properties due to observed deformation under high beam currents, could still serve as a viable option owing to its low elastic neutron cross-section in the keV range, making it suitable for measurements at low beam currents. Among platinum, tungsten, and tantalum backings, only tantalum exhibited no structural changes under irradiation. Despite the apparent lack of impact on neutron yields by these alterations, tantalum emerges as the preferred choice, not only due to its stability but also its cost-effectiveness. Another option to consider would be copper, not studied by

Lamirand [64]. This option is suitable in the case of lithium, so it could also be suitable for this reaction, although it still needs to be studied.

For this reaction, the total cross-section has been measured using the activation foil method, particularly focusing on the p-n cross-section several times. Experimental data for the cross-section of this reaction have been documented in the literature [70], as well as evaluated data [52]. Figure 2.3 presents experimental data from Refs. [71]–[74] and the TENDL 2021 evaluation [52]. Notably, intriguing resonances are present at values close to the threshold.

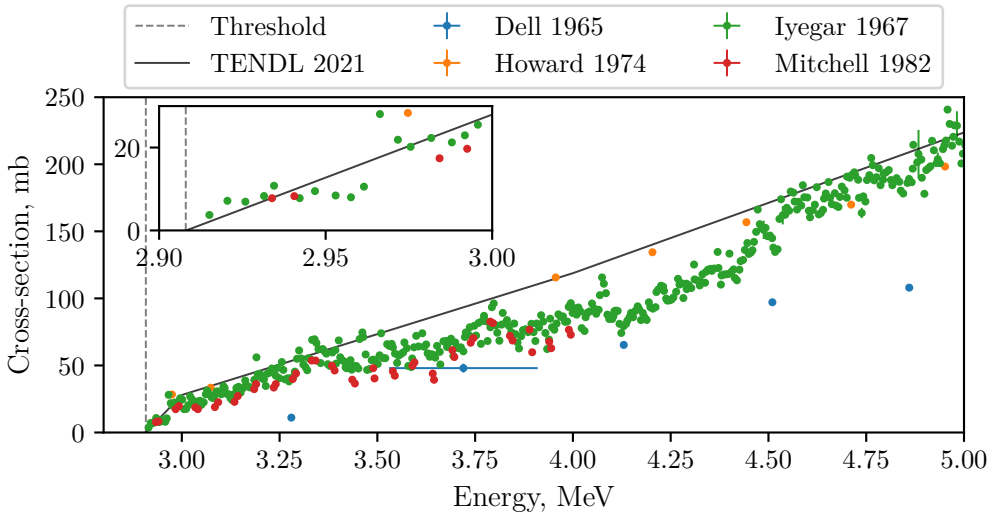

Figure 2.3. ^{45}Sc(p,n)^{45}Ti reaction near-threshold cross-section data. Experimental data from Dell 1965 [71], Howard 1974 [72], Iyegar 1967 [73], and Mitchell 1982 [74], taken from EXFOR [70]. Evaluated data from TENDL 2021 [52] and threshold of reaction are also included, respectively marked by a solid black line and a dashed grey line.

From 1949 to the present day, numerous measurements of angle-dependent cross-sections have been documented in the literature. For instance, Brugger, Bonner, and Marion [61] conducted experiments at proton energies from 2.90 to 5.60 MeV using Sc_2O3 with a target thickness of approximately 120 keV (at Ep=2.9 MeV) and a tungsten backing, focusing on yield measurements with a Long Counter (LC). Similarly, Rogers [62] performed measurements within the 2.89 to 3.02 MeV range using pure Sc and Sc_2O3, with a target thickness of 43 μg/cm^2 (3.2 keV at Ep=3.0 MeV), comparing the yield with the ^{7}Li(p,n) reaction.

Cosack, Lesiecki, and Hunt [75] studied the reaction at proton energies of 2.90–2.95 MeV using pure Sc, with a target thickness of 5 μg/cm^2 (0.3 keV at Ep = 2.9 MeV). Their work employed both the Time-Of-Flight (TOF) method with lithium-glass detectors and yield measurements with an LC. Similarly, Tanimura, Saegusa, Shikaze, *et al.* [66] investigated the same energy range (2.90–2.95 MeV) with pure Sc but used a thicker target of 50 μg/cm^2 (3.7 keV at Ep = 3.0 MeV)

with a platinum backing. Their experiments included TOF measurements, yield assessments, and resonance measurements at 8 keV and 27 keV.

It is worth emphasizing that the reaction exhibits a complex resonance structure for the cross-section at 0 degrees. A comprehensive excitation curve illustrating the yield variation with proton energy is detailed in Ref. [75]. Within this monoenergetic spectrum, several significant resonances appear just above the threshold, as illustrated in Fig. 2.4. In particular, the neutron energy peaks at 8.15 and 27.4 keV are crucial and frequently utilized. Precisely adjusting the ion beam energy to a resonance minimizes neutron energy uncertainty during irradiation. The narrow width of these resonances, typically less than 0.5 keV [75], results to a rapid decrease in yield with any deviation in energy. Consequently, the beam energy can be fine-tuned with an uncertainty of less than 100 eV.

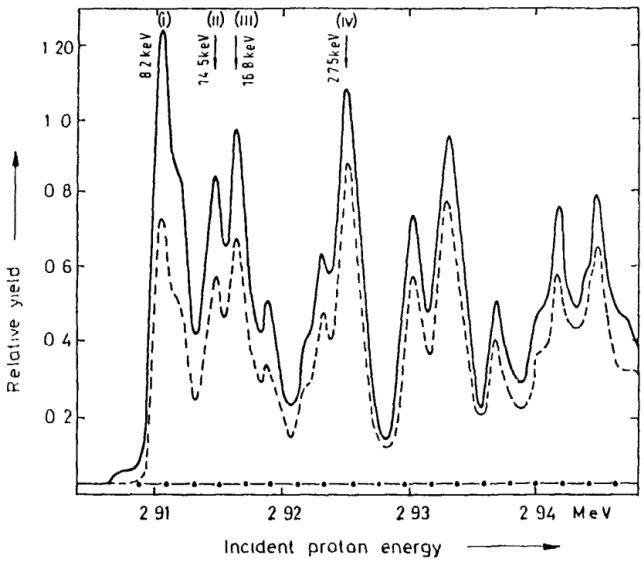

Figure 2.4. Relative spectrum neutron yield of ^{45}Sc(p,n) reaction as a function of proton energy for a thin target at angles 0° (- -) and 60° (–) with respect to the incoming proton beam measured with a Long Counter. Figure from [75].

As mentioned, Cosack, Lesiecki, and Hunt [75] characterized the neutron energy spectrum and verified the 8 keV resonance using the time-of-flight method with both thin and thick Sc targets. The various resonances exhibit clear energy distinctions, with the main ones identified at 8.2, 14.5, 16.8, 27.5 and 36.7 keV, measured at 0 degrees of emission. The purity of the spectrum, notably demonstrated by thin target Time-Of-Flight measurements, renders the reaction highly suitable for generating low-energy monoenergetic neutron fields.

If we study the resonance at 8.15 keV at different neutron emission angles, we can see a decrease in emission energy as the angle increases. This is justified by the kinematics described in Section 2.1. The same occurs if we examine the 27.4 keV resonance [76]–[78].

In Ref. [64], they performed a TOF experiment to identify the resonances observed in Figure 2.4. Subsequently, the excitation function was characterized using both a thin and a thick target. The final values for the cross-section at 0° are 3.39 ± 0.08 and 2.93 ± 0.07 mb·sr^{-1} for 8.15 and 27.24 keV respectively. Additionally, in Ref. [79], a TOF measurement for these two peaks was performed.

Finally, the photon contribution of this reaction must be taken into account in BNCT for dose considerations. When a proton interacts with scandium (^{45}Sc), it can overcome the Coulomb and nuclear potential barriers, forming excited ^{46}Ti* nuclei. These nuclei can decay by emitting particles such as neutrons or photons:

$$^{45}Sc + p \rightarrow ^{46}Ti^{*} \rightarrow ^{45}Ti + n \quad \text{or} \quad ^{46}Ti^{*} \rightarrow ^{46}Ti + \gamma.$$

If the ^{46}Ti* nucleus is sufficiently excited, its decay to ^{45}Ti may occur in two consecutive steps ((p,nγ) reaction). However, in this study, the proton energy remains below that threshold. The formed ^{46}Ti is stable, but ^{45}Ti decays via electron capture and β^{+} emission (100%, $T_{1/2}$=184.8 minutes):

$$^{45}Ti \rightarrow ^{45}Sc* + e^{+} + \upsilon_{e} \rightarrow ^{45}Sc + X \quad \text{or} \quad ^{45}Ti^{*} \rightarrow ^{45}Sc + e^{-}.$$

In Ref. [80], a comparison between the neutron and photon yields is shown in the proton energy range of 1.4-3.8 MeV. Below the neutron threshold, the gammas probably originate from ^{45}Sc(p,γ)^{46}Ti or ^{45}Sc(p,p'γ)^{45}Sc. However, after this energy threshold, there are some coincident resonances between the photon and neutron yields, in most cases within an error of ± 20 keV. The photon emission when the (p,n) process has started is due to the ^{45}Ti gamma emissions. The energy levels of the ^{45}Ti resulting from the ^{45}Sc(p,n) reactions are studied in Ref. [81].

Despite contamination concerns, it is important to note that the photon contribution to the total dose from the ^{45}Sc(p,n) reaction is minimal [64]. The main dose from this study comes from interactions in the tantalum backing. Even though in small amounts, the low-energy gammas produced must be considered for gamma-sensitive devices.

2.4 ^{51}V(p,n)^{51}Cr Reaction as a Neutron Source

The vanadium (p,n) reaction or ^{51}V(p,n)^{51}Cr reaction has been utilized as a monoenergetic neutron source in various applications. It has a threshold of 1565.28 ± 0.24 keV and a Q-value of -1534.92 ± 0.24 keV, measured multiple times in Refs. [82]–[88]. This reaction produces neutrons in the keV range and has many similarities to the Sc(p,n) reaction described above.

Figure 2.5 illustrates the kinematics associated with the reaction, as derived from the equations presented in Section 2.1. Notably, the ^{51}V(p,n) reaction exhibits a pronounced angular dependence. However, this angular dependence diminishes rapidly once the energy of the incoming proton exceeds the threshold.

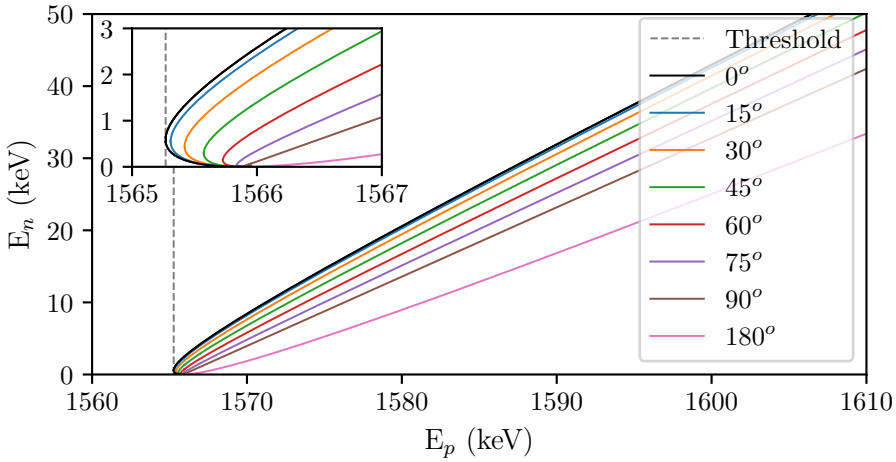

Figure 2.5. Kinematics of ^{51}V(p,n)^{51}Cr reaction near-threshold. Maximum neutron energy versus the initial proton energy across a range of emission angles (0, 15, 30, 45, 60, 75, 90, and 180 degrees). The energy threshold is shown by a grey dashed line.

Again, there is a bi-valuated region near the reaction threshold, where an angle and an initial proton energy can produce neutrons of two different energies.

Near the threshold, Ballini *et. al* [89] measured the angular distribution of neutrons from this reaction to the ground state and to the first two excited states of Chromium-51 at a mean proton energy of 4.07 MeV. They observed that the neutrons emitted leading to the ground state of ^{51}Cr exhibited isotropic behavior within a margin of error of 5%. Similarly, the neutrons leading to the first two excited states of ^{51}Cr were found to display isotropic characteristics within a margin of error of 10%.

In addition, Deconninck and Royen [90] described a slow variation of neutron energy with emission angle. The authors analyzed this reaction at energies between 2.2 and 4 MeV (where the reaction is open to all emission angles), using a thin vanadium target. They stated that, to achieve monoenergetic field production, this reaction could be interesting if it were deployed at a later angle to reach exceptionally low energies. However, its feasibility depends on the neutron emission rate.

The kinematic relations of the ^{45}Sc(p,n) reaction (Fig. 2.2) is similar to ^{51}V(p,n) (Fig. 2.5), and the production of low-energy neutrons is fundamentally the same. However, the significant difference between the thresholds, makes the neutron yield near-threshold much higher for the Sc reaction than the V reaction. The yield in the forward direction for the scandium reaction is approximately 40 times larger compared to the vanadium reaction near-threshold [91].

The potential applications of the ^{51}V(p,n)^{51}Cr reaction are quite diverse [92]. This reaction can serve as a neutron source for measuring the absolute cross-section

of the ^{197}Au(n,γ)^{199}Au reaction at various neutron energies [93]. Additionally, it is an excellent source for obtaining absolute neutron fluxes, which are crucial for calibrating neutron detectors, as demonstrated in Ref. [94]. In particular, it is well-suited for calibrating 4π-geometry neutron detectors, which are relatively insensitive to neutron energy [95]. Finally, this reaction may also be useful as a neutron source in spherical-shell transmission experiments [96], allowing for measuring selected non-elastic neutron cross-sections as a function of neutron energy.

When discussing a vanadium target, it is important to note that V is a malleable transition metal that is rarely found in its pure form in nature. The only stable isotope is V-51, while V-50 has a long half-life of $1.5 \cdot 10^{17}$ years (decaying via β^- or ϵ). Naturally occurring vanadium consists of 99.75% V-51 and 0.25% V-50. Consequently, some contamination occurs when natural vanadium is used as a target. Therefore, the ^{51}V(p,n) ^{51}Cr reaction is systematically contaminated by the ^{50}V(p,n)^{50}Cr and ^{50}V(p,γ) ^{51}Cr reactions. These latter reactions are exothermic, with Q-values of 0.25 MeV and 9.50 MeV, respectively [92]. This results in a not strictly monoenergetic field, even within the monoenergetic range of the ^{51}V(p,n) reaction. However, the contamination is very low, less than 0.2 percent from the ^{50}V(p,n) reaction, with no significant gamma production.

Thin vanadium targets are readily produced via vacuum evaporation, often using tungsten, as described in Refs. [84], [92]. Vanadium is easy to fabricate into thin blanks, making it efficient for repetitive experiments. It also exhibits excellent thermal and electrical conductivity, with a high melting point of 1710°C. This makes it suitable for relatively high beam currents, which can help compensate for the low cross-section of the ^{51}V(p,n) reaction. Harris, Grench, Johnson, *et al.* [92] improved target adhesion by cooling the backing and highlighted the importance of both mechanical and chemical surface cleaning, allowing for beam currents of approximately 10 μA. Gibbons, Macklin, and Schmitt [84] achieved successful measurements with a 30 μA proton beam. Additionally, while ^{51}V was once relatively inexpensive, the rising cost of high-purity ^{51}V [90] has increased the demand for more material-efficient production methods, such as the implantation technique developed at the SIDONIE facility [97], [98].

There are available experimental data for the cross-section of this ^{51}V(p,n) reaction [70], as well as evaluated data [52]. Figure 2.6 displays experimental data from Refs. [71], [86], [92], [99]–[110] and the TENDL evaluation [52]. This figure reveals numerous discrepancies or resonances in the near-threshold energy range, suggesting that a more precise evaluation near the threshold may be necessary.

In addition to the presented total cross-section values in the Fig. 2.6, Gibbons and Macklin [112] conducted a detailed measurement of the cross-section from the threshold up to 2.25 MeV, which is precisely within the region of interest for this thesis. Their findings agree with the Johnson 1958 [99] data presented.

The total cross-section of this vanadium reaction is lower than that of the conventional ^{7}Li(p,n) reaction. For example, in ^{51}V(p,n) neutron production with proton energies between 2 and 4 MeV, the cross-section is about one-fifth that

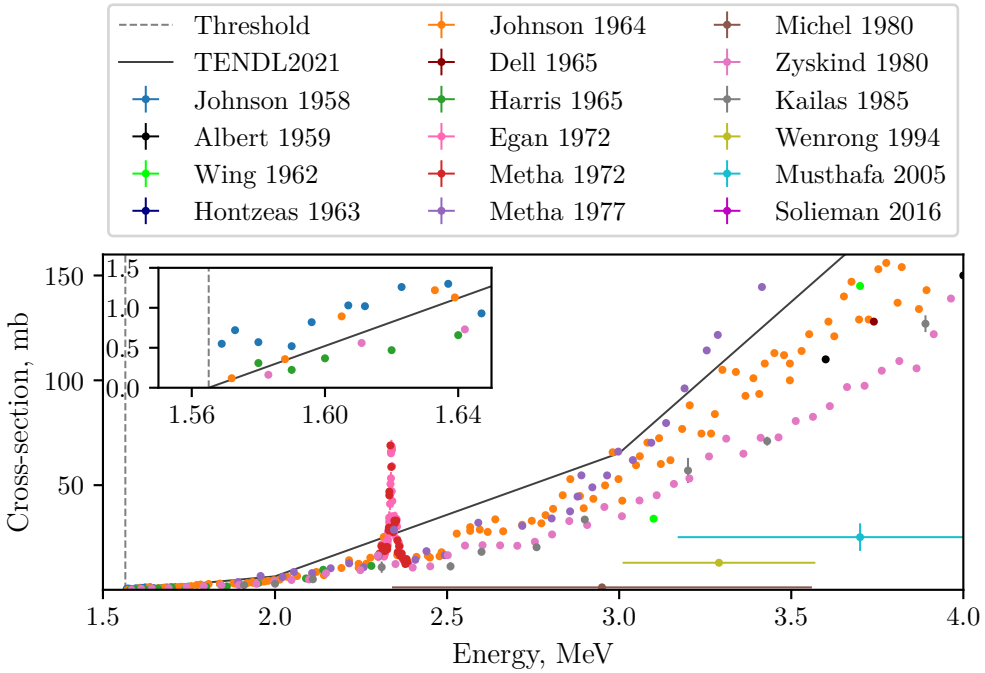

Figure 2.6. ^{51}V(p,n)^{51}Cr reaction near-threshold cross-section data. Experimental data from Johnson 1958 [99], Albert 1959 [100], Wing 1962 [101], Hontzeas 1963 [102], Johnson 1964 [86], Dell [71], Harris [92], Egan 1972 [103], Metha 1972 [104], Metha 1977 [105], Michel 1980 [74], Zyskind 1980 [107], Kailas 1985 [108], Wenrong 1994 [111], Musthafa 2005 [109] and Solieman [110], taken from EXFOR [70]. Evaluated data from TENDL 2021 [52] and threshold of reaction are also included, respectively marked respectively by a solid black line and a dashed grey line.

of ^{7}Li(p,n) [90]. Additionally, Gibbons and Macklin [112] reported a total cross-section of 1 mb for producing 100 keV neutrons with a proton energy of 1655 keV, which contrasts sharply with the several hundred millibarns observed in the ^{7}Li(p,n) reaction.

Specifically at 0 degrees, neutrons generated in the direction of the ion beam have an energy of 2.36 keV, according to Ref. [90], or 2.41 keV based on kinematic calculations, at the monoenergetic threshold. The first excitation level of the residual nucleus ^{51}Cr occurs at over 750 keV, requiring a proton energy of 2.335 MeV to produce a competing second neutron group [90].

In 1955, Gibbons, Macklin, and Schmitt [84] measured the neutron yield for the ^{51}V(p,n)^{51}Cr reaction using a thin vanadium target with a thickness of 1 keV. The yield was recorded from 1.55 to 1.68 MeV, revealing numerous resonances. Several intense peaks in the ^{51}V(p,n) reaction were identified along with their corresponding 0° neutron energies: at Ep = 1.568 MeV, a peak at En = 4.8 keV; at Ep = 1.573 MeV, a peak at En = 11.3 keV; at Ep = 1.575 MeV, a peak at En = 13.6 keV; and at Ep = 1.592 MeV, a peak at En = 34 keV. This neutron yield

was successfully reproduced in Ref. [64] with excellent agreement.

One of the first neutron spectrum measurements was performed by Stelson *et al.* [113] at E_p=3.23 and 3.72 MeV. Later, Kneff, Lefevre, and Din [87] obtained a neutron Time-Of-Flight (nTOF) spectrum for this reaction using a thick target and a proton energy of 1595 keV. Figure 2.7 shows the results. A pulsed proton beam with an energy near 1595 keV was directed at a ^{51}V target, resulting in neutron emissions detected along a 40 cm flight path. The resulting spectrum reveals a pronounced peak at 6.49 ± 0.04 keV. This prominent peak, along with smaller resonance peaks, corresponds to specific energy states achieved as protons slow down within the target and satisfy resonance conditions. In Ref. [87], the authors did not identify the II and III peaks by energy. However, using the energy scale shown in Fig. 2.7, we can estimate that the II peak is approximately 12.2 ± 0.2 keV, and the III peak is roughly at 14.8 ± 0.2 keV.

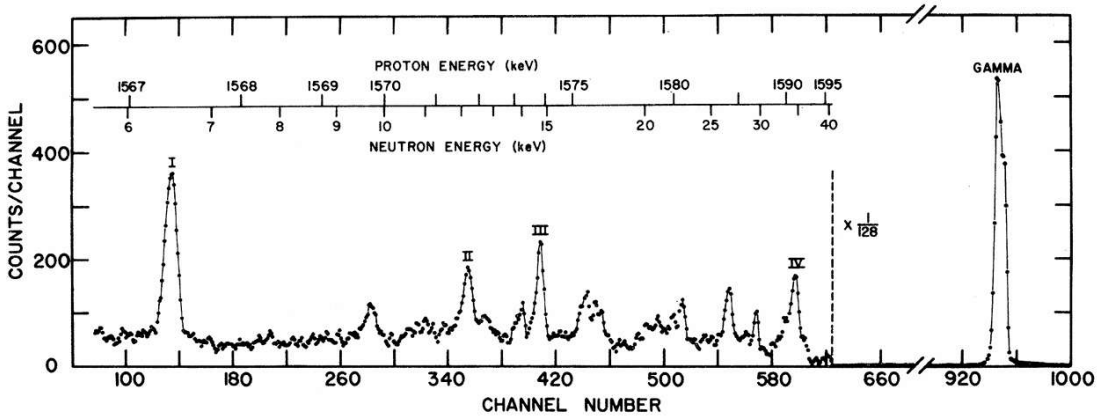

Figure 2.7. Neutron Time-Of-Flight spectrum from ^{51}V(p,n) near-threshold measured in Ref. [87], at 1595 keV using a thick vanadium target. The prominent peak at 6.49 ± 0.04 keV indicates a resonance.

Moreover, Scholermann and Bottger [88] analyzed the resonance structure of the ^{51}V(p,n) cross-section immediately above the threshold using time-of-flight measurements. Their results are shown in Figure 2.8. They irradiated a target with a thickness of 50 keV with protons at an energy approximately 50 keV higher than the reaction threshold. A single discernible peak corresponding to a neutron energy of 6.44 ± 0.195 keV was identified. This peak was confirmed by the measurement in Ref. [64].

The main difference between the spectrum shown in Fig. 2.7 and the one presented in Fig. 2.8 is the energy range of neutron production. In the experiment performed by Scholermann and Bottger [88], a higher energy was used compared to the experiment conducted by Kneff, Lefevre, and Din [87], resulting in a higher maximum neutron energy. However, the peaks shown in both spectra correspond well to each other. The most significant peak is at 6.49 ± 0.04 keV in the first case and 6.44 ± 0.195 keV in the second, and they align closely. The peaks marked II

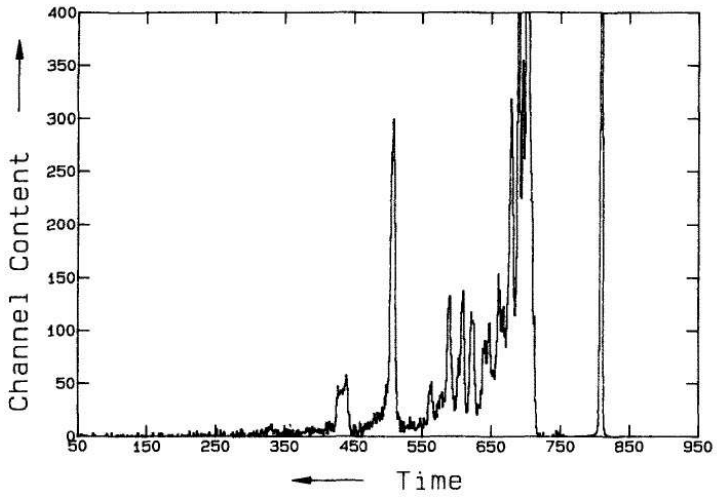

Figure 2.8. Neutron Time-Of-Flight spectrum from ^{51}V(p,n) near-threshold. The peak at channel 508 corresponds to the 6.44 keV neutrons [88].

and III in Fig. 2.7 can also be seen in Fig. 2.8.

Regarding the photon contribution, chromium-51 has a mean lifetime of 27.704 days and a decay mode of ϵ (100%). It can decay to the ground state directly (90.070%) or to an excited state and emit a gamma particle of 320.1 keV (9.930%). In Ref. [80], the thin target yields (neutron and gamma-ray) are measured from 1.6 to 3.6 MeV. Above the (p,n) threshold energy, the peaks coincide in most cases within the experimental error of $\pm$ 20 keV. Additionally, in Refs. [107], [114], extensive studies of emitted photons are performed.

Chapter 3

Experimental Method

In this chapter, we present a detailed explanation of the experimental method used to produce and measure the ^{7}Li(p,n)^{7}Be and ^{51}V(p,n)^{51}Cr reactions near the threshold using the Time-Of-Flight technique. This includes a description of the experimental facility, the setup components, including the targets, the detectors, and the data acquisition system, and finally the calibration of the accelerator used to ensure accurate measurements.

The beamline for the measurements, along with a three-month early-researcher stay for the PhD candidate (Antònia Verdera), has received funding from the Euratom Research and Training Programme 2014-2018 under grant agreement No. 847594 [115]. The EURATOM coordination and support project "Accelerator and Research Reactor Infrastructures for Education and Learning (ARIEL)" brings together the most modern and state-of-the-art European neutron beam laboratories, utilizing the full range of neutron sources from high-energy proton synchrotrons to research reactors.

3.1 The Time-Of-Flight Technique

The Time-Of-Flight (TOF) technique allows the measurement of particle energy based on the time it takes for them to travel a certain distance. This technique is particularly effective for neutrons, where alternative methods typically used for charged particles are not applicable. For neutron detection, this method is referred to as neutron Time-Of-Flight (nTOF), and it is commonly used for measuring cross-sections and neutron yields as a function of energy.

A schematic representation of the technique is illustrated in Figure 3.1. A pulsed beam of charged particles strikes a target, generating neutrons almost simultaneously. The produced neutrons then travel to a detector located at a certain distance from the neutron-producing target, known as the flight path length or flight path, denoted as L. The neutrons are emitted as a pulse, consisting of neutrons with different energies traveling at varying velocities, which causes the expansion of the pulse as it moves toward the detector. In addition to the neutron

pulse, a gamma pulse is also generated in the target. This gamma pulse is referred to as a gamma flash (γ-flash), and it is detected by the detector almost immediately, as it travels at the speed of light and does not expand like the neutron pulse. Fig. 3.1 shows our specific measurement, where the emitted particles are protons.

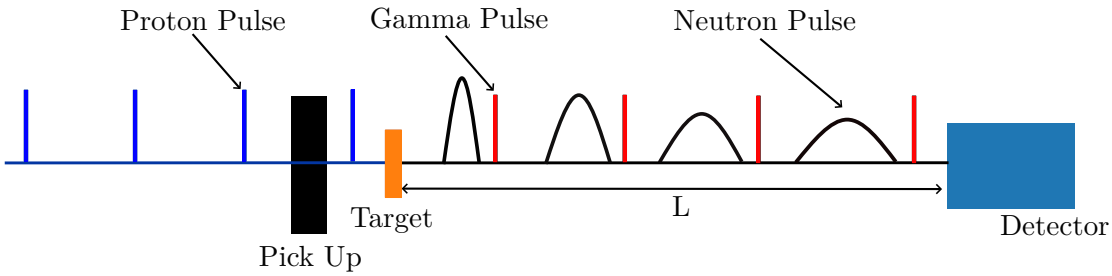

Figure 3.1. Schematic representation of the neutron Time-Of-Flight technique. The pulse interacts with the target, generating neutrons (neutron pulse) and gamma rays (gamma pulse) which travel along a flight path length, L, to the detector. The indicated Pick Up is measuring the signal of the pulsed proton pulse.

The time-of-flight of the neutrons, denoted directly as TOF, is the time that the neutrons spend to go from the production target where the reaction takes place to the detector. Knowing this TOF, the neutron energy (E_n) can be determined as follows:

$$E_n = E - m_n c^2 = (\gamma - 1) m_n c^2, \tag{3.1}$$

where $\gamma = \left(\sqrt{1 - {v_n}^2/c^2}\right)^{-1}$ is the Lorentz factor, c is the speed of light, m_n is the neutron mass and v_n is the velocity of the neutron. The velocity of the neutron in this case is determined by $v_n = L/TOF$, therefore we can simplify the equation for the neutron energy as:

$$E_n = m_n c^2 \left(\frac{1}{\sqrt{1 - \left(\frac{L}{\mathrm{TOF} \cdot c}\right)^2}} - 1 \right). \tag{3.2}$$

At energies below tens of MeV, such as in our cases where we are interested in epithermal neutrons, relativistic effects are negligible. The relationship can be simplified to the classical formula:

$$E_n \approx \frac{1}{2} m_n \left(\frac{L}{\mathrm{TOF}} \right)^2. \tag{3.3}$$

As mentioned, the TOF is defined as the time it takes for a neutron to travel the flight path from its production at the target until its detection at the detector. Therefore, it is calculated as the difference between the detection or measured time (t) and the time when it was generated in the target, termed reference time (t_{ref}).

The reference time is defined using an external reference, such as the Pick-Up (as illustrated in Fig. 3.1) or the acceleration tower pulse. This t_{ref} acts like a starting "clock" in our system.

The γ-flash consists of a significant amount of gamma radiation, potentially accompanied by other ultra-relativistic particles, generated in the target and detected in our detector. The ability to distinguish between the γ-flash peak and neutrons depends on the chosen flight path value and the beam time resolution. The time associated with the γ-flash can be defined using the reference time as $t_\gamma = t_{ref} + L/c$.

The energy resolution in this technique is mainly characterized by the uncertainties in the neutron flight time (ΔTOF) and in the flight path (ΔL). On one hand, the uncertainty in the flight path arises from the finite sizes of the detector and the neutron-producing target. On the other hand, the TOF uncertainty is influenced by the time resolution of the detector and the acquisition system, as well as the quality of the pulse in the beam. Therefore, the energy uncertainty can be described as:

$$\Delta E_n = 2E_n \sqrt{\left(\frac{\Delta \mathrm{TOF}}{\mathrm{TOF}}\right)^2 + \left(\frac{\Delta L}{L}\right)^2}, \tag{3.4}$$

taking into account this relation, the energy resolution (less uncertainty, ΔE) can be increased when the flight path is raised, with a trade-off in neutron flux, which decreases proportionally to $1/L^2$. This equation will directly provide us with the energy resolution of our setup, if we consider a constant time resolution and flight path. It is important to find a compromise between neutron yield and energy resolution. If we use a short L, we will have many counts but a low energy resolution, and if we use a very long L, we will have fewer counts.

At this point, we have a good understanding of the TOF technique. With this knowledge, we can see that it is indeed possible to measure neutron spectra that depend on angle. This can be accomplished by placing a neutron detector at a specific distance L from the source and orienting it at a certain angle. By doing so, we can capture how the neutron spectra vary with direction, providing valuable information for our analysis.

It should be noted that in full forward neutron production measurements, we will try to cover the entire production aperture with measurements taken at different angles. For instance, Li(p,n) has a maximum degree aperture of 65° at 1912 keV, while V(p,n) at 20 keV above the threshold is completely open. These measurements are then weighted, and the angle-integrated neutron spectrum is obtained. One point to note is that if we want to cover all angles in steps of 5 degrees using detectors with a radius of 2.54 cm, we need a distance L of approximately 58 cm. If we wish to do this with steps of 10 degrees, a distance L of approximately 29 cm is sufficient.

3.2 MONNET Facility in JRC

The Joint Research Centre (JRC) is the European Commission's science and knowledge service. Its mission is to support European Union policies with independent scientific evidence throughout the entire policy cycle. One of the six JRC sites is located in Geel (JRC-Geel), Belgium, while the other sites are in Ispra (Italy), Petten (Netherlands), Karlsruhe (Germany), Seville (Spain), and Brussels (Belgium). The JRC-Geel site is home to several multidisciplinary research facilities and laboratories. Two particle accelerators, MONNET [116], [117] and GELINA [118], are primarily dedicated to nuclear physics research.

The MONNET facility (an acronym for MONo-energetic NEutron Tower) is a tandem-accelerator-based fast-neutron source, which became operational in 2020. It operates at high intensity, driven by a vertical 3.5 MV tandem accelerator to generate either continuous or pulsed streams of protons, deuterons, or helium ions, as shown in Figure 3.2a. Quasi-monoenergetic neutrons, with energies reaching up to 24 MeV, are produced through charged particle-induced reactions employing various beam/target combinations, such as protons or deuterons on lithium-7, tritium, or deuterium targets. MONNET can also be used as a photon source or for studies where proton, deuteron, or alpha beams are needed, with less focus on neutron output. The main research topics of this facility are high social impact activities, nuclear safeguards and security, and fundamental physics.

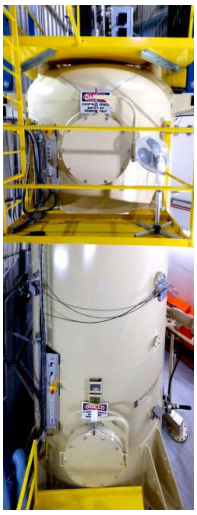

(a) Vertical 3.5 tandem accelerator [116].

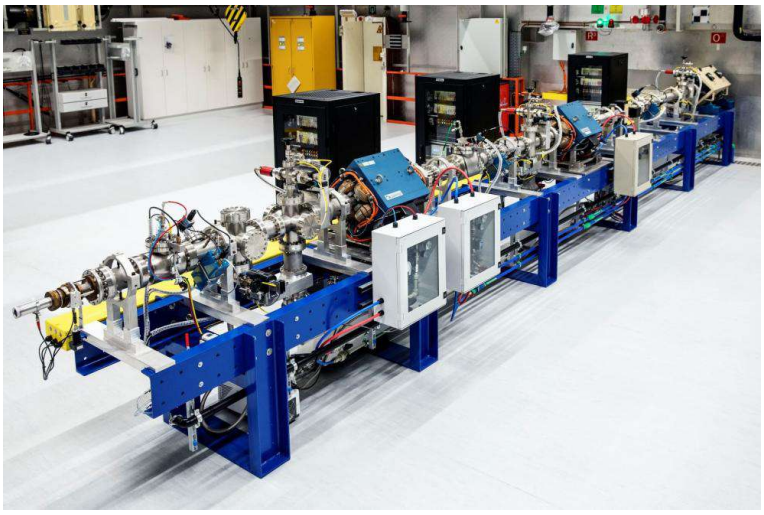

(b) Beamline in 2020 [119].

Figure 3.2. MONNET facility pictures.

For all the measurements included in this thesis, we have used the pulsed and continuous proton beam to produce neutrons via the reactions: ^{7}Li(p,n)^{7}Be and ^{51}V(p,n)^{51}Cr. The used beamline is illustrated in Fig. 3.2b. For the lithium reaction, we will measure a near threshold spectrum at 0 and 30 degrees to use it

as a reference; it will be presented in Chapter 4. The measurement of the vanadium reaction will be more detailed; all angles from 0 to 90 degrees will be measured, as addressed in Chapter 5. Subsequently, we will provide a detailed description of all the components of our experimental setups.

3.3 Experimental Setup

The main components for measuring ^{7}Li(p,n)^{7}Be and ^{51}V(p,n)^{51}Cr using the time-of-flight technique, in addition to the accelerator itself, are the targets, the detectors, and the data acquisition system.

3.3.1 Targets: LiF and Vanadium

The target thickness in (p,n) reactions directly affects the monoenergeticity of the beam, but the yield increases with both thickness and energy width. Therefore, most experiments aim to find a balance between the two. In our case, we have prioritized using a thicker target to maximize yield, with less concern for energy degradation.

In this measurement campaign, thick targets were used for both materials, lithium and vanadium. In this context, a thick target is defined as a target material thick enough that all particles traversing it have energies below the threshold for the (p,n) reaction of interest. In both cases, the target assembly was cooled by forced airflow on the external side of the target, while the internal side was in a vacuum.

LiF Target

For the measurements of the ^{7}Li(p,n)^{7}Be reaction, a target of lithium fluoride of 3.78 mg/cm^2 deposited on a aluminium plate has been used. To perform our measurement, LiF was selected as the target because it is simpler to manage than pure solid or liquid lithium. In fact, lithium fluoride is preferred over elemental lithium in many applications due to its greater stability and safety. While lithium is highly reactive and hazardous, reacting violently with water and air, lithium fluoride is chemically stable, non-flammable, and easier to handle and store. Additionally, LiF possesses valuable properties such as high thermal stability, a high melting point, and excellent optical characteristics. For our application, it is appropriate to use both options, but in this case, the selected material was LiF.

The LiF target used belongs to the MONNET facility and is sealed by the MONNET team. The technical geometry of this target was provided and is illustrated in Figure 3.3a. The aluminum plate, shown in grey, has a thickness of 1 mm, while the LiF target is depicted in blue. This target was placed at the end of the beamline, as shown in the image in Fig. 3.3b.

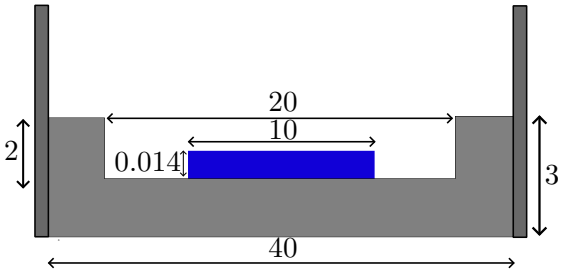

(a) Geometry of the LiF target. The blue area represents the LiF target, while the grey area corresponds to the aluminum backing and tube. The dimensions in the figure are not to scale, and all values are given in millimeters.

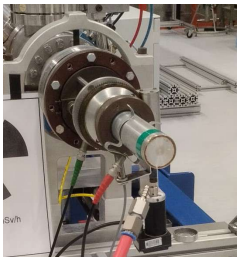

(b) A real picture of the LiF target placed at the end of the beamline. The airflow is shown.

Figure 3.3. Lithium fluoride target geometry and image.

The thickness of the LiF is 14.3 μm for this target, as shown in Fig. 3.3a. To ensure that this is a thick target for the proton energy used in our experiment, a Monte Carlo (MC) simulation was performed using Stopping power and Range of Ions in Matter (SRIM) [120]. In this simulation, protons with an initial energy of 2.27 MeV were propagated through a 14.3 μm thick lithium fluoride layer. The results are illustrated in Figure 3.4. This target does not completely stop the protons with an initial energy of 2.27 MeV, but the energy profile of the transmitted protons shows that it is lower than the threshold of the reaction (1880 keV). This confirms that a layer with a thickness of 14.3 μm qualifies as a thick target if the energy of the proton beam ranges from 1.88 to 2.27 MeV. Since we measure the Li(p,n) reaction near the threshold, this target qualifies as thick.

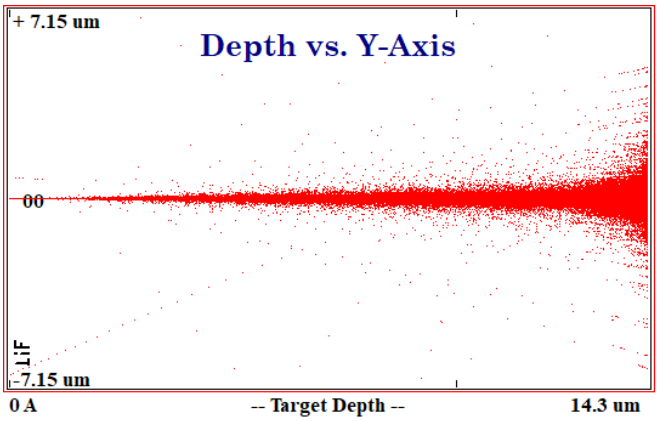

(a) Proton penetration in lithium fluoride target depth.

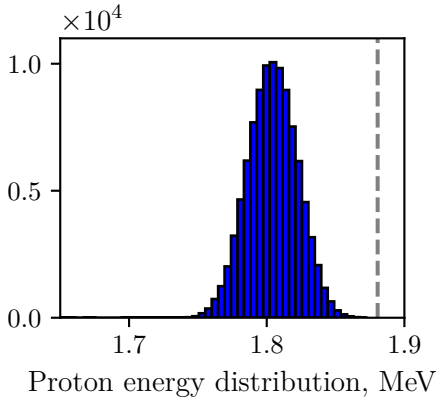

(b) Energy distribution of the transmitted protons.

Figure 3.4. Results from 2.27 MeV protons incident on a 14.3 μm layer of lithium fluoride conducted with SRIM [120] Monte Carlo software. The grey dashed line is marking the ^{7}Li(p,n) threshold.

Vanadium Target

The case of the vanadium target is simpler, as it is not a pre-designed target and lacks backing. We purchased a sheet of pure vanadium-51 with a thickness of 500 μm and cut multiple circles from it to use as targets. To position these vanadium cut sheets at the end of the beamline, a fixing system was employed. A photo of the vanadium target at the end of the beamline, secured by the fixing system, is shown in Figure 3.5a. In this photo, the air flow is also illustrated.

In 3.5b, a used ^{51}V target foil is shown, in this picture we can see a mark made by the proton beam. This mark confirms that the proton beam has a circular shape with an approximate radius of 6 mm, a dimension that was maintained throughout the experiment as the beam focus remained unchanged. It should be noted that many vanadium foils were used as targets, as a new one was employed for each measurement.

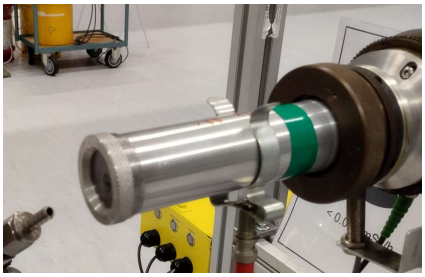

(a) Real picture of the ^{51}V target placed in the beamline with the fixing system. The air flow is illustrated.

(b) ^{51}V target foil with a mark left by the proton beam.

Figure 3.5. Vanadium target pictures.

Vanadium's high mechanical strength, high melting point (around 1910°C), good thermal conductivity, low chemical reactivity, and durability make it suitable for use as a target material without backing and in direct air flow. These properties allow vanadium sheets to maintain structural integrity, dissipate heat, resist corrosion, and withstand repeated proton beam impacts, ensuring effective performance during experiments.

Therefore, all the measurements for the vanadium study were conducted using the described pure Vanadium-51 sample. A target thickness of 500 μm was selected, which is sufficient to stop all the protons of energies near the ^{51}V(p,n) reaction threshold. To confirm that the energy of the protons is reduced below the threshold within the vanadium target, a MC simulation was performed using SRIM [120]. In this simulation, protons with an initial energy of 10 MeV were propagated through a 500 μm thick vanadium layer. As is illustrated in Figure 3.6, the maximum proton penetration depth in vanadium is approximately 350 μm, verifying that a 500 μm thick layer is more than adequate to stop protons with an energy of 10 MeV. Furthermore, since the proton energy used in our ex-

periment is below this high-energy limit, we can confirm that the target qualifies as a "thick target" in this context. This thickness was chosen as it represents a standard value and is the easiest to obtain. However, a thinner target could have been a viable alternative.

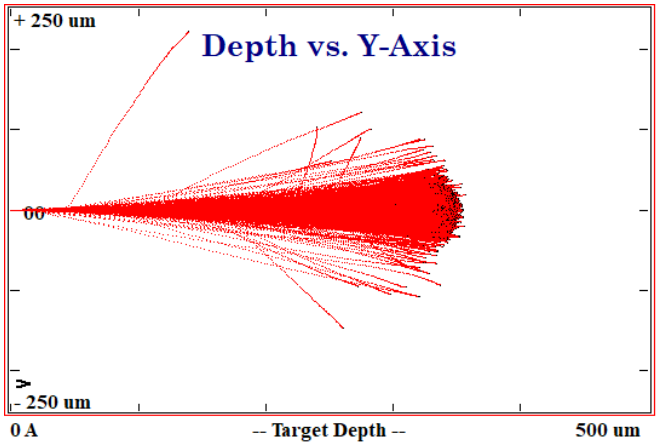

Figure 3.6. Results from 10 MeV protons incident in a 500 μm layer of ^{51}V realized with SRIM [120] Monte Carlo software.

3.3.2 ^{6}Li-glass Detector

The ^{6}Li-glass detectors are ideal for neutron measurements in the epithermal or keV energy range. The principle of operation for these detectors is very simple. They function by neutron capture by ^{6}Li nuclei, a reaction in which a gamma is emitted, which can then be detected by a scintillating material. Due to the high cross-section of this capture reaction in the thermal range of neutrons, the ^{6}Li-glass detectors are perfect for low-energy neutron measurements. Moreover, with this type of detector, we can discriminate between neutrons and gammas, which is why they are useful in nTOF measurements.

At MONNET, five ^{6}Li-glass detectors purchased from Scionix®[121] are available, with different thicknesses : one of 1 inch (2.54 cm), one of 1/2 inch (1.27 cm), one of 1/4 inch (0.635 cm), and two of 1/8 inch (0.3175 cm). During different parts of the experiment, most measurements have been performed using the 1/2 inch ^{6}Li-glass, and some additional evaluations have been conducted with the 1 inch and 1/4 inch ^{6}Li-glass detectors. We discarded the 1/8 inch detectors because it was deemed necessary to use relatively thick detectors to keep beam time within practical limits. The ^{6}Li enrichment is 96% for all the mentioned glass detectors.

In Table 3.1, a detailed chemical composition of the detectors is presented. The schematic internal structures of the detectors measuring 1, 1/2, and 1/4 inch are illustrated in Figure 3.7 [55]. The materials described in Table 3.1 are visually represented in Fig. 3.7: aluminum is depicted in light grey, Si rubber in purple, Teflon in orange, glass in blue, borosilicate in green, μ-metal in deep grey, and

tape in brown. This detailed geometry is the one we have considered in all the simulations throughout the thesis.

Component	Chemical composition	Density (g/cm^3)
Aluminium	Al alloy	2.7
Si rubber	H 8.2%, c 32.4%, O 21.6%, Si 37.8%	1.1
Teflon	$(C_2F_4)_n$	2.2
Glass	SiO_2 56%, MgO 4%, Ce_2O_3 4%, Al_2O_3 18%, $^6Li_2O$ 18%	2.6
Borisilicate	SiO_2 81%, B_2O_3 13%, Na_2O 4%, Al_2O_3 2%	2.2
μ-metal	C 0.02%, Mn 0.5%, Si 0.35%, Ni 80%, Fe 14.93%, Mo 4.2%	8.75
Tape	SiO_2 50%, Si rubber 50%	0.9

Table 3.1. List of chemical compositions and densities of the ^{6}Li-glass detector [121]. ^{6}Li enrichment is 96%.

The intrinsic efficiency of the ^{6}Li-glass detectors can be studied using Monte Carlo N-Particle version 6.2 (MCNP6.2) [122] simulations. This efficiency, which depends on neutron energy, relates the counts in the detector spectrum to the number of particles incident on the detector. The mentioned geometry and composition (Figure 3.7 and Table 3.1) have been taken into account in the simulation code.

For each detector type, monoenergetic neutrons with energies from 1 eV to 1 MeV were simulated as the neutron source. The neutron efficiency is primarily defined for the ^{6}Li(n, α)^{3}H capture reaction. The flux averaged over the ^{6}Li-glass material when a neutron produces an α-particle and a tritium is scored by Tally 4 with the FM card.

The FM card, or tally multiplier card, is used to multiply any tallied quantity (such as flux) by a specified cross-section to compute various reaction rates. The FM card calculates quantities according to the following expression:

$$F4_{FM} = \int \phi(E) R_m(E) dE \tag{3.5}$$

where ϕ(E) is the energy-dependent fluence (neutron·cm^{-2}) and R$_m$(E) is an operator representing an additive and/or multiplicative response function from the MCNP6.2 cross-section libraries or a specially designed quantity. The result's units depend on the tally mode. For instance, if a normalization factor of -1 (c = -1) is applied, the result is scaled by the cell's atom density. In such cases, it is necessary to specify both the material and the Evaluated Nuclear Data File (ENDF) reaction number corresponding to the desired microscopic reaction cross-section. In this calculation, we are particularly interested in the (n,α) reaction, designated by the ENDF reaction number 105. Given that cross-sections are measured in

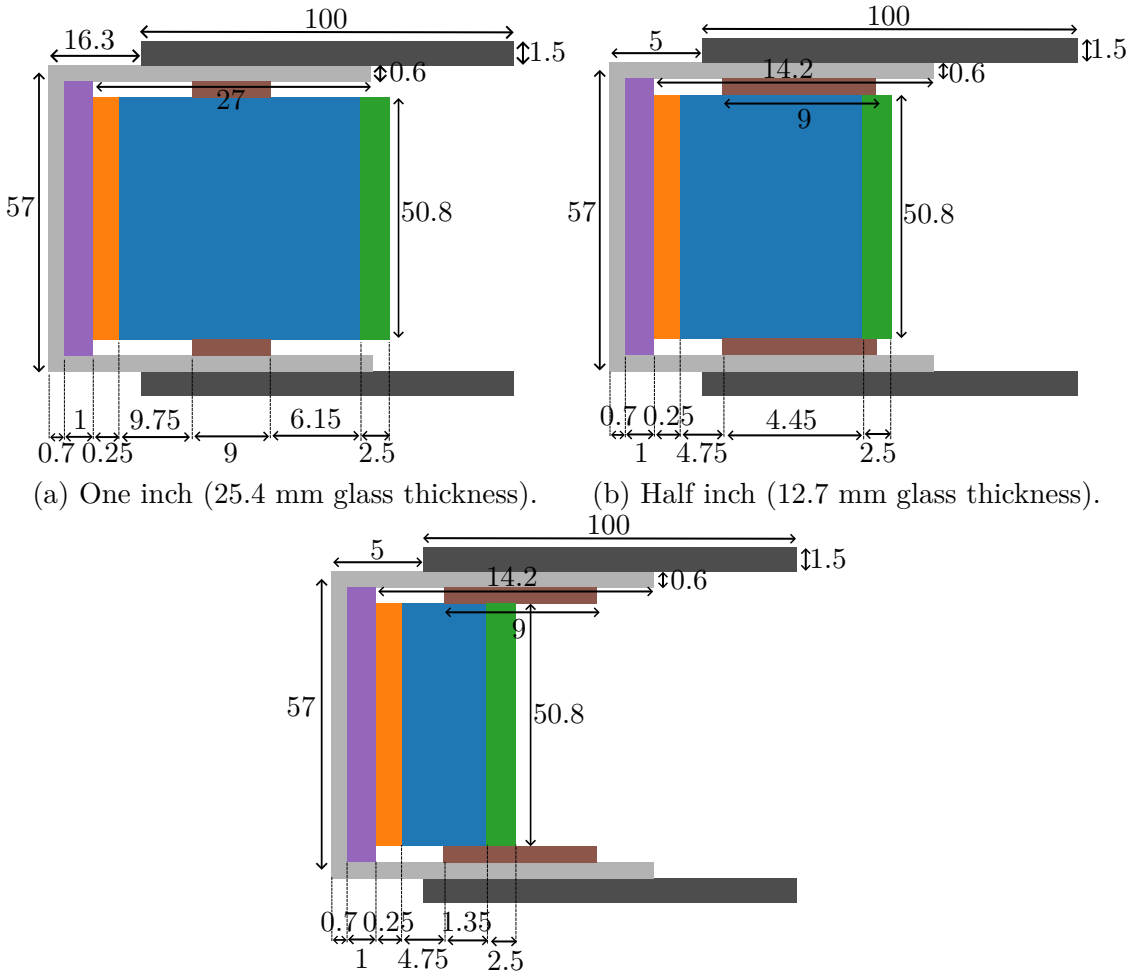

(a) One inch (25.4 mm glass thickness).

(b) Half inch (12.7 mm glass thickness).

(c) Quarter inch (6.35 mm glass thickness).

Figure 3.7. Geometry sketch of the ^{6}Li-glass detectors: aluminum can (light grey), silicone rubber (purple), Teflon layer (orange), ^{6}Li-glass (blue), photomultiplier tube formed from borosilicate (green), μ-metal (dark grey), and tape (brown, between the aluminum can and the ^{6}Li-glass). All quantities are in millimeters; dimensions in the figure are not to scale.

barns, the units for the Tally 4 output using the FM card are expressed as (atom $\cdot$ particles)/(cm^3 $\cdot$ particles$_{initial}$).

Using this method for each detector type, the intrinsic efficiency of the detectors is shown in Fig. 3.8. The efficiency tends to increase with greater thickness of the ^{6}Li-glass, due to the presence of more active material. All detectors exhibit a similar efficiency trend, demonstrating higher effectiveness in the thermal and epithermal energy ranges compared to the fast neutron region. An efficiency resonance around 200 keV is observed across all three detectors, directly resulting from a resonance in the lithium-6 capture cross-section.

This type of detector has characteristic signals; the one shown in the Figure 3.9

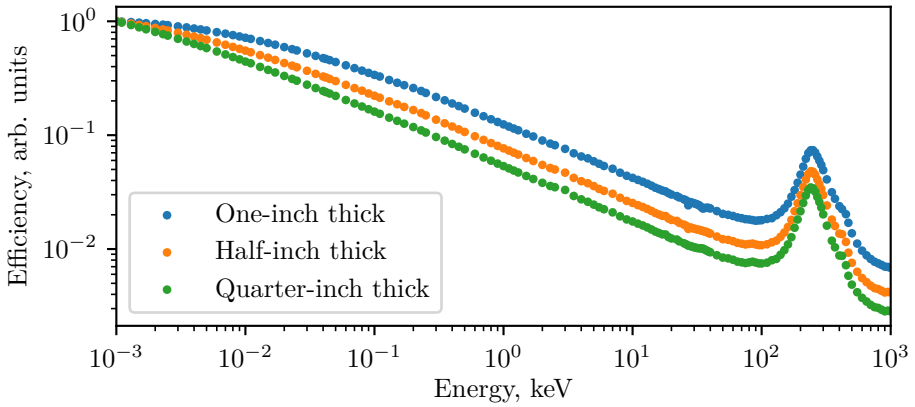

Figure 3.8. Intrinsic efficiency for neutron detection with one inch, half and quarter inch thick ^{6}Li-glass detectors calculated with the MCNP6.2 simulation code [122]. Simulations were run for a sufficient duration until the errors became negligible.

corresponds to a neutron. As we have mentioned, these detectors operate using lithium-6 to capture thermal neutrons, resulting in the emission of characteristic particles such as alpha particles and tritons. The signal observed in the figure represents the response of the detector to neutron interactions, providing valuable data for various applications in nuclear physics, radiation monitoring, and research. In addition to neutrons, these detectors can also detect charged particles, although the quality of those signals is poorer, and the shape is different; therefore, we are able to distinguish between them.

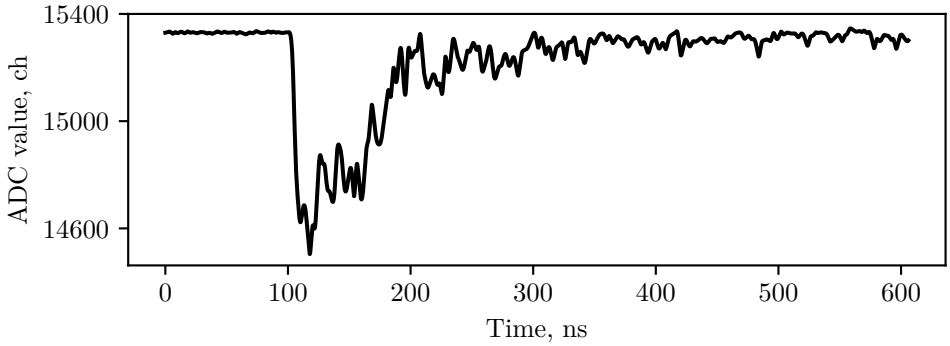

Figure 3.9. Neutron signal obtained from a neutron detected by a half inch ^{6}Li-glass. Data acquisition system ABCD. Typical signal for the neutrons in this type of detector.

3.3.3 Data Acquisition System

The Data Acquisition System (DAQ) used in our experiment is ABCD [123]–[126]. ABCD is an open-source framework, maintained by the team at MONNET, that can be utilized with signal digitizers from multiple vendors [127]. ABCD was designed for use in Nuclear Physics experiments, focusing on the efficient acquisition of data from signal digitizers. The framework is structured with independent modules, each running in its own separate process. These modules are connected via communication sockets. ABCD has several useful features, including an easy-to-use web interface, the ability to launch a replay of our experiments, and a module to analyze the time of flight by coincidence, among others.

ABCD supports various signal digitizers; in our case, we have used the CAEN digitizer model DT5730 [128], shown in Fig. 3.10. The CAEN digitizer DT5730 is a desktop module that houses an 8-channel, 14-bit, 500 MS/s ADC FLASH waveform digitizer with software-selectable 2 Vpp (peak-to-peak) or 0.5 Vpp dynamic range input on single-ended MCX coaxial connectors. DC offset is adjustable ±1 V (at 2 Vpp) or ±0.25 V (at 0.5 Vpp) via a 16-bit DAC on each channel.

Figure 3.10. Picture of the CAEN digitizer DT5730 used in our experiment.

For our experiments, the acquisition process utilized the photomultiplier from each detector. Signals were split into two parts: pulse shape (from which the Qlong is extracted) and timing (referred to as timestamp). The timing part included a timing filter amplifier and a constant-fraction discriminator. The pulse shape part comprised a preamplifier, a spectroscopy amplifier, and signal integration to obtain the Qlong and the Qshort. When performing the TOF technique, the timing signal from each detector served as the stop signal or detector time, t. The accelerator tower pulse acted as the start signal or reference time, t_{ref}, for the time in coincidence, processed through a timing filter amplifier and constant fraction discriminator. Data from each detector were collected separately, ensuring that the timing and pulse height information matched. At this point, it is important to describe the ABCD Web interface and what constitutes an event within our DAQ to follow all the steps in our data analysis.

ABCD Web Interface

The structure of the ABCD web interface is easy to navigate. The digitizer interface page contains all the initial parameters for our CAEN digitizer. For each channel, we define an acquisition window with a trigger. The waveform display page operates similarly to an oscilloscope, allowing us to view the signals that our system captures. The waveform analysis page is dedicated to processing these signals. Each signal that our system detects is referred to as an 'event,' which includes a timestamp, Qlong, Qshort, and Pulse Shape Discrimination (PSD) parameters (explained below). The spectrum calculator page utilizes these event parameters to generate a histogram spectrum using Qlong and PSD. Additionally, there is a module designed for time-of-flight experiments, displaying the time coincidence between events from selected channels. Lastly, there is a dedicated page for saving data.

Event: Timestamp, Qlong, Qshort and PSD.

As we have mentioned, for each of the signals arriving to the channels, an event with all these parameters is stored. In the following, we will define these parameters:

1. **Timestamp:** It provides a precise reference point in time when an event, such as the detection of a signal or an experimental measurement, occurred.

2. **Qlong:** Represents the integrated loading of the signal pulse over a period of time that we set in the configuration and which must include the entire signal. It typically captures the total charge deposited by the signal over a wider time window compared to Qshort.

3. **Qshort:** This parameter is similar to Qlong but integrates the signal pulse over a shorter time window. It captures the charge deposited by the signal over a brief period, usually corresponding to the peak or immediate surroundings of the signal.

4. **PSD parameter:** This parameter is a way to see if the tail of the signal is changing the shape. It is described as:

$$\text{PSD parameter} = \frac{\text{Qlong} - \text{Qshort}}{\text{Qlong}}, \tag{3.6}$$

   and it is really useful for identifying neutrons.

For each signal, our DAQ will store these four important parameters. The Qlong represents the energy in the signal, while the Qshort and the PSD parameter will assist us in the filtering process, and the timestamp is essential for our TOF measurements.

Start Signal or Reference Signal

For the TOF technique, a start signal or reference time (t_{ref}) for the time-of-flight calculation is needed. In our data acquisition system, we have two possible channels to use as this start or reference signal. First, the Accelerator Pulse signal is the signal from the accelerator tower shown in Fig. 3.11. This signal comes directly from the accelerator, not from the beamline where we perform the measurement. Secondly, the Pick Up is the signal coming from the end of our beamline, shown in Fig. 3.12. This illustrates how the pulse exiting the beamline will appear.

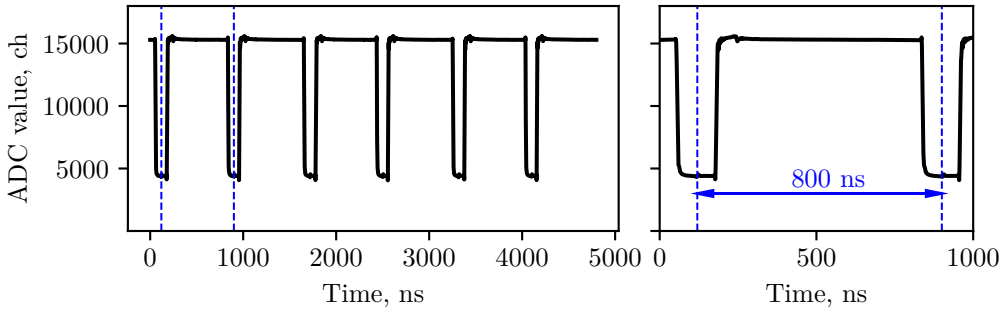

Figure 3.11. Accelerator tower pulse signal acquired by the data acquisition system ABCD. The left graph shows the complete signal, while the right one is a zoom where the distance between pulses is indicated.

In Figs. 3.11 and 3.12, the used period for the accelerator has been 1600 ns. In the MONNET facility pulsing system, the 1600 ns period pulsing is achieved in two steps. The pulse generated for the accelerator tower signal has a period of 800 ns, as shown in Fig. 3.11, and then, in the signal from the Pick Up, we observe a much finer signal with a period of 1600 ns, as depicted in Fig. 3.12. This arises from the two-step period pulsing. Although this phenomenon occurs, both signals are valid. In the case of the tower signal, we will only need to count once for every two pulses. Moreover, this event only occurs for this period; when we use the 800 ns mode, the period is the same in both signals.

The Pick Up signal presents two peaks, one negative and the other positive. The negative peak is higher than the positive one. To determine the time resolution of our experiment, we need to analyze the peak-to-peak width. In the bottom graph of Fig. 3.12, we see a black signal, which is the smoothed signal with a width between the peaks of 3.5 ns, and a red signal, which is the real signal given by ABCD with a peak-to-peak difference of 2 ns. Therefore, the crucial peak-to-peak width is the one between the red peaks, measuring 2 ns. This value represents the time resolution of our data acquisition system, making it entirely logical.

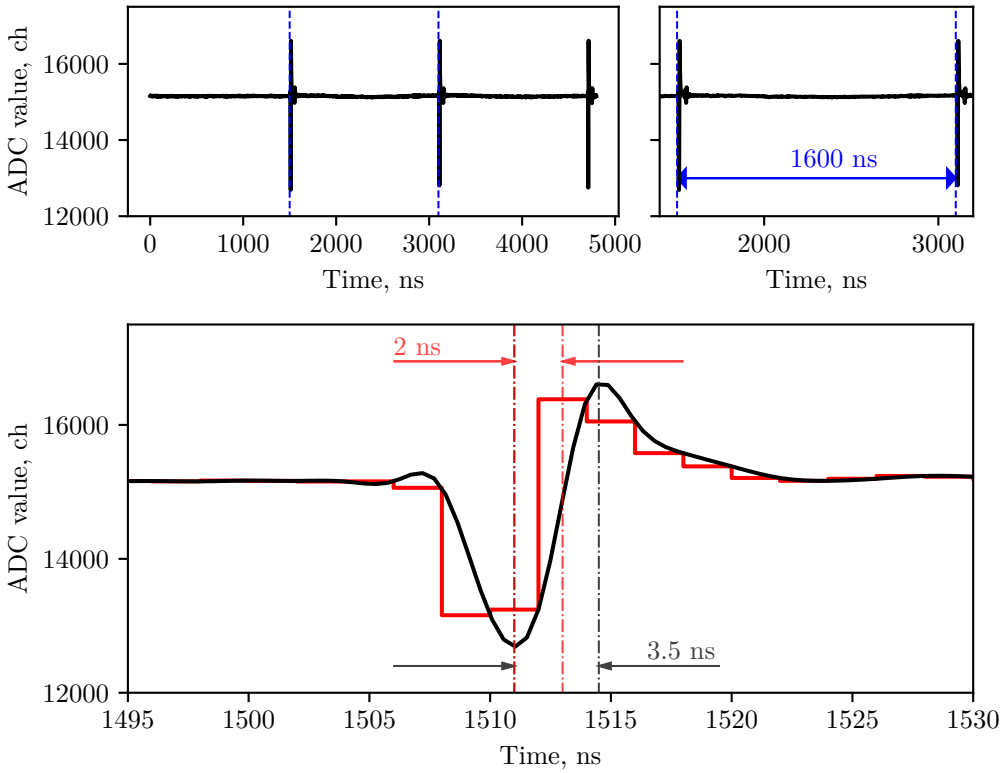

Figure 3.12. Pick Up pulse signal acquired by the data acquisition system ABCD. On the top, the left graph displays the complete signal, and the right one is a zoom where the distance between pulses is shown. At the bottom, there is a zoom of the peaks of the signal, where the red line represents the real signal and the black line represents the smoothed one. The peak-to-peak width is indicated. The period for the accelerator is 1600 ns for this measurement.

Accelerator parameters: Extra channels

AABCD is a very versatile code. For the measurements of this thesis, in addition to all the channels corresponding to the CAEN digitizer, i.e., to the detectors, the pulse of the accelerator tower, and the Pick Up, we have been able to include extra channels with different accelerator data.

1. **Channel 100:** Timestamp of the computer clock.

   48 bits number in th Qshort, Qlong and baseline entries in the event_PSD structure which counts the number of milliseconds since 1/1/1970 (UNIX epach)

2. **Channel 101:** Current on the target.

   Value from the accelerator control system that indicates the current of the target in x1000 nA.

3. **Channel 102:** High Voltage terminal.

   Reads the HV terminal in the accelerator in kV.

4. **Channel 103:** Extra decimals for the HV.

   Difference between the set value of HV and the actual reading of Gvm, in V. Offset of 30000.

5. **Channel 104:** Magnetic field.

   Value of the magnetic field in the analyzing magnet, in dG.

Using the described data acquisition system, we carried out all the necessary measurements for our experiment. This system allowed us to collect precise data and view it in real-time, ensuring that each measurement was performed with maximum efficiency and reliability.

3.4 Accelerator Calibration

The accelerator was calibrated by the MONNET team in February 2023, using standard reactions. The resulting relationship from this calibration is linear and follows the equation:

$$E_p = 66.8 + 1.9V, \tag{3.7}$$

where V is the accelerator voltage in kV. Considering the voltage uncertainty is 1 kV, the uncertainty for the energy will be $\Delta E_p = 1.9$ keV. Many factors can influence the accelerator calibration, such as the repair of some components, the changing of the filament, etc. To ensure that this calibration is valid for us, we performed measurements of the ^{51}V(p,n) and ^{7}Li(p,n) reaction thresholds, conducting an energy scan of these two reaction thresholds.

In both reactions, ^{51}V(p,n) and ^{7}Li(p,n), neutrons are produced when proton energies exceed the reaction thresholds of 1565.1 and 1880.6 keV, respectively. In these measurements, the accelerator was used in continuous mode. The detector signal employed to perform this scan was the De Pangher precision Long Counter (PLC).

A Long Counter (LC) neutron detector is a device designed to measure the neutron rate in a specific environment, recognized for its ability to measure neutron fluxes with relatively uniform efficiency over a wide range of neutron energies. In MONNET, a De Pangher precision Long Counter detector, made of BF_3 tubes, was fully characterized. This detector is ideal for confirming the presence of neutrons, making it perfect for verifying whether our reactions are generating them. To confirm the neutron range of this detector, a prior calibration was conducted using an AmBe source. The PLC was placed directly in front of the target, at 12 cm for vanadium and 20 cm for lithium, to ensure that all the neutrons were detected.

3.4.1 Vanadium Energy Sweep

The first measurement we performed was the energy sweep for Vanadium. The setup used is illustrated in Fig. 3.13. The De Pangher precision Long Counter was positioned at 0 degrees and 12 cm from the target. To obtain an additional measurement of the produced neutrons, two ^{6}Li-glass detectors were used in this measurement: one, 1 inch in size, was placed at 1 m and +90°, while the other, 1/2 inch in size, was placed at 1 m and +160°. Finally, for photon monitoring, a Cerium Bromide detector was located at 1 m and -90°, and a NaI detector was positioned at 1 m and +110 degrees.

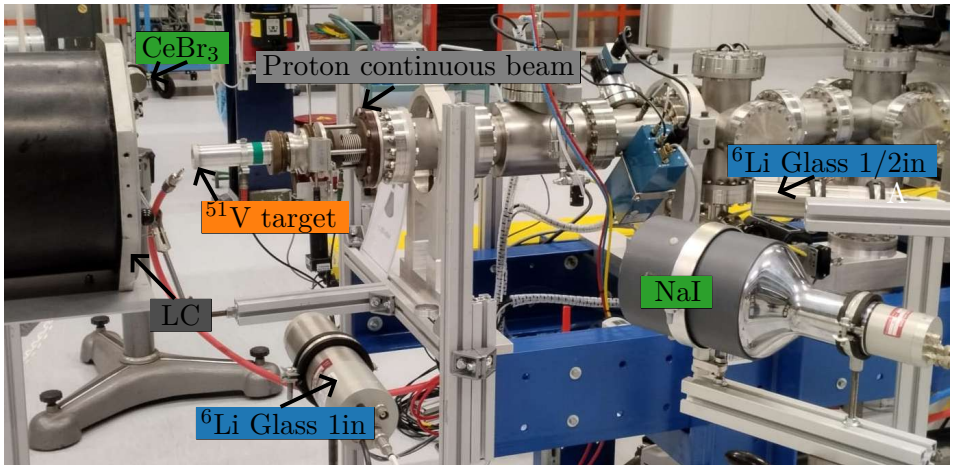

(a) Photo of the setup for the Vanadium energy sweep measurements. All the detectors and the target are tilted.

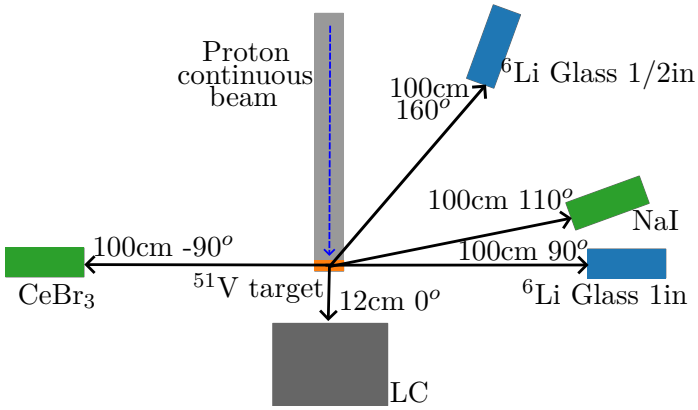

(b) Diagram of the setup for the Vanadium energy sweep measurements. Quantities are in cm and degrees. The diagram is not to scale.

Figure 3.13. Setup for the Vanadium energy sweep measurements.

Using this setup (Fig. 3.13), we performed 25 runs over 2 days (on October 4th and 5th, 2023). The measurements averaged 10 minutes each, ranging from 750 to 836 kV in non-uniform steps. The current was approximately 20 μA for all the runs.

As we mentioned, the De Pangher precision Long Counter detector was a key component of this experiment and will allow us to determine the threshold. In Figure 3.14 (**left**), the spectrum of the PLC detector for some of the measured voltages is shown in the neutron detection range for this detector. The results indicate that as the voltage, and hence the initial energy of the protons, increases, the neutron flux also increases, resulting in a higher production of neutrons.

In Figure 3.14 (**right**), the PLC detector rate is displayed for all measured voltages. Statistical uncertainties, in this case, are the sum of the uncertainty due to the number of counts, calculated as the square root of the number of counts, plus the uncertainty of the accelerator current. Neutrons are clearly detected for the first time at (785 ± 1) kV, which corresponds to an energy of (1565.5 ± 1.9) keV, as calculated using Equation 3.7. At (780 ± 1) kV, no neutrons are detected, so we can consider this as the threshold voltage, which, according to Equation 3.7, equates to an energy of (1565.7 ± 1.9) keV. Given that the reaction threshold is 1565.1 keV, this measurement confirms the accuracy of the calibration relationship established by the MONNET team within the energy range we will use for the Vanadium measurements. We observed only a discrepancy of (0.6 ± 1.9) keV, which is negligible within the uncertainty range. Therefore, the accelerator calibration used for the ^{51}V(p,n) near the threshold energy range will be directly presented in Equation 3.7.

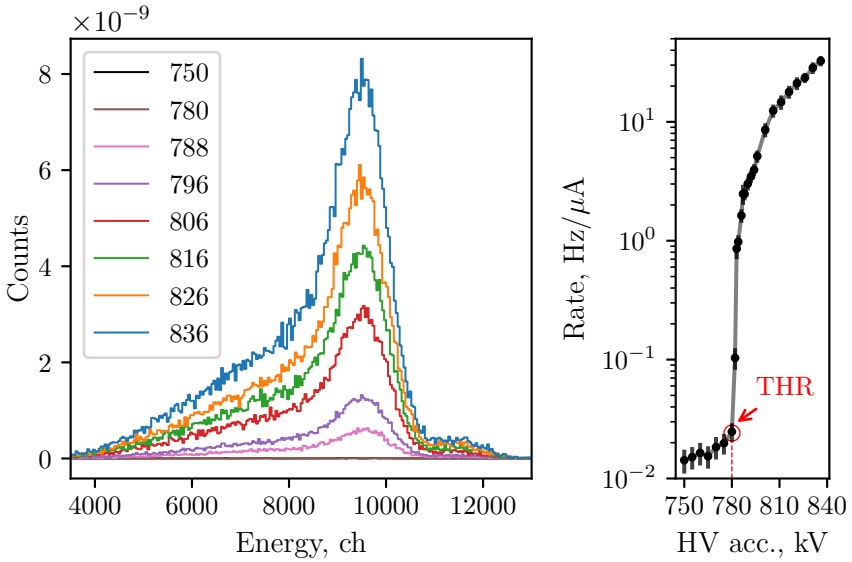

Figure 3.14. PLC detector measurements for the Vanadium energy sweep. **Left:** PLC detector spectrum acquired with the ABCD software for different HV values of the accelerator. **Right:** Rate of the PLC detector versus the HV of the accelerator. The statistical uncertainties are shown by error bars. The threshold (THR) found is indicated.

In addition to the PLC, more detectors were available for these runs (Fig. 3.13). On one hand, ^{6}Li-glass detectors were too far from the target to effectively detect neutrons just above their threshold. In Figure 3.15 (**left**), we compare three spectra for the ^{6}Li-glass 1/2 inch at three different voltages. It can be seen that when the threshold of the reaction (set at 780 keV) is exceeded, a disturbance appears in the range of 5500-8000 channels. This area corresponds to the channel region where neutrons are detected by this detector.

On the other hand, a significant increase in the number of counts can be seen in the gamma detectors, as we can see in the Figure 3.15 (**right**), which presents three spectra from the $CeBr_3$ detectors. The cerium bromide detectors are gamma detectors with high resolution. In this case, the spectra presented from this detector have been calibrated to identify any new gamma contributions that appear as the high voltage is increased. The peaks seen in Figure 3.15 (**right**) are attributed to natural background radiation, with ^{40}K at 1.46 MeV and ^{214}Bi at 1.12 MeV being identifiable. The increase in HV only leads to an increase in the total number of counts; we do not see any change in the shape of the spectrum.

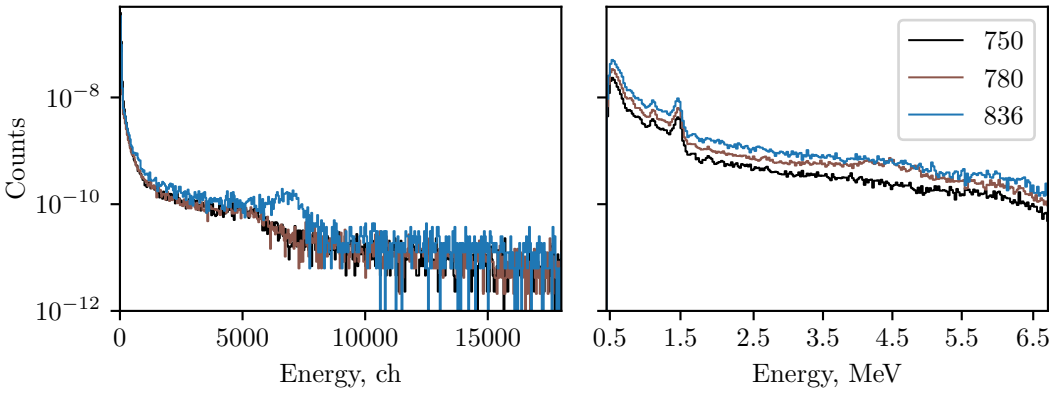

Figure 3.15. Spectra acquired during the Vanadium energy sweep measurements. **Left:** ^{6}Li-glass detector half inch spectrum acquired with the ABCD software for 3 HV of the accelerator. **Right:** $CeBr_3$ detector spectrum acquired with the ABCD software and calibrated for 3 HV of the accelerator.

In conclusion, all detector signals coincide at the threshold, confirming the accelerator calibration presented in Eq. 3.7.

3.4.2 Lithium Energy Sweep

The energy sweep for lithium was simply a cross-check of the calibration we had already validated with vanadium. We want to determine the calibration at the ^{7}Li(p,n) energy range. The setup for this measurement was quite similar to the previous one, with some differences. The main difference from the previous setup is that this measurement was conducted in pulsed mode for the accelerator, at a

frequency of 625 kHz. Here, the De Pangher precision Long Counter was positioned at 0 degrees and 20 cm from the target, and all the other detectors had the same configuration. The diagram for this setup is presented in Figure 3.16.

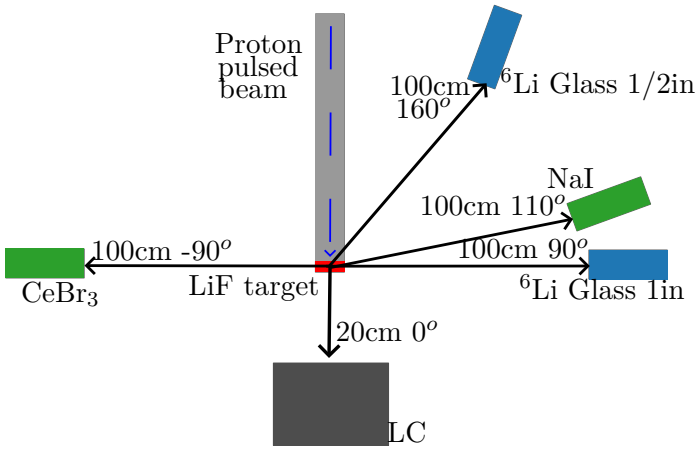

Figure 3.16. Diagram of the setup for the Lithium energy sweep measurements, the quantities are in cm and degrees. The diagram is not in scale.

Using this setup, an energy sweep from 942 to 965 kV was performed; in this case, the mean current was ≈ 0.8 μA for all the runs. Figure 3.17 (**left**) shows the spectra of the PLC detector at various voltages, in the neutron range for this detector. It is evident that the flux increases with voltage. Figure 3.17 (**right**) presents the PLC detector rate across all measured voltages. The statistical uncertainties shown are the sum of the uncertainty from the count number (the square root of the counts) and the uncertainty from the accelerator current. There is a very noticeable rise at (948 $\pm$ 1) kV; meanwhile, at (946 $\pm$ 1) kV, no neutrons are detected. Therefore, the threshold of this reaction can be established at (946 $\pm$ 1) kV. Using equation 3.7, this corresponds to an energy of (1884.6 $\pm$ 1.9) keV. Knowing that the threshold of the reaction is 1880.6 keV, we can consider that there is a shift of (-4.0 $\pm$ 1.9) keV, with respect to the original equation. This is entirely plausible because this reaction and the ^{51}V(p,n) reaction have different energy ranges. Therefore, for this reaction, we will take into account this shift of (-4.0 $\pm$ 1.9) keV.

Therefore, the accelerator calibration used for the ^{7}Li(p,n) near the threshold, will be:

$$E_p = 66.8 + 1.9V - 4.0 = 62.8 + 1.9V \tag{3.8}$$

where the uncertainty for this energy is $\Delta E_p = 3.8$ keV, due to the added shift.

Again, more detectors were available for these runs (Figure 3.16). As for the Vanadium sweep, ^{6}Li-glass detectors were too far from the target and the measurements were too short to see neutrons just in the threshold in them. In the Figure 3.18 we compare three spectra for the ^{6}Li-glass 1/2 inch for the different voltages. Once more, it can be seen that when the threshold of the reaction (set at 946 keV)

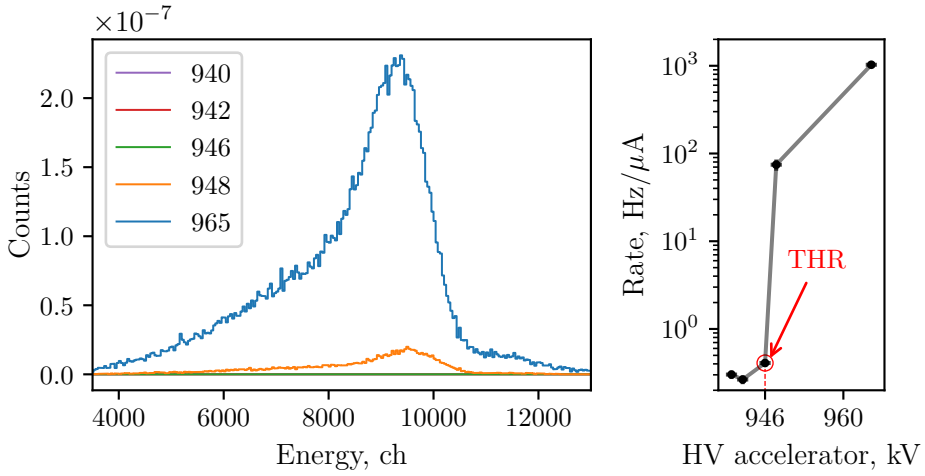

Figure 3.17. PLC detector measurements for Lithium energy sweep. **Left:** PLC detector spectrum acquired with the ABCD software for different HV values of the accelerator. **Right:** Rate of the PLC detector versus the HV of the accelerator. The statistical uncertainties are shown by error bars. The found threshold (THR) is indicated.

is exceeded, a disturbance appears in range 5500-8000 ch, which corresponds to the neutron generation.

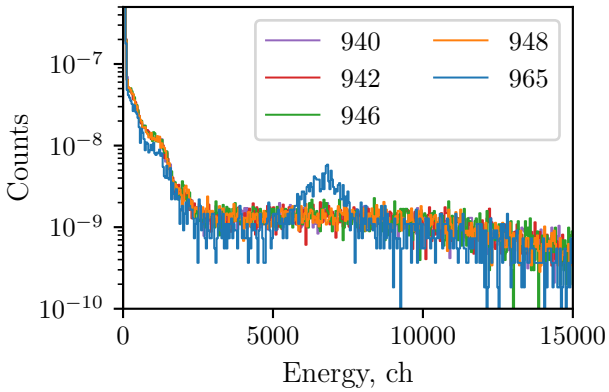

Figure 3.18. Spectra for ^{6}Li-glass detector half inch spectrum acquired with the ABCD software for 5 HV of the accelerator.

Once the testing have been satisfactorily carried out for all the systems and elements, and after describing and learning their correct functioning, the measurements of ^{7}Li(p,n) and ^{51}V(p,n) near the threshold at MONNET in JRC-Geel have been performed. These measurements are presented in the next chapters (Chapter 4 and 5).

Chapter 4

Measurement of the ^{7}Li(p,n)^{7}Be Reaction Near the Threshold

The measurement of the well-known neutron field from the ^{7}Li(p,n)^{7}Be reaction near the threshold is an excellent reference measurement. In this chapter, we will use the experimental method described in Chapter 3 to perform this measurement at 0 and 30 degrees for two different flight paths and test our acquisition system as well as our data analysis.

4.1 Ratynsiki & Käppeler Neutron Field

In 1988, Ratynski and Käppeler [54] published the Maxwellian-Averaged Cross Sections (MACS) for the reaction ^{197}Au(n, γ) at $kT = 30$ keV. They generated the neutron field by directing protons at 1912 keV onto a thick lithium target. This neutron field has been crucial in nuclear astrophysics because it closely approximates the stellar environments relevant to key nucleosynthesis processes [129], [130]. The measurement of ^{7}Li(p,n) at 1912 keV is considered a standard in neutron physics and is known as the Ratynski & Käppeler (R&K) neutron field.

The experimental setup used to measure the neutron spectra in the aforementioned Ref. [54] is very similar to the one performed in our study, which is described in detail, part by part, in Chapter 3. Using flight paths of 51.5 and 27.8 cm, they measured the TOF spectra at 5° intervals from 0° to 65°. In Figure 4.1a, the neutron spectra obtained at various angles, measured by R&K, are presented. It is evident from the figure that the spectrum at 30° presents the highest neutron yield. This is attributed to the reaction kinematics, which favor this angle for optimal neutron production.

Moreover, the angle- integrated neutron spectrum is represented in Figure 4.1b. For the presented proton energy of 1912 keV, the neutron spectrum extends to $E_n^{max} = 106\,\text{keV}$ and includes data from measurements at the short flight path (open squares). The solid line represents a least squares fit of a Maxwellian distribution (at $kT = 25.3\,\text{keV}$), demonstrating excellent agreement with the integral

spectrum. Specifically, the fit closely matches the data from 80 keV down to the lowest neutron energies.

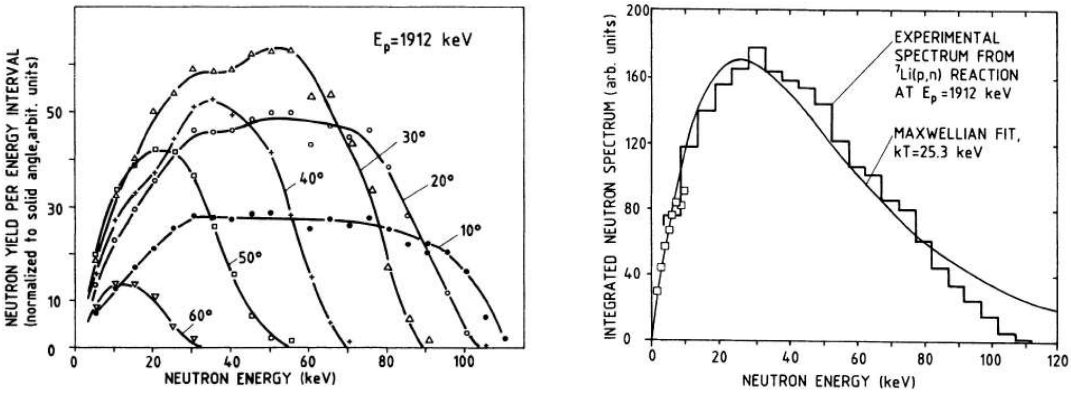

(a) Neutron spectra for different emission angles.

(b) Total neutron spectrum after integration over all angles.

Figure 4.1. Neutron spectrum for ^{7}Li(p,n)^{7}Be at E$_p$=1912 keV in the Ratynski and Käppeler experiment [54].

In recent years, multiple experimental studies have aimed to confirm the R&K field as a standard for neutron measurements. In 2012, Lederer, Käppeler, Mosconi, *et al.* [56] and Feinberg, Friedman, Krása, *et al.* [55] presented consistent results with R&K, demonstrating the robustness of the method and its results. Lederer *et al.* [56] measured the neutron spectrum using an initial proton energy of (1910 ± 1) keV, while Feinberg *et al.* [55] used a proton energy of (1913 ± 6) keV. Other authors have also confirmed this measurement [131], [132]. All these experiments have employed the TOF technique to perform consistent neutron spectrum measurements, utilizing similar setups.

In particular, in our measurement, we are going to report some important angles measured in these experiments: 0° and 30°, using a proton energy near the reaction threshold. However, it is important to note that obtaining a complete forward neutron spectrum requires measurements at all production angles. For the 1912 keV case, it is necessary to measure from 0° to 65°, as done in the aforementioned experiments.

Besides experimental measurements, this reaction has also been studied theoretically. Lee and Zhou [133] detailed the kinematics of the ^{7}Li(p,n) reaction. In their study, the authors devised a methodology to calculate angular distributions, energy spectra, and total yields of this reaction for energies up to 120 keV above the threshold for thick and thin targets, drawing from a compilation of data compiled by Liskien and Paulsen [134]. Reifarth *et al.* [135] developed PINO, a program employing MC techniques to simulate neutron production from protons interacting with lithium. However, PINO is limited by the poor results it provides, as it only computes the differential production at 0° and the integral neutron spectrum in energy. In the same vein, the NEBOAS project [136], [137], funded by the

MONNET - European Commission's Joint Research Center, provides the double differential neutron yields, $\frac{d^2Y}{dE_n d\Omega}(\theta, E_n)$, as a function of the energy and angle of neutron emission, from proton-induced reactions at any projectile energy on thin and thick targets, including the ^{7}Li(p,n)^{7}Be reaction.

In Fig. 4.2, the total forward spectra measured by the mentioned experiments, along with the spectra calculated by the computational codes described, are presented. These results validate the established result for the Ratynski & Käppeler neutron field for the ^{7}Li(p,n)^{7}Be reaction. As noted, the experiments by Lederer, Käppeler, Mosconi, *et al.* [56] and Feinberg, Friedman, Krása, *et al.* [55] demonstrate similar results, which are consistent with the original R&K measurement. The dN/dE spectrum of Lederer, Käppeler, Mosconi, *et al.* [56] is available in EXFOR [70], while the spectrum of Feinberg, Friedman, Krása, *et al.* [55] can be found in the paper itself. The black line represents the result obtained from the code implemented in our group, based on the equations by Lee and Zhou [133]. The result obtained using PINO [135] aligns perfectly with the code based on Lee and Zhou. The same agreement is observed with the NEBOAS result [136], [137]. NEBOAS, PINO, and the results from Lee and Zhou are presented using an energy binning of 1 keV.

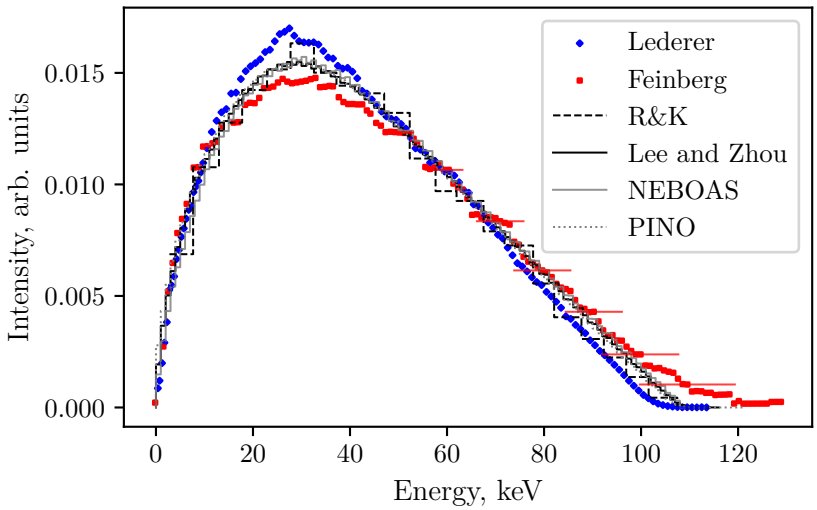

Figure 4.2. Comparison between experimental and calculated R&K measurement neutron integrated spectrum. Lederer *et al.* [56] and Feinberg *et al.* [55] results are shown as blue diamonds and red squares, respectively. The corresponding uncertainties for these experimental measurements are indicated by red and blue error bars. The black dashed line represents the original result of R&K [54]. The solid black line shows the results of the code implemented by our group based on the Lee and Zhou [133] equations at 1912 keV. The grey lines, both solid and dotted, present the results obtained by the NEBOAS [136], [137] and PINO [135] codes, respectively.

As mentioned, our ^{7}Li(p,n)^{7}Be measurement is only a test of our experimental method and data acquisition within the context of this thesis; for this reason, only two angles have been measured. Consequently, Figure 4.3 presents a comparison between the literature 's experimental measurements at 0 and 30 degrees (Refs. [55], [56]) and the theoretical results based on Lee and Zhou [133]. The PINO results are not included because this code only provides total integrated spectra. The NEBOAS and Lee and Zhou results agree very well with the Feinberg measurement for both angles. The Lederer measurement was at (1910 ± 1) keV; accordingly, it is expected that the agreement is not as good as with the Feinberg results.

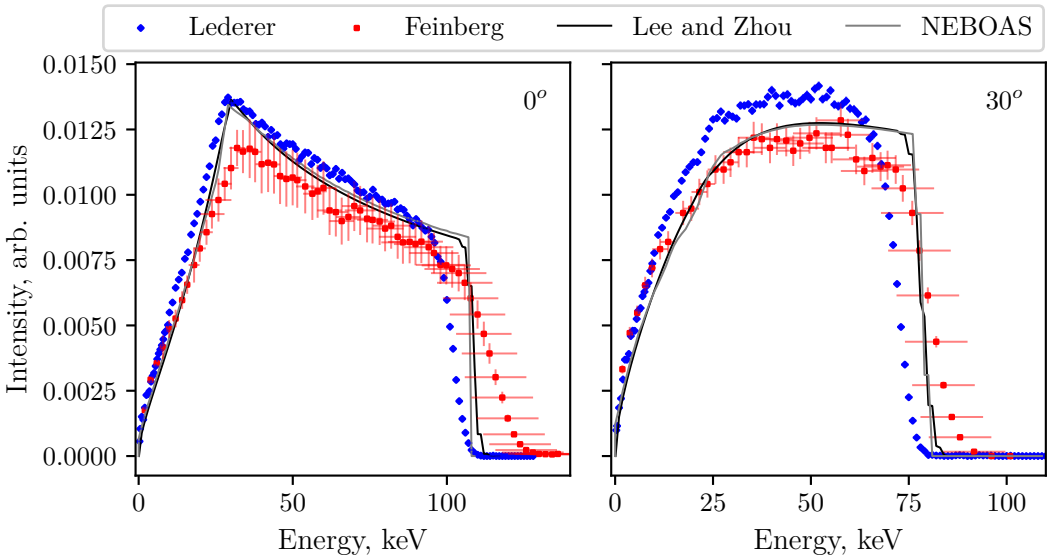

Figure 4.3. Comparison between experimental and calculated R&K measurement neutron spectra for 0° and 30°. Lederer *et al.* [56] and Feinberg *et al.* [55] results are shown with blue diamonds and red squares, respectively. The corresponding uncertainties for these experimental measurements are indicated by red and blue error bars. The black line shows the result of an implemented code of the Lee and Zhou [133] equations for 1912 keV. The grey line gives the result obtained by NEBOAS [136], [137].

4.2 TOF Measurements

The neutron spectrum of the ^{7}Li(p,n)Be^{7} reaction near threshold at 0 and 30 degrees was measured at MONNET-JRC using the experimental method described in the previous chapter. Several measurements have been conducted using the described TOF technique. Two different flight paths-31 cm and 100 cm-three ^{6}Li-glass detectors (one, half, and quarter inch, presented in Figure 3.7), and two

different periods for the accelerator pulse (800 and 1600 ns) were used.

The measurement parameters are presented in Table 4.1. This table includes details about the ^{6}Li-glass detector used, its position, the measurement period, the measurement time, the charge, the intensity, and the counts for both the PLC and $CeBr_3$ detectors for all the ^{7}Li(p,n)Be^{7} neutron spectrum measurements. For our analysis, we will use the PLC events, gamma events, and charge to normalize our spectrum.

^{6}Li-Glass Detector: thickness and position	Period, ns	Time, min	Charge, μA/Hz	Intensity, μA	PLC events	$CeBr_3$ events
1/4 in at 0°, 31cm	1600	66.97	3469	0.863(17)	$4.1{\cdot}10^{5}$	$6.5{\cdot}10^{6}$
1/2 in at 0°, 31cm	800	91.15	4015	0.41(35)	$5.4{\cdot}10^{5}$	$1.0{\cdot}10^{7}$
1/2 in at 0°, 100cm	800	59.33	2246	0.63(10)	$8.0{\cdot}10^{5}$	$1.7{\cdot}10^{7}$
1 in at 0°, 31cm	1600	10.20	521	0.852(21)	$6.2{\cdot}10^{4}$	$9.7{\cdot}10^{5}$
1 in at 0°, 100cm	1600	14.09	698	0.827(11)	$7.6{\cdot}10^{4}$	$1.3{\cdot}10^{6}$
1/2 in at 30°, 31cm	1600	66.97	3469	0.863(17)	$4.1{\cdot}10^{5}$	$6.5{\cdot}10^{6}$
1/2 in at 30°, 100cm	1600	14.09	698	0.827(11)	$7.6{\cdot}10^{4}$	$1.3{\cdot}10^{6}$

Table 4.1. TOF measurement parameters for ^{7}Li(p,n)^{7}Be at E_p= (1915.2 ± 3.8) keV. The uncertainty for the PLC and $CeBr_3$ counts is not included in the table because it is equivalent to the square root of the number of events. The same applies to the uncertainty of the charge. The notation *value*(*number*)indicates the value followed by the uncertainty of the last digits in parentheses, the uncertainty representing the statistical fluctuation of the intensity.

The uncertainties in the presented parameters are primarily related to statistical fluctuations. The event counts in the PLC and $CeBr_3$ detectors are subject to statistical uncertainty, which is the square root of the number of events. The same applies to the charge, as it is calculated by integrating the intensity channel over time. In contrast, the intensity value has associated uncertainties, as indicated in the table. These uncertainties arise from fluctuations in the signal measurement. The uncertainty in the intensity is closely related to the measurement time and the stability of the current throughout the measurement. Although the measurement times are provided in the table, their associated uncertainties are generally small and can be considered negligible.

A notable aspect of these measurements is the high variability in the measurement times. Some measurements were conducted for testing purposes, while others, such as the one-and-a-half-hour measurement, will serve as a reference for our vanadium TOF measurements. Given that the mean intensity is similar for all the 1600 ns measurements (approximately 0.85 μA), the charge is strongly dependent on the measurement time.

For all the ^{7}Li(p,n)^{7}Be measurements, the setup was as shown in Figure 4.4, with only the flight path of the Li-Glass detectors and their angular positions being

adjusted. In some measurements, the NaI detector was disconnected; however, for all runs, the PLC and $CeBr_3$ detectors were always operational to monitor neutron and gamma production. For this reason, the counts from these detectors are presented in the last two columns of Table 4.1.

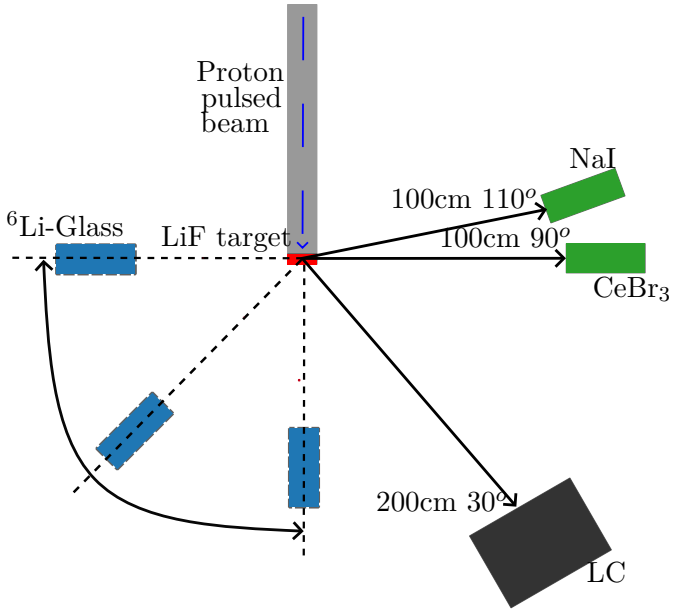

Figure 4.4. Diagram of the setup for ^{7}Li(p,n)^{7}Be TOF measurements at a proton energy of (1915.2 ± 3.8) keV.

For technical reasons and beam stability, the final chosen voltage for conducting the near-threshold measurement of the ^{7}Li(p,n)^{7}Be reaction was set to (964 ± 1) kV. The corresponding energy to this HV is (1915.2 ± 3.8) keV, based on the calibration in Equation 3.8 in Chapter 3. Since these measurements were made at this energy, we will directly compare them with the experimental measurements of Feinberg [56], with a proton energy of (1913 ± 6) keV, and Lederer [55], with a proton energy of (1910 ± 1) keV.

4.3 Data Analysis

The data analysis is now illustrated step by step, starting from the raw data collected by our DAQ (ABCD) to the convoluted neutron energy spectra.

It is important to note that the reference time was provided by the Accelerator Pulse. Across all TOF experimental setups, we had access to both the Pick Up signal and the accelerator pulse signal. However, the signal from the accelerator pulse was found to be significantly more stable. This selection is particularly important; due to the finite time resolution of the ABCD, some Pick Up signals were not registered, leading us to prioritize the accelerator pulse signal for accurate timing.

As result, all TOFs presented in this thesis are calculated by determining the difference between the time of detection, t, and the time of the previous acceleration pulse, t_{ref}. ABCD registered events across different channels, and knowing the channel of the ^{6}Li-Glass detector and the channel of the accelerator pulse allows us to see the difference between the timestamps of each event. This fact enabled us to construct precise TOF spectra.

Additionally, it is important to mention that all calculated TOFs account for the gamma-flash as well. The gamma-flash serves as a critical calibration point in our measurements, and it is essential to ensure that the TOF associated to the gamma-flash is centered at c/L, where c is the speed of light and L represents the flight path length.

To clarify our data analysis, we will outline the step-by-step process we followed using one key measurement as an example, and then present the final results for all the other measurements. The chosen key measurement that we will present first is from the half-inch ^{6}Li-Glass detector at zero degrees and a 31 cm flight path, shown in the second row of Table 4.1. This measurement is significant because the exact same setup will be presented for the vanadium in the next chapter.

In Figure 4.5 (**left**), we present TOF versus Rate (number of counts per time bin normalized by the charge) in the upper figure and TOF versus Qlong in the lower figure. The uncertainties associated with the neutron rate arise from the statistical uncertainty of the number of counts plus the uncertainty of the charge. This figure illustrates the typical shape of the TOF neutron spectra, featuring two peaks: the first, known as the γ-flash, represents all gamma particles traveling at the speed of light, while the second peak corresponds to the neutron signal. The data shown are raw data, directly extracted from all the coincidences of the detected events.

As previously discussed, the ^{7}Li-glass detectors are highly effective in distinguishing between gammas and neutrons using their Qlong parameter. By identifying the neutron detection region, we can apply a Qlong filter to reduce background noise. The filtered area is highlighted in blue in Fig. 4.5 (**left**), and in the subsequent Figure 4.5 (**right**), we display the data after applying this Qlong filter.

As we can see in the zoom-in of the upper parts of Figs. 4.5, the background appears to be temporally uniform; the region between the gamma flash and the neutrons is flat in both figures. This uniformity allows us to subtract the background contribution effectively, ensuring that the resulting data accurately reflects the actual neutron events. Therefore, the final filter that needs to be applied to the TOF data is the flat background filter, indicating that there is a consistent neutron contribution across all measurements. By accounting for this consistent background, we can isolate the true signal more precisely.

In Figure 4.6, the final TOF spectrum for this measurement is shown as a solid black line, representing the data after the subtraction of the flat background component. This background, which was removed to improve the visibility of the signal and isolate the features of interest in the TOF spectrum, is depicted

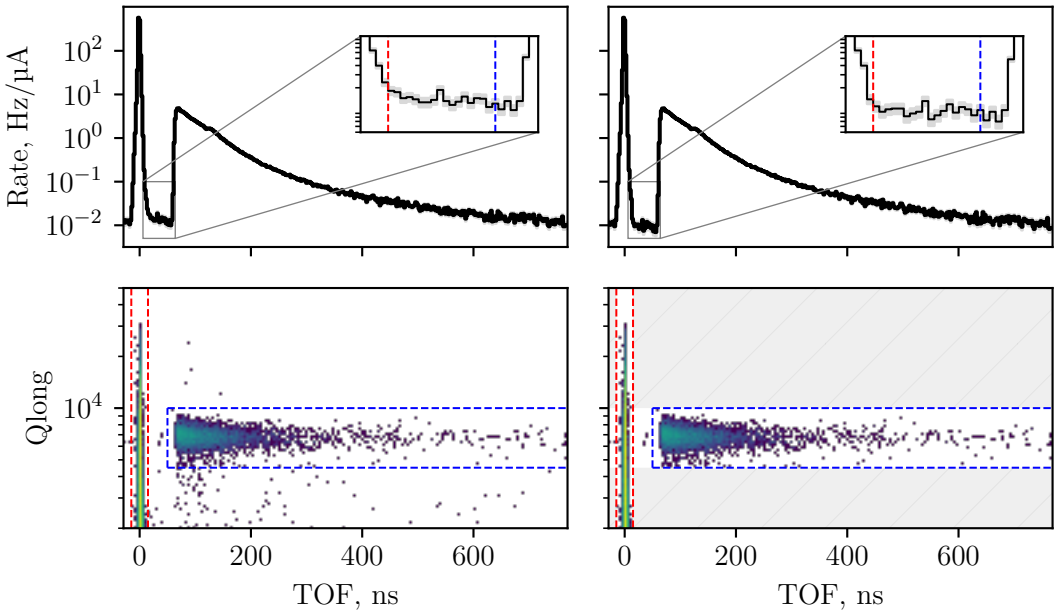

Figure 4.5. TOF spectra for the ^{7}Li(p,n) reaction at (1915.2 ± 3.8) keV, measured with a half-inch ^{6}Li-glass detector at 31 cm and 0°. Raw (**left**) and filtered (**right**) data are shown, using an 800 ns pulse period. The upper sections zoom into the flat region, while the lower sections display the Qlong distribution, highlighting the neutron (blue dashed) and gamma-flash (red dashed) regions. Rate uncertainties are shown in grey.

separately as a dashed grey line for reference. Additionally, the TOF spectrum with the background included is represented by a blue line for comparison.

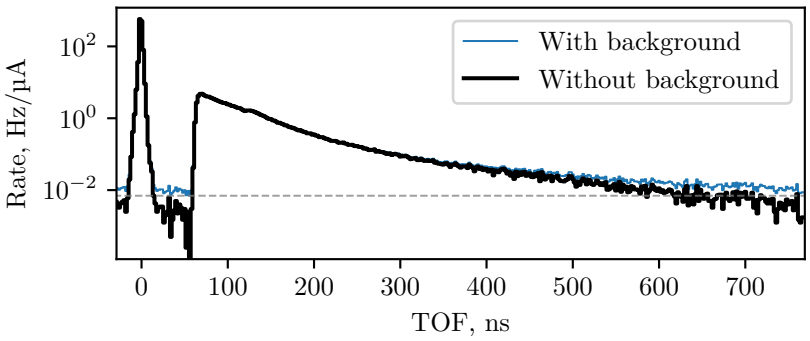

Figure 4.6. Final filtered TOF spectrum for the ^{7}Li(p,n)^{7}Be reaction at (1915.2 ± 3.8) keV, measured with a half-inch ^{6}Li-glass detector at 31 cm and 0°. The Qlong filter was applied, and a flat background was subtracted (solid blue line). Rate uncertainties are shown in blue/grey shading. The background indicated by a dashed grey line.

In Figure 4.7, we present the TOF spectra for all the measurements of ^{7}Li(p,n)^{7}Be at (1915.2 ± 3.8) keV, as presented in Table 4.1, except for the TOF spectrum of the measurement taken by the half-inch detector at 0 degrees and 31 cm, which has already been shown. In these spectra, the mentioned filters have been applied: Qlong and flat background filters. It is important to note that since the measurements were taken using different ^{7}Li-glass detectors, the Qlong filter has been adapted for each detector. The area of interest, where the neutrons are found, exhibits variations among the different detectors.

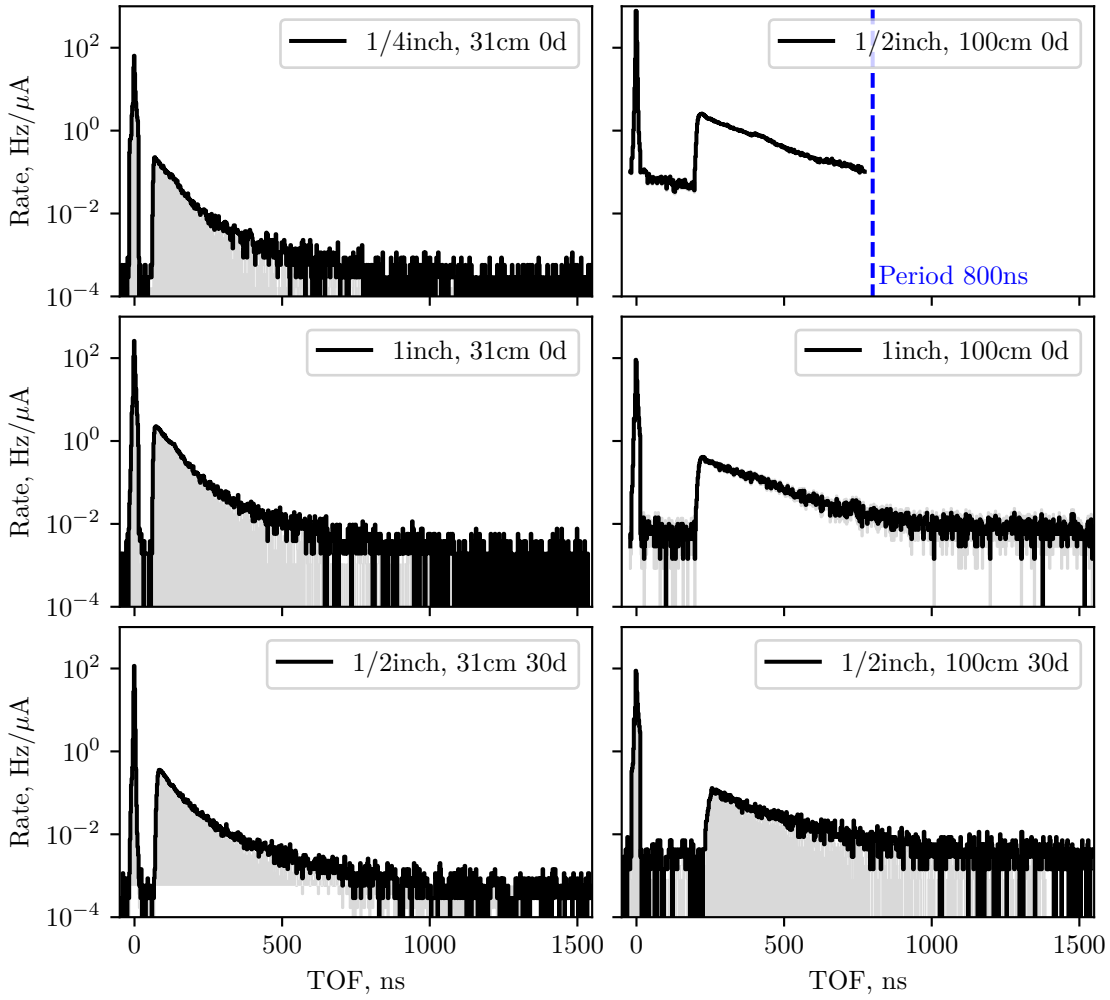

Figure 4.7. Time-of-flight measurements for the ^{7}Li(p,n) reaction at (1915.2 ± 3.8) keV performed with different detectors at 0° or 30° and 31 cm and 100 cm, annotated in each figure. The associated uncertainties are shown by a grey shadow, this shadow is not appreciated in the printed version.

From Fig. 4.7, we can observe significant differences between the various measurements. The measurements were conducted using two different flight paths.

The measurements displayed on the right side of the figure were performed with a flight path of 31 cm, while those on the left side were taken with a flight path of 100 cm. This variation in flight paths influences the shapes of the TOF spectra. For instance, we see that as the distance L between the neutron source and the detector decreases, the time interval between the gamma flash and the neutron peak becomes shorter. This indicates that the geometry of the experiment plays a crucial role in the timing and detection of neutron events.

Moreover, the first four graphs display measurements taken at zero degrees, while the last two are taken at an angle of 30 degrees. The shape of the TOF spectra seems similar, and the order of magnitude does not change abruptly.

Additionally, the measurement shown in the top left was conducted with a shorter time period of 800 ns compared to the other measurements, which is why the time range appears different. Specifically, this shorter period affects the resolution and width of the TOF spectrum. It also directly impacts the region between the gamma-flash and the neutron pulse, making this the only spectrum where this region is not flat. However, this can be explained. Since a very short period is being used, the pulses overlap, and what we are seeing in this region is the tail of the low-energy neutrons. To clarify this, Fig. 4.8 provides a representation of this TOF spectrum.

Figure 4.8 presents the final TOF spectrum for the mentioned measurement, zooming in on two important areas: the end of the neutron pulse and the region between the γ-flash and the neutron pulse. It is evident that the slope of the TOF spectra in these two areas demonstrates a relationship; the final step and the initial step coincide. We can reaffirm that the slope in the region between the γ-flash and the neutron pulse is due to the contribution of low-energy neutrons. In the other cases presented in Fig. 4.7, this overlap does not occur because the accelerator period is adequately adjusted to the experimental setup.

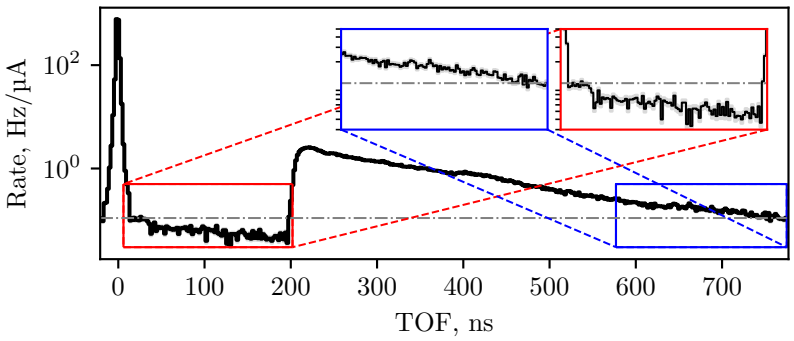

Figure 4.8. The final filtered TOF spectrum for the ^{7}Li(p,n)^{7}Be reaction at (1915.2 ± 3.8) keV, measured with a half-inch ^{6}Li-glass detector at 100 cm and 0°, is shown as a solid black line. The associated uncertainties are indicated by a grey shadow. The figure zooms in on two critical regions: the end of the neutron pulse (blue region) and the area between the gamma flash and the neutron pulse (red region).

4.3.1 Study of the γ-flash: Time and Energy Resolution

The γ-flash represents the time pulses distribution along the run, with each pulse corresponding to a two-nanosecond peak, as described in Section 3.3.3. All the presented measured TOFs, Figs. 4.6 and 4.7, exhibit a sigma lower than (1.39 $\pm$ 0.02) ns and a Full Width at Half Maximum (FWHM) lower than (3.26 $\pm$ 0.08) ns, obtained from the Gaussian fit of the γ-flash. These values are corroborated by the time resolution of the DAQ (2 ns) and the width of our proton signal (Fig. 3.12).

For illustrative purposes, in Figure 4.9, two fits for γ-flash histograms are shown, both corresponding to measurements taken using a half-inch ^{7}Li-glass placed at zero degrees. Specifically, Fig. 4.9 (**right**) presents the γ-flash for the measurement at a flight path of 31 cm, while Fig. 4.9 (**left**) shows the one at 100 cm. It is clear that the γ-flash in both figures is of the same order, and the observed difference is due to the distance between the detector and the target. Given that gamma emission is isotropic, this difference is therefore justified.

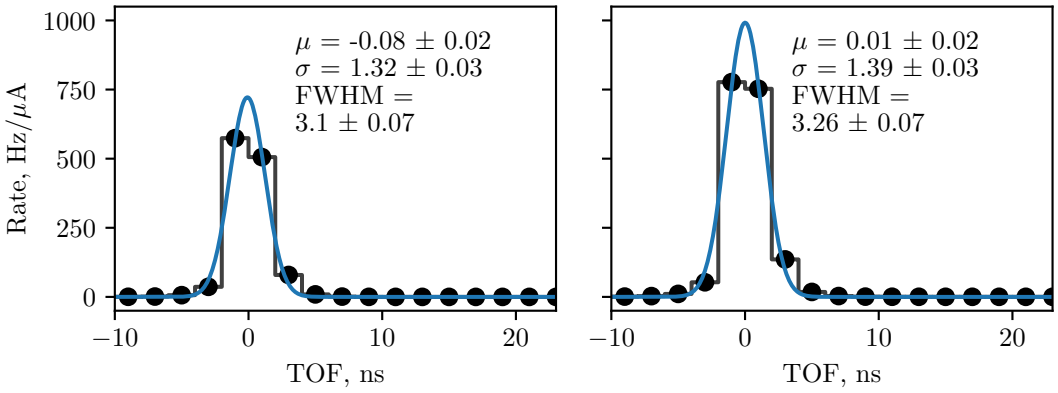

Figure 4.9. Gamma flashes for the ^{7}Li(p,n) at (1915.2 $\pm$ 3.8) keV TOF measurement at 0 degrees, with a ^{6}Li-glass of 1/2 inch at L= 31 cm (**left**) and L= 100 cm (**right**). The mean (μ), sigma (σ), and FWHM of the Gaussian fits are indicated in the figures; all these quantities are in ns.

4.3.2 Time-to-Energy Conversion

To measure a produced neutron energy spectrum using the Time-Of-Flight technique, a crucial step is converting the measured TOF spectrum into an energy spectrum. The measured time spectra are represented as histograms, indicating the number of detected particles per time bin. In this section of the data analysis, we will focus on the process required to transform the counts from time bins to energy bins, ensuring an accurate representation of the neutron energy distribution.

Hence, a precise determination of the neutron spectrum as a function of both angle and energy at a TOF facility relies critically on understanding the time-energy relationship of the neutron beam. In our facility and experimental setups, in terms of dimensions, the target thickness, whether ^{51}V or LiF, contributes negligibly to the neutron flight path of either 31 cm or 100 cm. However, when measuring the neutron field, the dimensions of the ^{6}Li-glass detector become significant, as they are comparable to the flight path. For instance, the most commonly used detector in our experiment, with a half-inch thickness (1.27 cm), represents approximately 4% of the 31 cm flight path. Consequently, the effective distance traveled by neutrons includes the defined flight path, the processes in the target, and the moderating distance within the ^{6}Li-glass, up to the point where the ^{6}Li(n, α)^{3}H reaction takes place.

To take into account the effect of our experimental setup when converting from time-to-energy, we will design the so-called Response Matrix (RM). This RM will be a matrix that relates the neutron detection times to their corresponding energies. To construct this Response Matrix, we need to define both a temporal and an energy binning.

The temporal binning will be in steps of 2 ns, determined by the resolution of the DAQ, ABCD. For the energy, we are going to create a binning, which will be called "natural" binning. We will consider the real energy binning of our measurement; thus, this used binning is the one that appears in a "natural" way when we apply Eq. 3.3. The energy resolution is a function of the flight path uncertainty and the time resolution. Therefore, using equation 3.4, an energy binning has been calculated, knowing that the time uncertainty is 2 ns and the flight path uncertainty is 0.1 cm. This binning will vary depending on the flight path and the frequency used in the measurement.

Consequently, with this binning established, we can construct the RM for each experimental setup. Using the simulation code MCNP6.2 [122], we will simulate our entire system. For each energy bin, we will run a simulation that acquires a Tally time 4 using the FM card. We will utilize the same F4 card employed to determine the efficiency of the detectors, but in a completely analogous manner, incorporating a more comprehensive geometry and utilizing the "time" function to obtain a time histogram. These simulations include the target (with its backing in the case of LiF), the detector located at the corresponding L and angle and the shape of the proton pulse itself. All the RM used in this thesis have been simulated for a sufficient duration until the errors became negligible.

An example of two different RMs is shown in Figures 4.10, each corresponding to different energy binning and experimental setups. Both RM are very similar to each other, since the only difference is the flight path, the reactions taken into account are the same, and the simulations are very similar. The main difference is the energy binning, because, as mentioned, it is calculated using the Eq. 3.4, which depends strongly on the flight path. The considered values of L are 31 cm for Fig. 4.10 (**left**) and 100 cm for Fig. 4.10 (**right**). As mentioned, each experimental

setup will require a distinct Response Matrix.

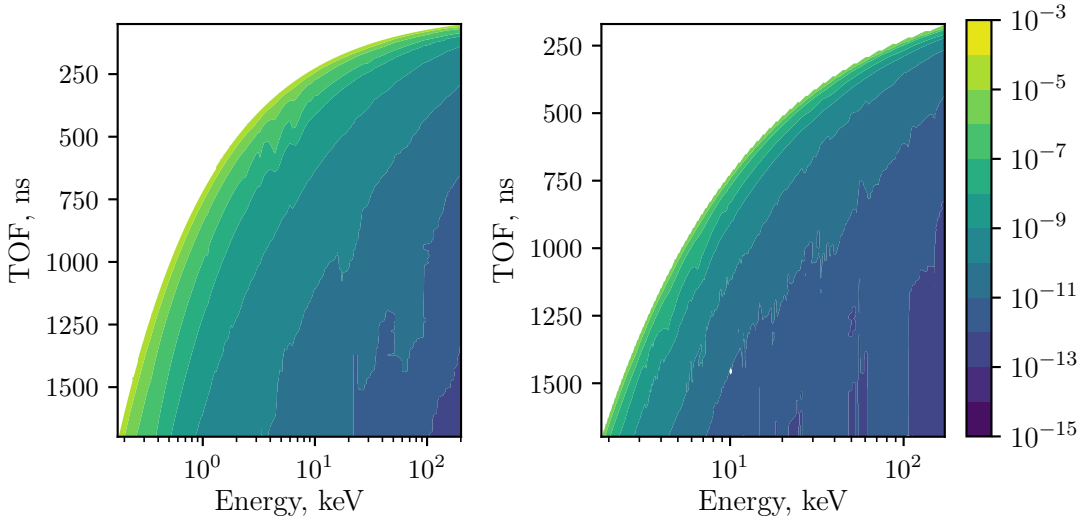

Figure 4.10. Response matrices for the ^{7}Li(p,n)^{7}Be measurement at 31 cm (**left**) and 100 cm (**right**) using a ^{6}Li-glass detector of 1/2 inch and a LiF target with Al backing.

To perform all conversions between TOF and energy across different experimental setups, a Response Matrix will be utilized. Below, several methods will be explained; these have been employed and found useful for bridging the gap between TOF and energy. The first method involves directly applying the formula relating time and energy, Eq. 3.3, incorporating the efficiency provided by the RM. The second method is centered on the definition of the RM; however, this method requires matrix inversion, introducing significant statistical errors. Finally, the third method, which proves to be the most effective for our application, employs the RM as a distributed probability of events.

To compare the different methods that we are going to show, we will conduct a comparison between R&K spectra at zero degrees and one of our measurements. The measurement we will present here is the ^{7}Li(p,n)^{7}Be at (1915.2 $\pm$ 3.8) keV, using a ^{6}Li-glass detector of 1/2 inch at 0° and an $L = 31$ cm. This measurement has good statistics and has been used to demonstrate all the steps of the data analysis; therefore, it is the perfect one to present here.

The first step to perform each of these methods will be to cut the gamma flash, because we only want to convert the part of the neutrons into energy. In Figure 4.11, the final filtered TOF is shown, and the part that we are going to transform is marked in blue. In this figure, the vertical lines indicate the limits of our TOF spectrum. The lower limit, 56 ns, is set there because below this time we do not find neutrons, and the upper limit, 709 ns, is equivalent to 1 keV (for this flight path); below this limit, the resolution is considered not good enough.

Knowing that Lederer, Käppeler, Mosconi, *et al.* [56] and Feinberg, Friedman,

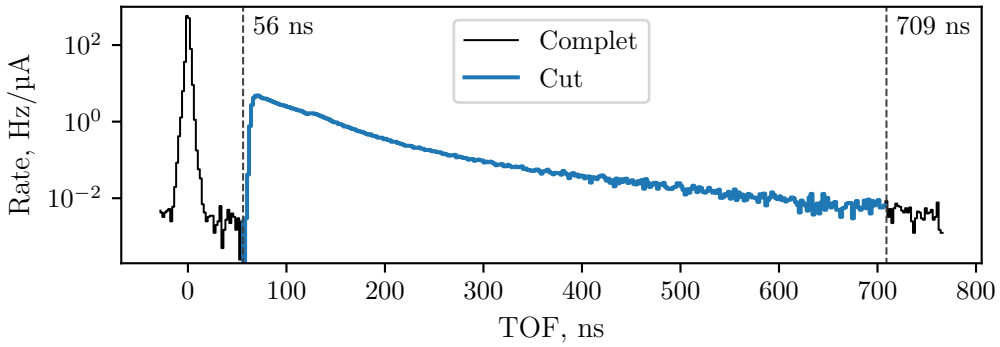

Figure 4.11. Cut TOF spectrum for the ^{7}Li(p,n) reaction at (1915.2 ± 3.8) keV, measured with a half-inch ^{6}Li-glass detector at 31 cm and 0 degrees. Black line is the complete filtered TOF spectrum and blue line is the cut TOF. The vertical lines show the limits. The 56 ns is marked because below this time we do not find neutrons. The 709 ns is equivalent to 1 keV, below this limit the resolution is not good enough.

Krása, *et al.* [55] present consistent results with R&K, we are going to use this experimental results to compare with our experiment. These results have been already presented at the begging of this chapter.

First method: Time-energy direct conversion using the RM efficiency

This first method is very simple. By using the kinematic equation for neutron energy, Eq. 3.3, we can transform the TOF range into an energy range by direct application of the equation. With this energy binning, we can account for the efficiency of our system by dividing the counts in each energy bin by the efficiency value for that bin. This efficiency can be extracted from the RM as the sum of all columns.

In order to be consistent in our development and to illustrate the form in which the efficiency of our setups will take, we will represent this efficiency for two specific cases. Using the two RMs shown in Fig. 4.10, we sum all columns and obtain the efficiency functions represented in Figure 4.12. The similarities between the shapes of these efficiencies and the intrinsic efficiencies presented in Fig. 3.8 are evident, primarily due to the significant contribution of our experimental setup's efficiency with the ^{6}Li-glass detector. Additionally, some aluminum resonances are present due to the Al backing of the target. The main difference between the two figures is the energy range. The uncertainty associated with the efficiency is negligible due to the extensive simulation time used to construct the RM.

In Figure 4.13, we present a comparison between the experimental data from the literature and our result obtained using this method. The direct application of the kinematic equation is also shown (grey line), without taking into account the efficiency of the experimental setup. If we apply only the kinematic equation,

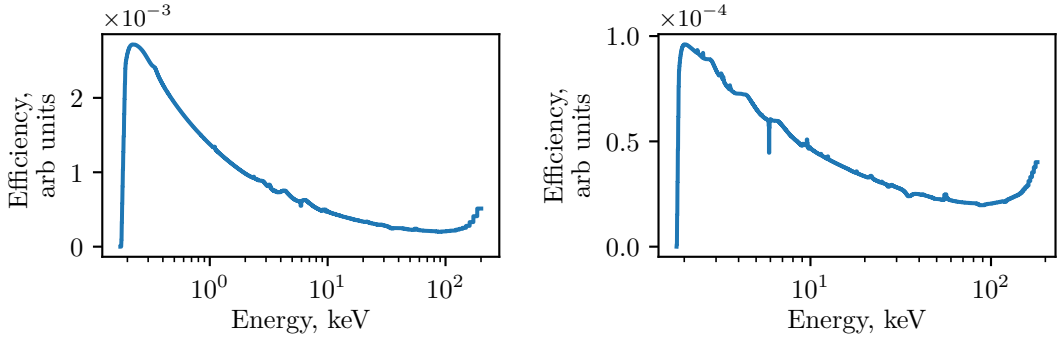

Figure 4.12. Experimental setup efficiency for the ^{7}Li(p,n)^{7}Be measurement at 31 cm (**left**) and at 100 cm (**right**), using a half-inch ^{6}Li-glass detector and a LiF target with Al backing. The sum of the columns of the Response Matrices is presented in 4.10.

our result does not correctly match with R&K at zero degrees, as presented in the figure with the results from Lederer, Käppeler, Mosconi, *et al.* [56] and Feinberg, Friedman, Krása, *et al.* [55], showing many resonances at low energy. The uncertainties shown in this case are directly due to the rate uncertainties observed in the TOF spectra.

In contrast, when we incorporate the efficiency of the experimental setup into our calculations, the shape of the resulting spectrum aligns much better with the literature experimental data, and the previously observed resonances are corrected. This adjustment, represented by a green line, allows for a more accurate comparison, which improves the reliability of our results. In this case, the statistical uncertainties are, again, due to the rate uncertainties observed in the TOF spectra.

An important point to note is that the binning used in the Lederer and Feinberg experimental results and our binning is completely different. To enable comparison, in Fig. 4.13 and in the subsequent figures, we have rebinned these experimental results. The binning used is the "natural" one; therefore, due to the nature of Eq. 3.3, we have many more energetic bins in the low-energy range than in the high-energy range. In this case, the smallest width binning is 5.684 eV (considering the lower energy limit of 1 keV), and the largest is 15.130 keV (if we consider the energy range up to 200 keV).

This figure demonstrates that the first method we used improves the precision of our results while remaining straightforward to apply. The simplicity of this approach makes it an effective tool for analyzing experimental data, ensuring that the impact of experimental conditions is adequately addressed.

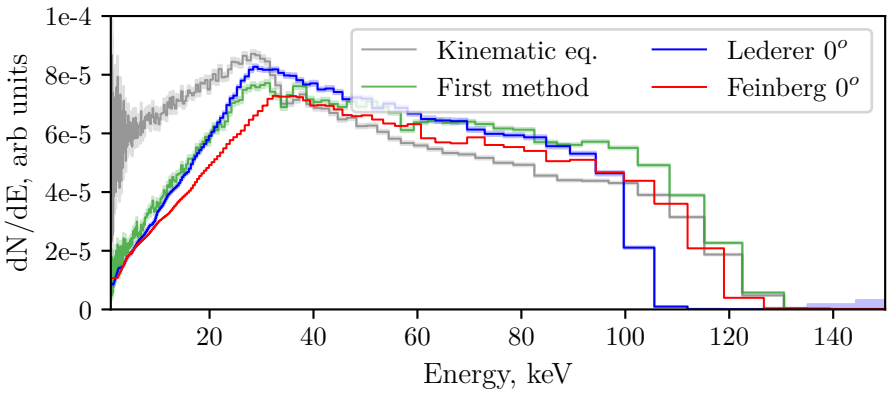

Figure 4.13. Energy spectrum obtained by the first method for the ^{7}Li(p,n) reaction at (1915.2 ± 3.8) keV, measured with a half-inch ^{6}Li-glass detector at 31 cm and 0 degrees. A comparison is made between Lederer at 0° [56], Feinberg at 0° [55], the direct conversion using the kinematic equation, and my first method. The associated uncertainties are indicated by a shadow for each case.

Second method: Inversion RM by the EM method

As discussed above, the Response Matrix is a relation between the neutron energy and the time when it is detected by the detector. Therefore, using this matrix, we can describe the temporal distribution or TOF spectrum, as a vector $\vec{T}$, of the n detected events within the detector. This can be expressed as:

$$\vec{T} = \hat{RM} \times \vec{E}, \tag{4.1}$$

where $\hat{RM}$ represents the system's Response Matrix in matrix form, and $\vec{E}$ is the energy distribution vector necessary to produce $\vec{T}$. The key point here is that we have $\vec{T}$ and $\hat{RM}$, and we need $\vec{E}$, so an inversion of the Response Matrix is required :

$$\vec{E} = \hat{RM}^{-1} \times \vec{T}. \tag{4.2}$$

To perform this calculation, we have various options. Knowing that the Response Matrix ($\hat{RM}$) is a matrix populated with many small numbers and values of various ranges, the mathematical inversion process can become quite complicated and unstable. The presence of small values in the matrix can lead to numerical inaccuracies and make the inversion process sensitive to errors, complicating the direct application of conventional inversion techniques. To address these challenges and achieve a more stable and reliable solution, we decided to employ the Expectation-Maximization (EM) method [138]. The EM method is a powerful iterative algorithm commonly used in statistical data analysis, especially for dealing with incomplete or noisy data. By utilizing the EM method, we can iteratively estimate the energy distribution $\vec{E}$ that maximizes the likelihood of observing the

detected TOF spectrum $\vec{T}$ given the $\hat{RM}$. This approach helps mitigate the numerical instability issues and provides a robust way to obtain the desired energy distribution. In summary, choosing the EM method allows us to handle the complexities of the inversion process effectively, ensuring that we obtain accurate and significant results despite the challenges posed by the values with varying ranges in the Response Matrix.

In Figure 4.14, the result of our measurement using this EM method, or second method, is shown. We have applied a convergence tolerance of ≤ 0.1. In this case, the uncertainties attached to the method are very small; therefore, the uncertainties of our result here are due to the uncertainties of the TOF spectrum. The result exhibits a similar general shape compared to the experimental literature references, but the fit is not as good in the low-energy range as it is at higher energies. In the low-energy range, many resonances are present, and these do not decrease with the decreasing convergence tolerance; on the contrary, they become larger. An important issue with this method is that it is an iterative process, requiring more computational time to obtain a good result and necessitating a RM with high resolution.

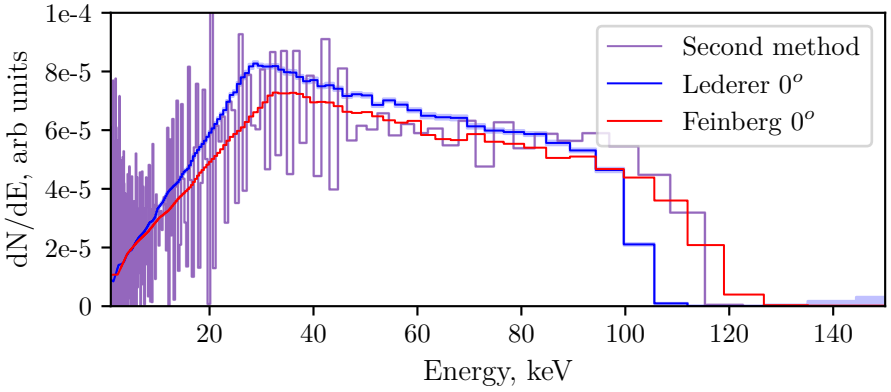

Figure 4.14. Energy spectrum obtained by the second method for the ^{7}Li(p,n) reaction at (1915.2 ± 3.8) keV, measured with a half-inch ^{6}Li-glass detector at 31 cm and 0 degrees. Comparison between Lederer 0° [56], Feinberg 0° [55] and my second method. The associated uncertainties are shown by a shadow for each case.

Third Method : Energy Distribution

This method is simpler than the previous one because it does not require the inversion of the Response Matrix. Instead, it converts the RM into a probability matrix by normalizing each row so that the sum of its elements equals one. Since each row corresponds to a fixed neutron energy, this normalization process transforms the values into probabilities of detecting neutrons with that energy at different time intervals. As a result, the detected time spectra can be redistributed into energy spectra.

Once the probability matrix is prepared, the method transforms the detected TOF spectrum into an energy distribution through matrix multiplication. The detected neutron counts, represented in time bins, are multiplied by the probability matrix, converting them from the time domain to the energy domain and producing an estimated energy distribution. At the same time, the same operation is applied to the vector of experimental errors to determine the corresponding uncertainties in the energy distribution.

A crucial step in this method is the efficiency correction, which compensates for the loss of detector efficiency information during the normalization of the RM. To address this, an external efficiency function is applied to adjust both the energy distribution and its associated errors. This function accounts for various experimental and calibration factors that influence neutron detection, ensuring that the final energy distribution accurately reflects the true physical scenario while correcting for systematic biases in the detection process.

Overall, this third method effectively addresses the numerical instability inherent in direct matrix inversion by converting the Response Matrix into a probability matrix and avoiding the inversion of the Response Matrix. Additionally, it corrects for experimental factors to provide an accurate and reliable energy distribution of detected neutrons. This method is adaptable to different experimental setups and detector types, utilizing only their Response Matrices, making it a robust tool for neutron energy analysis.

In Figure 4.15, the results of this third method are presented by a black line, compared with the results of Feinberg [55] and Lederer [56] at 0 degrees. The uncertainties of our result here stem from the uncertainties of the TOF spectrum, along with the statistical uncertainty of the Response Matrix. Notably, the data show excellent agreement with the established data from Lederer and Feinberg in the lower energy range. As we progress through the energy spectrum, it becomes clear that the overall energy distribution continues to closely match Feinberg's results across the entire range under consideration. This consistency not only reinforces the validity of the third method but also demonstrates its robustness over a broader range of energy. The simplicity and effective performance of this method position it as the best of the three methods proposed in this section.

Comparison the three conversion methods

By Figures 4.13, 4.14, and 4.15, we are able to compare the three proposed methods for obtaining the energy spectrum by converting the TOF spectrum. To better observe the discrepancies between the shapes of the spectra, constant energy binning is preferred. Therefore, we will rebin the data into 2 keV intervals and determine which method fits best.

Figure 4.16 illustrates a comparison of the three methods rebinned to 2 keV steps. All uncertainties are represented in the figure by error bars. The second method, even after rebinning, clearly exhibits oscillations due to the convergence behavior of the EM method for inverting the RM. In contrast, the first and third

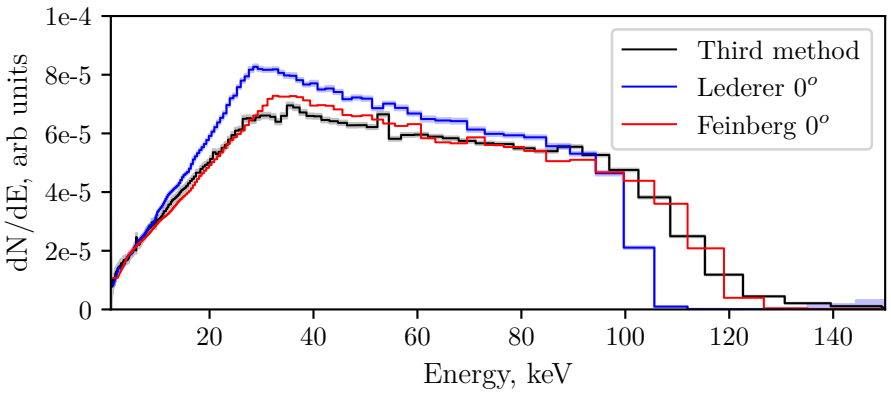

Figure 4.15. Energy spectrum obtained by the third method for the ^{7}Li(p,n) reaction at (1915.2 ± 3.8) keV, measured with a half-inch ^{6}Li-glass detector at 31 cm and 0 degrees. A comparison is made between Lederer at 0° [56], Feinberg at 0° [55], and my third method. With uncertainties showed by a shadow.

methods align well with the shapes of the R&K and Feinberg spectra. The third method shows a longer tail at high energies compared to the first method.

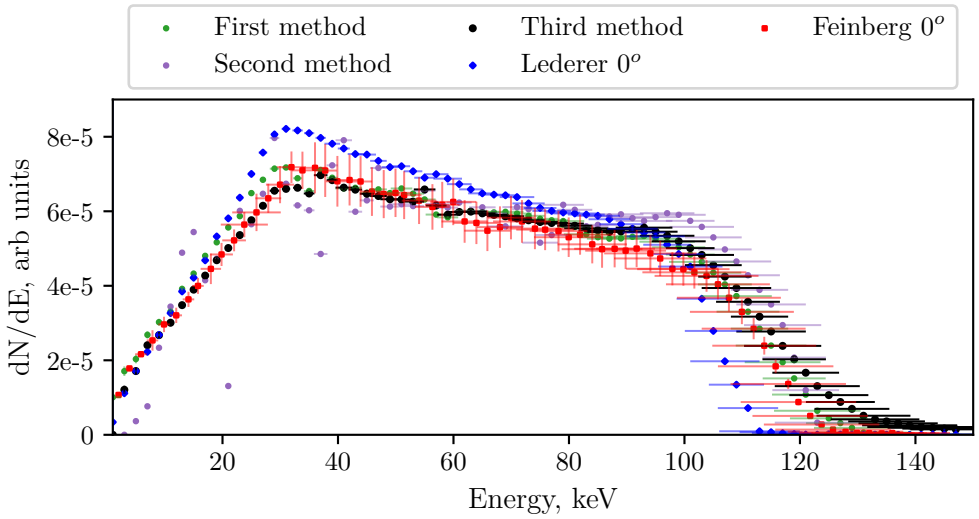

Figure 4.16. Energy spectrum for the ^{7}Li(p,n) reaction at (1915.2 ± 3.8) keV, measured with a 0.5-inch ^{6}Li-glass detector at 31 cm and 0°. Comparison between Lederer 0° [56], Feinberg 0° [55], and my methods, with uncertainties shown as error bars.

Nonetheless, we have decided to select the third method as the best option because it is the best fit with Feinberg for the entire energy range. We will use the third method to transform TOF to energy in the subsequent steps, as it provides a good fit and demonstrates high stability.

4.4 Results and Discussion

In the previous section, we discussed the different methods for converting the TOF spectrum into an energy spectrum. The third method was chosen as the most suitable for our application. Therefore, we will now present the energy conversion for all the measured TOFs shown in Figures 4.6 and 4.7, which include all the runs listed in Table 4.1. From now on, we will only compare with the Feinberg result [55] as we obtained a better agreement in the previous section. This better fit can be justified by the proton energy used in the different experiments. In our case, the proton energy was (1915 ± 4) keV, while for Lederer *et al.* [56], it was (1910 ± 1) keV, and for Feinberg *et al.* [55], it was (1913 ± 6) keV. This agreement suggests consistency across the different experimental setups but shows a better alignment with the Feinberg results.

In Figure 4.17, the results of five different measurements are shown, using two distinct flight path lengths (L) and three separate detectors (1, 1/2, and 1/4 inch). These measurements represent all the energy spectra obtained at zero degrees. Notably, all the results fit very well with the Feinberg result [55] at 0 degrees, which is in agreement with the R&K spectrum and is also represented in the figure by the red squares. All the results are presented using a rebinning of 2 keV, which was implemented to facilitate a direct comparison between the different measurements. This rebinning helps smooth out fluctuations and allows for a clearer interpretation of the energy spectra.

However, it is important to note that the statistical errors in some of the results are relatively large. This can be attributed to the fact that, in certain cases, the measured time was limited, leading to lower statistical precision. This is the case of the measurement taken by a one-inch ^{6}Li-glass detector at 100 cm, represented by purple dots.

Moreover, the comparison between the two different path lengths allows us to observe how the experimental setup influences the energy spectrum's uncertainty. The shorter path length (31 cm, represented on the left) provides a different resolution compared to the longer path length (100 cm, represented on the right), highlighting how variations in the setup can influence the precision and clarity of the measured energy spectra. It should be noted that the results are favorable for both flight paths.

Figure 4.18 presents two energy spectra measured using the same detector (a half-inch ^{6}Li-glass) positioned at 30 degrees, with two different flight path lengths of 31 cm and 100 cm. These measurements are compared to the Feinberg spectrum at this angle. The left figure depicts the measurement taken with the shorter path length of 31 cm. This measurement demonstrates good agreement with the Feinberg result and exhibits relatively small statistical errors due to sufficient measurement time.

On the other hand, the right figure corresponds to the measurement taken with the longer path length of 100 cm. This result does not align as well with the

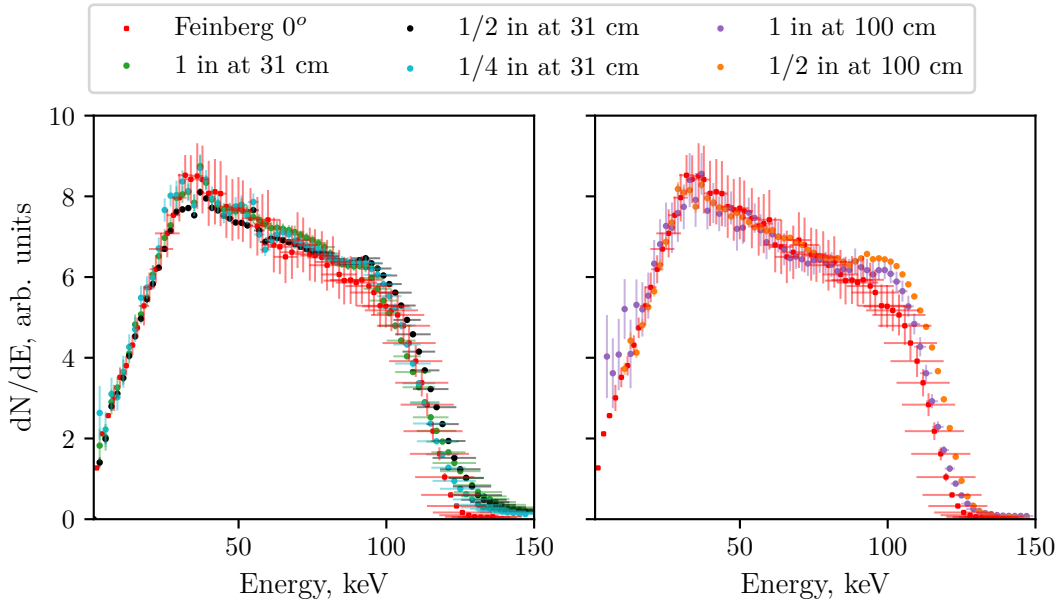

Figure 4.17. Energy spectrum of LiF measurements at 0° compared with Feinberg, Friedman, Krása, *et al.* [55] measurements. Data are rebinned by 2 keV. The left figure shows data taken at 31 cm, while the right figure displays data for the 100 cm flight path. The uncertainties are represented by error bars in each case.

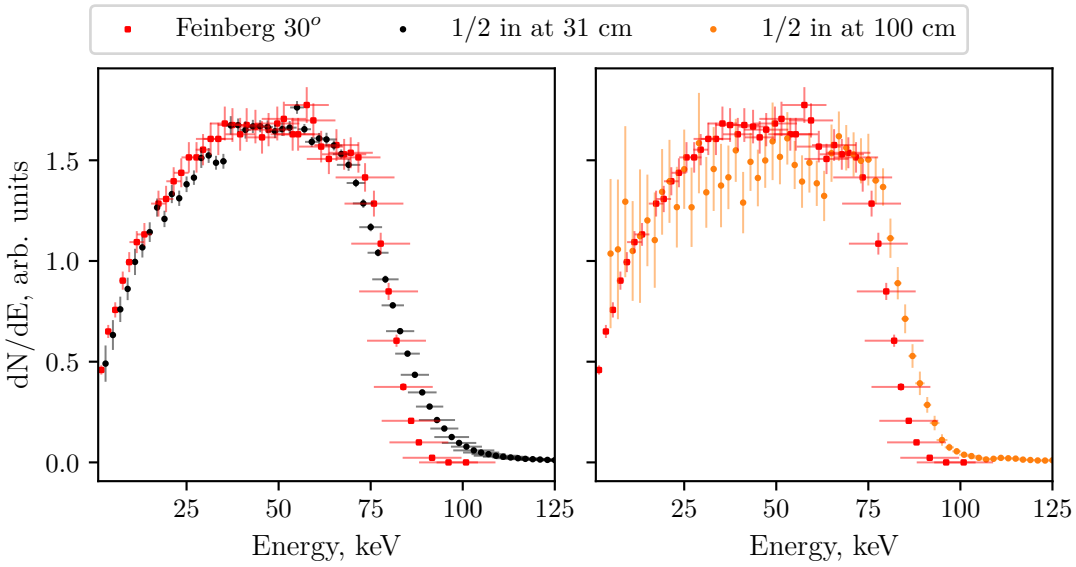

Figure 4.18. Energy spectrum of LiF measurements at 30° compared with Feinberg, Friedman, Krása, *et al.* [55]. Data rebinned by 2 keV. The left figure shows data taken at 31 cm, while the right figure displays data for the 100 cm flight path. The uncertainties are represented by error bars in each case.

Feinberg spectrum, largely due to the short duration of the measurement, which is reflected in the much larger statistical uncertainties. As shown in Table 4.1, the total measurement time for this dataset was only 14 minutes, significantly limiting the statistical precision. Consequently, the larger statistical errors in this case make it more difficult to draw definitive conclusions about the alignment with the Feinberg spectrum.

This comparison between the two flight path lengths provides valuable insights into how measurement time and path length influence the quality and precision of the energy spectra. The shorter path (31 cm) allows for higher resolution and better agreement with reference data due to the smaller uncertainties, while the longer path (100 cm), with its inadequate measurement time, introduces larger errors, thus reducing the reliability of the results. These observations highlight the importance of ensuring adequate measurement time, especially when using longer flight paths, to achieve results with lower uncertainty and greater accuracy.

A crucial aspect of our investigation is the normalization process in our measurements. This step is essential, as the primary goal of these measurements is to validate the method and subsequently use it to normalize the neutron yield from the vanadium reaction, which will be discussed in the next chapter.

For the Li spectrum measured at a distance of 31 cm, at 0 degrees, using a half-inch detector, we observed a production rate of 1483 $\pm$ 20 neutrons·Hz/μA within the energy range of 1 to 150 keV. This high production rate indicates a strong reaction yield at closer proximity to the detector. In contrast, the energy spectrum measured at 100 cm, also at 0 degrees and using the same half-inch detector, showed a production rate of 781 $\pm$ 15 neutrons·Hz/μA within the energy range of 8.5 to 150 keV. The lower production rate at this increased distance highlights the spatial dependence of the neutron yield, which is crucial for understanding the behavior of the reaction at varying distances.

These two measurements provide a comprehensive understanding of neutron production rates across various distances and energy ranges. The data collected will serve as a reference to normalize the neutron yield of the vanadium reaction, ensuring that our results are both accurate and reliable.

At an energy of 1910 keV, the total neutron yield using a thick LiF target is $7.29 \cdot 10^{6}$ neutrons·Hz/μA, following Ref. [133]. Using NEBOAS [136], we determined that the total forward neutron yield at $E_p = 1915.2$ keV is $8.25 \cdot 10^{6}$ neutrons·Hz/μA, completely in agreement with our code based on the Lee and Zhou equations. The neutron spectra at a distance of 31 cm amount to $1.43 \cdot 10^{5}$ neutrons·Hz/μA, again using NEBOAS. This value will be utilized to standardize the neutron yield for the vanadium reaction.

4.4.1 Comparison between Our Experimental Data and Theoretical Data

All the results have been compared with experimental data in agreement with R&K. In this section, we will study the comparison between our experimental results and computational codes. As we mentioned at the beginning of this chapter, the NEBOAS code [136], [137] and our direct application code of the Lee and Zhou [133] equations can provide us with the angle- dependent energy spectra. Since the experiment has been conducted at the MONNET facility and the NEBOAS code has been developed for use in this specific installation, we will utilize it to compare with our experimental results.

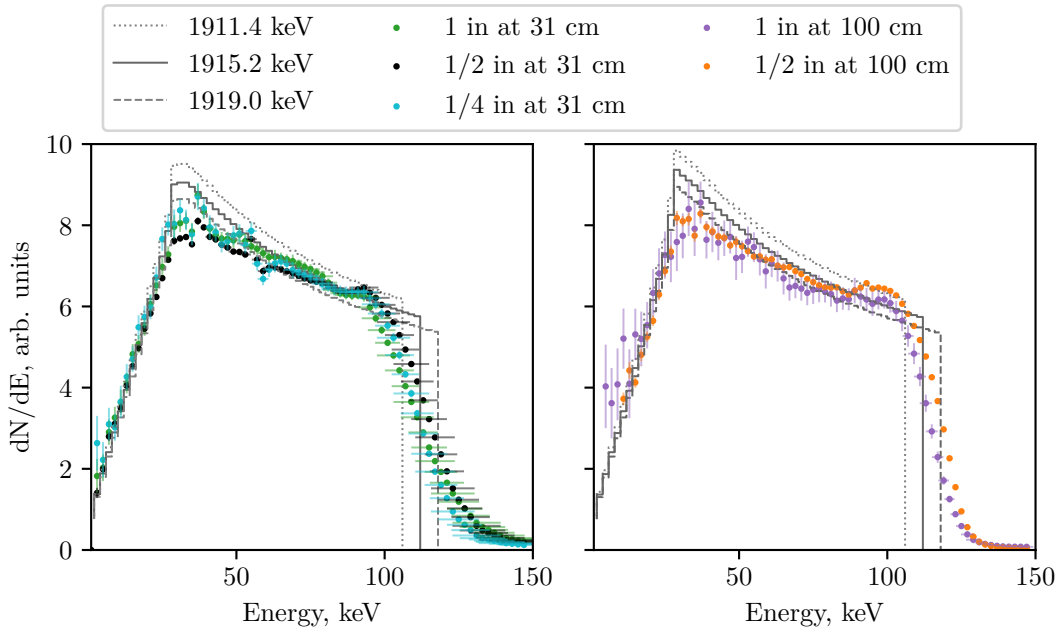

Figure 4.19. Energy spectrum (dN/dE) of LiF measurements at 0° compared with the energy spectra from the NEBOAS code for proton energy of 1911.4, 1915.2 and 1919.0 keV. Data are rebinned by 2 keV. The left figure shows data taken at 31 cm, while the right figure displays data for the 100 cm flight path. The associated uncertainties are shown by an error bar for the measured cases.

Depending on the flight path length and the degree the obtained spectra with this code is different. For this reason, we are going to split our results in angle and length. Here the real measured proton energy will be taken into account, (1915.2 ± 3.8) keV. To be consistent we will present the results of three energies: 1911.4, 1915.2 and 1919.0 keV.

In Fig. 4.19, our experimental results for an angle of 0 degrees are shown. On the left side, we have the measurements using $L = 31$ cm, and on the right side, the measurements using $L = 100$ cm. Both figures include a comparison with the

NEBOAS results. All results have been rebinned to 2 keV for consistency. This figure is analogous to Fig. 4.17, as the same experimental results are presented.

The NEBOAS results are presented alongside our experimental data to highlight the similarities and differences between the datasets. This comparison is essential for assessing the validity of our experimental findings. Overall, the experimental results agree very well with the simulated data. However, some discordance is observed in the tail at higher energies. This discrepancy can be attributed to beam degradation.

In Figure 4.20, the experimental results for an angle of 30 degrees are presented and compared with the NEBOAS results. Once again, the data are rebinned to 2 keV for consistency, and this figure is analogous to Fig. 4.18. For the measurement at a flight path of 31 cm, the experimental data align very well with the simulated results, with discrepancies primarily observed in the tail. In contrast, for the measurement at a flight path of 100 cm, the uncertainties are substantial due to the limited measurement time. Despite this, the overall shape of the energy spectrum still agrees with the simulated data, with the exception of the tail.

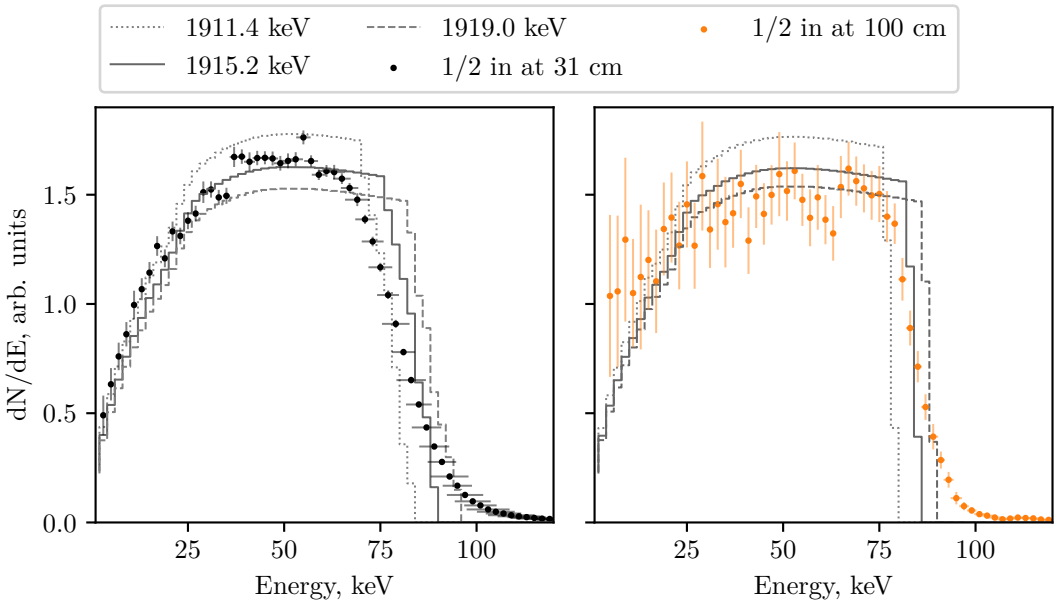

Figure 4.20. Energy spectrum (dN/dE) of LiF measurements at 30° compared with the energy spectra from the NEBOAS code for proton energies of 1911.4, 1915.2, and 1919.0 keV. Data are rebinned by 2 keV. The left figure shows data taken at 31 cm, while the right figure displays data for the 100 cm flight path. The associated uncertainties are represented by an error bar for the measured cases.

In conclusion, our experiments have demonstrated that the results obtained at different distances and angles align remarkably well with the NEBOAS simulations, validating the methodology used and confirming the robustness of the experimental data. Despite some discrepancies observed in the tails of the spectra, which can be

attributed to beam degradation, the overall agreement indicates that the approach used for the normalization and analysis of the energy spectra is effective.

Chapter 5

Measurement of the ^{51}V(p,n)^{51}Cr reaction neutron near the threshold

The measurement of the ^{51}V(p,n)^{51}Cr reaction near the threshold was conducted at the JRC-MONNET facility using the experimental method described in Chapter 3. Most of the experimental results discussed in this chapter have been previously published in Ref. [139].

Despite the extensive nuclear data available for the ^{51}V(p,n)^{51}Cr reaction, significant discrepancies exist among the reported cross-sections from different experiments, particularly near the threshold, where values diverge by an order of magnitude, as shown in Figure 2.6. Furthermore, there is a notable lack of data: while some experiments have reported total neutron and gamma yields, no experimental information is available on the angular-dependent energy distribution near the threshold (see Chapter 2). In addition to these data limitations, it is worth noting the potential use of the ^{51}V(p,n)^{51}Cr reaction as a low-energy neutron source for BNCT without moderation.

The angle-energy emission of the ^{51}V(p,n)^{51}Cr reaction near the threshold was measured using a 500 μm-thick vanadium target. Vanadium is known for its relevance in neutron-induced reactions at the neutron energies considered in this study. Therefore, to account for possible neutron interactions within the target, a transmission measurement was also performed using the same target. For this measurement, the neutron field produced by the ^{7}Li(p,n)^{7}Be reaction was used, as described in Chapter 4. The data obtained from the transmission experiment are crucial for correcting the ^{51}V(p,n)^{51}Cr measurement.

5.1 Transmission Measurement of ^{51}V(n,tot)

Using the described TOF technique, a neutron transmission measurement was conducted. This measurement was crucial to verify the resonances associated

with neutron absorption in the vanadium target, specifically represented by the ^{51}V(n,tot) reaction.

In Figure 5.1, the cross-section data for vanadium neutron interactions, from the TENDL library [52], are presented. These data are crucial for understanding the interactions between neutrons and vanadium. The figure illustrates how these interactions are distributed across the energy range under study. The first key contribution depicted is elastic neutron scattering (^{51}V(n,n')). In this process, a neutron collides with a vanadium nucleus and scatters without transferring energy to the nucleus or undergoing any nuclear transformation. The second contribution is gamma emission neutron capture (^{51}V(n,γ)). Here, the vanadium nucleus absorbs the incoming neutron and transitions to an excited state. The nucleus then emits a gamma photon to release the excess energy and stabilize itself. Finally, the total cross-section, denoted as ^{51}V(n,tot), is also shown in the figure. This value represents the sum of all possible neutron interactions with the vanadium nucleus in the specified energy range.

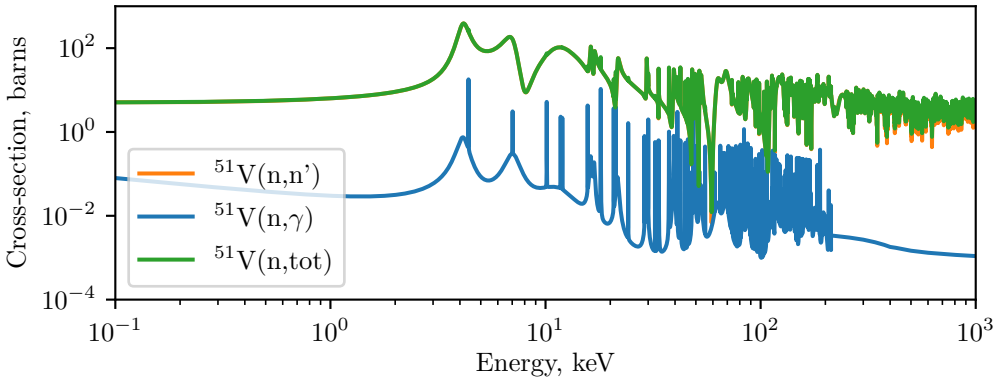

Figure 5.1. Vanadium neutron-induced TENDL [52] cross-sections.

In our case, the transmission measurements were performed using three different setup configurations, with their parameters listed in Table 5.1. The positions of the detector and the ^{51}V foil, along with the irradiation time, charge, intensity, PLC, and $CeBr_3$ events, are specified. All measurements were conducted using the same half-inch ^{6}Li-glass detector positioned at 0 degrees, the previously described LiF target placed at the end of the beamline, and a cut foil with a thickness of 0.5 mm located at a specific position.

As noted in Table 5.1, the first measurement was performed by placing the detector at 31 cm and positioning it 12 cm from the LiF target. The second measurement is similar to the previous one, but the flight path for the detector was set at 100 cm, and the vanadium foil was placed 31 cm from the target. Finally, the last measurement was conducted with a flight path of 100 cm, positioning it also 100 cm from the target, close to the detector.

All these measurements have been performed at a high voltage of (764 $\pm$ 1) kV; this is equivalent to 1915.2 $\pm$ 3.8 keV following the calibration of the accelerator.

Detector L, cm	^{51}V foil distance, cm	Time, min	Charge, μA/Hz	Intensity, μA	PLC events	$CeBr_3$ events
31	12	186.27	8453	0.756(13)	$1.1 \cdot 10^6$	$2.1 \cdot 10^7$
100	31	99.77	2376	0.752(18)	$3.8 \cdot 10^5$	$4.9 \cdot 10^7$
100	100	75.26	3396	0.397(10)	$2.6 \cdot 10^6$	$8.3 \cdot 10^6$

Table 5.1. TOF measurements parameters for the vanadium-51 neutron transmission. The uncertainty for the PLC and $CeBr_3$ counts is not included in the table because it is equivalent to the square root of the number of events. The same happens with the uncertainty of the charge. The notation value(number) indicates the value followed by the uncertainty of the last digits in parentheses, the uncertainty representing the statistical fluctuation of the intensity.

The same energy is used in the previous chapter (Chapter 4) to calculate the ^{7}Li(p,n) spectrum near the threshold at 0 and 30 degrees. Therefore, for these transmission measurements, the chosen angle for measurement was zero degrees because it is a known neutron spectrum for us, as it has been studied in this thesis. The experimental setup for this measurement is shown in Fig. 5.2. As mentioned, the foil was placed between the LiF target and the ^{6}Li-glass detector, using an aluminum structure and tape to secure it. The fixing elements of the setup were basically transparent to the neutrons. Once more, the $CeBr_3$ and PLC detectors were used as monitors.

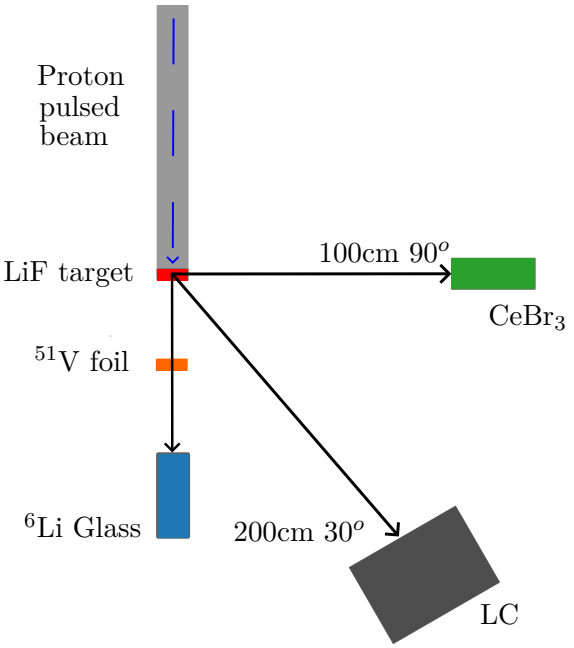

Figure 5.2. Diagram of the setup for for ^{51}V neutron transmission TOF measurements. Quantities are in cm and degrees. The diagram is not to scale.

A key aspect of these measurements is comparing the neutron spectra with and without the vanadium foil to study neutron transmission. It is evident that the three measurements presented in Table 5.1 have their corresponding measurements without vanadium in Table 4.1, allowing for direct comparison. Our study focuses on analyzing the differences between the energy spectra of these paired measurements to understand the impact of the vanadium foil. Through this analysis, we aim to identify the specific effects of vanadium on neutron transmission and gain a deeper understanding of its influence on the observed spectral characteristics.

Transmission neutron vanadium TOF measurements have followed the same filters as the lithium TOFs presented in Chapter 4, namely the Qlong and flat background filters. Figure 5.3 shows the three TOFs from the measurements detailed in Table 5.1. In the figure on the right, two TOF spectra are presented with the same flight path but different positions for the vanadium foil. The difference in the number of neutrons is noticeable between these two measurements; this is because the neutron scattering is higher when the vanadium foil is at 31 cm compared to when it is at 100 cm. Meanwhile, in the figure on the left, only one TOF is shown. There are alterations in the left figure that could indicate resonances, observable solely by examining the TOFs. These alterations will become more evident when viewing the energy spectra. In the right figure, the resonances are not as evident due to the energy range that this time represents. For the two TOFs with L=100 cm as the flight path, the minimum measured energy has been 8.5 keV; therefore, some of the main resonances present in the left figure are not visible in the right one.

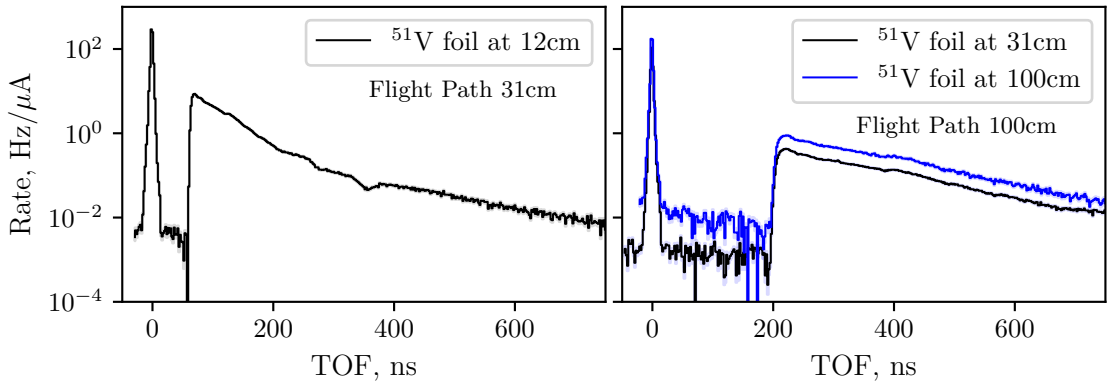

Figure 5.3. Time-Of-Flight spectra for the vanadium neutron transmission measurements with a vanadium foil placed between the LiF target and the half-inch ^{6}Li-glass detector. The distance of the vanadium foil from the target is indicated in each figure. The flight path to the ^{6}Li-glass detector is $L = 100$ cm in the **right** figure and $L = 31$ cm in the **left**. The proton energy was (1915.2 ± 3.8) keV for all measurements. The associated uncertainties are shown by a shadow in each case.

Using the same method described in Chapter 4 to convert TOF into energy, we obtain the energy spectrum for the mentioned transmission measurements. Here, however, we focus on the difference between the TOF measurements with and without the ^{51}V foil. Therefore, in Figs. 5.4, 5.5 and 5.6, we present the energy spectrum and the difference with and without the 0.5 mm vanadium foil. Each figure follows the same structure, the energy spectrum at zero degrees, with and without vanadium is shown on the left figures, while the difference between the two spectra is shown on the right ones. The figures include uncertainties for each energy spectrum. The statistical uncertainty of the difference is the sum of both spectra's uncertainties, making it larger.

On the right side of Figs. 5.4, 5.5, and 5.6, additional data is presented alongside the experimental difference. The calculated difference from MCNP6.2 [122] simulations is shown in blue. In these simulations, we modeled the experimental conditions with and without vanadium and then subtracted the resulting neutron spectra to obtain the difference. The initial neutron spectrum used for these simulations was the angle-dependent spectrum for ^{7}Li(p,n) at 1915.2 keV, obtained by our code based on Lee and Zhou's equations [133], as explained in the previous chapter. Additionally, we show the ^{51}V(n,tot) TENDL [52] cross-section in green to evaluate whether the effect aligns with our expectations. In this energy range, contributions to the ^{51}V(n,tot) cross-section come solely from two reactions: ^{51}V(n,γ)^{52}V and ^{51}V(n,el)^{51}V.

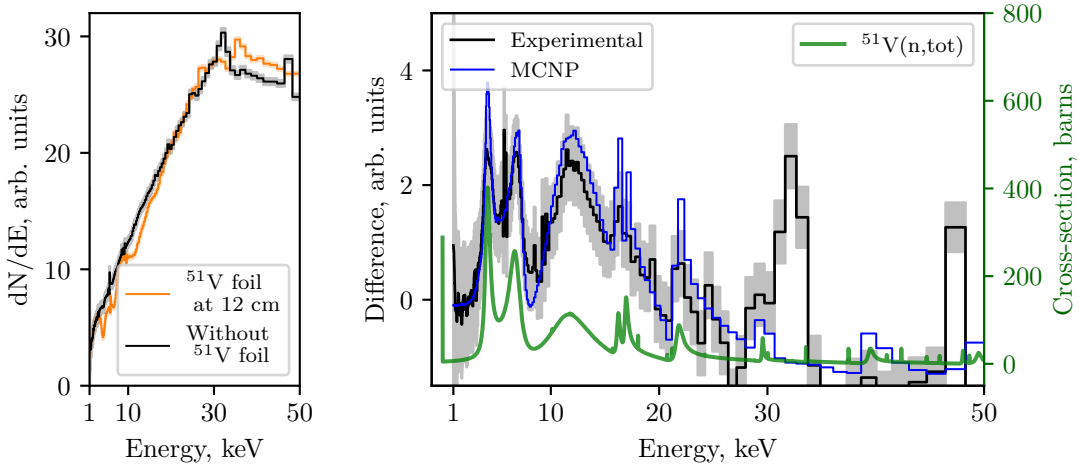

Figure 5.4. **Left:** Energy spectra measurements with Vanadium at 12 cm (orange line) and without Vanadium (black line), measured with a half inch ^{6}Li-glass detector at 31 cm. **Right:** Black line - Difference between the two spectra with and without Vanadium. Grey shadow - Error of the difference between the two spectra with and without Vanadium. Green line - ^{51}V(n,tot) TENDL [52] cross-section. Blue line - Difference between the two spectra with and without Vanadium results from MCNP6.2 simulations.

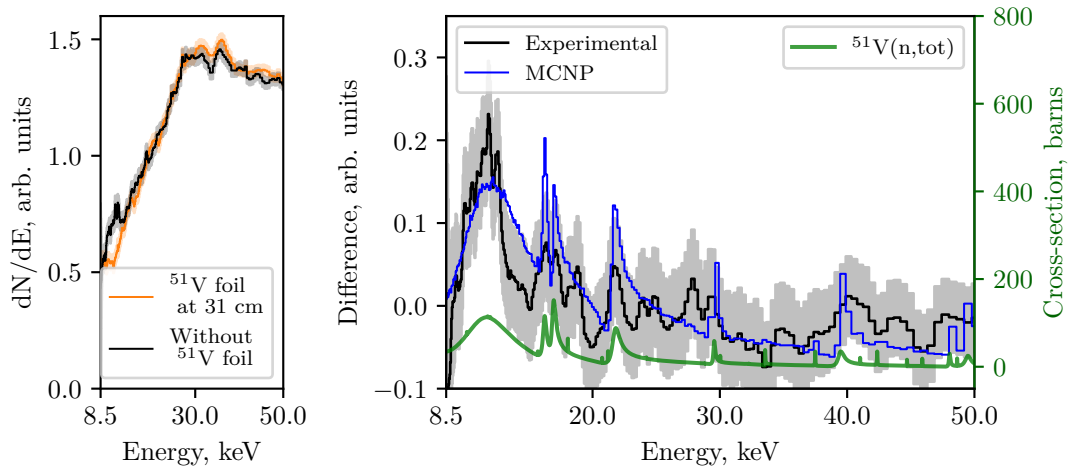

Figure 5.5. **Left:** Energy spectra measurements with Vanadium at 31 cm (orange line) and without Vanadium (black line), measured with a half inch ^{6}Li-glass detector at 100 cm. **Right:** Black line - Difference between the two spectra with and without Vanadium. Grey shadow - Error of the difference between the two spectra with and without Vanadium. Green line - ^{51}V(n,tot) TENDL [52] cross-section. Blue line - Difference between the two spectra with and without Vanadium results from MCNP6.2 simulations.

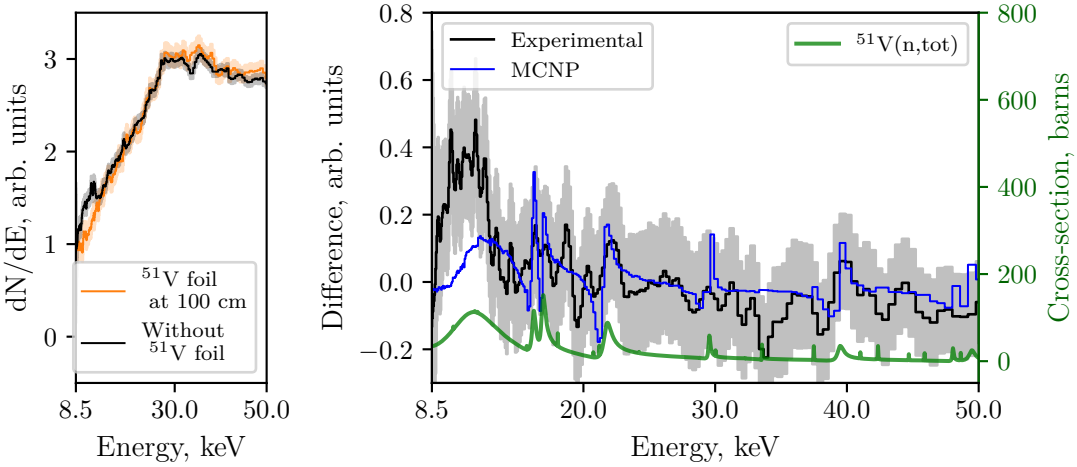

Figure 5.6. **Left:** Energy spectra measurements with Vanadium at 100 cm, placed on the detector, (orange line) and without Vanadium (black line), measured with a half inch ^{6}Li-glass detector at 100 cm. **Right:** Black line - Difference between the two spectra with and without Vanadium. Grey shadow - Error of the difference between the two spectra with and without Vanadium. Green line - ^{51}V(n,tot) TENDL [52] cross-section. Blue line - Difference between the two spectra with and without Vanadium results from MCNP6.2 simulations.

The purpose of these measurements is to check to quality of the simulations with MCNP6.2 for determining the RM in the case of the vanadium experiments. This step is important due to specific behavior observed in the neutron spectrum measurements involving the described thick vanadium target. In such cases, a significant number of neutrons are absorbed by the vanadium almost immediately after production. During the process of deconvoluting the TOF spectrum into energy spectrum using Response Matrices, we have to take this neutron absorption into account. As a result, it is essential to validate the ^{51}V(n,tot) cross-section data and ensure the accuracy of the corresponding MCNP6.2 simulations. In conclusion, the integrity of the data and simulations directly impacts the reliability of our results, especially since neutron interactions with vanadium play a key role in the experiment due to the target's thickness.

In Figure 5.4, there is a strong agreement between the experimental and simulated differences, particularly in the energy resonances, which are identified with high resolution. However, the most significant aspect of the figures is not only the agreement in numerical values but also the fact that the overall shape of the experimental and simulated differences closely mirrors one another. The experimental data, similar to the simulation, reveals five distinct and clearly defined peaks, which are consistent with the structure observed in the represented cross-section. This consistency in shape suggests that, despite any minor quantitative discrepancies, the simulation successfully reproduces the key features of the experimental results, especially the positions and relative heights of the energy resonances.

Figure 5.4 shows better results than Figs. 5.5 and 5.6. This is because the energy range in the first measurement starts at 1 keV, whereas in the other two cases it begins at 8.5 keV. As a result, an important region of interest is not captured when using a flight path of 100 cm with an accelerator frequency of 800 ns. In Figs. 5.5 and 5.6, the peak around 12 keV is still visible, but the shape of the subsequent peaks is harder to discern due to larger uncertainty differences.

The difference in the order of magnitude between the three figures is significant. The energy spectra display completely different orders of magnitude due to the measurement flight paths. In Figs. 5.5 and 5.6, the flight path was 100 cm, resulting in a lower order of magnitude for dN/dE compared to Fig. 5.5, where the flight path was 31 cm. This directly affects the order of magnitude of the difference between the spectra.

In conclusion, these three transmission measurements provide a check for the cross-section of TENDL that will be used in MCNP6.2 [122] in the following sections. Figure 5.7 displays the transmission results from all measurements together, allowing for a comprehensive comparison. The data is presented in terms of relative difference, expressed as a percentage, to highlight variations more clearly. The effects of energy resonances on the transmission are evident across all measurements, with particularly pronounced resonance behavior observed in the 31 cm flight path measurement.

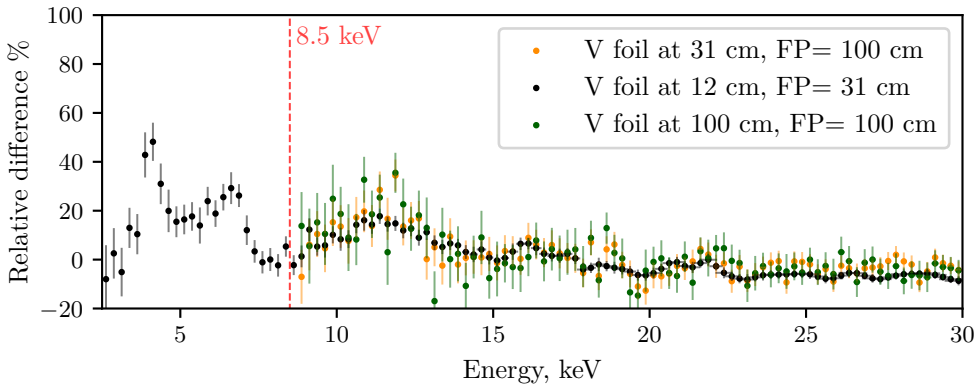

Figure 5.7. Relative difference between the three ^{51}V neutron transmission measurements. Energy binning of 0.25 keV for all measurements. The data below 8.5 keV were obtained in the measurement at FP = 31 cm. The associated uncertainties are shown by an error bar for each case.

5.2 Measurements of ^{51}V(p,n)^{51}Cr at 1585 keV

The primary objective of this measurement was to obtain a complete forward neutron spectrum of the ^{51}V(p,n)^{51}Cr at a proton energy close to the reaction threshold. Utilizing the kinetic equations provided in Chapter 2, it is established that 5 keV above the threshold, the reaction becomes fully open, resulting in emission in all directions. Therefore, to accurately acquire neutron spectra at 20 keV above the reaction threshold, measurements over a wide angular range were necessary. This extended approach required data collection at various angles, specifically covering the entire range from 0° to 90°, which is crucial for BNCT.

Specifically, the measured voltage was (790 ± 1) kV. According to the accelerator calibration (Eq. 3.7), this corresponds to (1584.9 ± 1.9) keV, which is just 20 keV above the reaction threshold. At this energy level, the reaction is fully initiated, leading to consistent rates across all angles. All the ^{51}V(p,n) TOF measurements were conducted using the same ^{6}Li-glass 1/2-inch detector (Figure 3.7b), positioned at $L = 31$ cm, with a period of 800 ns for the accelerator pulse. The TOF measurement was performed for all angles between 0 and 90 degrees in steps of 10°.

The relevant run parameters are presented in Table 5.2: degree, measured time, charge, mean intensity, and counts of the PLC and $CeBr_3$ detectors. The uncertainties associated with the presented parameters are primarily related to statistical fluctuations; the uncertainty related to the measured time is not provided because it is considered negligible.

Figure 5.8 shows the setup for all the TOF measurements. The setup closely resembled that of the previous chapter's lithium reaction, but here only a $CeBr_3$ gamma detector was used. The target, as described in the experimental setup

Degree	Time, min	Charge, μA/Hz	Intensity, μA	PLC events	$CeBr_3$ events
0°	625.21	51000	1.360(78)	$3.2{\cdot}10^5$	$2.8{\cdot}10^6$
10°	419.27	27551	1.095(66)	$1.6{\cdot}10^6$	$1.9{\cdot}10^5$
20°	419.70	23213	0.922(42)	$1.6{\cdot}10^6$	$2.1{\cdot}10^5$
30°	419.97	17312	0.69(10)	$1.5{\cdot}10^6$	$2.2{\cdot}10^5$
40°	420.04	8051	0.319(74)	$1.2{\cdot}10^6$	$2.3{\cdot}10^5$
50°	419.97	16220	0.64(46)	$1.7{\cdot}10^6$	$2.4{\cdot}10^5$
60°	419.71	25517	1.014(58)	$2.1{\cdot}10^6$	$2.5{\cdot}10^5$
70°	420.09	16220	0.67(13)	$1.5{\cdot}10^6$	$2.1{\cdot}10^5$
80°	419.80	12556	0.50(24)	$1.6{\cdot}10^6$	$3.2{\cdot}10^5$
90°	328.43	21468	1.090(74)	$1.8{\cdot}10^6$	$2.2{\cdot}10^5$

Table 5.2. TOF measurement parameters for ^{51}V(p,n)^{51}Cr (790 $\pm$ 1) kV, equivalent to E_p= (1584.9 $\pm$ 1.9) keV. The uncertainty for the PLC and $CeBr_3$ counts is not included in the table because it is equivalent to the square root of the number of events. The notation value(number) indicates the value followed by the uncertainty of the last digits in parentheses, with the uncertainty representing the statistical fluctuation of the intensity.

section, was clearly the target, and the detector used for the TOF measurement was the half-inch ^{6}Li-glass detector. As mentioned, the target was an aluminum cylinder with a 0.5 mm self-supported foil as a beam stopper.

To perform this measurement conveniently, we used a movable arm support for the ^{6}Li-glass detector. We programmed the arm to move every 7 hours. The intensity was decreasing slowly because most of the measurements were conducted over a weekend. It is notable from Table 5.2 that the first measurement (zero degrees) was longer than the others because it was important for us to obtain a good measurement of the spectrum at 0° to compare this one with the ^{7}Li(p,n) reaction. Finally, the last measurement lasted about 5.5 hours because the current was higher, and considering the charge, we deemed it sufficient. If we compare the measured time here with the ^{7}Li(p,n) measurements, it is much longer because the neutron reaction rate was smaller.

Figure 5.9 illustrates the evolution of the intensity over time observed during this measurement. The grey dashed lines indicate changes in the position angle of the ^{6}Li-glass detector used during the measurement. The intensity varied significantly because the measurement was conducted over a weekend, during which it declined without technical staff available to correct it. The abrupt rises correspond to manual adjustments made when technicians were present. Despite the variations, the beam remained operational throughout, ensuring the measurement's validity. These fluctuations were taken into account when calculating the average current and the current for each angle, which are presented with their associated values in the table. The intensity value at the 50-degree measurement

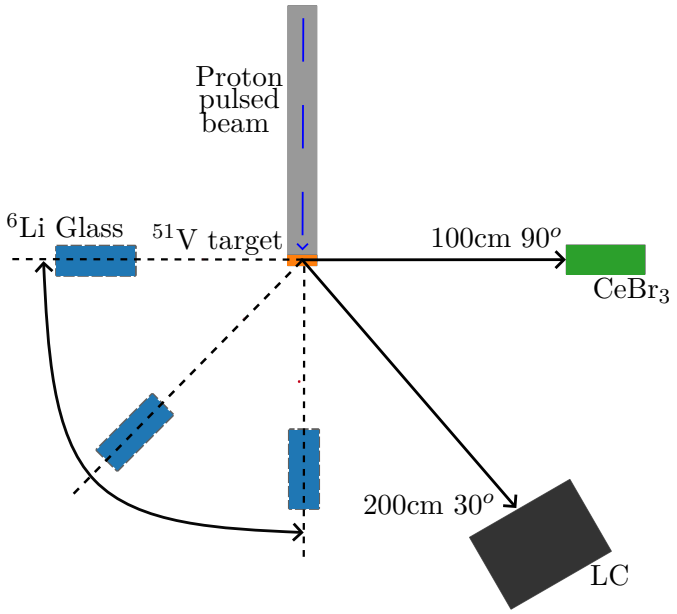

Figure 5.8. Diagram of the setup for TOF measurement for ^{51}V(p,n)^{51}Cr reaction. Quantities are in cm and degrees. The diagram is not to scale.

shows significant dispersion due to a very abrupt change occurring at that angle.

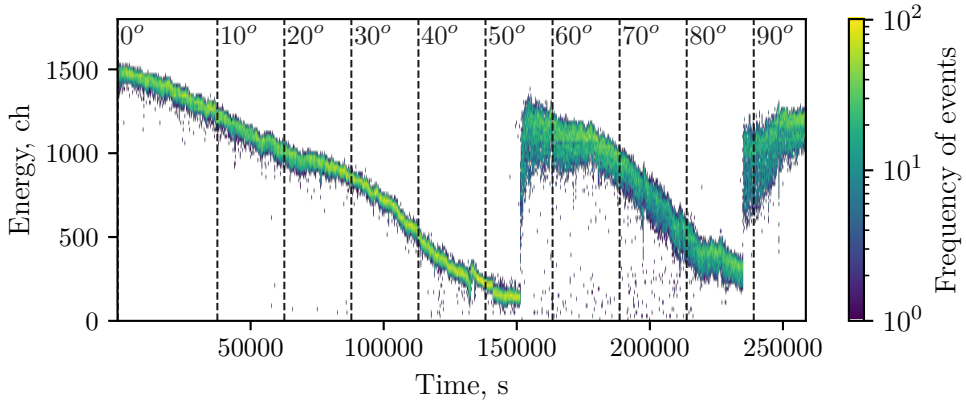

Figure 5.9. Intensity (ch 102) during the angle-dependent measurement of ^{51}V(p,n) at (1584.9 ± 1.9) keV. Dotted lines show the change of the angle of measurement.

The data analysis for the TOF vanadium measurements followed the detailed steps outlined in Section 4.3. These steps have been applied consistently across all measurements presented in Table 5.2. Figure 5.10 displays all the TOFs for the measured angles at just 20 keV above the V(p,n) reaction threshold. As mentioned, and in contrast to the measures presented in Chapter 4, all the TOFs have been taken with the same detector (^{6}Li-glass 1/2 inch) at the same L = 31 cm, and a period of 800 ns.

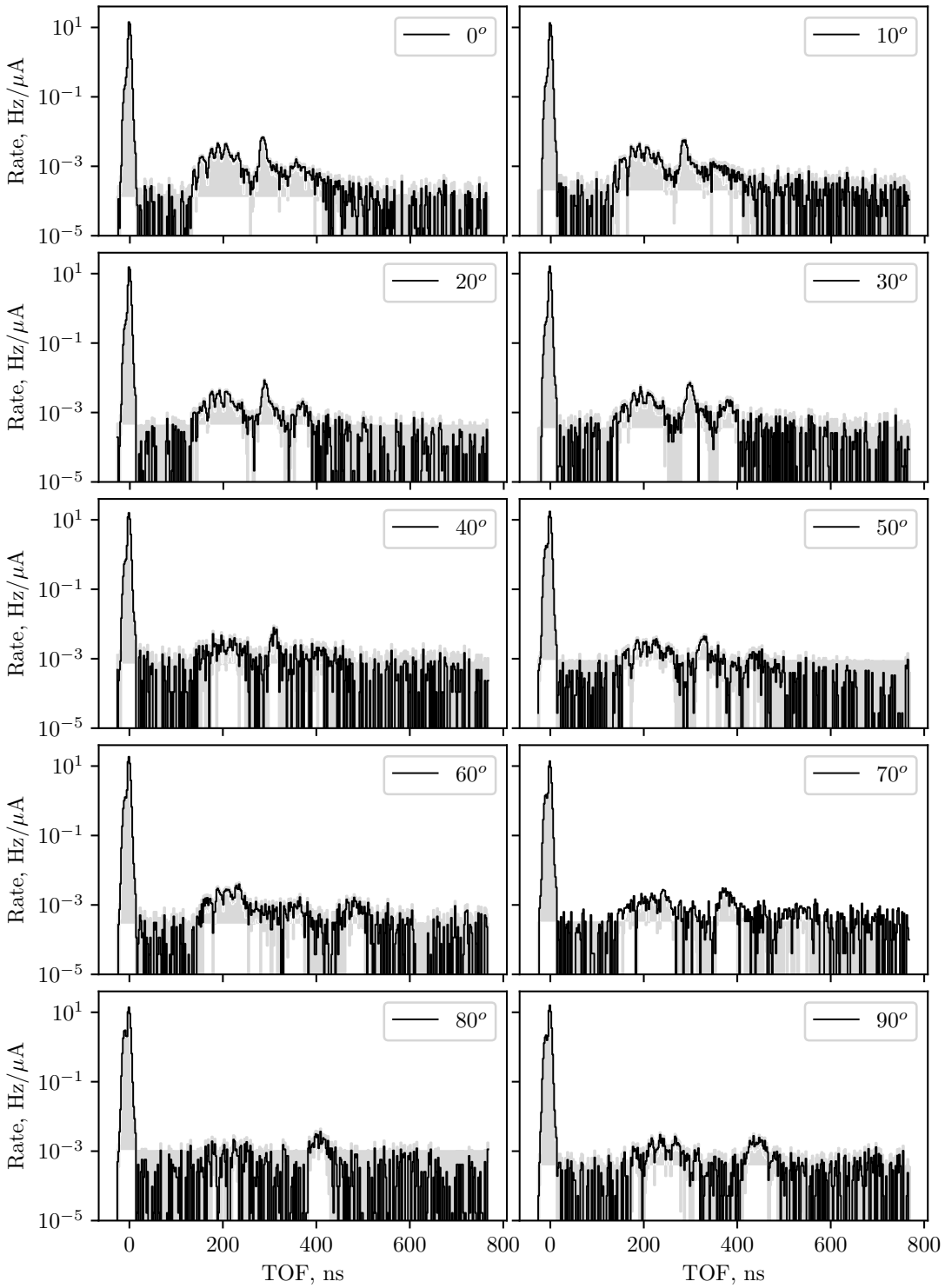

Figure 5.10. Time-of-flight measurements for the ^{51}V(p,n) at (1584.9 ± 1.9) keV, just 20 keV above the threshold for different angles. The associated uncertainties are shown by a grey shadow.

Some resonances are present in these TOF spectra, as can be seen in Fig. 5.10. It is evident that the energy spectrum for the vanadium reaction will differ significantly from that of lithium. A closer examination of the TOF spectra reveals distinct resonances at all angles, which expand progressively as the angle increases. Additionally, it can be observed that the arrival time of these resonances at the detector increases with larger angles. This behavior is consistent with the expected dynamics of neutron production near threshold energies, providing valuable insight into the angular dependence of the ^{51}V(p,n) reaction. These resonances have been observed by other authors at various proton energies, as we stated in Chapter 2.

5.2.1 Background Characterization

In the previous chapter, we demonstrated a flat background by showing the area between the γ-flash and the neutron pulse. For the presented TOF measurements of the V(p,n) reaction, the beginning of the neutron pulse is not well defined. For this reason, a background measurement was conducted using the vanadium target.

To investigate the background, a measurement of the V(p,n) reaction below the threshold was conducted. The accelerator voltage was set at (770 $\pm$ 1) kV, which corresponds to (1546.4 $\pm$ 1.9) keV, as detailed in Section 3.4. The accelerator pulse duration was 800 ns, with an average current of (0.62 $\pm$ 0.18) μA. The measurement lasted for 15.08 hours, and the charge recorded was 33705 μA/Hz. Utilizing the reference channel of the accelerator pulse, Figure 5.11 (**right**) presents the raw data from a ^{6}Li-glass detector positioned 31 cm from the target at an angle of 0 degrees.

The background was found to be consistent and flat over time, as we considered in our previous data analysis. This allows us to subtract it from the TOF spectra measured at each angle. By cleaning the signal due to the gammas in the neutron range, we can obtain Figure 5.11 (**left**), following the same Qlong filter presented above. This again shows that the background is completely flat. A few neutron signals are present, but they are due to neutron scattering from the floor or the walls and do not contribute to the shape of the TOF. This measurement validates all the Qlong filters that have been applied in this thesis.

5.2.2 Study of the γ-flash: Time and Energy Resolution

Similarly to the analysis performed on the gamma-flash for the ^{7}Li(p,n) TOFs in Section 4.3.1, we present here two fits corresponding to the γ-flashes found in the Vanadium TOFs. Considering all the measurements presented in Fig. 5.10, the Gaussian fit of the gamma-flash yields a standard deviation (σ) of (2.24 $\pm$ 0.08) ns and a FWHM of (5.26 $\pm$ 0.19) ns. These values are largely determined by the time resolution of the DAQ, which is 2 ns, and the width of the proton signal, as shown in Fig. 3.12.

For illustrative purposes, Figure 5.12 shows the fits of the γ-flash histograms. Specifically, in Figure 5.12 (**left**), the γ-flash for the 0-degree measurement is

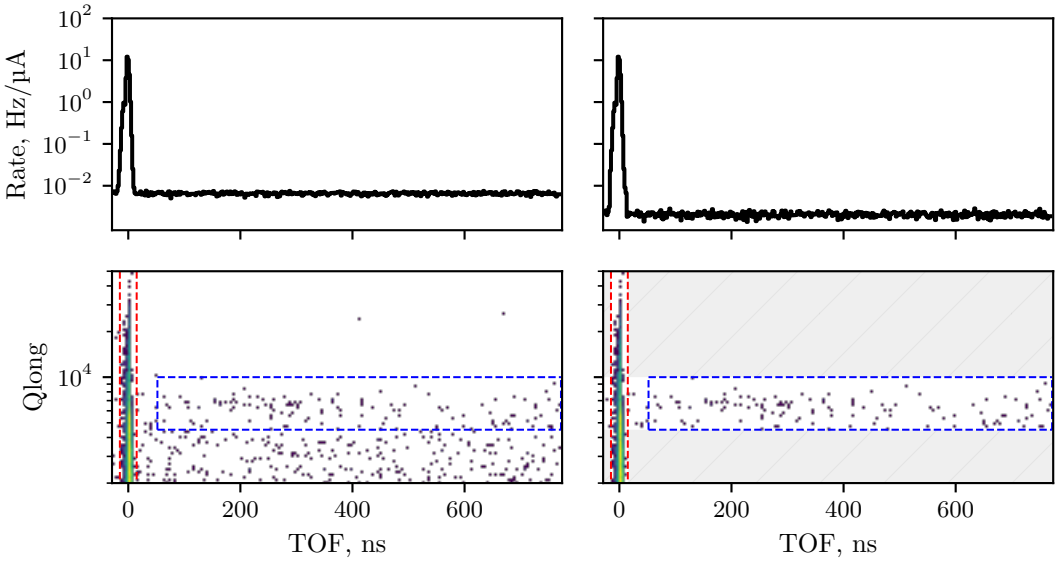

Figure 5.11. TOF background measurement for the ^{51}V(p,n) reaction. TOF spectrum, raw (**right**) and filtered (**left**) data for the ^{51}V(p,n) reaction at E_p=(1546.4 ± 1.9) keV, measured with a half-inch ^{6}Li-glass detector at 31 cm and 0 degrees. The associated uncertainties are shown by a grey shadow.

presented, and in Figure 5.12 (**right**), the γ-flash for the 90-degree measurement is shown. The difference is evident; for the 90° γ-flash, we observe a perturbation next to the gamma-flash. This effect is caused by the position of the detector at an angle, leading to a reflection or bounce. Such perturbations become more pronounced as the detection angle increases.

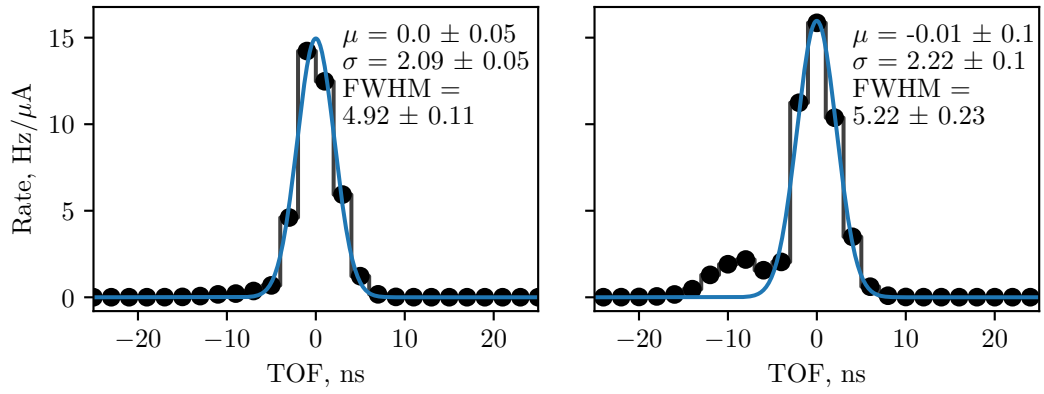

Figure 5.12. ^{51}V(p,n)^{51}Cr gamma-flashes at (1584.9 ± 1.9) keV TOF measurement at 0 degrees (**left**) and 90 degrees (**right**), with a ^{6}Li-glass of 1/2 inch at L= 31 cm.. The mean (μ), sigma (σ) and FWHM of the Gaussian fits are indicated in the figures, all these quantities are in ns.

5.2.3 Time-to-Energy Conversion

In Chapter 4, we detailed the entire procedure to transform TOF to energy for our TOF experiments. We presented three different methods, ultimately selecting the third method as the most suitable. Consequently, to transform the TOFs presented in Figure 5.10, we will use the same method, known as the energy distribution method. To apply this method, it is essential to compute a Response Matrix (RM) for this specific setup. In particular, an RM must be calculated for each measurement angle. We need to consider the variation in the thickness of the vanadium target through which the proton beam passes, as it changes with each positional angle.

To exemplify these Response Matrices, the RM for the measurement at 0 degrees is shown in Fig. 5.13 (**left**). Since the RMs for each angle present only small variations, by looking at the RM presented we can comment in general on the resonances that will appear in all of them. The previously measured resonances from the ^{51}V(n,tot) reactions are clearly visible. In Fig. 5.13 (**right**), the efficiency of this setup is shown, calculated by adding all the columns of the RM. Once again, it is easy to see the ^{51}V(n,tot) resonances. Using the third method described earlier to transform time to energy, we will correct all these resonances. Another option to improve this correction would be to use a thinner vanadium target for more precise measurements. However, this was not feasible in the present experiment due to the availability of only a 0.5 mm thick target, but this could be considered for future measurements.

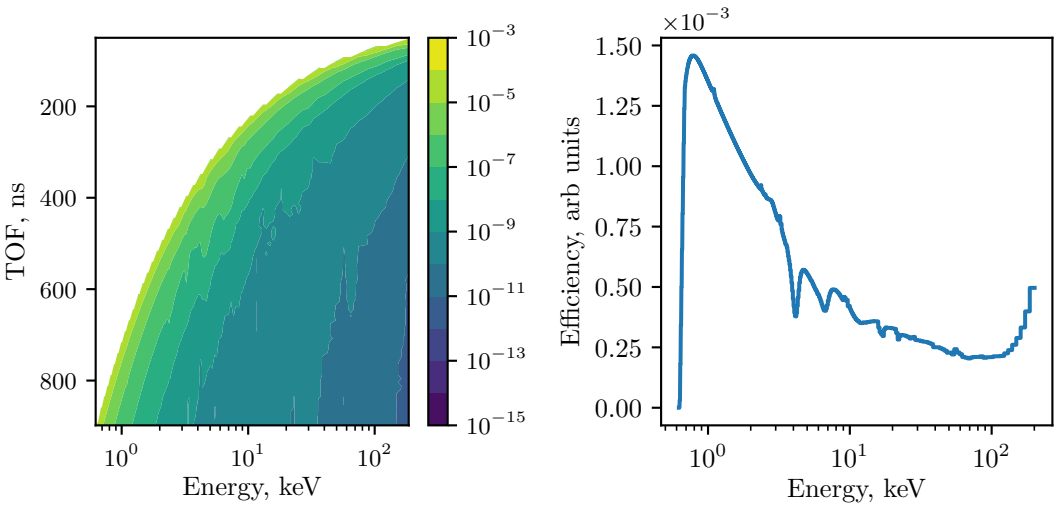

Figure 5.13. Response Matrix (**left**) and efficiency (**right**) of the ^{51}V(p,n)^{51}Cr measurement at 0 degrees. For the Vanadium target, a flight path of 31 cm and a ^{6}Li-glass detector of 1/2 inch are used at 0 degrees.

The energy uncertainty in the TOF measurements is a function of the flight path uncertainty and the time resolution. Furthermore, the binning used was the

"natural" energy binning. This energy binning, utilized in Figs. 5.13, has been calculated using equation 3.4, considering that the time uncertainty is 2 ns and the flight path uncertainty is 0.1 cm. The RMs for all angles will employ the same energy binning. As mentioned above, this "natural" binning represents the real-energy binning of the experiment.

5.3 Results and Discussion

The V(p,n) TOF spectra, shown in Figure 5.10, have been converted into energy spectra, following the validated method explained in Section 4.3.2. The obtained spectra for the different angles are displayed in Figure 5.14. A significant energy resonance is indicated, which, as the angle increases, shifts towards lower energy spectra. The energy binning used is the aforementioned "natural" binning.

Specifically, for the measurement taken at 0 degrees, we convert the TOF data presented in Fig. 5.10 upper left into the energy spectrum using the Response Matrix illustrated in Fig. 5.13 (**left**). As explained, to construct this Response Matrix, the 0.5 mm thickness of the vanadium target has been taken into account, addressing the resonances caused by neutron absorption within the vanadium itself. Through our validation using transmission measurements, we confirmed that the resonances of the V(n,tot) reactions are accurately represented within the simulation code MCNP6.2 [122], which was used to generate the Response Matrix for each specific setup.

Moreover, we have developed distinct Response Matrices for each measurement angle. For each angle, the specific thickness of vanadium traversed by the neutrons is considered. This approach ensures that the energy spectra derived from the TOF data accurately reflect the influence of neutron interactions with the vanadium target at various angles.

In Fig. 5.14, it is evident that the spectrum displays energetic resonances, marked with blue lines for each angle. These resonances shift their position as the angle changes, consistent with the reaction kinetics. Therefore, the observed resonances are intrinsic to the primary ^{51}V(p,n) reaction, not from secondary reactions.

Table 5.3 details the energy values of the resonances observed at various angles, from 0° to 90°. It complements Figure 5.14. Each row represents a specific observation angle, while each column shows the energy values for different resonances measured in keV. Such as, we label the energy associated with the dashed line in Fig. 5.14 as E_a. For lower angles, such as 0° and 10°, higher resonance energies are observed, while at larger angles (up to 90°), the resonance energies generally decrease.

The main resonances, marked with dark blue lines and the letter b, are in agreement with the (6.44 ± 0.195) keV resonance peak at 0 degrees measured by Schölermann and Böttger [88] and confirmed by Lamirand [64]. Specifically, in Ref. [88], a thick target was irradiated with protons at an energy approximately

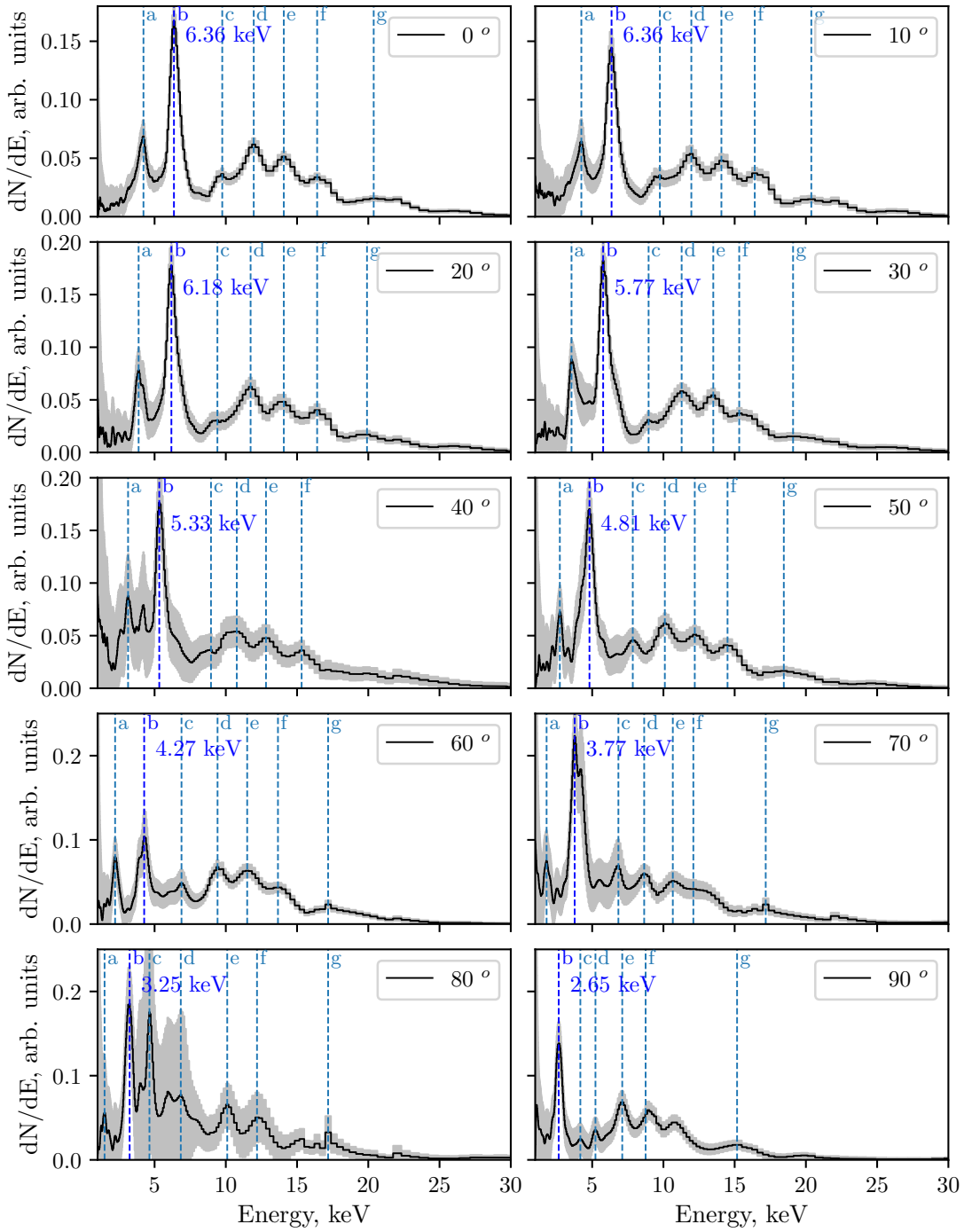

Figure 5.14. Energy spectrum for the ^{51}V(p,n)^{51}Cr reaction at (1584.9 ± 1.9) keV for 10 different angles. The shadowed grey indicates the statistical error. All the resonances are marked with dashed blue lines and an identification letter (a-g), detailed in Table 5.3. The main resonance for each angle (b) is marked with dark blue dashed lines, and the energy value in keV is annotated for each graph.

	E_a, keV	E_b, keV	E_c, keV	E_d, keV	E_e, keV	E_f, keV	E_g, keV
0°	4.221(25)	6.362(47)	9.749(87)	11.95(12)	14.06(15)	16.40(19)	20.38(26)
10°	4.220(43)	6.362(47)	9.749(87)	11.95(12)	14.06(15)	16.40(19)	20.38(26)
20°	3.398(40)	6.185(48)	9.415(86)	11.72(13)	14.06(15)	16.40(19)	19.87(29)
30°	3.534(34)	5.772(42)	8.943(92)	11.28(11)	13.49(15)	15.33(18)	18.90(42)
40°	3.155(31)	5.330(35)	8.943(92)	10.86(20)	12.94(26)	15.33(18)	18.90(42)
50°	2.729(13)	4.815(35)	7.848(63)	10.102(93)	12.19(13)	14.36(29)	-
60°	2.226(12)	4.270(25)	6.840(50)	9.415(86)	11.50(11)	13.77(26)	18.45(23)
70°	1.795(12)	3.771(21)	6.840(50)	8.649(72)	10.66(11)	12.19(21)	17.18(20)
80°	1.4882(69)	3.253(19)	4.641(29)	6.840(50)	10.102(93)	12.19(13)	17.18(20)
90°	-	2.655(17)	4.172(26)	5.261(65)	7.15(10)	8.80(12)	15.33(33)

Table 5.3. Energetic resonances identified from the ^{51}V(p,n) reaction measured at various angles, as shown in Fig. 5.14. The notation value(number) indicates the value followed by the uncertainty of the last digits in parentheses.

50 keV higher than the reaction threshold. In addition to this measurement, Kneff, Lefevre, and Din [87] also measured this peak and obtained a value of (6.49 ± 0.04) keV, which is very close to our result. In Refs. [88] and [87], several additional peaks are shown but are not identified by the authors. These peaks correspond to those identified in our experiment, as shown in Table 5.3.

By comparing these results with the energy spectrum obtained from the ^{7}Li(p,n) reaction measurements, we can determine a relative ratio of production between the two sets of data. Notably, the zero-degree measurement, depicted in Figure 5.14 at the upper left, was conducted under identical conditions as the one taken at 0° using a half-inch ^{6}Li-glass detector positioned at 31 cm, as presented in Fig. 4.17. This allows for a direct comparison between the two spectra. Both measurements followed identical procedures, from the initial TOF data to the final energy spectrum. The calculated ratio of production between the two reactions is 1944.8 at zero degrees, indicating a significant comparative difference in reaction yields under these specific experimental conditions. Using the value for the ^{7}Li(p,n) reaction at 31 cm of $1.36 \cdot 10^5$ neutrons/s μA, we can utilize it for normalization.

To obtain the integrated spectra by summing the contributions of each angle-dependent spectrum, each spectrum must be scaled according to its corresponding solid angle. Various scaling factors are discussed in the literature [56], [140], [141]. Following these guidelines, we use the following scaling factor, f_α, for each angle α:

$$f_\alpha = \begin{cases} 2\pi L^2 \left(1 - cos(\theta)\right) & \text{if } \alpha = 0. \\ 2\pi L^2 \left(cos(\alpha - \theta) - cos(\alpha + \theta)\right), & \text{if } 0 > \alpha > 90. \\ 2\pi L^2 \left(cos(90 - \theta)\right), & \text{if } \alpha = 90. \end{cases} \tag{5.1}$$

Here, r is the detector radius, α represents the detector's angular position, and θ is the angle covered by the detector, calculated by:

$$\theta = arctan\left(\frac{r}{L}\right), \tag{5.2}$$

where L is the flight path from the source to the detector. This set of equations is derived purely from the setup geometry and the solid-angle definition. The solid angle of a cone, with its vertex at the apex of the cone and an angle of apex of 2β, is defined as the area of a spherical cap on a unit sphere. The solid angle, Ω, is given by: $\Omega = 2\pi(1 - cos(\beta))$. Therefore, following this definition, we have obtained the Eq. 5.1.

Additionally, for our integration, we set the maximum emission angle to 90 degrees, as we are only interested in the forward-integrated spectrum. This choice ensures that we capture the relevant contributions from angles up to 90°, yielding an accurate integrated spectrum within the forward detection range.

In the current setup, with 5.08 cm diameter detectors and a 31 cm flight path, the entire forward hemisphere is largely excluded. Nevertheless, previous studies by other researchers have investigated potential variations in the angle-integrated spectrum for the ^{7}Li(p,n) reaction at a proton energy of 1912 keV [56], [132].

Figure 5.15 shows the spectra for each angle, scaled by the corresponding solid angle coefficient. This figure is similar to Fig. 5.14, with the resonances again highlighted by dashed lines. The energy values associated with the resonances have not changed from one figure to the other. The main difference between the two figures is the range of the dN/dE spectra. Essentially, scaling the spectra by their solid angle factors helps to normalize the data, offering a more complete picture of the reaction across all angles and allowing for a direct comparison of the resonance features that might otherwise be influenced by geometric factors.

In Figure 5.16, the integrated spectrum for the ^{51}V(p,n)^{51}Cr reaction is shown. This spectrum is derived by adding all the angle-energy dependence spectra from the Fig. 5.15 and then normalizing the data using the ^{7}Li(p,n) measurement at 1915.2 keV with the same experimental setup. The figure shows two different binnings. The black line represents the spectrum obtained using the "natural" binning, extracted from the 2 ns steps in time, while the blue dots correspond to rebinning, with steps of 0.5 keV. The grey-shaded region around the blue line denotes the statistical error, which appears quite large. This is due to the fact that it represents the sum of the statistical errors from the measurements at all the different angles.

As Fig. 5.14 illustrates, certain angles display poor statistics, which lead to the larger statistical uncertainty in the integrated spectrum. Despite the significant error bars, this integrated result remains valid, as it offers an overall perspective of the reaction yield. The considerable statistical error is anticipated when aggregating results from different measurements, some of which may not possess optimal statistical significance. Nonetheless, this comprehensive spectrum provides a robust representation of the ^{51}V(p,n)^{51}Cr reaction.

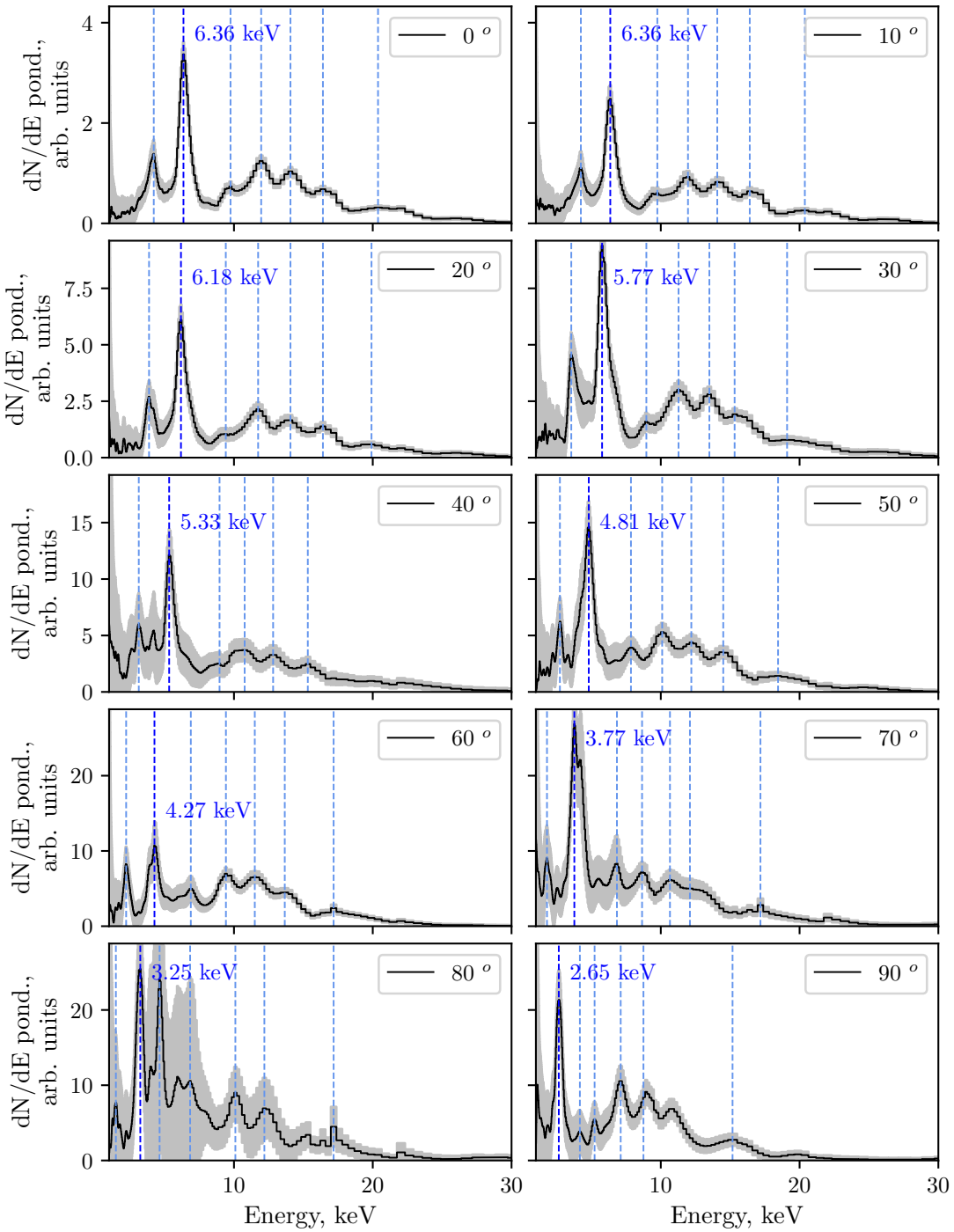

Figure 5.15. Energy spectrum pondered by solid angle for the ^{51}V(p,n)^{51}Cr at (1584.9 ± 1.9) keV for 10 different angles. The shadow grey indicates the statistical error. All the resonances are marked in dashed blue lines, and the main resonance for each angle is marked in dark blue dashed lines, and the energy value is annotated in for each graph.

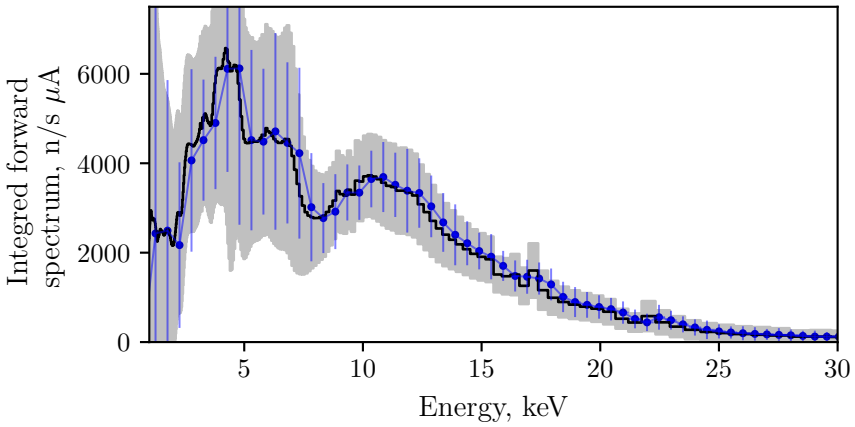

Figure 5.16. Integrated energy spectrum for ^{51}V(p,n) at (1584.9 ± 1.9) keV. The shadow grey indicates the statistical error. It is worth mentioning that the major source of uncertainty is the measurement at 80°.

The energy spectrum shown in Figure 5.16 also displays a distinct shape, primarily due to the presence of the main resonance, which is observed across all measured angles, as shown in Figure 5.14. The integrated result indicates that the total forward neutron yield for the ^{51}V(p,n) reaction at (1584.9 ± 1.9) keV is 64477 n/sμA.

5.3.1 Comparison between Our Experimental Data and Theoretical Data

Following the work of Lee and Zhou [133], the NEBOAS project, funded by the MONNET program under the European Commission's Joint Research Center, provides double differential neutron yields, denoted as $\frac{d^2Y}{dE_n d\Omega}(\theta, E_n)$. This data characterizes the energy and angular distribution of neutrons emitted from proton-induced reactions across various projectile energies on both thin and thick targets. As discussed in Chapter 4, the comparisons between NEBOAS outputs and experimental data for multiple reactions and proton energies have shown excellent agreement.

Figure 5.17 displays the angle-dependent spectra for the ^{51}V(p,n)^{51}Cr reaction at 1585 keV, derived using the NEBOAS code, where we have considered the EXFOR and TENDL cross-section data shown in Fig. 2.3 and the stopping power from the SRIM [120] code. The **left** panel presents the angle-energy matrix obtained using EXFOR cross-section data, while the center panel illustrates the results using TENDL cross-section data. Both datasets cover an energy range of up to 25 keV, yet they exhibit significant differences in shape and neutron flux. The right panel shows clear differences between the integrated forward spectra obtained from the two data sets, emphasizing the need for validation.

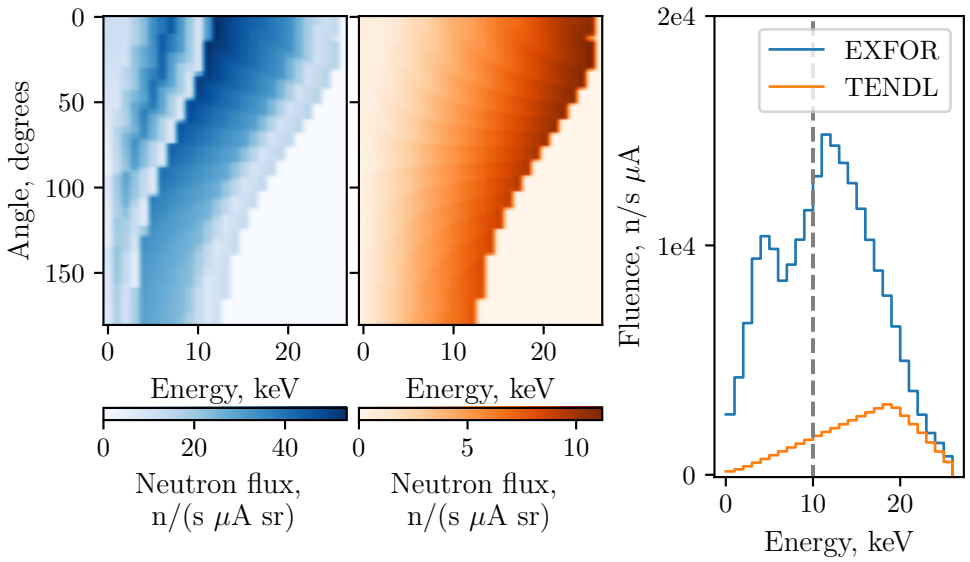

Figure 5.17. NEBOAS results for angle-dependence spectra for ^{51}V(p,n) at 1585 keV. **Left:** Angle-dependence matrix obtained with EXFOR cross-section data. **Center:** Angle-dependence matrix obtained with TENDL cross-section data. **Right:** Integrated forward spectra for ^{51}V(p,n) at 1585 keV using EXFOR or TENDL cross-section data.

To enable a direct comparison between the simulated results generated by the NEBOAS code and our experimental data, we first normalized all the data. Subsequently, we analyzed, in detail, first the shapes of the angle-dependent spectra and then the integrated spectra.

We began with a detailed comparison between the angle-dependent spectra presented in Figure 5.14 and the corresponding spectra produced by the NEBOAS simulations, as depicted in the matrices shown in Figure 5.17. This comparative analysis, displayed in Figure 5.18, provides us with valuable insights into how well the NEBOAS theoretical predictions, which are based on different cross-section datasets (EXFOR and TENDL), replicate the angular distributions of emitted neutrons observed in our experiments.

As expected, the agreement between our experimental results and the NEBOAS predictions is notably stronger when using the EXFOR-based data (represented by the blue lines) compared to the results based on the TENDL cross-sections (represented by the orange lines). This better consistency in shape is observed across all angles. The EXFOR dataset, rooted in experimentally measured cross-sections from various sources, demonstrates its reliability by more closely matching the intricate details of neutron emission behavior. On the other hand, the TENDL-based simulations present a different shape in the angle-dependent spectra.

Turning to the integrated spectra, Figure 5.19 presents a comparison between our experimentally integrated data and the corresponding NEBOAS results. Here,

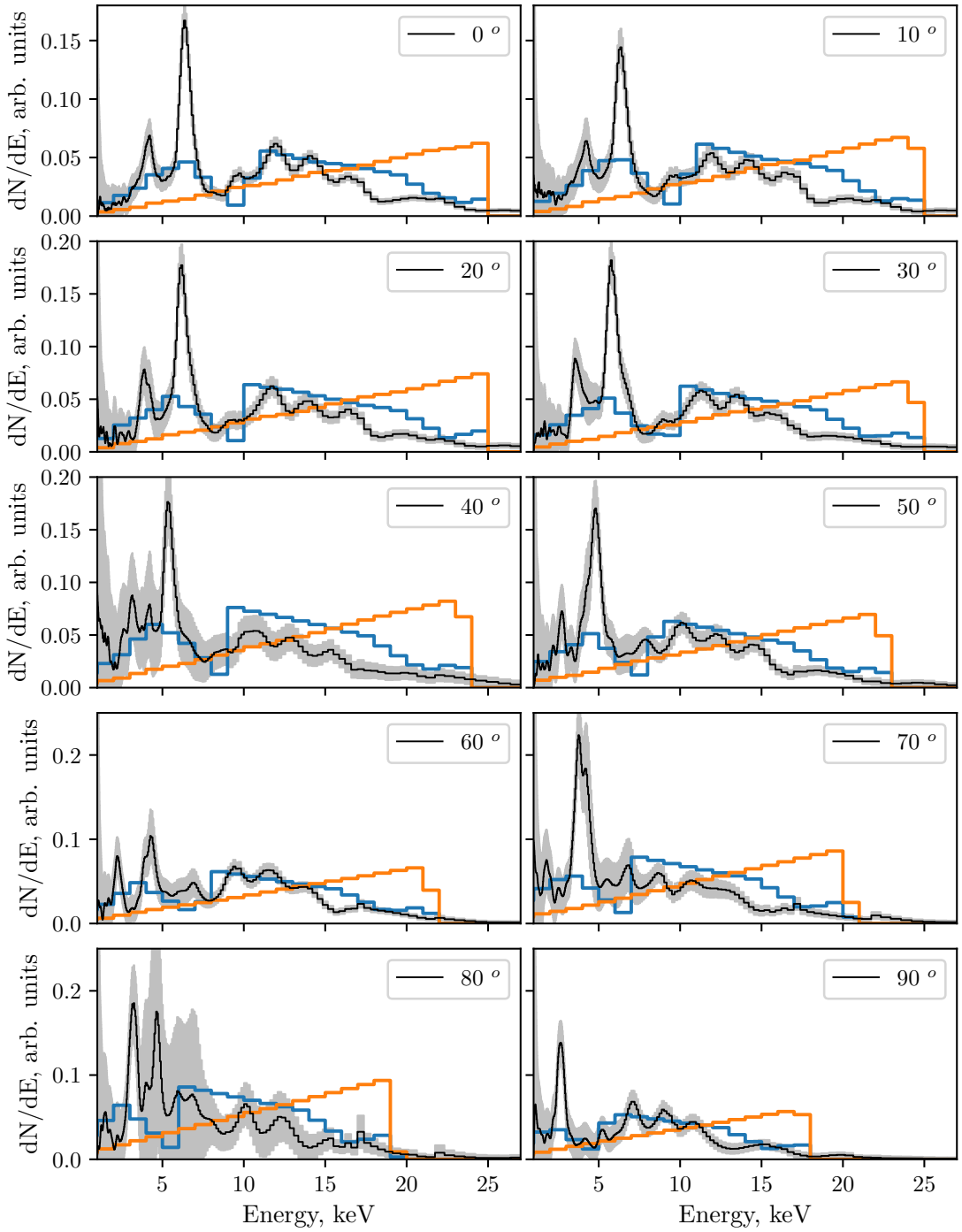

Figure 5.18. Energy spectrum for the ^{51}V(p,n)^{51}Cr reaction at (1584.9 ± 1.9) keV for 10 different angles. The shadow grey indicate the statistical error. Compared with the NEBOAS results, using EXFOR (blue) and TENDL (orange) cross-sections.

it is particularly notable that the main resonance observed in our integrated forward spectra is absent from the NEBOAS simulations. While some similarities exist with the EXFOR-based data, the resonance appears either poorly quantified or slightly shifted in energy. Despite this, the energy ranges in all datasets are closely aligned, indicating that the general energy distribution is consistent across the datasets. However, the details of the resonance structure require further investigation.

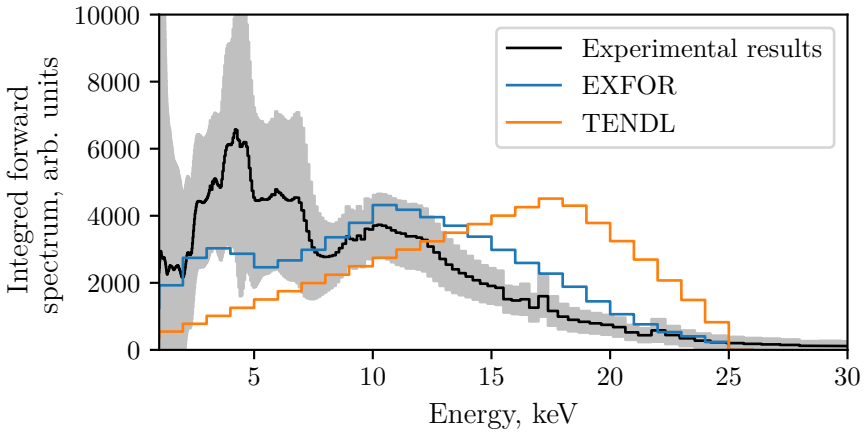

Figure 5.19. Integrated energy spectrum for ^{51}V(p,n) at (1584.9 ± 1.9) keV compared with the two obtained results with NEBOAS, using the EXFOR (blue) or TENDL (orange) cross-section data. The shadow grey indicate the statistical error.

This comparative analysis highlights the complexities of accurately modeling the ^{51}V(p,n)^{51}Cr reaction and underscores the importance of precise experimental data in refining theoretical frameworks like those developed by the NEBOAS project. This is why the measurement detailed in this chapter and published in Ref. [139] is highly significant.

Chapter 6

Novel Boron Neutron Capture Therapy Technique: Beam Shaping Assembly-Free Approach

In BNCT, the design of neutron beams suitable for therapeutic purposes is one of the key technical challenges in research. As discussed in Chapter 1, accelerator-based neutron sources are gaining significant traction. Due to the indispensable role of epithermal neutrons in the effective treatment of patients, sources based on the ^{7}Li(p,n)^{7}Be and ^{9}Be(p,n)^{9}B reactions are conventionally the most widely used. In Chapter 2, we introduced these two proton-induced neutron production reactions, as well as two novel alternatives for directly generating epithermal neutrons, ^{51}V(p,n)^{51}Cr and ^{45}Sc(p,n)^{45}Ti. For a complete comparison, in Chapter 4, we measured the conventional ^{7}Li(p,n)^{7}Be reaction as a reference. Subsequently, in Chapter 5, we conducted detailed angle-dependent measurements of the ^{51}V(p,n)^{51}Cr reaction near its threshold.

In this chapter, we will present a new BNCT technique that takes advantage of these studied novel reactions, ^{51}V(p,n)^{51}Cr and ^{45}Sc(p,n)^{45}Ti, with the potential to enhance neutron generation. This approach introduces a Beam Shaping Assembly-Free (BSA-free) neutron source, eliminating the need for a Beam Shaping Assembly, potentially simplifying the neutron delivery system. The feasibility of this concept will be validated through simulations of MCNP6.2 [122], using data from the literature for the scandium reaction and experimental data for the vanadium reaction.

Most of the findings presented in this chapter have been previously published in Ref. [142], where the results of using a BSA-free configuration with scandium are thoroughly analyzed and validated. In addition, the BSA-free approach is currently under evaluation as patent (Internal reference: IPR-1070).

6.1 Novel BNCT Technique

The ^{51}V(p,n)^{51}Cr and ^{45}Sc(p,n)^{45}Ti near threshold reactions, which generate neutrons directly in the therapeutic energy range of BNCT, have always been discarded as neutron sources due to their much lower neutron yield compared to ^{7}Li(p,n)^{7}Be or ^{9}Be(p,n)^{9}B. The reason behind this has been the necessity of neutron moderation, thus the need for a BSA, either for nuclear reactors or AB-BNCT facilities. Since moderation means the absorption of neutrons, vanadium or scandium cannot achieve the minimum flux for patients. However, if a BSA were not needed, vanadium and scandium could be options worth studying. Moreover, the new and recent recommendations from the IAEA for therapeutic neutron beams inspired the original idea of this thesis. In particular, the recommended neutron flux has been decreased by half. It is worth mentioning that these new recommendations are based on the results of clinical treatments.

The present work proposes a novel concept of an ABNS for BNCT that eliminates the need for a BSA, referred to as the BSA-free approach. This innovation has the potential to reduce operational costs while improving the effectiveness of the therapy by enhancing neutron penetration within the human body and facilitating more complex irradiation field configurations.

To illustrate this novel BNCT technique, the BSA-free proposal, Figure 6.1 presents a schematic comparison between the proposed concept and conventional schematics. On the left side, Fig. 6.1a depicts a sketch of the main components of the facilities. On the right side, Fig. 6.1b shows a block diagram illustrating the changes in neutron fluxes during the process. This visual representation simplifies the new approach, demonstrating that neutron delivery to the patient remains largely similar to existing methods. The primary goal of this proposal is to provide additional alternatives in the design of neutron sources for BNCT while recognizing the benefits of the current options.

The upper section of Figure 6.1 (**A**) shows the use of nuclear reactors as neutron sources for BNCT. This schematic illustrates a nuclear reactor that generates a neutron beam, which is subsequently shaped by the BSA system. This configuration ultimately achieves a neutron flux of the appropriate order and energy range for patient BNCT treatment. A classical BSA is composed of four different parts in these facilities: the shielding (**2A**), the moderator material (**2B**), the collimator (**2C**), and finally the beam aperture (**2D**).

In the center of Fig. 6.1 (**B**), the components of proton ABNS for Neutron Capture Therapy (NCT) are illustrated. This schematic corresponds to the majority of the facilities mentioned in Table 1.1, specifically those with Be or Li targets and a proton beam. This sketch features an accelerator that emits proton beams with energies on the order of MeV. Following the accelerator is a target composed of Beryllium-9 or Lithium-7. The two commonly used reactions, ^{7}Li(p,n)^{7}Be and ^{9}Be(p,n)^{9}B, both provide a neutron flux on the order of 10^{11} n/s·cm^2, generating a contribution of fast neutrons. Consequently, these neutrons must pass through a

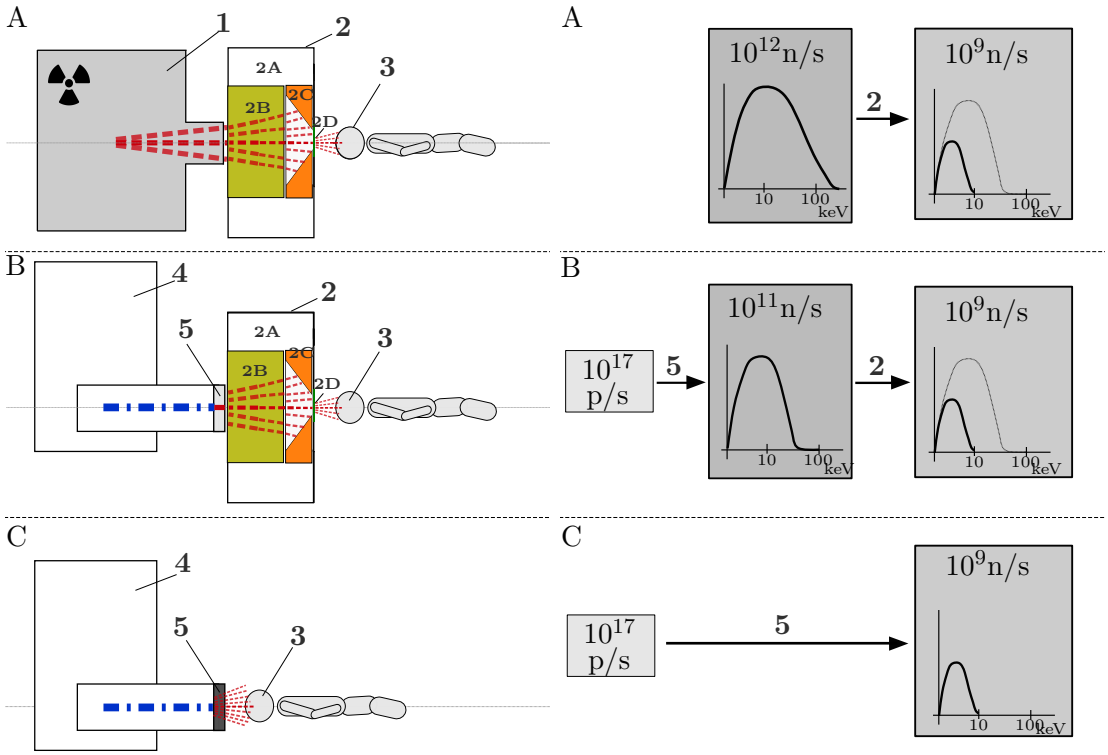

(a) Diagram of the different BNCT neutron sources.

(b) Block diagram showing the changes in fluxes.

Figure 6.1. Comparison diagram between the BSA-free approach and conventional BNCT facilities. (**A** and **B**) represent traditional BNCT setups, including nuclear reactors or proton accelerators with Beam Shaping Assemblies (BSA), while (**C**) illustrates the BSA-free concept. Grey areas indicate neutron production regions, red lines represent neutron paths, and blue lines indicate charged particle (proton) trajectories. The key components are: (**1**) nuclear reactor, (**2**) Beam Shaping Assembly (comprising: **2A** - shielding/reflector, **2B** - moderator, **2C** - collimator, **2D** - beam aperture), (**3**) patient, (**4**) proton accelerator, and (**5**) neutron-producing targets: (5-B) Li or Be target for conventional BNCT, and (5-**C**) Sc or V target for the BSA-free approach.

BSA to achieve a predominantly epithermal neutron spectrum. The BSA consists of the same components as those in reactor installations. During the moderation process, the energy of the neutrons is altered, and their flux is reduced to approximately $5 \cdot 10^8$ n/s·cm^2. Finally, the patient is depicted.

In the lower section of Fig. 6.1 (**C**), a schematic representation of the device proposed in this thesis is presented. Again, there is a proton accelerator with the same characteristics as that in the upper schematic (**B**) to produce a proton beam in the MeV range. The primary difference between the two schematics (**B** and **C**) lies in the target, which, in this case (**C**), is made of vanadium-51 or scandium-

45, leading to the reactions ^{45}Sc(p,n)^{45}Ti and ^{51}V(p,n)^{51}Cr. Both reactions, when using energies near their threshold, generate neutron spectra on the order of keV and can produce a flux of $5 \cdot 10^8$ neutrons/(cm^2·s) with sufficient intensity. This means that the neutrons produced in these targets can be directly used for patient irradiation, eliminating the need for moderation or BSA. As illustrated in Figure 6.1b, the final fluxes have the same intensity and energy range, but the processes to achieve them are completely different.

Figure 6.2 shows the TENDL cross-sections of the two reactions currently used to generate neutrons for BNCT via proton acceleration, ^{7}Li(p,n)^{7}Be and ^{9}Be(p,n)^{9}B, alongside the cross-sections of the newly proposed reactions, ^{45}Sc(p,n)^{45}Ti and ^{51}V(p,n)^{51}Cr. This figure is useful in providing an additional comparison between the conventional and the proposed reactions for ABNS in BNCT. When examining energies near the thresholds, it is evident that the reactions involving scandium and vanadium exhibit significantly lower cross-sections than those associated with beryllium and lithium. This disparity results in the neutron flux produced by V and Sc targets being 100 times lower, as discussed in Chapter 2.

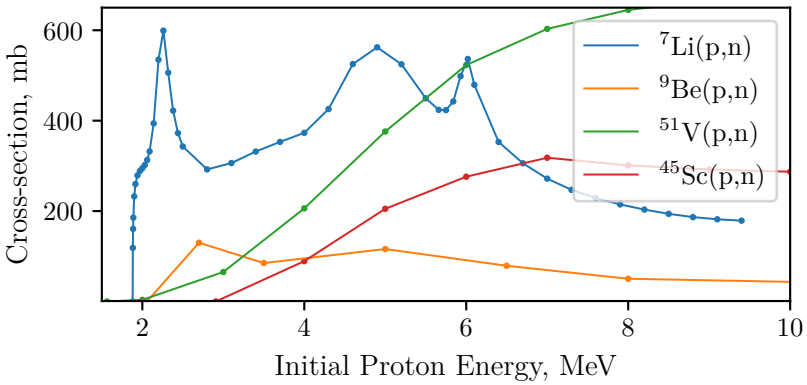

Figure 6.2. Comparison of cross-sections for neutron generation reactions as reported in TENDL 2021 [52]. The reactions analyzed include ^{7}Li(p,n)^{7}Be, ^{9}Be(p,n)^{9}B, ^{45}Sc(p,n)^{45}Ti, and ^{51}V(p,n)^{51}Cr over an energy range of 1.5-10 MeV.

Additionally, the proposed targets offer several advantages over traditional materials. Their formation is simple, as they consist of nearly pure metals, which simplifies the manufacturing process. These metals possess appropriate melting points and electrical conductivity for this application. Furthermore, their radioactivity is significantly lower than that of lithium and beryllium, eliminating the need for extensive target disassembly procedures. Lastly, the economic cost of these materials is considerably lower, making them a more viable option for BNCT implementation.

In conclusion, our innovative BSA-free concept is based on a neutron source utilizing a thick scandium or vanadium target and a proton accelerator. It will be demonstrated that scandium would be feasible with current accelerators; however, higher proton currents than those currently available would be required. As

mentioned, it is essential to note that this novel approach is currently under evaluation for a patent. This patent proposal has been submitted to the Oficina de Transferencia de Resultados de Investigación (OTRI) of the University of Granada (UGR), and it is being assessed by this pertinent institution. The internal reference is IPR-1070.

6.2 Neutron Beam Criteria for BNCT

To propose a new neutron beam approach, it is essential to determine whether the beam requirements are met. This section outlines the key criteria for neutron beams in BNCT, focusing on neutron interactions with patient tissues and the parameters for effective treatment.

6.2.1 Dose Calculation

Understanding how neutrons interact with patient tissue is crucial for establishing specific beam requirements. In BNCT, neutrons must effectively penetrate the body and deposit energy primarily in cancerous tissues. The effectiveness of this energy deposition process depends on the neutron energy spectrum, which influences both the depth of penetration and the probability of interactions with boron atoms that have been selectively accumulated in tumor cells.

The most suitable neutron energy for BNCT depends on various factors, including the tumor's depth, size, and location within the body. Epithermal neutrons are ideal for penetrating surface tissues and reaching deeper tumors, where they can thermalize or lose energy, becoming more likely to be captured by boron. In contrast, thermal neutrons, which have much lower energy (less than 0.5 eV), are primarily absorbed near the surface, making them suitable for treating superficial tumors. The effectiveness of neutron capture by boron is crucial for maximizing the therapeutic effect of BNCT while minimizing damage to surrounding healthy tissue.

The challenge lies in delivering a neutron beam with an energy spectrum that optimally balances penetration depth and boron capture efficiency. Achieving this balance is crucial for ensuring the best therapeutic outcome. We need to carefully select the energy range that maximizes energy deposition within the tumor while minimizing the dose delivered to normal tissue. This involves considering both the physical characteristics of neutron interactions and the biological response of the surrounding tissue.

Once the energy spectrum of the beam has been established, we focus on calculating the dose administered to the patient. The absorbed dose or dose, denoted as D, for a given material is defined as the ratio of the net energy deposited in a specified volume of matter to the differential mass of that volume, as follows:

$$D = \frac{d\epsilon}{dm}. \tag{6.1}$$

In this equation, the unit of dose in the International System of Units (known by the acronym SI, from French Système international d'unités) is J/kg, referred to as the Gray (Gy). The provided definition and the following ones, are detailed in numerous reports by the International Commission on Radiological Units and Measurements (ICRU) [143]. Calculating the absorbed dose is crucial in the BNCT context, as it helps determine the effectiveness of neutron interactions with tumor cells while minimizing damage to surrounding healthy tissues.

Depending on how the particle interacts with matter, the deposited energy and, consequently, the dose will differ. In the case of neutrons, these particles do not have an electric charge and, therefore, do not ionize the medium directly. Instead, they deposit energy through the production of secondary particles during their interactions. It is essential to consider the interactions of the low-energy neutron beam with the patient, where the dominant processes for the elements present in the human body include elastic scattering, the ^{14}N capture reaction, radiative capture reactions (with ^{1}H being the most significant), and the desired ^{10}B capture reaction. Each of these interactions contributes to the overall energy deposition within the tumor and surrounding tissues, influencing the treatment's effectiveness.

In BNCT, the biologically weighted dose, denoted as D_W, is the relevant dose for treatment planning. As mentioned, neutrons transfer energy to the medium by producing secondary particles through different processes. The main interactions of a BNCT neutron beam with the body include elastic scattering, which dominates in the fast dose (D_{H}); the $^{14}\mathrm{N}(n,p)$ reaction, which is the most relevant for the thermal dose (D_t); radiative capture reactions that generate radiation contributing to the gamma dose (D_γ); and the $^{10}\mathrm{B}(\mathrm{n},\alpha)^{7}\mathrm{Li}$ reaction, which results in the boron dose (D_B). These dose components have different LET. To compare BNCT with photon therapy, it is customary to weigh these components with their Relative Biological Effectiveness (RBE) factors [48]. The weighted dose D_W is determined as:

$$D_W = w_f D_H + w_t D_t + w_\gamma D_\gamma + w_B D_B \tag{6.2}$$

where, if the individual dose terms are in Gray, the values obtained are expressed as Gray-equivalent or Gray-weighted, denoted as Gy(w). The weighting factors reflect the differences in the biological effectiveness of the various interaction mechanisms [144] and the differences in absorption in tumor and normal tissue. It is worth mentioning that many studies in BNCT investigate the dependence of such factors on the tissue type and energy (see [145] and references therein). Nevertheless, as stated by International Atomic Energy Agency (IAEA), the commonly used weighting factors for BNCT clinical trials are: $w_f = w_t = 3.2$, $w_B = 1.3$ for normal tissue, $w_B = 3.8$ for tumor, and $w_\gamma = 1$ [48]. Unless otherwise stated, these are the weighting factors we will use in our study.

6.2.2 IAEA Neutron Beam Quality Factors

The characteristics of the neutron beams used for irradiating a BNCT patient are defined by IAEA criteria, which must be strictly followed to conduct this therapy. In our study, we will focus specifically on deep tumors.

Table 6.1 indicates the current IAEA quality factors for deep-seated tumors (those located deeper than 2 cm). The neutron energies and fluxes are categorized into different ranges: thermal flux (denoted as Φ_{th}) with energies from 0.025 to 500 eV, epithermal flux (denoted as Φ_{epi}) ranging from 0.5 to 10 keV, and fast flux (denoted as Φ_{fast}) with energies higher than 10 keV. These energy ranges are the standard conventions for BNCT, as outlined in Chapter 1.

Beam quality component	Symbol or definition	Reference value
Therapeutic epithermal flux	Φ_{epi}	$\geq 5 \cdot 10^{8}$ cm^{-2}s^{-1}
Thermal to epithermal flux ratio	Φ_{th} / Φ_{epi}	≤ 0.05
Beam directionality	J / Φ_{epi}	≥ 0.7
Fast neutron dose per unit epithermal fluence	D_{H} / $\int \Phi_{\text{epi}}(t) \cdot \text{dt}$	$\leq 7 \cdot 10^{-13}$ Gy·cm^2
Gamma dose per unit epithermal fluence	D_{γ} / $\int \Phi_{\text{epi}}(t) \cdot \text{dt}$	$\leq 2 \cdot 10^{-13}$ Gy·cm^2

Table 6.1. Current reference IAEA quality factors for BNCT of deep tumors (more than 2 cm deep) [48].

In Table 6.1, D refers to the absorbed dose for a given material. In particular, D_{H} denotes the absorbed dose due to fast neutrons, while D_{γ} represents the gamma dose, as explained above. Additionally, J is the neutron current density (in $cm^{-2}s^{-1}$), which is a vectorial measure. Therefore, the ratio J / Φ_{epi} serves as a measure of the beam parallelism.

For deep-seated tumors, epithermal neutrons produce a therapeutic effect due to their thermalization throughout the tissue, allowing them to reach the tumor with thermal energy. This maximizes the probability of the ^{10}B(n,α)^{7}Li reaction, which irreversibly damages the tumor cells. Consequently, epithermal neutrons penetrate sufficiently into the patient to reach the tumor while delivering a minimal dose to healthy tissues. In contrast, thermal and fast neutrons provide a much higher and undesirable dose, primarily to the skin. This is why the IAEA quality factors limit the fast dose and thermal flux, ensuring that the contributions of both thermal and fast fluxes are minimized.

The quality factors for BNCT were updated in 2023 to reflect the latest standards established by the IAEA. The previous quality factors, shown in Table 6.2, have been replaced by the reference values presented in Table 6.1.

The main changes between the old and updated IAEA quality factors are in the fast neutron dose per unit epithermal fluence and the structure of the values. In the previous version, the fast neutron dose limit was $\leq 1.3 \cdot 10^{-13}$ Gy·cm^2, with

Beam quality component	Limit value	Target value
Therapeutic epithermal flux	$\geq 5 \cdot 10^8$ cm^{-2}s^{-1}	$\geq 10^9$ cm^{-2}s^{-1}
Thermal to epithermal flux ratio	≤ 0.05	≤ 0.05
Beam directionality	≥ 0.7	≥ 0.7
Fast neutron dose per unit epithermal fluence	$\leq 1.3 \cdot 10^{-13}$ Gy·cm^2	$\leq 2 \cdot 10^{-13}$ Gy·cm^2
Gamma dose per unit epithermal fluence	$\leq 1.3 \cdot 10^{-13}$ Gy·cm^2	$\leq 2 \cdot 10^{-13}$ Gy·cm^2

Table 6.2. Old IAEA quality factors for BNCT of deep tumors (more than 2 cm deep) [146].

a target of $\leq 2 \cdot 10^{-13}$ Gy·cm^2. In the updated version, the reference value has increased to $\leq 7 \cdot 10^{-13}$ Gy·cm^2, allowing for a higher dose. This change is justified in the IAEA document [48], as although a higher fast neutron component could increase superficial toxicities, no significant adverse effects have been observed in patients treated with higher doses, as demonstrated in recent clinical studies involving both accelerator and reactor systems. Additionally, dose distribution studies in patients show that moderate increases in the fast neutron dose have minimal impact on the deeper regions of the body, without significantly affecting the therapeutic dose to the tumor. This adjustment also takes into account that the design and optimization of accelerator systems, along with proper shielding, can help reduce adverse effects, allowing for a higher fast neutron dose to be delivered without negatively impacting the effectiveness of the treatment.

Another significant change is that, in the updated table (Table 6.1), most parameters no longer distinguish between target and limit values. For example, the therapeutic epithermal flux previously had a target value of $\geq 10^9$ cm^{-2}s^{-1}, but now only the minimum reference value of $\geq 5 \cdot 10^8$ cm^{-2}s^{-1} is listed. This allows for the use of less powerful and less expensive neutron generators compared to the accelerators currently in use or under design. This is one of the foundations of our proposal. Finally, the thermal-to-epithermal flux ratio and beam directionality remain unchanged between both tables, maintaining the same reference values of ≤ 0.05 and ≥ 0.7, respectively.

As mentioned, the quality factors outlined are specified in relation to the epithermal neutrons, with an upper limit of 10 keV. However, it is important to note that 10 keV is not a strict cutoff value. For instance, neutrons in the range of 20–40 keV can also beneficial, depending on the tumor's location and size, as the relative biological effectiveness does not exhibit a sudden change at 10 keV [48]. Several studies have explored the possibility to increasing the upper limit of epithermal neutrons in BNCT [147]–[150]. In fact, our group demonstrated in Ref. [150] that neutrons between 20 to 30 keV can produce a therapeutic effect depending on the tumor's location within the body. Thus, in certain treatments, it may be appropriate to raise the epithermal limit.

In this thesis, we will adopt a conservative value of 10 keV for our analysis, as our goal is to demonstrate that the BSA-free approach is viable within the current criteria. It is important to note, however, that with the commented extension of the fast dose limit, we now have greater flexibility to use slightly more energetic neutrons. Nevertheless, we leave open the possibility of future exploration to assess the potential impact of adjusting this limit, particularly by utilizing proton energies further from the threshold for the ^{51}V(p,n)^{51}Cr and ^{45}Sc(p,n)^{45}Ti reactions.

6.2.3 Figures of Merit

In addition to quality factors, Figures of Merit (FOMs) have been proposed and are commonly studied in standard BNCT phantoms as a more reliable reference for beam quality [48]. The most widely used FOMs include the Advantage Depth (AD), which represents the depth at which the tumor dose equals the maximum normal tissue dose. This metric is crucial for evaluating the effectiveness of treatment while minimizing damage to healthy tissues.

Another important figure is the Therapeutic Range (TR), defined as the tissue interval, TR_1 to TR_2, where the tumor dose is at least double the maximum dose received by normal tissue. In some studies, the end of this therapeutic range (TR_2) is referred to as the Double Dose Depth (DDD). Similarly, the Triple Dose Depth (TDD) indicates the maximum tumor depth where the dose is at least three times greater than the maximum dose in normal tissue, providing insights into the efficacy of the neutron beam at depth.

Lastly, the Maximum Therapeutic Ratio (MTR) highlights the highest ratio between the tumor dose and the dose in normal tissue, serving as a critical indicator of the treatment's effectiveness. All these FOMs not only ensure the quality of the neutron beam but also provide metrics for optimizing treatment outcomes. Therefore, we will also calculate these FOMs to evaluate the quality of the novel approach proposed in this thesis.

6.2.4 Out-of-field Dose

To establish the out-of-field criteria for BNCT, we have used the requirements set forth for other radiotherapy modalities as a basis. An international standard for light ion beam systems [151] specifies the following recommended limits for out-of-field dose based on the distance from the field edge: the maximum absorbed dose from all radiation types should not exceed 0.5% of the maximum dose at distances 15 cm to 50 cm from the field edge, and at distances $\geq$ 50 cm from the field edge, the maximum absorbed dose shall not exceed 0.1%.

Extrapolating these standards to BNCT, we conclude that the ratio between out-of-field dose and maximum tumor dose should be less than 5 mSv/Gy(w) for distances between 15 and 50 cm from the field edge, and less than 1 mSv/Gy(w) for distances beyond 50 cm. These criteria are indeed the recommendations proposed by the BNCT working group sponsored by the IAEA [152].

In Ref. [153], we proposed all these criteria for the out-of-field dose in BNCT and evaluated them for a specific BSA facility design [43]. To quantify the out-of-field dose, we have two options: either the ambient dose equivalent (in-air) or the effective dose (in-phantom). These two approaches provide different perspectives and potential applications for the aforementioned criteria.

Field Edge

The calculation of the field edge is essential for determining whether our facility is fulfilling the out-of-field dose criteria. In conventional radiotherapy, the field edge is defined as the lateral distance from the field axis to the 50% weighted dose line within a phantom. For source-to-surface distance treatments, the field edge is defined at the skin surface, while for isocentric treatments using source-to-axis distances, it is defined at a specific depth of the axis, typically around 10 cm. However, in BNCT, the exact location of the field edge has not yet been established [48]. Due to the significant scattering of low-energy neutrons within the patient, the useful radiation field in BNCT can be more extensive than that observed in other radiotherapy modalities.

In brain cancer BNCT, when the maximum dose to normal brain tissue is limited to 10 to 12 Gy(w), the maximum tumor dose along the beam axis can range from 60 to 70 Gy(w). Using typical RBE and Clinical Biological Effectiveness (CBE) factors and assuming a T/N Ratio of 3.5, for head and neck cancer, the minimum desired tumor dose is considered to be around 20 Gy(w) [154]. Based on these considerations, the field edge in BNCT could be defined as the lateral point where the dose reaches 20 Gy at the depth where the concentration of thermal neutrons is highest. This depth, which represents the highest tumor dose, can be directly measured using activation detectors. To determine the field edge accurately, measurements should be taken in a sufficiently large water phantom, at least 50 to 60 cm on each side, depending on the beam size, to ensure proper scattering of radiation at the edges.

In conclusion, based on the above discussion and the guidelines in Refs. [48], [152], the field edge quantity can be defined as the radial distance from the beam's central axis to the point where the tumor-weighted dose reaches 50%, measured in a large water phantom at the reference depth where the thermal neutron dose is at its maximum. To determine the depth at which this maximum thermal dose occurs, a simulation should be conducted using a large cylindrical water phantom, typically with a diameter and depth of 100 cm.

Maximum Tumor Dose

To determine the figures for the out-of-field dose criteria, the maximum weighted dose in a tumor located along the beam axis must first be calculated, as it will serve as the normalization. An ICRU 4- component biological tissue model, placed within a cylindrical phantom with a radius of 10 cm and a height of 20 cm, sur-

rounded by air and positioned 1 cm from the beam aperture, should be used. To calculate the dose along the depth, a set of voxels, each 1 cm in height and 1 cm in diameter, must be created along the beam axis to accurately identify the maximum tumor dose.

The choice of this phantom geometry simulates human tissue and typical tumor size, allowing for accurate neutron transport and dose distribution. The ICRU 4-components tissue model closely matches human organs, ensuring reliable results for absorbed dose calculations. This material has a density of 1 g/cm^3 and the following composition: 10.1% of ^{1}H, 11.1% of ^{12}C, 2.6% of ^{14}N and 76.2% of ^{16}O. Voxelizing the region provides fine spatial resolution, which is crucial for identifying the exact depth of maximum tumor dose.

Ambient Dose Equivalent

The ambient dose equivalent, H*(10), is used for monitoring radiation in a given area. According to International Commission on Radiological Protection (ICRP) [155], it is defined as the dose equivalent at a point in a radiation field, assuming that the radiation field is uniform and aligned. This measurement is taken at a depth of 1 cm within a simple spherical phantom known as the ICRU sphere, which is 30 cm in diameter and made of tissue-equivalent material. This definition facilitates consistent radiation field measurements by considering the fluence, as well as directional and energy distribution, as uniform across the volume of interest.

To calculate the ambient dose equivalent in air using Monte Carlo simulations, the flux in air is weighted with the conversion coefficients provided by Siebert and Schuhmacher [156] for neutrons, and Ferrari and Pelliccioni [157] for photons. A cylindrical mesh filled with air, with a depth of 1 cm and a radius of 100 cm, is employed at a distance of 5 cm from the beam exit plane, which is a typical treatment distance for head and neck cancer [48]. This analysis focuses on the relationship between leakage dose and tumor dose, considering only the primary radiation while excluding subsequent interactions of neutron and gamma radiation within the body. Therefore, an air-filled mesh is utilized for the calculation. In particular, in this thesis, the $H^*(10)$, due to neutrons and secondary photons, has been evaluated using ring-like voxels with a radial width of 1 cm.

Effective Dose

In radiation protection, the effective dose, denoted asH_T, is used, which accounts for the w_R factor for different types of radiation. It is measured in Sieverts (Sv) and is calculated using the following formula:

$$H_T = \sum_R w_R D_{R,T} \tag{6.3}$$

Here, H_T is the effective dose in a specific tissue T. R represents the different types of radiation contributing to the dose. For gamma radiation, $w_R = 1$. For

neutrons, the factor w_R depends on the energy and is defined by ICRP-116 [155] as follows, where E_n is the neutron energy:

$$w_R = \begin{cases} 2.5 + 18.2e^{-\ln(E_n)^2/6} & \text{for } E_n < 1 \text{ MeV}; \\ 5.0 + 17.0e^{-\ln(2E_n)^2/6} & \text{for } E_n \in [1, 50] \text{ MeV}; \\ 2.5 + 3.25e^{-\ln(0.04E_n)^2/6} & \text{for } E_n > 50 \text{ MeV}. \end{cases} \tag{6.4}$$

To quantify this effective dose, a cylindrical phantom of a standard soft tissue (ICRU 4-components tissue), with a length of 10 cm and a radius of 100 cm, is placed 1 cm from the beam. In the subsequent calculations of this dose, contributed by neutrons and photons, $D_{R,T}$ is evaluated in hollow cylindrical voxels with a radial width of 1 cm and a depth of 10 cm. This configuration not only measures the leakage dose contribution, but also captures the subsequent interactions inside the dummy.

6.3 V(p,n) as a BNCT Neutron Source

In this study, we will analyze the Beam Shaping Assembly-Free proposal using the ^{51}V(p,n)^{51}Cr reaction near its threshold as a neutron source. The measured angle-energy dependent spectrum, shown in Chapter 5, will be used in this study.

6.3.1 Near-threshold Neutron Spectra

The measured ^{51}V(p,n) neutron spectra at 1585 keV is a suitable candidate for BNCT. Figure 6.3 (**right**) shows the energy angle-dependent spectra that we will use in this section, extracted directly from the results of our experiment, presented in the Chapter 5. Additionally, We are showing again here the forward integrated spectra obtained in the measurement, Fig. 6.3 (**left**). Both representations have the "natural" energy binning. The total forward neutron yield of our measurement is 64477 n/sμA, this value will be employed as neutron yield throughout this section.

This BSA-free based on ^{51}V(p,n) approach takes advantage of the specific energy range of the ^{51}V(p,n)^{51}Cr reaction to generate neutrons that are suitable for BNCT, particularly for deep-seated tumors. The proximity of this reaction at 1585 keV to its threshold energy allows greater control over neutron production, effectively minimizing the generation of unwanted fast neutrons that could unintentionally increase the dose to healthy tissues. By using this direct neutron source without a BSA, the goal is to optimize the therapeutic neutron flux while simultaneously reducing exposure to non cancerous tissues. MCNP6.2 simulations are particularly well-suited for this BSA-free validation, as they accurately model neutron transport and interactions, allowing for detailed analysis of neutron energy spectra and flux in the absence of a BSA.

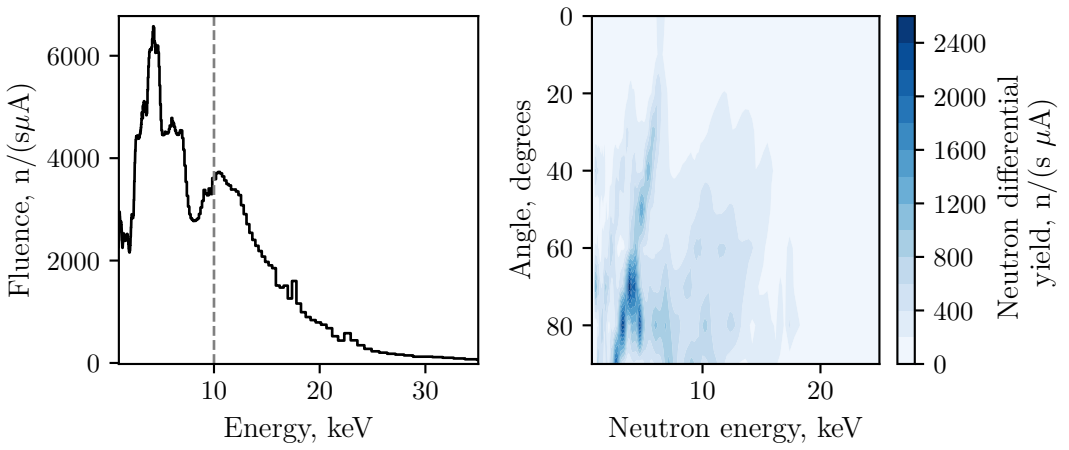

Figure 6.3. Results of the ^{51}V(p,n)^{51}Cr reaction for thick target at 1585 keV proton energy, measured experimentally in the Chapter 5. **Right:** Energy spectrum (dN/dE) pondered by the solid angle for 10 different angles dependent the neutron energy in keV. **Left:** Fluence or forward angle-integrated neutron spectrum. BNCT epithermal limit, 10 keV, is indicated.

Neutron Flux and Neutron Dose in Air

Figure 6.4 presents a detailed map of the neutron flux and dose distribution at the beam aperture, based on MCNP6.2 [122] simulations that utilize the experimental data from Chapter 5, depicted in Fig. 6.3. These simulations incorporate all the results from the angle-energy-dependent measurements of the ^{51}V(p,n) reaction at 1585 keV. It is important to note that the simulations were conducted in air rather than in a phantom, which indicates that this map provides only a general overview of the distribution and cannot be used directly to obtain the quality factors, as these must be evaluated under specific conditions.

As observed in Fig. 6.4, the neutron distribution is not isotropically uniform, meaning that the neutrons are not emitted or detected evenly in all directions. The exact experimental results have been included, showing that the yield varies depending on the angle. This variation explains why certain angles exhibit higher intensity compared to others. Additionally, it is important to highlight that the figures use a logarithmic scale, which amplifies the visual representation of small differences, making them appear more pronounced than they actually are. This should be taken into account when interpreting the results.

The main difference between the two figures presented in Fig. 6.4 is the scale. The neutron flux is measured in neutrons per second per μA, while the neutron dose is expressed in grays per second per μA. The shapes also display slight differences due to neutron interactions with the air in the dose map. For clarity, an ellipse representing a Snyder phantom (to scale) is included.

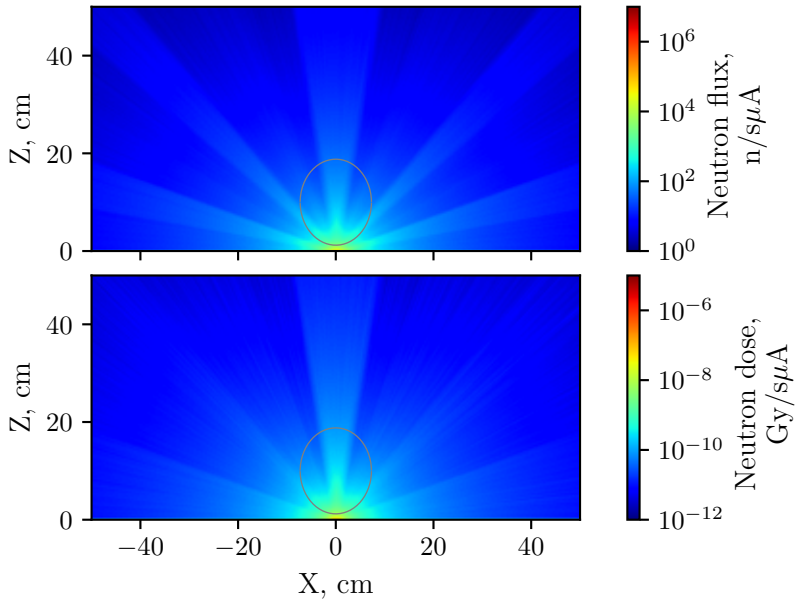

Figure 6.4. Neutron (**upper**) and neutron dose (**lower**) at the beam aperture for the ^{51}V(p,n) reaction spectrum at 1585 keV based on the experimental data. The grey ellipse represents the size of a Snyder phantom (to scale) at 1 cm of the beam aperture. **Upper:** Neutron flux at the beam aperture in neutrons per second per μA. **Lower:** Neutron dose map at the beam aperture in gray per second per μA.

6.3.2 IAEA Neutron Beam Quality Factors

The IAEA quality factors using the neutron reaction source presented in Fig. 6.3 (**right**) are shown in Table 6.3. This table compiles various results for the V target, considering different target diameters and varying distances to an ICRU 4-components tissue cylinder, which has a 10-cm diameter and 1-cm height. We adopted target and distance configurations similar to those used in several BNCT studies [48]. While changes in the target size resulted in minimal variation, significant differences were observed when altering the distance between the target and the cylinder. The uncertainties are negligible for all the presented parameters, as all the simulations were run for a sufficiently long duration.

The range of epithermal flux values spans from 496 to 1357 $\frac{\text{n}}{\text{cm}^2\mu\text{A}\cdot\text{s}}$, highlighting the impact of different target configurations and the distances to the tissue cylinder on neutron production. The highest epithermal flux is achieved when the cylinder is placed directly adjacent to the target; however, this configuration incurs the cost of lower beam directionality, with J/Φ_{epi} consistently meeting the threshold of 0.7 across all configurations.

Importantly, the thermal-to-epithermal flux ratio criterion (≤ 0.05) is satisfied across all configurations, ensuring that the neutron source predominantly produces epithermal neutrons. Additionally, the fast neutron dose per unit of epithermal

fluence (D_{H} / $\int \Phi_{\mathrm{epi}}(t) \cdot \mathrm{dt} \leq 7 \cdot 10^{-13}$ Gy cm^2) and gamma dose per unit of epithermal fluence (D_γ / $\int \Phi_{\mathrm{epi}}(t) \cdot \mathrm{dt} \leq 2 \cdot 10^{-13}$ Gy cm^2) are both well within acceptable limits for all configurations.

Finally, the fourth column (I-ABNS) of the Table 6.3 indicates the required intensity of the accelerator-based neutron source to achieve a therapeutic epithermal flux above $5{\cdot}10^8$ cm^{-2}s^{-1}. The required intensities range from 368 to 1008 mA, indicating that our BSA-free approach is not feasible with the current accelerators [41], [48]. However, we will continue with our analysis, as these accelerators may exist in the future.

ØV target (cm)	Dist. (cm)	Φ_{epi} ($\frac{\mathrm{n}}{\mathrm{cm}^2 \mu\mathrm{A}\cdot\mathrm{s}}$)	I-ABNS (mA)	$\frac{\Phi_{\mathrm{th}}}{\Phi_{\mathrm{epi}}}$	$\frac{J}{\Phi_{\mathrm{epi}}}$	$\frac{D_{\mathrm{H}}}{\int \Phi_{\mathrm{epi}}(t)\cdot\mathrm{dt}}$ (Gy cm^2)	$\frac{D_\gamma}{\int \Phi_{\mathrm{epi}}(t)\cdot\mathrm{dt}}$ (Gy cm^2)
	0	1357	368.4	0.030	0.7343	$4.22{\cdot}10^{-14}$	$1.28{\cdot}10^{-13}$
1	1	845	592.0	0.026	0.7822	$4.90{\cdot}10^{-14}$	$1.07{\cdot}10^{-13}$
	2	512	975.7	0.026	0.7846	$5.94{\cdot}10^{-14}$	$1.13{\cdot}10^{-13}$
	0	1356	368.8	0.030	0.7348	$4.23{\cdot}10^{-14}$	$1.25{\cdot}10^{-13}$
2	1	838	596.6	0.026	0.7836	$4.92{\cdot}10^{-14}$	$1.10{\cdot}10^{-13}$
	2	509	982.7	0.026	0.7879	$5.95{\cdot}10^{-14}$	$1.15{\cdot}10^{-13}$
	0	1348	371.1	0.029	0.7372	$4.25{\cdot}10^{-14}$	$1.08{\cdot}10^{-13}$
4	1	813	615.2	0.026	0.7872	$4.98{\cdot}10^{-14}$	$1.27{\cdot}10^{-13}$
	2	496	1007.8	0.025	0.7980	$5.94{\cdot}10^{-14}$	$1.24{\cdot}10^{-13}$

Table 6.3. IAEA quality factors for deep-seated tumor using the neutron source based on ^{51}V(p,n) reaction spectrum at 1585 keV based on the experimental data. Data for three different diameters for the target (1 or 2 cm) and three different distances between the target and the cylinder of the aperture (0 or 1 cm) are considered. Measurements on ICRU 4-components tissue cylinder, with a radius of 5 cm and a thickness of 1 cm. The results of the following quantities are presented: Epithermal flux (Φ_{epi}), required intensity for the beam to fulfills the requirement of epithermal flux (I-ABNS), ratio between thermal and epithermal flux ($\Phi_{\mathrm{th}}/\Phi_{\mathrm{epi}}$), ratio of current and epithermal flux (J/Φ_{epi}), rate fast neutron dose to epithermal flux ($D_{\mathrm{H}}/\int \Phi_{\mathrm{epi}}(t) \cdot \mathrm{dt}$) and rate gamma dose to epithermal flux($D_\gamma/\int \Phi_{\mathrm{epi}}(t) \cdot \mathrm{dt}$).

6.3.3 Figures of Merit

The following simulations were conducted using the optimal configuration obtained from Table 6.3, which includes a target with a diameter of 1 cm and a phantom cylinder with a diameter of 10 cm positioned at a distance of 1 cm from the target. Figure 6.5 shows the dose profiles from the different contributions, considering a boron concentration of 18 ppm for normal tissue and 63 ppm for tumor tissue.

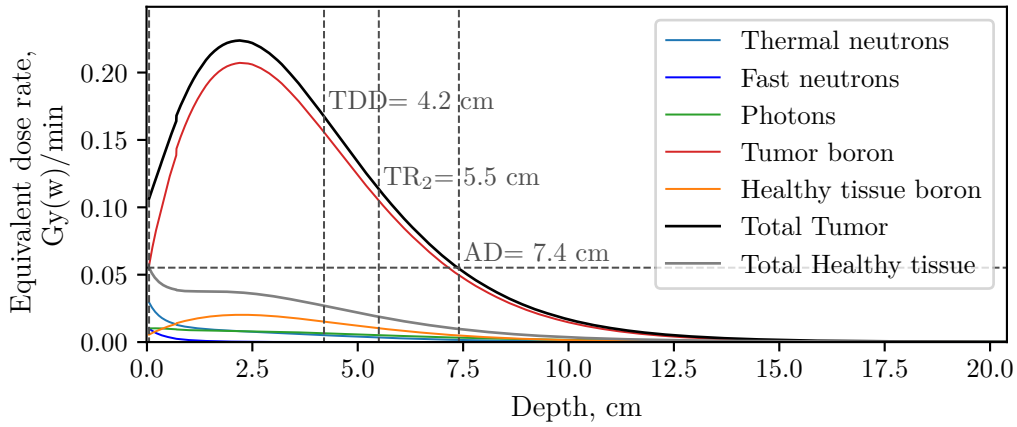

Figure 6.5. The depth dose profile for ^{51}V(p,n) reaction spectrum at 1585 keV based on experimental data, using a target with a diameter of 1 cm and an ICRU 4-components tissue cylinder with a diameter of 10 cm, with an intensity of 592.0 mA. Boron concentrations of 18 ppm in normal tissue and a T/N=3.5. The AD, TR_2 and TDD Figures of Merit are shown in the figure in cm. Simulations were run for a sufficient duration until the errors became negligible.

In this configuration, the Advantage Depth (AD) is 7.4 cm, the Therapeutic Range (TR) ranges from 0 to 5.5 cm, and the Triple Dose Depth (TDD) is 4.2 cm. The Maximum Therapeutic Ratio (MTR) is 6.2521. The primary contribution for the tumor or healthy dose is the boron dose component.

Table 6.4 presents the most relevant FOMs for ICRU 4-components and brain tissues, considering three boron uptake values (10, 18, and 25 ppm) and utilizing a tumor-to-normal tissue boron concentration ratio (T/N) ranging from 2.5 to 4.0. For ICRU 4-components tissue, the AD spans from 5.40 to 8.30 cm, TR_2 ranges from 3.20 to 6.60 cm, and TDD varies between 3.60 and 5.50 cm. The MTR fluctuates between 3.67 and 7.92. For the brain, the AD ranges from 5.40 to 8.00 cm, with TR_2 values between 2.70 and 6.40 cm and TDD spanning from 2.70 to 5.40 cm. The MTR for the brain varies from 3.52 to 7.68. In all instances, the values for ICRU 4-components tissue are higher. A broader treatment region and a larger AD are observed for any combination of boron uptake compared to brain tissue. Additionally, the maximum therapeutic ratio increases significantly with higher boron concentration and T/N Ratio.

The uncertainties in the distances presented in Table 6.4 have a margin of uncertainty of 0.10 cm, as the MCNP simulations were discretized using this value. In contrast, the uncertainty associated with the MTR is smaller because it represents the ratio of two doses calculated with negligible uncertainty due to the long simulation time. Consequently, the MTR parameter has no associated uncertainty.

Tissue	Boron Uptake (ppm)	T/N	AD (cm)	TR_2 (cm)	TDD (cm)	MTR
ICRU 4-comp.	10	2.5	5.40	-	-	3.6687
		3.5	6.20	3.90	-	4.9055
		4	6.50	4.30	-	5.5238
	18	2.5	6.70	4.60	-	4.5890
		3.5	7.40	5.50	4.20	6.2521
		4	7.70	5.90	4.70	7.0837
	25	2.5	7.30	5.40	4.00	5.0815
		3.5	8.00	6.30	5.10	6.9730
		4	8.30	6.60	5.50	7.9187
Brain	10	2.5	5.40	2.70	-	3.5216
		3.5	6.10	4.00	-	4.6901
		4	6.40	4.40	2.70	5.2744
	18	2.5	6.50	4.60	3.00	4.4390
		3.5	7.20	5.40	4.30	6.0327
		4	7.40	5.70	4.70	6.8295
	25	2.5	7.10	5.30	4.10	4.9409
		3.5	7.70	6.10	5.10	6.7671
		4	8.00	6.40	5.40	7.6802

Table 6.4. Relevant FOMs extracted from the simulations for ^{51}V(p,n) reaction spectrum at 1585 keV based on experimental data, are given. Data for ICRU 4-components (ICRU 4-comp.) tissue and brain tissue is given, considering boron concentrations in normal tissue of 10, 18 or 25 ppm, and T/N radios from 2.5 to 4.0.

6.3.4 Snyder Phantom

Figure 6.6 illustrates a 2-D dose map of a central cross-section of the brain, utilizing the Snyder head phantom for the vanadium BSA-free approach. The color map visually represents the ratio of the tumor dose to the maximum dose delivered to normal tissue across various regions of the brain, providing a comprehensive view of the dose distribution.

The highest tumor-to-normal tissue dose ratio observed is 10.21, occurring at z = 6.38 cm and x = -0.34 cm, as depicted in Figure 6.6. This high ratio suggests a favorable treatment scenario, where the dose to the tumor is significantly greater than that to the healthy tissue, potentially enhancing the therapeutic effect while minimizing damage to normal brain tissue.

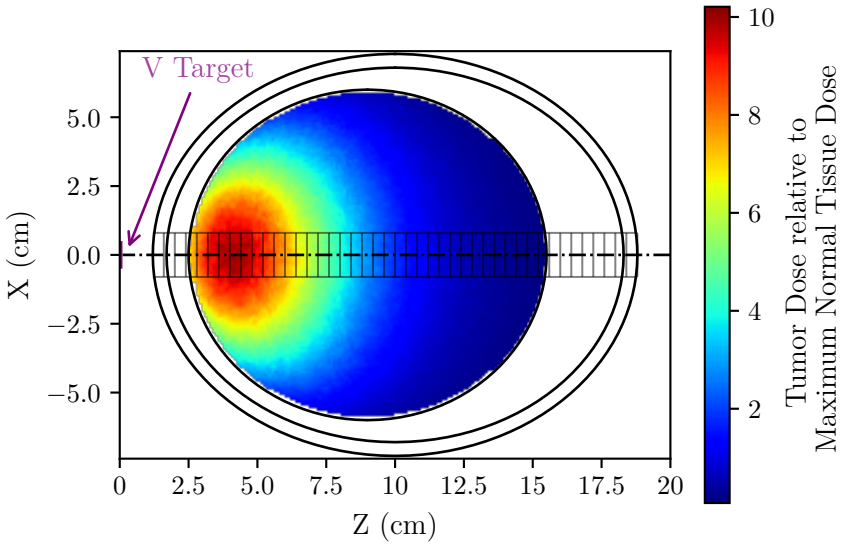

Figure 6.6. Ratio of the tumor dose to the maximum dose in normal tissue in a central cut of a Snyder head phantom for ^{51}V(p,n) at 1585 keV at a distance of 1 cm from a target with a diameter of 1 cm. Boron concentrations of 18 ppm (normal tissue) and 63 ppm (tumor tissue), with a ratio of T/N=3.5.

6.3.5 Out-of-field Dose

The out-of-field dose must be taken into account for this Vanadium BSA-free proposal, to ensure that our proposed system is safe for the patient. As explained, the first step is to quantify the field edge and the maximum tumor dose.

Figure 6.7 (**left**) presents the results of simulations conducted to determine the field edge of our system. The field edge is identified at a distance of (4.5 ± 0.1) cm, indicating where the dose falls below a significant threshold. In this simulation, a large water cylinder was positioned 1 cm from the 1 cm diameter V target to model the dose distribution effectively, using the optimal configuration for the Vanadium proposal. The uncertainty of the field edge value is due to the discretization method applied to the cylinder. Notably, the maximum weighted tumor dose occurs at the center of the target, while 50% of this maximum dose is achieved at (4.5 ± 0.1) cm, confirming this distance as the field edge.

In Figure 6.7 (**right**), the dose distribution within an ICRU 4-component tissue cylindrical phantom is shown. This figure illustrates the depth dose profile, showing that the maximum tumor dose occurs at a depth of 3 cm along the beam axis. At this point, the measured dose is $1.07{\cdot}10^{-6}$ Gy(w)/min/μA, with negligible uncertainty due to the prolonged simulation time.

With the field edge at (4.5 ± 0.1) cm and the maximum tumor dose at $1.07{\cdot}10^{-6}$ Gy(w)/min/μA established, we can now calculate the out-of-field dose. Figure 6.8 shows the ambient dose equivalent and effective dose, meeting all criteria from Ref. [153], a key factor for patient safety.

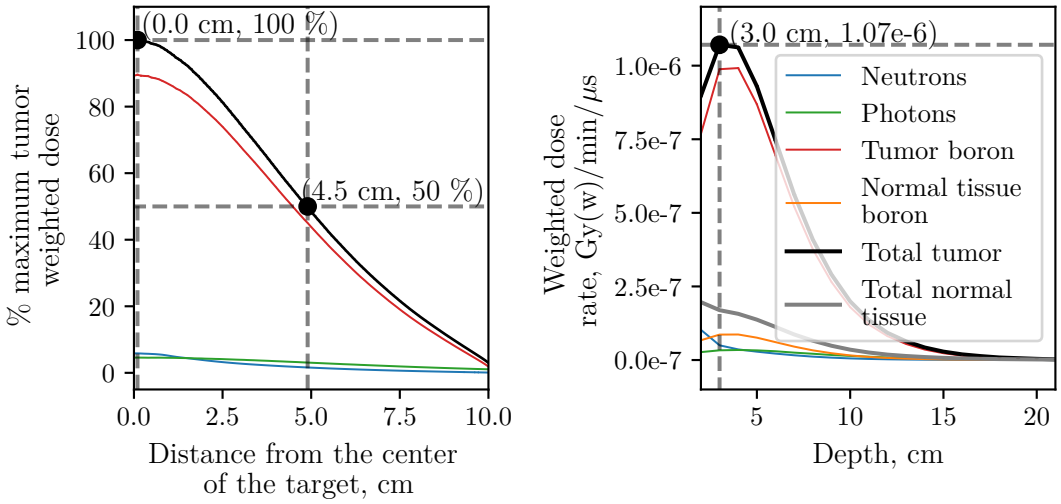

Figure 6.7. Field edge and maximum tumor dose for the ^{51}V(p,n) reaction spectrum at 1585 keV based on experimental data. The legend for both figures is represented in the left one. Simulations were run for a sufficient duration until the errors became negligible. **Left:** Simulation of the field edge determination, using a large water cylinder is positioned at 1 cm from the 1 diameter V target. The maximum weighted tumor dose occurs at 0 cm, with 50% of the maximum dose measured at (4.5 ± 0.1) cm, defining the field edge at this distance. **Right:** Simulation of the maximum tumor dose using a cylindrical phantom with standard ICRU 4-components biological tissue, positioned 1 cm from the 1 diameter V target. The highest dose, located 3 cm deep along the beam axis, is $1.07{\cdot}10^{-6}$ Gy(w)/min/μA in tumor tissue.

In the upper part of Fig. 6.8, the ambient dose equivalent in air, expressed relative to the maximum tumor dose (Sv/Gy(w)), is displayed. The criteria are met across the full range (15-50 cm and beyond); however, at 15 cm, the value of 3.956 mSv/Gy(w) is close to the limit. Neutron contributions to the dose are higher than those from photons at all distances. The total ambient dose ranges from 3.956 to 0.563 mSv/Gy(w) within the 15-50 cm range. Beyond 50 cm, the values are at least 1.19 times below the 1 mSv/Gy(w) limit and decrease with distance.

Similarly, the lower part of Fig. 6.8 presents the effective dose, which also meets the criteria at all distances with a significant margin. In this case, photon contributions are higher due to interactions inside the phantom, especially from the $^1H(n,\gamma)^2H$ reaction. The effective dose is lower than the ambient dose equivalent, ranging from 1.388 to 0.049 mSv/Gy(w) within the 15-50 cm range and remaining below 0.049 mSv/Gy(w) beyond 50 cm, decreasing further with distance. The major difference between the two out-of-field doses is due to the geometry and composition of the cylinders where measurements were taken.

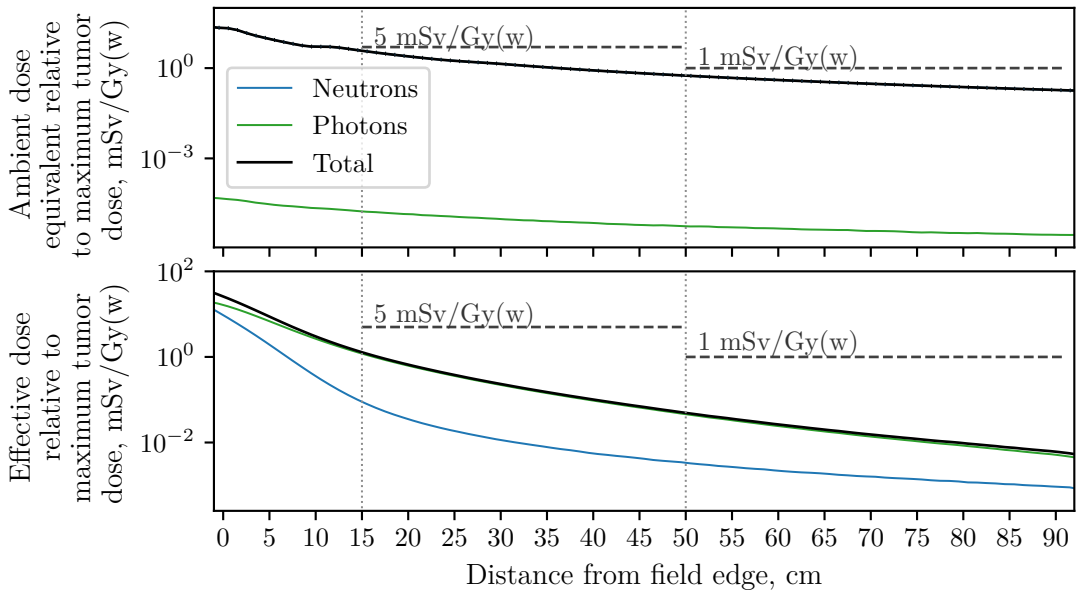

Figure 6.8. Out-of-field dose for the ^{51}V(p,n) reaction spectrum at 1585 keV based on experimental data. **Upper**: Ambient dose equivalent $H*$ for air cylindrical rings of 1 cm depth and 1 cm radius, 5 cm away from the for ^{51}V(p,n) at 1585keV source. **Lower**: Effective dose H_T normalized for cylindrical rings of 10 cm depth and 1 cm radius, 1 cm away from the ^{51}V(p,n) at 1585keV source. All the quantities are normalized to the tumor therapeutic dose, at a rate of, $1.07{\cdot}10^{-6}$ Gy(w)/min/μA. The y-axis has logarithmic scale. The horizontal lines mark the upper limits, respectively 5 mSv/Gy(w) and 1 mSv/Gy(w) (from left to right). The vertical lines indicate 15 cm and 50 cm from the field edge, as defined by the criteria. Simulations were run for a sufficient duration until the errors became negligible.

6.4 Sc(p,n) as BNCT Neutron Source

In this section, we investigate the potential of the ^{45}Sc(p,n)^{45}Ti reaction as a neutron source for BNCT. The analysis follows the same methodology outlined in the previous section, which focused on the ^{51}V(p,n) reaction as a BNCT neutron source.

6.4.1 Near-threshold Neutron Spectra

Based on the kinematics and previously presented data for the ^{45}Sc(p,n)^{45}Ti reaction in Chapter 2, we determined that a proton energy of 2918 keV on a thick Sc target is optimal for producing a neutron beam suitable for BNCT. This proton energy is just 10 keV above the reaction threshold; therefore, the produced neutrons will have a maximum energy of 18 keV, as determined by the kinemat-

ics equations. To proceed with the analysis, it is essential to obtain the neutron spectra as a function of both emission angle and energy for this specific proton energy. These neutron spectra will then be incorporated into the MC simulations to evaluate the quality factors and FOMs for the proposed setup.

Due to the lack of experimental angle-energy data for the ^{45}Sc(p,n)^{45}Ti reaction at 2918 keV, an effective approach is to generate these spectra using the NEBOAS code [136], [137]. This code, as discussed and applied in Chapters 4 and 5, has shown excellent agreement with experimental data across a range of nuclear reactions and proton energies, making it a reliable tool for simulating neutron spectra in our study.

Therefore, we employed the NEBOAS code to calculate the angle-energy spectra of neutrons emitted from the ^{45}Sc(p,n)^{45}Ti reaction at 2918 keV, incorporating the experimental cross-section data from Fig. 2.3 and the stopping power from SRIM code [120]. Figure 6.9 (**right**) shows the resulting differential yield in units of $\frac{n}{sr \cdot \mu A \cdot s}$, for 2918 keV which will be used in the MC simulations.

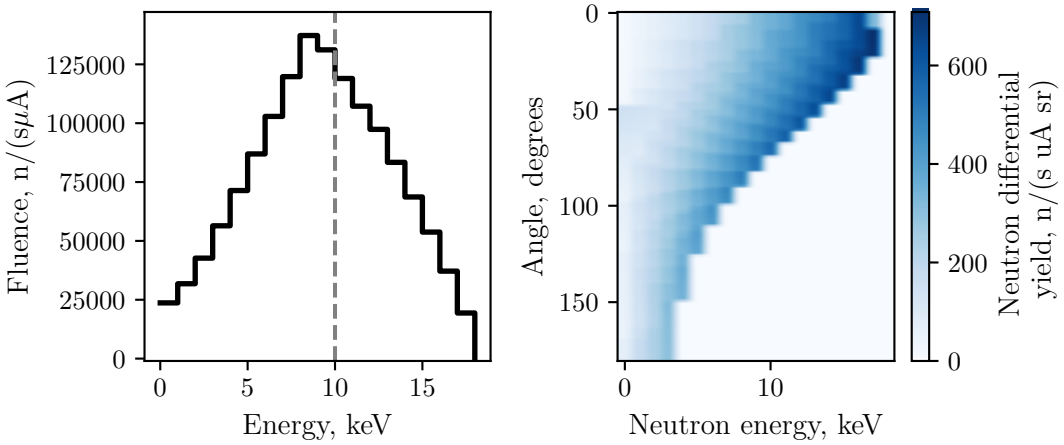

Figure 6.9. NEBOAS results of the ^{45}Sc(p,n)^{45}Ti reaction for thick target at 2918 keV proton energy, calculated by NEBOAS [136], [137]. **Left:** Fluence or forward angle-integrated (from 0 to 90 degrees) neutron spectrum. BNCT epithermal limit, 10 keV, is indicated.. **Right:** Neutron differential yield $\frac{d^2Y}{dE_n d\Omega}$ dependent of the angle in degrees and the neutron energy in keV..

The angle-integrated yield is a quantity that provides a direct and easy description of the neutron spectrum at the emission point (the Sc target). If we integrated in angle the double differential yield we obtain the fluence (or angle-integrated yield). This can be done numerically with the expression:

$$F = \sum_{E_{n_j}} \sum_{\theta_i} \frac{d^2Y}{dE_n d\Omega}(\theta_i, E_{n_j}) \cdot 2\pi \cdot sin(\theta_i), \tag{6.5}$$

where the fluence, F, has units of $\frac{n}{s\mu A}$. In Figure 6.9 left we represent the integrated spectra for the forward part of the emission (from 0 to 90 degrees). The

energy ranges from 1 to 17.7 keV with 10 keV as the maximum. The total fluence, integrated in energy, is $1.4{\cdot}10^6$ n/(s·μA).

Neutron flux and neutron dose in air

To fully evaluate the neutron spectrum presented, it is essential to consider both the neutron flux and the neutron dose in air. These parameters are fundamental to understanding the radiation field and its potential impact. Figure 6.10 shows a detailed map distribution of both the neutron flux (**upper**) and the neutron dose (**lower**) at the beam aperture. The neutron flux is measured in neutrons per second per μA, while the neutron dose is expressed in Grays per second per μA. These simulations were carried out in air, though in practice, biological tissue will be present within the field. In Fig. 6.10 for clarity, an ellipse representing a Snyder phantom (to scale) is included.

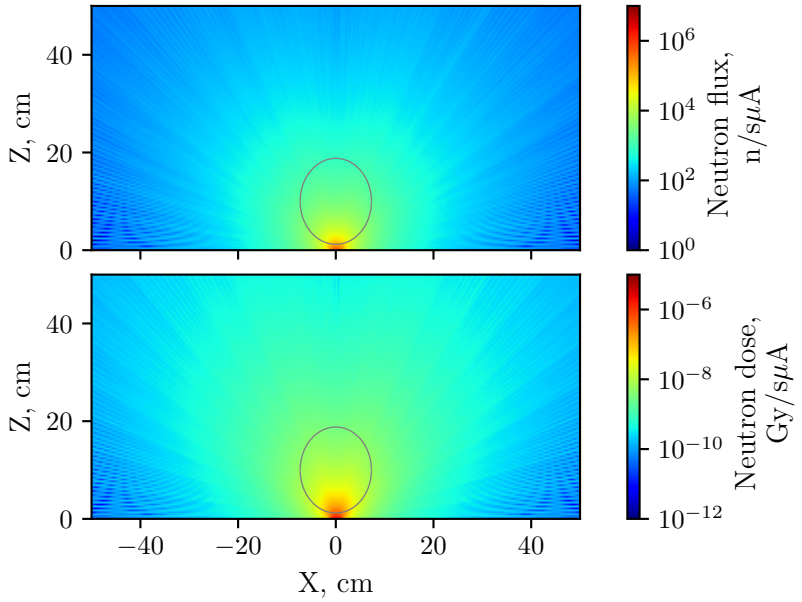

Figure 6.10. Neutron flux (**upper**) and neutron dose (**lower**) at the beam aperture for the ^{45}Sc(p,n) reaction spectrum at 2918 keV based on NEBOAS. The grey ellipse represents the size of a Snyder phantom (to scale) at 1 cm of the beam aperture. **Upper:** Neutron flux at the beam aperture in neutrons per second per μA. **Lower:** Neutron dose map at the beam aperture in gray per second per μA.

Notably, the results indicate that using a collimator to focus the neutron beam is unnecessary. It is worth mentioning that Fig. 6.10 cannot be used directly to obtain the quality factors because they must be evaluated in ICRU 4-components tissue.

6.4.2 IAEA Neutron Beam Quality Factors

Table 6.5 summarizes our results for 2918-keV protons on Sc target and different diameters of the target and varied distances to a cylinder of ICRU 4-components tissue with a 10-cm diameter and a 1-cm height. Once more, the uncertainties for all the presented parameters are negligible, as the simulations were conducted for a sufficiently long duration.

ØSc target (cm)	Dist. (cm)	Φ_{epi} $(\frac{\text{n}}{\text{cm}^2\mu\text{A}\cdot\text{s}})$	I-ABNS (mA)	$\frac{\Phi_{\text{th}}}{\Phi_{\text{epi}}}$	$\frac{J}{\Phi_{\text{epi}}}$	$\frac{D_{\text{H}}}{\int \Phi_{\text{epi}}(t)\cdot\text{dt}}$ (Gy cm^2)	$\frac{D_\gamma}{\int \Phi_{\text{epi}}(t)\cdot\text{dt}}$ (Gy cm^2)
	0	$2.93 \cdot 10^4$	17.1	0.033	0.8031	$1.34 \cdot 10^{-13}$	$2.28 \cdot 10^{-14}$
1	1	$2.29 \cdot 10^4$	21.8	0.031	0.8495	$1.71 \cdot 10^{-13}$	$1.83 \cdot 10^{-14}$
	2	$1.70 \cdot 10^4$	29.5	0.030	0.9274	$2.31 \cdot 10^{-13}$	$1.67 \cdot 10^{-14}$
	0	$2.92 \cdot 10^4$	17.1	0.033	0.8037	$1.34 \cdot 10^{-13}$	$2.25 \cdot 10^{-14}$
2	1	$2.28 \cdot 10^4$	21.9	0.031	0.8519	$1.72 \cdot 10^{-13}$	$1.85 \cdot 10^{-14}$
	2	$1.68 \cdot 10^4$	29.7	0.029	0.9296	$2.33 \cdot 10^{-13}$	$1.68 \cdot 10^{-14}$
	0	$2.91 \cdot 10^4$	17.2	0.032	0.8063	$1.35 \cdot 10^{-13}$	$2.06 \cdot 10^{-14}$
4	1	$2.22 \cdot 10^4$	22.5	0.030	0.8618	$1.77 \cdot 10^{-13}$	$1.97 \cdot 10^{-14}$
	2	$1.63 \cdot 10^4$	30.7	0.029	0.9390	$2.38 \cdot 10^{-13}$	$1.74 \cdot 10^{-14}$

Table 6.5. IAEA quality factors for deep-seated tumor using the neutron source based on ^{45}Sc(p,n) at 2918 keV. Data for three different diameters for the target (1 or 2 cm) and three different distances between the target and the cilinder of the aperture (0 or 1 cm) are considered. Measurements on ICRU 4-components tissue cylinder, with a radius of 5 cm and a thickness of 1 cm. The results of the following quantities are presented: Epithermal flux (Φ_{epi}), required intensity for the beam to fullfils the requierement of ephithermal flux (I-ABNS), ratio between thermal and epithermal flux ($\Phi_{\text{th}}/\Phi_{\text{epi}}$), ratio of current and epithermal flux (J/Φ_{epi}), rate fast neutron dose to epithermal flux ($D_{\text{H}}/\int \Phi_{\text{epi}}(t)\cdot\text{dt}$) and rate gamma dose to epithermal flux($D_\gamma/\int \Phi_{\text{epi}}(t)\cdot\text{dt}$).

The fourth column (I-ABNS) represents the required intensity of the accelerator-based neutron source needed to fulfil a therapeutic epithermal flux higher than $5{\cdot}10^8$ cm^{-2}s^{-1}. The required intensity ranges from 17 to 31 mA, indicating that our BSA-free proposal is feasible, as proton accelerators capable of delivering such intensities are already available in the market [41], [48].

Moreover, the ratio of thermal to epithermal flux meets the stipulated criteria (≤ 0.05) for all configurations as well as the other quality factors. As previously mentioned, we have adhered to target configurations and distances that align with those utilized in several BNCT studies [48]. While variations in the size of the target do not significantly impact the results, notable differences emerge when assessing the cylinder at different distances from the target. When the cylinder is positioned directly adjacent to the target, we observe the highest epithermal flux

and this configuration also yields the lowest beam directionality, with a $J/\Phi_{\text{epi}} = 0.92$ (≥ 0.7).

In terms of safety and efficacy, the fast neutron dose per unit epithermal fluence ($D_{\text{H}} / \int \Phi_{\text{epi}}(t) \cdot \text{dt} \leq 7{\cdot}10^{-13}$ Gy cm^2) and gamma dose per unit epithermal fluence ($D_{\gamma}/\int \Phi_{\text{epi}}(t) \cdot \text{dt} \leq 2{\cdot}10^{-13}$ Gy cm^2) are comfortably met across all configurations.

6.4.3 Figures of Merit

As mentioned, several FOMs are also conventionally studied to evaluate a BNCT facility. The following simulations have been conducted with the best configuration obtained in Table 6.5, thus, a 1-cm diameter target and placing the phantom cylinder of 10-cm diameter at a distance of 1 cm from the target. The configuration chosen for this analysis closely mirrors that used in the previous study of the ^{51}V(p,n) reaction, owing to the similarities in the characteristics of the neutron spectra produced by both reactions.

Figure 6.11 shows the dose profiles of the different contributions considering a boron concentration of 18 ppm for normal tissue and 63 ppm for tumor tissue, in the same way as in Fig. 6.5. These concentrations are commonly used as a standard for BNCT simulations in brain tumors with BPA [43], [158], [159].

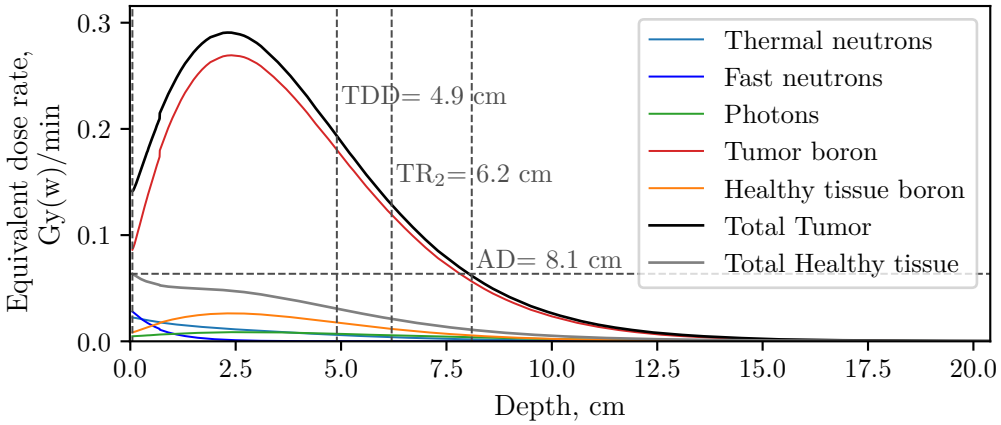

Figure 6.11. The depth dose profile for the ^{45}Sc(p,n) reaction spectrum at 2918 keV based on NEBOAS, using a target with a diameter of 1 cm and an ICRU 4-components tissue cylinder with a diameter of 10 cm, with an intensity of 21.81 mA. Boron concentrations of 18 ppm in normal tissue and a T/N=3.5. The AD, TR$_2$ and TDD Figures of Merit are shown in the figure in cm. Simulations were run for a sufficient duration until the errors became negligible.

In this configuration, the AD is 8.1 cm, the therapeutic range reaches from 0 to 6.2 cm, and the TDD is 4.9 cm. The MTR is 6.35. These values are particularly effective for tumors located at a depth of around 3 cm and with a size on the scale of centimeters.

We have also studied the performance of our scandium BSA-free approach in other cases. Table 6.6 shows the results for ICRU 4-components and Brain tissues of the FOMs for three boron uptake (10, 18, and 25 ppm), using a ratio of boron concentration between tumor and normal tissue (T/N) from 2.5 to 4.0. For ICRU 4-components tissue, AD ranges from 6.10 to 8.90 cm, TR2 from 3.20 to 7.20 cm, and TDD from 3.20 to 6.10 cm, with MTR varying from 3.73 to 8.02. In the brain, AD ranges from 6.00 to 8.60 cm, TR2 from 3.60 to 7.00 cm, and TDD from 3.00 to 6.00 cm, with MTR between 3.56 and 7.74. The ICRU 4-components tissue values are consistently higher, showing a broader treatment region and greater AD for any boron uptake compared to brain tissue. The maximum therapeutic ratio increases notably with higher boron concentration and T/N Ratio.

Material	Boron Uptake (ppm)	T/N	AD (cm)	TR_2 (cm)	TDD (cm)	MTR
ICRU 4-comp.	10	2.5	6.10	3.20	-	3.73
		3.5	6.90	4.60	-	5.00
		4.0	7.20	5.10	3.20	5.63
	18	2.5	7.20	5.20	3.50	4.65
		3.5	8.10	6.20	4.90	6.35
		4.0	8.40	6.50	5.30	7.19
	25	2.5	7.90	6.00	4.70	5.14
		3.5	8.70	6.70	5.70	7.06
		4.0	8.90	7.20	6.10	8.02
Brain	10	2.5	6.00	3.60	-	3.56
		3.5	6.70	4.70	3.00	4.74
		4.0	7.00	5.10	3.60	5.34
	18	2.5	7.10	5.20	3.80	4.48
		3.5	7.80	6.00	4.90	6.09
		4.0	8.00	6.40	5.30	6.89
	25	2.5	7.60	5.90	4.70	4.98
		3.5	8.30	6.70	5.60	6.82
		4.0	8.60	7.00	6.00	7.74

Table 6.6. Relevant FOMs extracted from the simulations for the ^{45}Sc(p,n) reaction spectrum at 2918 keV based on NEBOAS, are given. Data for ICRU 4-components (ICRU 4-comp.) tissue and brain tissue is given, considering boron concentrations in normal tissue of 10, 18 or 25 ppm, and T/N radios from 2.5 to 4.0.

The distances in Table 6.6 have an uncertainty of 0.10 cm, reflecting the discretization step used in the MCNP simulations. In contrast, the MTR parameter has no associated uncertainty, as it is derived from the ratio of two doses calculated with negligible uncertainty due to extended simulation times.

6.4.4 Snyder Phantom

In Figure 6.12, we present a 2-D dose map in a central cross-section of the brain for the Snyder head phantom for the Scandium BSA-free approach at 2918 keV proton energy. The map corresponds to a Sc target with a diameter of 1 cm at a distance of 1 cm. The colors in the map represent the ratio between the tumor dose and the maximum dose in normal tissue across different regions of the brain. Notably, there is a substantial region where the tumor dose exceeds the maximum dose in normal tissue. The maximum observed ratio of the tumor dose to the maximum dose in normal tissue is 3.55, produced in z=4.22 cm and x=-0.147 cm.

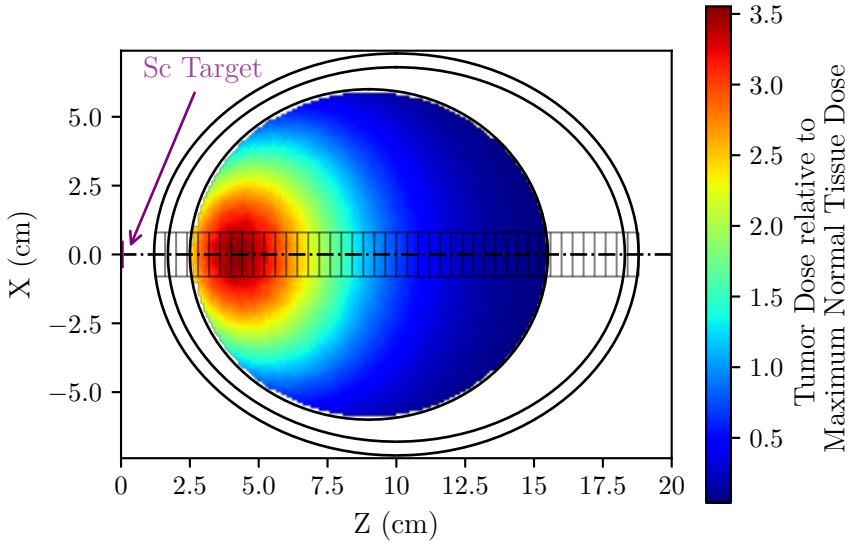

Figure 6.12. Ratio of the tumor dose to the maximum dose in normal tissue in a central cut of a Snyder head phantom for the ^{45}Sc(p,n) reaction spectrum at 2918 keV based on NEBOAS, at a distance of 1 cm from a target with a diameter of 1 cm. Boron concentrations of 18 ppm (normal tissue) and 63 ppm (tumor tissue), with a ratio of T/N=3.5.

For the dose evaluation in the brain regions (cells) indicated in Figure 6.12, the AD, TR_2 and TDD are obtained 9 cm, 7 cm and 5.4 cm, respectively. The value obtained for MTR is 8.14. These results plus the diagram shown the suitability of our Scandium BSA-free proposal, demonstrating that its performance is comparable to many existing or under-development beams for BNCT.

6.4.5 Out-of-field Dose

The out-of-field dose serves as a measurement of treatment safety. Following the same approach used for the Vanadium BSA-free proposal, the first step is to determine both the field edge and the maximum therapeutic dose delivered to the tumor, as illustrated in Figs.

In Fig. 6.13 (**right**) the calculation to obtain the maximum tumor dose is shown. For this we have considered standard ICRU 4-components biological tissue in a cylindrical phantom of 10 cm radius and 20 cm height surrounded by air, at 1 cm from the 1 cm diameter Sc target. A set of voxels along the beam axis were created in order to determine the dose along depth, each one of 1 cm of height and 1 cm diameter. The final result for this simulation is that the maximum dose in the center of the beam is located at 3 cm deep where the dose rate at the normal tissue is $6.27{\cdot}10^{-6}$ Gy(w)/min/μA and that of tumor tissue is $3.26{\cdot}10^{-5}$ Gy(w)/min/μA (ratio of 5.2 between tumor and normal tissue doses). The final result to normalize our ambiend dose equivalent and effective dose will be $3.26{\cdot}10^{-5}$ Gy(w)/min/μA, with negligible uncertainty due to the long simulation time.

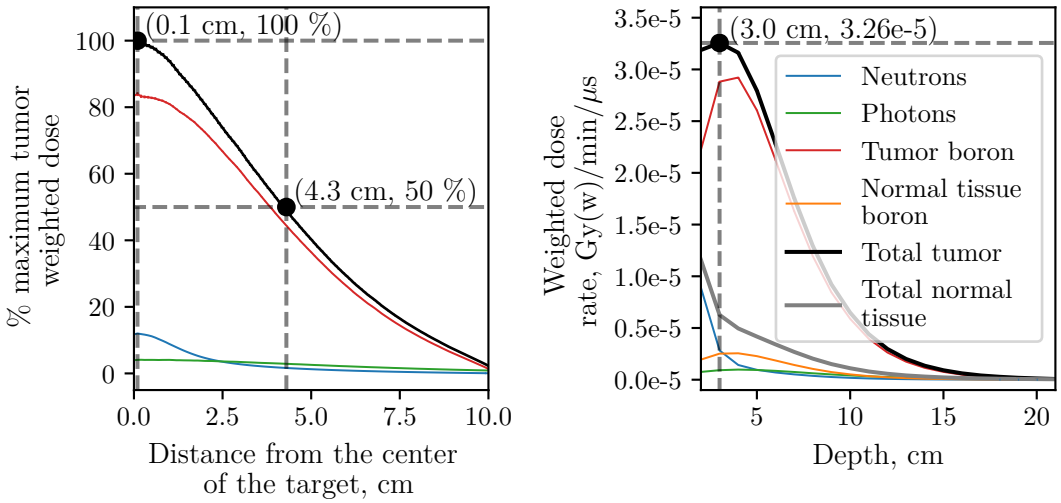

Figure 6.13. Field edge and maximum tumor dose for the ^{45}Sc(p,n) reaction spectrum at 2918 keV based on NEBOAS. The legend for both figures is represented in the left one. Simulations were run for a sufficient duration until the errors became negligible. **Left:** Simulation of the field edge determination, using a large water cylinder is positioned at 1 cm from the Sc target. The maximum weighted tumor dose occurs at 0.1 cm, with 50% of the maximum dose measured at (4.3 $\pm$ 0.1) cm, defining the field edge at this distance. **Right:** Simulation of the maximum tumor dose using a cylindrical phantom with standard ICRU 4-components biological tissue, positioned 1 cm from the Sc target. The highest dose, located 3 cm deep along the beam axis, is $3.26{\cdot}10^{-5}$ Gy(w)/min/μA in tumor tissue.

Fig. 6.13 (**left**) illustrates the simulation conducted to determine the field edge. The setup includes a large water cylinder positioned at 1 cm from the 1 cm diameter Sc target, and the corresponding results are displayed. The peak of the weighted tumor dose occurs at a distance of 0.1 cm, while 50% of this maximum dose is observed at (4.3 $\pm$ 0.1) cm. The uncertainty in the field edge value arises from the 0.1 cm discretization of the cylinder. Consequently, the field edge is

defined at (4.3 ± 0.1) cm. Therefore, knowing the field edge and the value of the maximum tumor dose we are able to study the out-of-field dose.

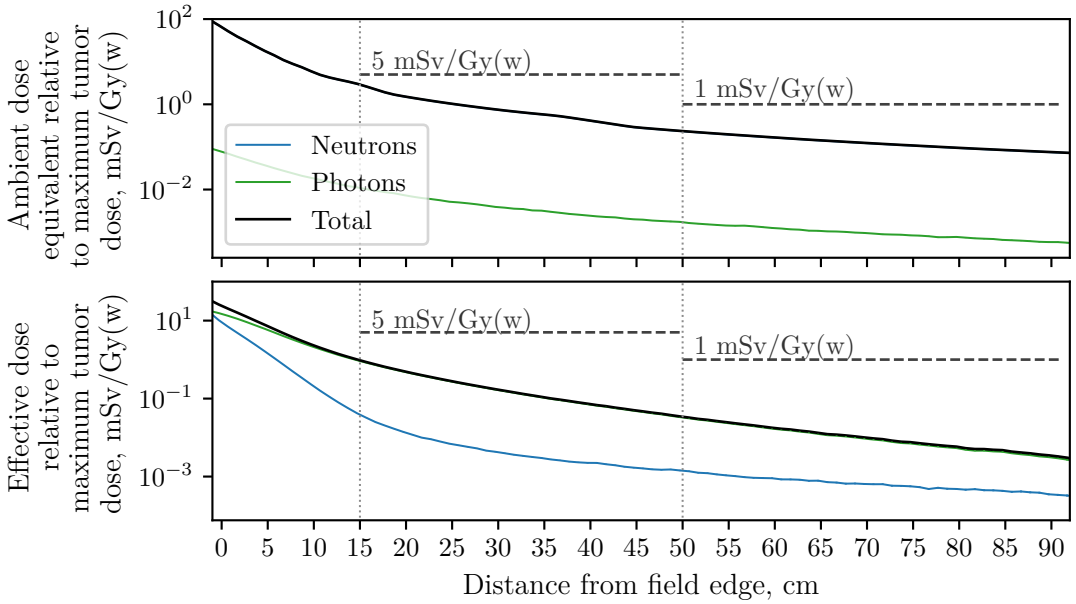

Figure 6.14. Out-of-field dose for the ^{45}Sc(p,n) reaction spectrum at 2918 keV based on NEBOAS. **Upper**: Ambient dose equivalent $H*$ for air cylindrical rings of 1 cm depth and 1 cm radius, 5 cm away from the for ^{45}Sc(p,n) at 2918keV source. **Lower**: Effective dose H_T normalized for cylindrical rings of 10 cm depth and 1 cm radius, 1 cm away from the ^{45}Sc(p,n) at 2918 keV source. All the quantities are normalized to the tumor therapeutic dose, at a rate of, $3.26{\cdot}10^{-5}$ Gy(w)/min/μA. The y-axis has logarithmic scale. The horizontal lines mark the upper limits, respectively 5 mSv/Gy(w) and 1 mSv/Gy(w) (from left to right). The vertical lines indicate 15 cm and 50 cm from the field edge, as defined by the criteria. Simulations were run for a sufficient duration until the errors became negligible.

In Fig. 6.14 (**upper**), the ambient dose equivalent in air relative to the maximum tumor dose is shown, with the proposed criteria also indicated. The criteria are met with a safety margin in both ranges (15-50 cm and farther from 50 cm). Across all distances, the neutron contribution to the dose is higher than the photon contribution. The total ambient dose has values from 2.899 to 0.234 mSv/Gy(w)/uA in the range 15-50 cm from the beam edge, representing a 12.5-fold reduction. Beyond 50 cm, the values are at least 4.9 times below the 1 mSv/Gy(w) limit, and this margin increases with distance. Thus, the proposed limits for ambient dose equivalent are comfortably satisfied, remaining below 2.899 mSv/Gy(w) within 15-50 cm, and below 0.234 mSv/Gy(w) beyond 50 cm.

Similar to the analysis of the ambient dose, we now consider the results for the effective dose. In the Figure 6.14 (**lower**), the effective dose is presented,

which also meets the criteria at all distances from the field edge. In this case the contribution of the photons is greater than that of the neutrons at any distance. This happens because when considering a deeper phantom we not only observe the leakage dose from the beam, but also the interactions that take place inside the phantom. The effective dose relative to the maximum tumor dose is lower than the ambient dose equivalent. Within the range of 15-50 cm from the beam edge, the values range from 0.957 to 0.032 mSv/Gy(w). Beyond 50 cm, the maximum value is 0.035 mSv/Gy(w), decreasing further with distance.

In conclusion, Figure 6.14 shows that our treatment accomplish the established criteria (Ref. [153]) for the ambient dose and the effective dose simulations.

6.5 Comparison between Conventional ABNS and Our BSA- Free Approach

A comprehensive and detailed study has been conducted on the BSA-free proposal, thoroughly analyzing both potential reactions under consideration. From this research, it has become evident that vanadium and scandium are promising candidates for BNCT in several important aspects.

However, one key challenge we encountered is that the yield of the vanadium reaction is too low for practical implementation using the current low-energy proton accelerators, which are currently limited to a maximum current of around 50 mA [41]. This limitation renders the vanadium reaction unsuitable for BNCT at present. In contrast, the scandium reaction has demonstrated highly favorable results across all parameters when considering an intensity of approximately 21 mA. Given the capabilities of today's proton accelerators, the ^{45}Sc(p,n) reaction stands out as the most viable option for our BSA-free proposal.

Although the vanadium reaction would require significantly higher proton currents, on the order of 600 mA, to meet the necessary criteria, the required proton energy in this case is much lower. This discrepancy suggests that, with advancements in accelerator technology, particularly in increasing current capacity while maintaining lower energy levels, the vanadium reaction could also become feasible in the near future. Therefore, we are optimistic that as accelerator technology progresses, the vanadium reaction may present a viable alternative for BNCT applications. Consequently, we will compare both candidate reactions: the vanadium BSA-free proposal (based on the ^{51}V(p,n) reaction at 1585 keV) and the scandium BSA-free proposal (based on the ^{45}Sc(p,n) reaction at 2918 keV).

In comparison with reactor-based BNCT facilities such as FiR-1 in Finland [160], [161], KUR-HWNIF (Kyoto University Research Reactor Institute or KURRI) in Japan [162]–[164], THOR in Taiwan [158], and Studsvik's R2-0 in Sweden [165], both BSA-free proposals generally present similar results for all FOMs.

For instance, FIR-1 reported an AD in the brain of 9 cm (with boron concentrations of 19 and 66.5 ppm for normal and tumor tissue, respectively) [161]. At

THOR [158], a phantom located 10 cm from the beam exit, with 18 ppm and 65 ppm for normal and tumor tissue, exhibited an AD of 8.9 cm and a maximum TR_2 of 6 cm. In the case of the scandium target proposal, comparing it with the most similar result in Table 6.6, we find that with a T/N ratio of 3.5 and a boron concentration of 18 ppm, our Scandium BSA-free proposal achieves an AD of 7.80 cm and an MTR of 6.09. For the vanadium target, with the same T/N ratio and concentration, Table 6.4 shows that our proposal yields an AD of 7.20 cm and an MTR of 6.03. Therefore, while FIR-1 and THOR beams perform slightly better for deeper tumors, our BSA-free proposals remain competitive.

For KUR-HWNIF, Tanaka et al. [163] reported ADs between 8 and 8.5 cm for boron concentrations of 10 to 25 ppm and a T/N ratio of 3.5. In comparison, our BSA-free proposals yield an AD of 8.70 cm for Scandium and 8.00 cm for Vanadium under the same conditions (T/N = 3.5 and 25 ppm). The maximum AD reported for KUR-HWNIF is 10 cm; however, this is only achieved at a T/N ratio of 4.5 with a boron concentration of 50 ppm. If we consider these values for our Scandium proposal, we obtain an AD of 9.9 cm, which aligns closely with KUR-HWNIF's results.

Finally, in Studsvik's R2-0 [165], the reported AD is 9.7 cm, and the MTR is 6.7 in a standard tissue phantom with 25 ppm and T/N = 3.5. Under these conditions, our Scandium BSA-free approach provides an AD = 8.70 cm and an MRT = 7.06 (see Table 6.6), while our Vanadium BSA-free approach shows an AD = 8.00 cm and an MRT = 6.97 (see Table 6.4). These comparisons reaffirm that our Scandium BSA-free approach at 2918 keV proton energy is better suited for shallower tumors at this proton energy. The Vanadium BSA-free approach at 1585 keV exhibits even lower penetrability. It's worth noting that BSA-free approaches at higher proton energies can enhance penetrability while fulfilling quality factors, as will be studied in the next section.

Moving forward to ABNS under design [47], there are projects in Russia, Obninsk [159] and Novosibirsk [33], USA [166], Rep. Korea [167], Argentina [46] or Japan (Osaka) [168], as noted in Table 1.1. The Novosibirsk facility currently presents the best AD value in brain phantoms at 9.7 cm with TR_2 of 5.38 cm (with 15 ppm boron and T/N = 3.5). Additionally, a design in Granada, Spain [43] reports an AD of 9.74 cm and a TR_2 of 7.85 cm for 18 ppm and T/N = 3.6. Although these ABNS under design could potentially reach slightly deeper tumors compared to our BSA-free approaches, the differences are not substantial.

To verify the suitability of the BSA-free approach, it is important to compare it with Cyclotron-based Epithermal Neutron Source (C-BENS), which was the first operational ABNS [21] and is the only one reporting clinical treatments [22]. The C-BENS generates an epithermal flux of $1.2 \cdot 10^9$ n/s·cm^2 at a proton current of 1 mA. The fast and thermal fluxes are $5{\cdot}10^6$ and $6{\cdot}10^7$ n/s·cm^2, respectively. The fast neutron and gamma doses per unit epithermal fluence are $5.8 \cdot 10^{-13}$ and $7.8 \cdot 10^{-14}$ Gy cm^2, respectively.

Following the nomenclature and setup of C-BENS, Figure 6.15 shows the RBE

dose distributions for tumors, normal tissue, and mucosal tissues in a cubic water phantom. C-BENS results are represented by dotted lines, while our BSA-free proposals are shown as solid lines (the left side for the Vanadium proposal and the right side for the Scandium one). These FOMs were utilized for medical trials [22]. For our BSA-free proposals, the same parameters have been considered : the weighting factors were 1 for gamma rays, 2.4 for fast neutrons, and 2.9 for thermal neutrons. The boron biological efficacy factors were 4.0 for tumors, 4.9 for healthy mucosa, and 1.34 for other healthy tissues. In this case, the RBE of the healthy mucosa is considered to be greater than that of the tumor. The boron concentration in normal tissue was set at 25 ppm, with a T/N Ratio of 3.5. Dose profiles were determined by normalizing the dose in healthy mucosa at a depth of 4 cm to 12 Gy (w). To avoid confusion, we refer to this as the RBE dose.

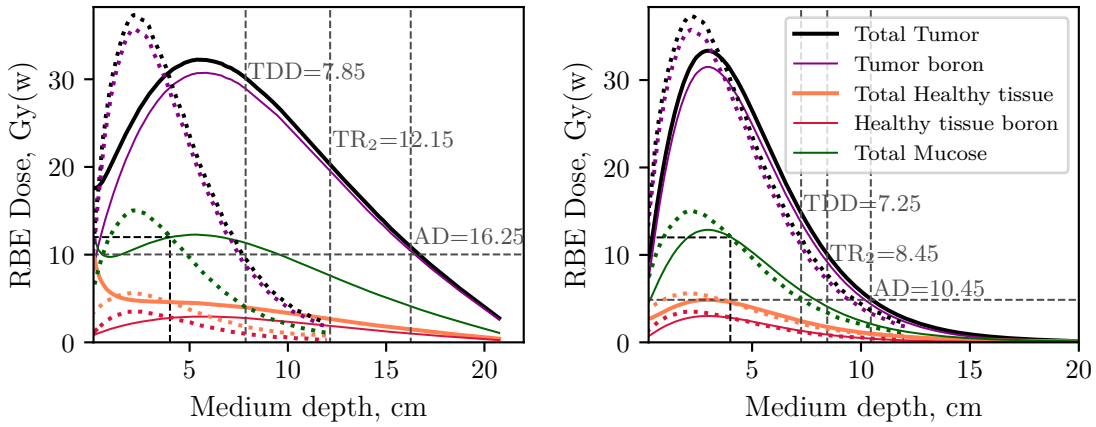

(a) BSA-free V proposal in solid lines.

(b) BSA-free Sc proposal in solid lines.

Figure 6.15. The depth dose profile in a cubic water phantom with a side of 20 cm for C-BENS [21] (dotted lines) and BSA-free proposals (solid lines). The AD, TR_2 and TDD Figures of Merit are shown for the BSA-free proposals, quantities in cm.The RBE dose is weighted dose but normalized by a mucosal dose of 12 Gy(w) at a depth of 4 cm. Boron concentrations of 25 ppm (normal tissue), and T/N=3.5. Simulations were run for a sufficient duration until the errors became negligible.

Comparing the results of C-BENS and the BSA-free Scandium proposal, shown in Figure 6.15b, the peak tumor dose occurs at 2.2 cm for the former and at 3.0 cm for the latter. There is a general depth offset, so our beam will be suitable for treating deeper tumors. Taking these parameters into consideration, we have an AD of 10.45 cm, TR_2 of 8.45 cm, TDD of 7.25 cm, and finally, an MTR of 6.86. In conclusion, the FOMs obtained for the BSA-free proposal at 2918 keV proton energy are very similar to the unique ABNS conducting clinical trials worldwide.

In contrast, the BSA-free vanadium proposal, shown in Figure 6.15a, exhibits significant changes in the depth dose profiles. This variation arises from the use of

a substantially larger cubic water phantom in this configuration. In this scenario, the AD increases to 16.25 cm, which is considerably larger than that of the C-BENS facility. The TDD for the vanadium proposal is 7.85 cm, while the TR_2 is 12.15 cm.

In conclusion, both BSA-free proposals are promising candidates for BNCT. However, when considering the current capabilities of accelerator technology, the ^{45}Sc(p,n) reaction emerges as the more viable option. The analysis indicates that this proposal not only achieves a suitable depth of dose distribution for effective treatment of deeper tumors but also maintains favorable FOMs comparable to existing clinical facilities. While the vanadium proposal shows impressive depth dose characteristics, it necessitates higher proton currents that may not be achievable with current accelerator technologies. As advancements in proton accelerator designs continue, particularly in increasing current capacities while maintaining lower energy levels, the feasibility of the vanadium reaction may improve.

6.6 Impact of Proton Energy Variations on Treatment Effectiveness

The BSA-free approach provides several advantages, one of the most significant being the ability to directly adjust proton energy to personalize treatment based on the specific tumor depth. By utilizing the most suitable reaction, ^{45}Sc(p,n), we can investigate how small variations in proton energy affect the FOMs, as long as the IAEA criteria are met.

As demonstrated in the calculation of the ^{45}Sc(p,n)^{45}Ti spectrum at 2918 keV, presented in Fig. 6.9 (**right**), we can use the NEBOAS code to calculate the angle-energy spectra of neutrons emitted from the ^{45}Sc(p,n)^{45}Ti reaction at various proton energies. These calculations will once again incorporate the experimental cross-section data shown in Fig. 2.3 and the stopping power data obtained from the SRIM code [120].

With the angle-energy spectra known, the first goal of this study is to determine which proton energies meet the IAEA criteria. To achieve this, we consider the optimal configuration: a 1 cm diameter Sc target positioned 1 cm from the ICRU 4-components cylindrical phantom. The results of the IAEA quality factors for this configuration at different proton energies are presented in Table 6.7. Proton energies between 2914 keV and 2924 keV satisfy all the IAEA criteria, while 2913 keV and 2925 keV fall short in some of the key quality factors, which are highlighted in red.

The epithermal flux (Φ_{epi}) increases with proton energy, peaking at 2925 keV. Correspondingly, the required proton accelerator intensity (I-ABNS) decreases as the epithermal flux rises, indicating that higher neutron fluxes can be achieved with lower proton intensities, thereby enhancing overall efficiency. Specifically, the I-ABNS ranges from 12.4 mA to 47.8 mA for the proton energies that meet all IAEA

Proton energy (keV)	Φ_{epi} ($\frac{\text{n}}{\text{cm}^2\mu\text{A}\cdot\text{s}}$)	I-ABNS (mA)	$\frac{\Phi_{\text{th}}}{\Phi_{\text{epi}}}$	$\frac{J}{\Phi_{\text{epi}}}$	$\frac{D_{\text{H}}}{\int \Phi_{\text{epi}}(t)\cdot\text{dt}}$ (Gy cm^2)	$\frac{D_{\gamma}}{\int \Phi_{\text{epi}}(t)\cdot\text{dt}}$ (Gy cm^2)
2913	$7.80 \cdot 10^{3}$	64.1	0.062	0.7838	$1.06 \cdot 10^{-30}$	$3.23 \cdot 10^{-14}$
2914	$1.05 \cdot 10^{4}$	47.8	0.043	0.7532	$3.09 \cdot 10^{-16}$	$2.31 \cdot 10^{-14}$
2915	$1.36 \cdot 10^{4}$	36.9	0.037	0.7678	$2.62 \cdot 10^{-14}$	$2.07 \cdot 10^{-14}$
2916	$1.65 \cdot 10^{4}$	30.3	0.034	0.7862	$5.87 \cdot 10^{-14}$	$1.95 \cdot 10^{-14}$
2917	$1.96 \cdot 10^{4}$	25.5	0.031	0.8119	$1.03 \cdot 10^{-13}$	$1.84 \cdot 10^{-14}$
2918	$2.29 \cdot 10^{4}$	21.8	0.031	0.8495	$1.71 \cdot 10^{-13}$	$1.83 \cdot 10^{-14}$
2919	$2.59 \cdot 10^{4}$	19.3	0.030	0.8944	$2.48 \cdot 10^{-13}$	$1.84 \cdot 10^{-14}$
2920	$2.88 \cdot 10^{4}$	17.3	0.029	0.9346	$3.31 \cdot 10^{-13}$	$1.85 \cdot 10^{-14}$
2921	$3.21 \cdot 10^{4}$	15.6	0.028	0.9762	$4.30 \cdot 10^{-13}$	$1.85 \cdot 10^{-14}$
2922	$3.51 \cdot 10^{4}$	14.2	0.028	1.0122	$5.15 \cdot 10^{-13}$	$1.88 \cdot 10^{-14}$
2923	$3.78 \cdot 10^{4}$	13.2	0.028	1.0426	$5.96 \cdot 10^{-13}$	$1.89 \cdot 10^{-14}$
2924	$4.05 \cdot 10^{4}$	12.4	0.028	1.0702	$6.73 \cdot 10^{-13}$	$1.91 \cdot 10^{-14}$
2925	$4.33 \cdot 10^{4}$	11.6	0.026	1.0976	$7.59 \cdot 10^{-13}$	$1.93 \cdot 10^{-14}$

Table 6.7. IAEA quality factors for relatively deep-seated tumor for ^{45}Sc(p,n) at different proton energies and BPA as boron carrier. The studied proton energies are in 2913-2925 keV range. I-ABNS is the required accelerator intensity. Sc target (1-μm height) of 1cm of diameter and ICRU 4-components tissue cylinder (5-cm radius and 1-cm thick) at 1cm of distance. Others quantities are: epithermal flux (Φ_{epi}), ratio thermal to epithermal flux ($\Phi_{\text{th}}/\Phi_{\text{epi}}$), ratio neutron current density to epithermal flux (J/Φ_{epi}), fast neutron dose per unit epithermal fluence (D_{H} / $\int \Phi_{\text{epi}}(t)\cdot \text{dt}$) and gamma dose per unit epithermal fluence (D_{γ} / $\int \Phi_{\text{epi}}(t)\cdot \text{dt}$). The quality factors that do not meet the required limits are highlighted in red.

requirements. These intensity levels are suitable for contemporary accelerators[41].

Another critical parameter is the thermal to epithermal flux ratio ($\Phi_{\text{th}}/\Phi_{\text{epi}}$), which measures the relative presence of thermal neutrons compared to epithermal neutrons. Proton energies of 2914 keV and above meet the IAEA criteria, with the ratio increasing as the energy decreases. However, at 2913 keV, this ratio exceeds the acceptable limit, rendering this proton energy unsuitable.

Additionally, the neutron current density to epithermal flux ratio (J/Φ_{epi}) remains relatively stable across the different proton energies, with minor increases as the proton energy rises. This indicates a more efficient delivery of neutron flux to the tumor site at higher energies. Lastly, the table shows the fast neutron dose per unit epithermal fluence ($D_{\text{H}}/\int \Phi_{\text{epi}}(t)\cdot \text{dt}$) and the gamma dose per unit epithermal fluence ($D_{\gamma}/\int \Phi_{\text{epi}}(t)\cdot \text{dt}$). The fast neutron dose increases with proton energy until 2925 keV, where it exceeds the acceptable limit, whereas the gamma dose shows minimal variation, remaining within acceptable bounds across the range of proton energies studied.

Having identified the proton energies that meet the IAEA requirements, we

can now analyze the Figures of Merit of the produced neutron spectra. Table 6.8 presents key FOMs for the ^{45}Sc(p,n)^{45}Ti reaction at validated proton energies, specifically ranging from 2914 keV to 2924 keV. These FOMs provide insights into how different proton energies affect treatment depth and dose distribution within tissue. These values were calculated assuming an ICRU 4-component tissue with a boron concentration of 18 ppm in normal tissue and a T/N ratio of 3.5.

As the proton energy decreases, all the FOMs exhibit an increase. This trend suggests that lower proton energies may facilitate deeper treatment penetration, potentially reaching tumors located further within the body. The MTR remains relatively stable across the proton energies studied, with only minor variations. The values indicate the overall range in which the treatment remains effective. Overall, the table suggests that proton energies in the range of 2914 keV to 2919 keV are optimal for deeper tumor penetration, while higher energies (2922 keV and above) may be less effective for deep-seated tumors due to their reduced penetration capacity.

Proton energy (keV)	AD (cm)	TR_2 (cm)	TDD (cm)	MTR
2914	8.50	6.80	5.70	6.40
2915	8.60	6.80	5.70	6.38
2916	8.50	6.70	5.60	6.37
2917	8.30	6.50	5.30	6.36
2918	8.10	6.20	4.90	6.35
2919	7.70	5.80	4.30	6.34
2920	7.40	5.30	3.60	6.32
2921	7.00	4.80	-	6.31
2922	6.70	4.40	-	6.30
2923	6.50	4.00	-	6.29
2924	6.30	3.60	-	6.29

Table 6.8. Relevant FOMs for the ^{45}Sc(p,n)^{45}Ti reaction at various proton energies, from 2914 to 2924 keV. Calculations assume an ICRU 4-component tissue with a boron concentration of 18 ppm in normal tissue and a tumor-to-normal tissue ratio of 3.5. Parameters include the Advantage Depth, the Therapeutic Range, the Triple Dose Depth, and the Maximum Therapeutic Ratio.

In conclusion, this section underscores the potential for personalizing cancer treatment by adjusting proton energy in the ^{45}Sc(p,n)^{45}Ti reaction. The findings indicate that proton energies between 2914 keV and 2924 keV meet IAEA criteria, allowing for tailored therapies that can be optimized to address individual patient needs.

Chapter 7

Conclusions & Outlook

The primary focus of this thesis has been the study of low-energy neutrons using Accelerator-based Neutron Sources (ABNS), with special emphasis to their application in Boron Neutron Capture Therapy (BNCT). This work has advanced the understanding of proton-induced reactions, particularly near their energy thresholds, and explored novel approaches to simplify epithermal neutron source systems, including the development of a Beam Shaping Assembly-Free (BSA-free) concept.

The introductory chapter established the promising potential of ABNS for BNCT, highlighting how neutron-producing reactions, such as ^{7}Li(p,n)^{7}Be or ^{9}Be(p, n)^{9}B, can achieve spectra suitable for therapy through moderation. A thorough literature review in Chapter 2 analyzed key proton-induced reactions, including ^{7}Li(p,n)^{7}Be, ^{9}Be(p,n)^{9}B, ^{45}Sc(p,n)^{45}Ti, and ^{51}V(p,n)^{51}Cr. These reactions were selected based on their conventional applications, favorable cross-sections, or appropriate neutron energy distributions. The review underscores the importance of accurate experimental data for these reactions.

The experimental component of this thesis, detailed in Chapters 3 to 5, was conducted at the MONNET facility in Geel, Belgium, and provided high-precision data for neutron spectra produced by ^{7}Li(p,n)^{7}Be and ^{51}V(p,n)^{51}Cr reactions. These experiments yielded detailed information on the energy and angular distributions of neutrons, particularly near the reaction threshold energy. The measurements were performed using the Time-Of-Flight (TOF) technique, which is described in Chapter 3. This chapter also offers comprehensive information on the experimental setup, including the data acquisition system, the detectors, the targets, and the accelerator, along with the calibration process.

With the aim of validating the experimental setup and data analysis, the well-known neutron field generated by the ^{7}Li(p,n)^{7}Be reaction near the threshold was measured first. In Chapter 4, two different angles (0 degrees and 30 degrees), various detectors, flight paths, and repetition rates were tested. Three different methods to convert time into energy binning were employed, ultimately selecting the best method. The results exhibited excellent agreement with experimental findings and theoretical predictions, confirming the good performance of the entire TOF system.

Following the satisfactory results obtained during the ^{7}Li(p,n)^{7}Be measurement, the characterization of the ^{51}V(p,n)^{51}Cr reaction near the reaction threshold has been conducted. The measurement, as detailed in Chapter 5, was performed at 1585 keV, just 20 keV above the reaction threshold. In this case, all the forward spectra have been covered, taking measurements from 0 to 90 degrees in 10 -degree steps. In the final result, the spectrum shows energy dependence and angular resonances due to the reaction itself have been identified. Additionally, the integrated measurement of the forward spectrum is also presented.

By characterizing neutron production near the threshold, the study identified the conditions under which these reactions can generate neutrons with optimal energy spectra for BNCT. This understanding was further expanded to propose a novel approach for designing ABNS, focusing on the use of reactions such as ^{45}Sc(p,n)^{45}Ti and ^{51}V(p,n)^{51}Cr. This Beam Shaping Assembly-Free (BSA-free) concept simplifies the neutron production system and demonstrates the feasibility of achieving therapeutic neutron beams with reduced system complexity.

In Chapter 6, we proposed a novel approach for delivering neutron beams in BNCT and thoroughly studied the IAEA (International Atomic Energy Agency) quality factors that ensure an adequate neutron beam for BNCT. All the quality factors are comfortably met. Additionally, these quality factors could be achieved using existing accelerators in the case of the Scandium BSA-free proposal. Besides the IAEA quality factors, we studied and calculated the conventional FOMs commonly used for BNCT facilities based on nuclear reactors or accelerators. The results of our BSA-free proposal are very close and similar to other facilities already under design. We also examined the possibility of varying penetration depths in the body through small changes in proton energy. As the BSA-free proposal is an innovative idea, it is currently being evaluated for patent by the relevant institutions.

In conclusion, this thesis has made significant contributions to the field of accelerator-based neutron sources by providing high-precision experimental data and proposing an innovative approach to neutron generation for BNCT. These findings not only advance the understanding of (p,n) reactions but also establish the groundwork for practical applications of ABNS in both medical and industrial contexts.

As for future perspectives, the most important task is the continuation of experimental studies for fully developing the BSA-free concept. Future work should include measurements of the ^{45}Sc(p,n)^{45}Ti reaction at viable energies for BNCT, as well as additional studies of the ^{51}V(p,n)^{51}Cr reaction using thinner targets to refine current results. In addition, a possible prototype of the Scandium BSA-free proposal could be manufactured and tested to check consistency with the simulations. These efforts will be essential to further validate and optimize the proposed approach, paving the way for its implementation in next-generation BNCT facilities.

Resumen extenso en español

En esta tesis doctoral se presentan mediciones de espectros de neutrones obtenidas mediante la técnica de tiempo de vuelo. Asimismo, se propone una alternativa viable para fuentes de neutrones basadas en aceleradores, orientadas a la terapia por captura de neutrones en boro. Esta propuesta simplifica considerablemente las instalaciones al eliminar la necesidad de moderación.

A continuación, se exponen las partes más relevantes del contenido de este manuscrito, incluyendo la motivación y los objetivos de la tesis, el estudio bibliográfico sobre reacciones (p,n) relevantes, los resultados experimentales obtenidos, la propuesta de una nueva fuente de neutrones para BNCT y las conclusiones que se derivan de este trabajo.

Introducción

Los neutrones, partículas subatómicas neutras, tienen múltiples aplicaciones en diversas áreas científicas y tecnológicas [2]. Según su energía, se clasifican en rápidos, epitérmicos, térmicos y fríos. En esta tesis se estudian específicamente los neutrones epitérmicos. Estas partículas pueden generarse en reactores nucleares, mediante fisión espontánea o a través de aceleradores de partículas (ABNS, por sus siglas en inglés) [6]. Entre estas opciones, las fuentes basadas en aceleradores, o ABNS, destacan por su versatilidad y control, lo que las hace especialmente útiles en campos como la biología, la electrónica y terapias innovadoras como la terapia por captura de neutrones en boro (BNCT, por sus siglas en inglés).

La BNCT, o terapia por captura de boro, es una radioterapia experimental que utiliza neutrones térmicos y boro-10 para destruir selectivamente células cancerígenas, protegiendo al mismo tiempo el tejido sano [12]. Ha demostrado ser particularmente efectiva en el tratamiento de tumores cerebrales y de cuello. Una de sus principales ventajas es que puede llevarse a cabo en una única sesión, lo que la diferencia de otras formas de radioterapia. Los avances recientes en tecnología de aceleradores han hecho posible el desarrollo de fuentes de neutrones compactas y seguras, especialmente diseñadas para su uso en entornos hospitalarios, marcando un paso significativo en la lucha contra cánceres agresivos [48].

El objetivo principal de esta tesis es explorar en profundidad los métodos de producción de neutrones de baja energía mediante reacciones nucleares (p,n) usando aceleradores. Además, se lleva a cabo una caracterización detallada de estos

neutrones producidos con dos reacciones específicas. Por último, se propone el diseño de una fuente de neutrones innovadora que prescinde del uso de un sistema de moderación convencional, optimizando así su aplicación en BNCT.

Estudio de reaciones (p,n)

Como se mencionó anteriormente, esta tesis se centra en el estudio de neutrones epitérmicos generados mediante aceleradores a través de reacciones (p,n). Por lo que el análisis de este tipo de reacciones constituye un paso fundamental. En primer lugar, se examina la cinemática asociada a estas reacciones para llevar a cabo un análisis energético riguroso.

Posteriormente, se realiza un estudio exhaustivo de cuatro reacciones de especial interés: ^{7}Li(p,n)^{7}Be y ^{9}Be(p,n)^{9}B, ampliamente documentadas en la literatura [50], y ^{51}V(p,n)^{51}Cr y ^{45}Sc(p,n)^{45}Ti, que destacan por su potencial en la producción directa de neutrones epitérmicos, eliminando la necesidad de moderación adicional.

Resultados experimentales

En la parte experimental de la tesis, se presentan las mediciones mediante la técnica de tiempo de vuelo (TOF) de dos reacciones nucleares en la instalación MONNET en el Joint Research Centre de Geel, Bélgica [116], [117]. La medición de los neutrones producidos por la reacción de litio, ^{7}Li(p,n)^{7}Be, se utiliza como referencia, mientras que el espectro de neutrones producidos por la reacción de vanadio, ^{51}V(p,n)^{51}Cr, se estudia con el objetivo de obtener datos novedosos.

Este manuscrito describe detalladamente el método empleado para producir y medir ambas reacciones cerca de sus umbrales de energía. Se incluye una descripción de la instalación experimental, los componentes del sistema (como los detectores y el sistema de adquisición de datos) y la calibración del acelerador, realizada para garantizar la precisión de las mediciones.

Se llevó a cabo una medición precisa de la reacción ^{7}Li(p,n)^{7}Be en proximidad a su umbral de energía. Los neutrones producidos fueron analizados en las direcciones de 0 grados y 30 grados, empleando detectores de litio situados a dos distancias distintas. Para convertir el tiempo de vuelo en energía y obtener el espectro de neutrones dependiente de la energía y el ángulo, se evaluaron tres métodos diferentes, seleccionándose finalmente el que ofreció los mejores resultados. Los datos obtenidos fueron consistentes con la literatura, validando así tanto la fiabilidad del método como la calidad de las mediciones realizadas.

Posteriormente, se realizó una medición detallada de la reacción ^{51}V(p,n)^{51}Cr cerca de su umbral de energía, cubriendo ángulos desde 0° hasta 90° en incrementos de 10°. Gracias a esta medición, se identificaron resonancias en el espectro energético para los distintos ángulos, coincidentes con resonancias encontradas en la literatura [64], [88]. Además, se obtuvo, por primera vez, el espectro delantero integrado de esta reacción. Para garantizar la coherencia y la robustez de

los resultados, se utilizó como referencia la caracterización previa de la reacción ^{7}Li(p,n)^{7}Be.

Propuesta de fuente de neutrones sin moderación para BNCT

Las fuentes de neutrones basadas en aceleradores son esenciales para la producción de neutrones epitérmicos, necesarios en BNCT. Aunque las reacciones ^{7}Li(p,n)^{7}Be y ^{9}Be(p,n)^{9}B son las más utilizadas, en esta tesis se exploran alternativas como ^{51}V(p,n)^{51}Cr y ^{45}Sc(p,n)^{45}Ti, que permiten generar neutrones epitérmicos de manera directa, sin necesidad de moderación.

La propuesta de esta tesis es una nueva técnica que utiliza estas reacciones innovadoras para mejorar la generación de neutrones. Este enfoque elimina la necesidad de un sistema convencional de blindaje de neutrones (BSA), lo que simplifica considerablemente el diseño del sistema de entrega de neutrones. Esta nueva propuesta se denomina "BSA-free assembly". La viabilidad de esta técnica se evalúa mediante simulaciones numéricas basadas en datos experimentales y referencias científicas sobre las reacciones de escandio y vanadio. Cabe destacar que, en el caso del vanadio, se utiliza como fuente el espectro medido dentro del marco de esta tesis doctoral, mientras que, en el caso del escandio, se usa un espectro obtenido con valores de la literatura.

Se presenta un estudio exhaustivo de las dos reacciones candidatas, evaluando si se cumplen los requisitos mínimos exigidos por la IAEA [48] ("International Atomic Energy Agency"), además de figuras de mérito que son muy útiles para evaluar la posible eficacia de los tratamientos. Se comparan los resultados de esta nueva propuesta con los de las instalaciones existentes, observando que los resultados son prometedores. La validación de esta nueva propuesta de fuente se ha realizado enteramente mediante simulaciones Monte Carlo, con el código MCNP.

Finalmente, se resalta la propuesta de "BSA-free" con escandio sobre la propuesta con vanadio, ya que la intensidad requerida para el acelerador será menor, lo que la convierte en una fuente viable a día de hoy con la tecnología en aceleradores disponible.

Además, se subraya el potencial para personalizar el tratamiento del cáncer mediante el ajuste de la energía del protón en la reacción ^{45}Sc(p,n)^{45}Ti. Los resultados muestran que diversas energías protónicas cumplen los criterios de la IAEA, lo que permite elaborar terapias adaptadas que pueden optimizarse para satisfacer las necesidades individuales de los pacientes.

Conclusiones

Para concluir, el principal objetivo de esta tesis fue estudiar la producción de neutrones de baja energía utilizando fuentes de neutrones basadas en aceleradores (ABNS), con un enfoque en su aplicación en la terapia por captura de neutrones en

boro (BNCT). Este trabajo ha permitido avanzar significativamente en la comprensión de las reacciones inducidas por protones, especialmente cerca de sus umbrales de energía, y ha propuesto un enfoque innovador para simplificar los sistemas de producción de neutrones, eliminando la necesidad de un sistema convencional de moderación, lo que se conoce como "BSA-free".

En el análisis del estado del arte, se ha resaltado el potencial de las ABNS para la BNCT, mediante el estudio de reacciones como ^{7}Li(p,n)^{7}Be, ^{9}Be(p,n)^{9}B, ^{45}Sc(p,n)^{45}Ti y ^{51}V(p,n)^{51}Cr. Estas reacciones fueron seleccionadas por sus aplicaciones convencionales y sus espectros de neutrones adecuados para BNCT. La revisión bibliográfica también subrayó la importancia de contar con datos experimentales precisos para optimizar su uso en terapias clínicas.

Los resultados experimentales obtenidos en el laboratorio MONNET (Geel, Bélgica) sobre los espectros de neutrones generados por las reacciones ^{7}Li(p,n)^{7}Be y ^{51}V(p,n)^{51}Cr, utilizando la técnica de Tiempo de Vuelo (TOF), permitieron caracterizar de manera precisa la distribución energética y angular de los neutrones. Los resultados obtenidos para la reacción ^{7}Li(p,n)^{7}Be fueron coherentes con datos previos, lo que valida el sistema experimental.

En el desarrollo del concepto BSA-free, se identificaron condiciones óptimas para generar neutrones adecuados para BNCT. Este enfoque simplifica significativamente el diseño de las fuentes de neutrones y cumple con los estándares internacionales establecidos por la IAEA. Los factores de mérito (FOMs) obtenidos son comparables a los de las instalaciones existentes, demostrando la viabilidad del concepto.

Las perspectivas futuras incluyen continuar con los estudios experimentales para optimizar el concepto BSA-free, realizando nuevos experimentos de la reacción ^{45}Sc(p,n)^{45}Ti y incorporando medidas adicionales de ^{51}V(p,n)^{51}Cr con blancos más delgados. También se sugiere desarrollar y probar un prototipo basado en el sistema BSA-free con escandio, lo que permitirá validar su implementación en instalaciones de BNCT de próxima generación.

En conclusión, esta tesis ha realizado contribuciones significativas al campo de las fuentes de neutrones basadas en aceleradores, proporcionando datos experimentales de alta precisión y proponiendo un enfoque innovador para la generación de neutrones que podría transformar las aplicaciones médicas e industriales de la terapia por captura de neutrones en boro.

Bibliography

[1] C. J. Christensen, A. Nielsen, A. Bahnsen, W. Brown, and B. Rustad, "Free-Neutron Beta-Decay Half-Life," *Physical Review D*, vol. 5, no. 7, p. 1628, 1972 (cit. on p. 1).

[2] K.-H. Beckurts and K. Wirtz, "Neutron Physics," in Springer Science & Business Media, 2013 (cit. on pp. 1, 10, 133).

[3] T. Mason, D. Abernathy, I. Anderson, *et al.*, "The Spallation Neutron Source in Oak Ridge: A powerful tool for materials research," *Physica B: Condensed Matter*, vol. 385, pp. 955–960, 2006 (cit. on p. 2).

[4] ESS, "European Spallation Source," Accessed: 2024-09-09, 2024 (cit. on p. 2).

[5] J. I. Watterson, "A review of accelerator based neutron sources and their applications," May 2000 (cit. on p. 2).

[6] International Atomic Energy Agency, *Compact Accelerator Based Neutron Sources*. International Atomic Energy Agency, 2021, ProQuest Ebook Central (cit. on pp. 2, 133).

[7] R. Hellborg, "Electrostatic Accelerators," in Springer, 2005 (cit. on p. 2).

[8] L. Voitsik, "Sealed ion accelerator tubes (survey)," Los Alamos National Laboratory, United States, Technical Report LA-TR–85-29, 1985, p. 20 (cit. on p. 2).

[9] J. Verbeke, K. Leung, and J. Vujic, "Development of a sealed-accelerator-tube neutron generator," *Applied Radiation and Isotopes*, vol. 53, no. 4, pp. 801–809, 2000 (cit. on p. 2).

[10] I. Anderson, C. Andreani, J. Carpenter, *et al.*, "Research opportunities with compact accelerator-driven neutron sources," *Physics Reports*, vol. 654, pp. 1–58, 2016, Research opportunities with compact accelerator-driven neutron sources (cit. on p. 3).

[11] Y. Kiyanagi, "Neutron applications developing at compact accelerator-driven neutron sources," *AAPPS Bulletin*, vol. 31, no. 1, p. 22, 2021 (cit. on p. 3).

[12] I. Porras, "Applications of Neutron Optics to Biomedicine: BNCT," in CRC Press, Nov. 2019, pp. 239–274 (cit. on pp. 4, 133).

[13] R. S. Medina, D. A. Téllez, E. Munévar, and J. A. Leyva, "Caracterización de la reacción nuclear de la terapia de captura neutrónica por boro (BNCT) por medio de Geant4," *Revista Investigaciones y Aplicaciones Nucleares*, vol. 2, pp. 43–54, Dec. 2018 (cit. on p. 4).

[14] G. L. Locher, "Biological effects and therapeutic possibilities of neutrons," *Am. J. Roentgen. Radium Ther.*, vol. 36, pp. 1–13, 1936 (cit. on p. 5).

[15] W. H. Sweet and M. Javid, "The Possible Use of Neutron-Capturing Isotopes such as Boron in the Treatment of Neoplasms," *Journal of neurosurgery*, vol. 9, pp. 200–209, 2 Mar. 1952 (cit. on p. 5).

[16] H. Hatanaka, K. Sano, and H. Yasukochi, "Clinical results of Boron Neutron Capture Therapy," in *Progress in Neutron Capture Therapy for Cancer*, Springer US, 1992, pp. 561–568 (cit. on p. 5).

[17] Y. Mishima, M. Ichihashi, S. Hatta, *et al.*, "First human clinical trial of melanoma neutron capture. diagnosis and therapy." *Strahlenther Onkol*, vol. 165, pp. 251–254, 1989 (cit. on p. 5).

[18] R. F. Barth, M. G. H. Vicente, O. K. Harling, *et al.*, "Current status of Boron Neutron Capture Therapy of high grade gliomas and recurrent head and neck cancer," *Radiation Oncology*, vol. 7, pp. 1–21, 1 Aug. 2012 (cit. on p. 5).

[19] R. F. Barth, Z. Zhang, and T. Liu, "A realistic appraisal of Boron Neutron Capture Therapy as a cancer treatment modality," *Cancer Communications*, vol. 38, no. 1, p. 36, 2018 (cit. on p. 5).

[20] F. Azaiez, A. Bracco, J. Dobeš, *et al.*, *Nuclear Physics for Medicine*. European Science Foundation, 2014, European Science Foundation. Nuclear Physics European Collaboration Committee (NUPECC) (cit. on p. 5).

[21] H. Tanaka, Y. Sakurai, M. Suzuki, *et al.*, "Experimental verification of beam characteristics for Cyclotron-Based Epithermal Neutron Source (C-BENS)," *Applied Radiation and Isotopes*, vol. 69, no. 12, pp. 1642–1645, 2011, Special Issue: 14th International Conference on Neutron Capture Therapy (cit. on pp. 6, 126, 127).

[22] K. Hirose, A. Konno, J. Hiratsuka, *et al.*, "Boron Neutron Capture Therapy using cyclotron-based epithermal neutron source and borofalan (^{10}B) for recurrent or locally advanced head and neck cancer (JHN002): An open-label phase II trial," *Radiotherapy and Oncology*, vol. 155, pp. 182–187, 2021 (cit. on pp. 6, 126, 127).

[23] NCT NEWS, "The accelerator-driven BNCT facility at Southern Tohoku General Hospital: The world's first BNCT hospital," Japanese Society of Neutron Capture Therapy Issue 1, May 2016 (cit. on p. 6).

[24] H. Kumada, T. Kurihara, M. Yoshioka, *et al.*, "Development of beryllium-based neutron target system with three-layer structure for accelerator-based neutron source for Boron Neutron Capture Therapy," *Applied Radiation and Isotopes*, vol. 106, pp. 78–83, 2015, The 16th International Congress on Neutron Capture Therapy (ICNCT-16). Representative person of the Organizing Committee: Dr Hanna Koivunoro (Secretary general of the ICNCT-16) (cit. on p. 6).

[25] H. Kumada, K. Takada, F. Naito, *et al.*, "Beam performance of the iBNCT as a compact linac-based BNCT neutron source developed by University of Tsukuba," in *AIP Conference Proceedings*, AIP Publishing, vol. 2160, 2019 (cit. on p. 6).

[26] S. Halfon, A. Arenshtam, D. Kijel, *et al.*, "Demonstration of a high-intensity neutron source based on a liquid-lithium target for Accelerator based Boron Neutron Capture Therapy," *Applied Radiation and Isotopes*, vol. 106, pp. 57–62, 2015, The 16th International Congress on Neutron Capture Therapy (ICNCT-16). Representative person of the Organizing Committee: Dr Hanna Koivunoro (Secretary general of the ICNCT-16) (cit. on p. 6).

[27] E. Pisent, E. Fagotti, and P. Colautti, "MUNES project: An intense Multidisciplinar Neutron Source for BNCT based on a high intensity RFQ accelerator," in *Proceedings of the 16th International Congress on Neutron Capture Therapy*, 2014, p. 66 (cit. on p. 6).

[28] J. Chen, J. Tong, Z. Hu, *et al.*, "Evaluation of neutron beam characteristics for D-BNCT01 facility," *Nuclear Science and Technology*, vol. 33, p. 12, 2022 (cit. on p. 6).

[29] S. Nakamura, S. Imamichi, K. Masumoto, *et al.*, "Evaluation of radioactivity in the bodies of mice induced by neutron exposure from an epi-thermal neutron source of an accelerator-based Boron Neutron Capture Therapy system," *Proceedings of the Japan Academy, Series B*, vol. 93, no. 10, pp. 821–831, 2017 (cit. on p. 6).

[30] S. Nakamura, H. Igaki, M. Ito, H. Okamoto, S. Nishioka, K. Iijima, *et al.*, "Characterization of the relationship between neutron production and thermal load on a target material in an accelerator-based Boron Neutron Capture Therapy system employing a solid-state Li target," *PLoS ONE*, vol. 14, no. 11, e0225587, 2019 (cit. on p. 6).

[31] S. Nakamura, H. Igaki, H. Okamoto, *et al.*, "Dependence of neutrons generated by $^{7}\mathrm{Li}(p,n)$ reaction on Li thickness under free-air condition in accelerator-based Boron Neutron Capture Therapy system employing solid-state Li target," *Physica Medica*, vol. 58, pp. 121–130, 2019 (cit. on p. 6).

[32] S. Nakamura, H. Igaki, M. Ito, *et al.*, "Neutron flux evaluation model provided in the accelerator-based Boron Neutron Capture Therapy system employing a solid-state lithium target," *Scientific Reports*, vol. 11, p. 8090, 2021 (cit. on p. 6).

[33] L. Zaidi, M. Belgaid, S. Taskaev, and R. Khelifi, "Beam shaping assembly design of $^{7}\mathrm{Li}(p,n)^{7}\mathrm{Be}$ neutron source for Boron Neutron Capture Therapy of deep-seated tumor," *Applied Radiation and Isotopes*, vol. 139, pp. 316–324, 2018 (cit. on pp. 6, 126).

[34] M. Bikchurina, T. Bykov, D. Kasatov, *et al.*, "The Measurement of the Neutron Yield of the $^{7}\mathrm{Li}(p,n)^{7}\mathrm{Be}$ Reaction in Lithium Targets," *Biology*, vol. 10, no. 9, 2021 (cit. on p. 7).

[35] Neuboron, "BNCT Information," Accessed: 2024-09-09 (cit. on p. 7).

[36] Z. Zhang, Y. Chong, Y. Liu, *et al.*, "A review of planned, ongoing clinical studies and recent development of bnct in mainland of china," *Cancers*, vol. 15, no. 16, 2023 (cit. on p. 7).

[37] S. Rossi, "BNCT@CNAO: Is CNAO the right place to experiment with BNCT?" *Health and Technology*, vol. 14, no. 5, pp. 1051–1057, 2024 (cit. on p. 7).

[38] L. Licitra, S. Cavalieri, C. Tinelli, J. Franzetti, and E. Orlandi, "Developing a trial design to establish bnct as clinical application: Insight for the national italian center for oncological hadrontherapy (CNAO)," *Health and Technology*, vol. 14, no. 5, pp. 1037–1041, 2024 (cit. on p. 7).

[39] K. Sato, A. Uritani, K. Watanabe, *et al.*, "Improved Design of the Exit of a Beam Shaping Assembly for an Accelerator-driven BNCT System in Nagoya University," in *Proceedings of the International Conference on Neutron Optics (NOP2017)*. JPS Conference Proceedings, 2018, vol. 22, ch. Design of beam shaping assembly for an accelerator-driven BNCT system in Nagoya University (cit. on p. 7).

[40] K. Watanabe, S. Yoshihashi, A. Ishikawa, *et al.*, "First experimental verification of the neutron field of Nagoya University Accelerator-driven neutron source for Boron Neutron Capture Therapy," *Applied Radiation and Isotopes*, vol. 168, p. 109 553, 2021 (cit. on p. 7).

[41] Neutron Therapeutics, "Neutron Therapeutics," Accessed: September 9, 2022, 2022 (cit. on pp. 7, 111, 119, 125, 129).

[42] BUSINESS WIRE, "Neutron Therapeutics and University Hospital of Brussels Announce Their Collaboration to Offer Cancer Patients a Revolutionary New Treatment Method at Institut Jules Bordet," Accessed: 2024-09-09, 2022 (cit. on p. 7).

[43] P. Torres-Sánchez, I. Porras, N. Ramos-Chernenko, F. Arias de Saavedra, and J. Praena, "Optimized beam shaping assembly for a 2.1-MeV proton-accelerator-based neutron source for Boron Neutron Capture Therapy," *Scientific reports*, vol. 11, no. 1, p. 7576, 2021 (cit. on pp. 7, 106, 120, 126).

[44] I. Porras, J. Praena, F. Arias de Saavedra, *et al.*, "BNCT research activities at the Granada group and the project NeMeSis: Neutrons for medicine and sciences, towards an accelerator-based facility for new BNCT therapies, medical isotope production and other scientific neutron applications," *Applied Radiation and Isotopes*, vol. 165, p. 109 247, 2020 (cit. on p. 7).

[45] D. Cartelli, M. Capoulat, M. Baldo, *et al.*, "Status of low-energy accelerator-based BNCT worldwide and in Argentina," *Applied Radiation and Isotopes*, vol. 166, p. 109 315, 2020 (cit. on p. 7).

[46] D. Minsky and A. Kreiner, "Beam shaping assembly optimization for ^{7}Li(p, n) ^{7}Be accelerator based BNCT," *Applied Radiation and Isotopes*, vol. 88, pp. 233–237, 2014, 15th International Congress on Neutron Capture Therapy Impact of a new radiotherapy against cancer (cit. on pp. 7, 126).

[47] Y. Kiyanagi, Y. Sakurai, H. Kumada, and H. Tanaka, "Status of accelerator-based BNCT projects worldwide," in *AIP Conference Proceedings*, AIP Publishing, vol. 2160, 2019 (cit. on pp. 7, 126).

[48] IAEA, *Advances in Boron Neutron Capture Therapy* (Non-serial Publications). Vienna: International Atomic Energy Agency, 2023 (cit. on pp. 7, 8, 13, 14, 102–107, 110, 111, 119, 133, 135).

[49] D. L. Chichester, "Production and applications of neutrons using particle accelerators," in *Industrial Accelerators and Their Applications*, World Scientific, 2012, pp. 243–305 (cit. on p. 9).

[50] H. Kumada, T. Sakae, and H. Sakurai, "Current development status of accelerator-based neutron source for Boron Neutron Capture Therapy," *EPJ Techn. Instrum.*, vol. 10, p. 18, 2023 (cit. on pp. 9, 134).

[51] J. B. Marion and F. C. Young, "Nuclear reaction analysis. graphs and tables.," Jan. 1968 (cit. on p. 10).

[52] A. Koning, D. Rochman, J.-C. Sublet, N. Dzysiuk, M. Fleming, and S. van der Marck, "TENDL: Complete Nuclear Data Library for Innovative Nuclear Science and Technology," *Nuclear Data Sheets*, vol. 155, pp. 1–55, 2019, Special Issue on Nuclear Reaction Data (cit. on pp. 12, 17, 21, 22, 74, 77, 78, 100).

[53] H. Beer and F. Käppeler, "Neutron capture cross sections on ^{138}Ba, ^{140,142}Ce, ^{175,176}Lu, and ^{181}Ta at 30 keV: Prerequisite for investigation of the ^{176}Lu cosmic clock," *Phys. Rev. C*, vol. 21, pp. 534–544, 2 Feb. 1980 (cit. on p. 13).

[54] W. Ratynski and F. Käppeler, "Neutron capture cross section of ^{197}Au: A standard for stellar nucleosynthesis," *Phys. Rev. C*, vol. 37, pp. 595–604, 2 Feb. 1988 (cit. on pp. 13, 47–49).

[55] G. Feinberg, M. Friedman, A. Krása, *et al.*, "Quasi-stellar neutrons from the ^{7}Li$(p,n)^{7}$Be reaction with an energy-broadened proton beam," *Phys. Rev. C*, vol. 85, p. 055 810, 5 May 2012 (cit. on pp. 13, 32, 48–50, 52, 59–67).

[56] C. Lederer, F. Käppeler, M. Mosconi, *et al.*, "Definition of a standard neutron field with the ^{7}Li$(p,n)^{7}$Be reaction," *Phys. Rev. C*, vol. 85, p. 055 809, 5 May 2012 (cit. on pp. 13, 48–50, 52, 59, 61–66, 89, 90).

[57] J. Praena, A. Verdera, J. G. López, and G. Martín-Hernández, "Production and measurement of a stellar neutron spectrum at 30 keV," *The European Physical Journal A*, vol. 60, no. 10, p. 199, 2024 (cit. on p. 13).

[58] B. W. Blackburn, "High-power target development for accelerator-based neutron capture therapy," Ph.D. dissertation, Massachusetts Institute of Technology, 2002 (cit. on p. 13).

[59] H. Horiike, I. Murata, T. Iida, *et al.*, "Liquid Li based neutron source for BNCT and science application," *Applied Radiation and Isotopes*, vol. 106, pp. 92–94, 2015, The 16th International Congress on Neutron Capture Therapy (ICNCT-16). Representative person of the Organizing Committee: Dr Hanna Koivunoro (Secretary general of the ICNCT-16) (cit. on p. 13).

[60] W. B. Howard, S. M. Grimes, T. N. Massey, *et al.*, "Measurement of the Thick-Target ^{9}Be(p,n) Neutron Energy Spectra," *Nuclear Science and Engineering*, vol. 138, no. 2, pp. 145–160, 2001 (cit. on p. 14).

[61] R. M. Brugger, T. W. Bonner, and J. B. Marion, "Study of the nuclear reactions Sc$^{45}(p,n)$Ti^{45}, Cu$^{63}(p,n)$Zn^{63}, Cu$^{65}(p,n)$Zn^{65}, and Zn(p,n)Ga," *Phys. Rev.*, vol. 100, pp. 84–90, 1 Oct. 1955 (cit. on pp. 15–17).

[62] D. Rogers, "The ^{45}Sc(p,n) reaction as a source of monoenergetic 10–50 keV neutrons," *Nuclear Instruments and Methods*, vol. 142, no. 3, pp. 475–478, 1977 (cit. on pp. 15–17).

[63] H. Schölermann and B. Siebert, "Calibration of a Van de Graaf accelerator and determination of the threshold of the reaction ^{45}Sc$(p,n)^{45}$Ti using a covariance analysis," *Nuclear Instruments and Methods in Physics Research Section A: Accelerators, Spectrometers, Detectors and Associated Equipment*, vol. 236, no. 2, pp. 225–230, 1985 (cit. on p. 15).

[64] V. Lamirand, "Determination of cross sections for the production of low-energy monoenergetic neutron fields," Ph.D. dissertation, Université de Grenoble, 2011 (cit. on pp. 16, 17, 19, 23, 87, 134).

[65] J. Hunt, M. Cosack, and H. Lesiecki, "Calibration of neutron survey meters over the energy range from 1 to 30 keV with accelerator produced monoenergetic neutrons," Commission of the European Communities (CEC), EUR–9762(v1), 1985, pp. 607–616 (cit. on p. 16).

[66] Y. Tanimura, J. Saegusa, Y. Shikaze, M. Tsutsumi, S. Shimizu, and M. Yoshizawa, "Construction of monoenergetic neutron calibration fields using ^{45}Sc$(p,n)^{45}$Ti reaction at JAEA," *Radiation protection dosimetry*, vol. 126, no. 1-4, pp. 8–12, 2007 (cit. on pp. 16, 17).

[67] *Reference neutron radiations – part 1: Characteristics and methods of production*, ISO 8529-1, International Organization for Standardization, 2001, pp. 8529–8531 (cit. on p. 16).

[68] V. Lamirand, V. Gressier, A. Martin, and D. Thomas, "Comparison of nuclear reactions for the production of monoenergetic neutron fields with energies below 100keV," *Radiation Measurements*, vol. 45, no. 10, pp. 1112–1115, 2010, PROCEEDINGS OF THE 11TH SYMPOSIUM ON NEUTRON AND ION DOSIMETRY (cit. on p. 16).

[69] V. Lamirand, D. Thomas, V. Gressier, S. Sorieul, and E. Liatard, "Study of scandium targets for production of monoenergetic neutron fields with energies below 100kev," *Radiation Measurements*, vol. 45, no. 10, pp. 1116–1119, 2010, PROCEEDINGS OF THE 11TH SYMPOSIUM ON NEUTRON AND ION DOSIMETRY (cit. on p. 16).

[70] N. Otuka, E. Dupont, V. Semkova, *et al.*, "Towards a More Complete and Accurate Experimental Nuclear Reaction Data Library (EXFOR): International Collaboration Between Nuclear Reaction Data Centres (NRDC)," *Nuclear Data Sheets*, vol. 120, pp. 272–276, 2014 (cit. on pp. 17, 21, 22, 49).

[71] G. F. Dell, W. D. Ploughe, and H. J. Hausman, "Total Reaction Cross Sections in the Mass Range 45 to 65," *Nuclear Physics*, vol. 64, p. 513, 1965 (cit. on pp. 17, 21, 22).

[72] A. J. Howard, H. B. Jensen, M. Rios, W. A. Fowler, and B. A. Zimmerman, "Measurement and Theoretical Analysis of Some Reaction Rates of Interest in Silicon Burning," *Astrophysical Journal*, vol. 188, pp. 131–140, Feb. 1974 (cit. on p. 17).

[73] K. V. K. Iyengar, S. K. Gupta, K. K. Sekharan, M. K. Mehta, and A. S. Divatia, "Fluctuations in the Integrated Cross Section of the Reaction ^{45}Sc$(p,n)^{45}$Ti," *Nuclear Physics, Section A*, vol. 96, p. 521, 1967 (cit. on p. 17).

[74] L. W. Mitchell, M. R. Anderson, S. R. Kennett, and D. G. Sargood, "Cross Sections and Thermonuclear Reaction Rates for ^{42}Ca(p,γ)^{43}Sc, ^{44}Ca(p,γ)^{45}Sc, ^{44}Ca$(p,n)^{44}$Sc and ^{45}Sc$(p,n)^{45}$Ti," *Nuclear Physics, Section A*, vol. 380, p. 318, 1982 (cit. on pp. 17, 22).

[75] M. Cosack, H. Lesiecki, and J. Hunt, "Monoenergetic neutrons of energies from 0.5 keV to 40 keV via the reaction ^{45}Sc$(p,n)^{45}$Ti," EUR–9762(v1), 1985, pp. 597–606 (cit. on pp. 17, 18).

[76] V. E. Lewis, "Comparison of 24.5 kev neutron fluence measurements, 1993-1996." Teddington, NPL Report CIRM 16, Dec. 1998 (cit. on p. 18).

[77] T. Matsumoto, H. Harano, T. Shimoyama, K. Kudo, and A. Uritani, "Characterisation of kilo electron volt neutron fluence standard with the ^{45}Sc(p,n) ^{45}Ti reaction at NMIJ," *Radiation protection dosimetry*, vol. 126, no. 1-4, pp. 155–158, 2007 (cit. on p. 18).

[78] T. Matsumoto, H. Harano, J. Nishiyama, A. Uritani, and K. Kudo, "Novel generation method of 24-keV monoenergetic neutrons using accelerators," in *AIP Conference Proceedings*, AIP Publishing, vol. 1099, 2009, pp. 924–927 (cit. on p. 18).

[79] M. Baba, M. Takada, T. Iwasaki, *et al.*, "Development of monoenergetic neutron calibration fields between 8 keV and 15 MeV," *Nuclear Instruments and Methods in Physics Research Section A: Accelerators, Spectrometers, Detectors and Associated Equipment*, vol. 376, no. 1, pp. 115–123, 1996 (cit. on p. 19).

[80] W. D. Baker, J. S. Howell, C. Goodman, and W. M. Preston, "The (p,n) reaction on scandium and vanadium: Energy levels of Ti^{46} and Cr^{52}," *Phys. Rev.*, vol. 81, pp. 48–50, 1 Jan. 1951 (cit. on pp. 19, 24).

[81] K. Iyengar, E. Wong, and G. Neilson, "Energy levels of ^{45}Ti excited in the ^{45}Sc$(p,n)^{45}$Ti reaction," *Nuclear Physics A*, vol. 155, no. 2, pp. 582–596, 1970 (cit. on p. 19).

[82] R. Smith and H. Richards, "Proton-neutron thresholds in V-51 and Mn-55," in *Physical Review*, American Physical Soc One Physics Ellipse, College PK, MD 20740-3844 USA, vol. 74, 1948, pp. 1257–1257 (cit. on p. 19).

[83] H. T. Richards, R. V. Smith, and C. P. Browne, "Proton-Neutron Reactions and Thresholds," *Phys. Rev.*, vol. 80, pp. 524–530, 4 Nov. 1950 (cit. on p. 19).

[84] J. Gibbons, R. Macklin, and H. Schmitt, "^{51}V$(p,n)^{51}$Cr Reaction as a 5-to 120-keV Neutron Source," *Physical Review*, vol. 100, no. 1, p. 167, 1955 (cit. on pp. 19, 21, 22).

[85] C. R. Gossett and J. W. Butler, "Neutron Thresholds in the ^{51}V$(p,n)^{51}$Cr, ^{55}Mn$(p,n)^{55}$Fe, ^{70}Zn$(p,n)^{70}$Ga, and ^{75}As$(p,n)^{75}$Se Reactions," *Phys. Rev.*, vol. 113, pp. 246–251, 1 Jan. 1959 (cit. on p. 19).

[86] C. Johnson, C. Trail, and A. Galonsky, "Thresholds for (p,n) reactions on 26 intermediate - weight nuclei," *Physical Review*, vol. 136, no. 6, pp. 1719–1729, Dec. 1964 (cit. on pp. 19, 21, 22).

[87] D. W. Kneff, H. W. Lefevre, and G. U. Din, "Reaction Q Values from Near-Threshold Neutron Spectra," *Phys. Rev. Lett.*, vol. 25, pp. 1210–1213, 17 Oct. 1970 (cit. on pp. 19, 23, 89).

[88] H. Scholermann and R. Bottger, "Q-values for (p, n) reactions on ^{65}Cu and ^{51}V," *Nuclear Physics A*, vol. 501, no. 1, pp. 86–94, 1989 (cit. on pp. 19, 23, 24, 87, 89, 134).

[89] R. Ballini, Y. Cassagnou, C. Levi, and L. Papineau, "Spectrometry of time-of-flight of neutrons from the (p, n) reaction on vanadium," *Compt. rend.*, vol. 251, 1960 (cit. on p. 20).

[90] G. Deconninck and J. Royen, "La reaction $^{51}V(p, n)^{51}Cr$ comme source de neutrons monoenergetiques," *Nuclear Instruments and Methods*, vol. 75, no. 2, pp. 266–270, 1969 (cit. on pp. 20–22).

[91] A. O. Hanson, R. F. Taschek, and J. Williams, "Monoergic Neutrons from Charged Particle Reactions," *Reviews of Modern Physics*, vol. 21, no. 4, p. 635, 1949 (cit. on p. 20).

[92] K. Harris, H. Grench, R. Johnson, and F. Vaughn, "The $^{51}V(p, n)^{51}Cr$ reaction as a neutron source of known intensity," *Nuclear Instruments and Methods*, vol. 33, no. 2, pp. 257–260, 1965 (cit. on pp. 20–22).

[93] K. Harris, H. Grench, R. Johnson, F. Vaughn, J. Ferziger, and R. Sher, "The au^{197}(n,γ)au^{197} cross section from 13 keV to 683 keV," *Nuclear Physics*, vol. 69, no. 1, pp. 37–48, 1965 (cit. on p. 21).

[94] Y.-T. Li, W.-P. Lin, B.-S. Gao, *et al.*, "Development of a low-background neutron detector array," *Nuclear Science and Techniques*, vol. 33, no. 4, p. 41, 2022 (cit. on p. 21).

[95] J. Marion, R. Levesque, C. Ludemann, and R. Detenbeck, "A Versatile, High Efficiency 4π Neutron Detector," *Nuclear Instruments and Methods*, vol. 8, no. 3, pp. 297–303, 1960 (cit. on p. 21).

[96] H. Schmitt and C. Cook, "Absolute neutron absorption cross sections for Sb-Be photoneutrons," *Nuclear Physics*, vol. 20, pp. 202–219, 1960 (cit. on p. 21).

[97] K. Alexandre, J. Camplan, M. Ligonniere, *et al.*, "Sidonie, the new electromagnetic isotope separator at Orsay: Part II: Performances," *Nuclear Instruments and Methods*, vol. 84, no. 1, pp. 45–54, 1970 (cit. on p. 21).

[98] J. Camplan, R. Meunier, and J. Sarrouy, "Sidonie, the new electromagnetic isotope separator at Orsay: Part I: Design and construction," *Nuclear Instruments and Methods*, vol. 84, no. 1, pp. 37–44, 1970 (cit. on p. 21).

[99] C. Johnson, A. Galonsky, and J. Ulrich, "Proton Strength Functions from (p, n) Cross Sections," *Physical Review*, vol. 109, no. 4, pp. 1243–1254, Feb. 1958 (cit. on pp. 21, 22).

[100] R. D. Albert, "(p, n) Cross Section and Proton Optical-Model Parameters in the 4- to 5.5-MeV Energy Region," *Phys. Rev.*, vol. 115, pp. 925–927, 4 Aug. 1959 (cit. on pp. 21, 22).

[101] J. Wing and J. R. Huizenga, "(p, n) Cross Sections of ^{51}V, ^{52}Cr, ^{63}Cu, ^{65}Cu,^{107}Ag, ^{109}Ag, ^{11}Cd, ^{114}Cd, and ^{139}La from 5 to 10.5 MeV," *Phys. Rev.*, vol. 128, pp. 280–290, 1 Oct. 1962 (cit. on pp. 21, 22).

[102] S. Hontzeas and L. Yaffe, "Interaction of Vanadium with protons of energies up to 84 MeV," *Canadian Journal of Chemistry*, vol. 41, no. 9, pp. 2194–2209, 1963 (cit. on pp. 21, 22).

[103] J. J. Egan, K. K. Sekharan, G. C. Dutt, J. E. Wiest, and F. Gabbard, "2.335-MeV Isobaric Analog Resonance in ^{51}V+p and the excited states of ^{51}Cr Studied via the (p, n) and (p,nγ) Reactions," *Phys. Rev. C*, vol. 5, pp. 1562–1572, 5 May 1972 (cit. on pp. 21, 22).

[104] K. Sekharan and M. K. Mehta, "Absolute Reaction Cross Section of the Reaction ^{51}V$(p, n)^{51}$Cr Over the Isobaric Analog Resonance near 2.340 MeV," *Physical Review C*, vol. 6, no. 6, p. 2304, 1972 (cit. on pp. 21, 22).

[105] M. Mehta, S. Kailas, and K. Sekharan, "Total (p, n) reaction cross section study on ^{51}V over the incident energy range 1.56 to 5.53 MeV," *Pramana*, vol. 9, pp. 419–434, 1977 (cit. on pp. 21, 22).

[106] R. Michel and G. Brinkmann, "On the depth-dependent production of radionuclides ($44 \leq a \leq 59$) by solar protons in extraterrestrial matter," *Journal of Radioanalytical Chemistry*, vol. 59, pp. 467–510, 1980 (cit. on p. 21).

[107] J. Zyskind, C. Barnes, J. Davidson, W. A. Fowler, R. Marrs, and M. Shapiro, "Competition effects in proton-induced reactions on ^{51}V," *Nuclear Physics A*, vol. 343, pp. 295–314, 1980 (cit. on pp. 21, 22, 24).

[108] S. Kailas, S. Gupta, S. Kerekatte, and C. Fernandes, "^{51}V$(p, n)^{51}$Cr reaction from E$_p$ 1.9 to 4.5 MeV," *Pramana*, vol. 24, pp. 629–635, 1985 (cit. on pp. 21, 22).

[109] M. Musthafa, M. Kumar Sharma, B. Singh, and R. Prasad, "Measurement and analysis of cross sections for (p, n) reactions in ^{51}V and ^{113}In," *Applied Radiation and Isotopes*, vol. 62, no. 3, pp. 419–428, 2005 (cit. on pp. 21, 22).

[110] A. Solieman, M. Al-Abyad, F. Ditroi, and Z. Saleh, "Experimental and theoretical study for the production of ^{51}Cr using p, d, ^{3}He and ^{4}He projectiles on V, Ti and Cr targets," *Nuclear Instruments and Methods in Physics Research Section B: Beam Interactions with Materials and Atoms*, vol. 366, pp. 19–27, 2016 (cit. on pp. 21, 22).

[111] Z. Wenrong, L. Hanlin, and Y. Weixiang, "Excitation function of V-51(p, n)Cr-51 up to 22 MeV," *Chin J Nucl Phys*, vol. 16, p. 67, 1994 (cit. on p. 22).

[112] J. Gibbons and R. Macklin, "$^{51}V(p,n)^{51}Cr$ cross section from threshold to 2.25 MeV," *Nuclear Instruments and Methods*, vol. 37, pp. 330–331, 1965 (cit. on pp. 21, 22).

[113] P. Stelson, W. Preston, and C. Goodman, "The $^{51}V(p,n)^{51}Cr$ Neutron Spectrum," *Physical Review*, vol. 80, no. 2, p. 287, 1950 (cit. on p. 23).

[114] K. Iyengar, S. Gupta, and B. Lal, "The study of the $^{51}V(p,n)^{51}Cr$ reaction," *Nuclear Physics A*, vol. 96, no. 2, pp. 417–439, 1967 (cit. on p. 24).

[115] A. H2020, "ARIEL Project," Accessed: 2024-06-06, 2020 (cit. on p. 25).

[116] C. L. Fontana, B. Cédric, W. Geerts, M. M. Martinez, M. Vidali, and S. Oberstedt, "JRC MONNET - the intense fast-neutron source for fundamental and application-driven research," in *EPJ Web of Conferences*, EDP Sciences, vol. 284, 2023, p. 06 002 (cit. on pp. 28, 134).

[117] A. Seibert, L. A. de las Heras, K. Boboridis, *et al.*, "The nuclear research infrastructures open access scheme of the Joint Research Centre (JRC) at the European Commission - Contributions to education, training, mobility and scientific excellence," *Nuclear Engineering and Design*, vol. 420, p. 113 000, 2024 (cit. on pp. 28, 134).

[118] W. Mondelaers and P. Schillebeeckx, "GELINA, a Neutron Time-of-Flight Facility for High-Resolution Neutron Data Measurements," in *Research Infrastructures II (2)*, JRC35644, 2006, pp. 19–25 (cit. on p. 28).

[119] Joint Research Centre, "New JRC Tandem Accelerator MONNET ready for operation," Jul. 2020 (cit. on p. 28).

[120] J. F. Ziegler, M. D. Ziegler, and J. P. Biersack, "SRIM - The stopping and range of ions in matter (2010)," *Nuclear Instruments and Methods in Physics Research Section B: Beam Interactions with Materials and Atoms*, vol. 268, no. 11-12, pp. 1818–1823, 2010 (cit. on pp. 30–32, 92, 117, 128).

[121] SCIONIX, "SCIONIX - Dedicated Scintillation Detectors," Accessed: 2024-06-07 (cit. on pp. 32, 33).

[122] C. J. Werner, J. S. Bull, C. J. Solomon, *et al.*, *MCNP6.2 Release Notes - report LA-UR-18-20808*. Los Alamos National Laboratory (LANL), 2018 (cit. on pp. 33, 35, 58, 77, 79, 87, 97, 109).

[123] C. L. Fontana, M. Lunardon, F. E. Pino, *et al.*, "A distributed data acquisition system for signal digitizers with on-line analysis capabilities," in *2017 IEEE Nuclear Science Symposium and Medical Imaging Conference (NSS/MIC)*, 2017, pp. 1–5 (cit. on p. 36).

[124] C. L. Fontana, M. Lunardon, F. Pino, L. Stevanato, and S. Moretto, "Resource Sharing in Nuclear Physics Laboratory Classes: A Distributed Data Acquisition System for Experiments with Shared Resources and Data Management," in *25th International Conference on the Application of Accelerators in Research and Industry (CAARI)*, Texas, USA: AIP Publishing, 2019, p. 050 024 (cit. on p. 36).

[125] C. L. Fontana, N. Tuccori, F. E. Pino, M. Lunardon, L. Stevanato, and S. Moretto, "Performance comparison between signal digitizers and low-cost digital oscilloscopes: Spectroscopic, pulse shape discrimination and timing capabilities for nuclear detectors," *Journal of Instrumentation*, vol. 15, no. 06, P06020, 2020 (cit. on p. 36).

[126] F. Pino, C. L. Fontana, G. Nebbia, *et al.*, "Performance evaluation of a new digital acquisition system for neutron detection and spectroscopy," *Nuclear Instruments and Methods in Physics Research Section A: Accelerators, Spectrometers, Detectors and Associated Equipment*, p. 164 743, 2020 (cit. on p. 36).

[127] J. R. C. European Commission, "Github - ABCD," Accessed: 2024-06-24 (cit. on p. 36).

[128] CAEN, *User manual um3148 dt5730 / dt5725*, CAEN, 2016 (cit. on p. 36).

[129] E. M. Burbidge, G. R. Burbidge, W. A. Fowler, and F. Hoyle, "Synthesis of the Elements in Stars," *Rev. Mod. Phys.*, vol. 29, pp. 547–650, 4 Oct. 1957 (cit. on p. 47).

[130] A. G. W. Cameron, "Nuclear reactions in stars and nucleogenesis," *Publications of the Astronomical Society of the Pacific*, vol. 69, no. 408, p. 201, Jun. 1957 (cit. on p. 47).

[131] R. Pachuau, B. Lalremruata, N. Otuka, L. R. Hlondo, L. R. M. Punte, and H. H. Thanga, "Thick and Thin Target ^{7}Li(p,n)^{7}Be Neutron Spectra Below the Three-Body Breakup Reaction Threshold," *Nuclear Science and Engineering*, vol. 187, no. 1, pp. 70–80, 2017 (cit. on p. 48).

[132] M. Macías, B. Fernández, and J. Praena, "The first neutron time-of-flight line in spain: Commissioning and new data for the definition of a neutron standard field," *Radiation Physics and Chemistry*, vol. 168, p. 108 538, 2020 (cit. on pp. 48, 90).

[133] C. Lee and X.-L. Zhou, "Thick target neutron yields for the $^{7}\mathrm{Li}(p,n)^{7}\mathrm{Be}$ reaction near threshold," *Nuclear Instruments and Methods in Physics Research Section B: Beam Interactions with Materials and Atoms*, vol. 152, no. 1, pp. 1–11, 1999 (cit. on pp. 48–50, 68, 69, 77, 92).

[134] H. Liskien and A. Paulsen, "Neutron production cross sections and energies for the reactions $^{7}\mathrm{Li}(p,n)^{7}\mathrm{Be}$ and $^{7}\mathrm{Li}(p,n)^{7}\mathrm{Be}^{*}$," *Atomic Data and Nuclear Data Tables*, vol. 15, no. 1, pp. 57–84, 1975 (cit. on p. 48).

[135] R. Reifarth, M. Heil, F. Käppeler, and R. Plag, "PINO—a tool for simulating neutron spectra resulting from the ^{7}Li(p,n) reaction," *Nuclear Instruments and Methods in Physics Research Section A: Accelerators, Spectrometers, Detectors and Associated Equipment*, vol. 608, no. 1, pp. 139–143, 2009 (cit. on pp. 48, 49).

[136] M. Macias, "NEBOAS PROJECT. Joint Research Centre. European Comission." (Cit. on pp. 48–50, 68, 69, 117).

[137] M. Macías, C. Bonaldi, C. Fontana, *et al.*, "NEBOAS: A Neutron yiElds Based On AcceleratorS application," *Computer Physics Communications*, p. 109 304, 2024 (cit. on pp. 48–50, 69, 117).

[138] J. Tain and D. Cano-Ott, "Algorithms for the analysis of β-decay total absorption spectra," *Nuclear Instruments and Methods in Physics Research Section A: Accelerators, Spectrometers, Detectors and Associated Equipment*, vol. 571, no. 3, pp. 728–738, 2007 (cit. on p. 62).

[139] A. Verdera, J. Praena, F. Arias de Saavedra, *et al.*, "Measurement of the neutron spectrum of the ^{51}V(p,n)^{51}Cr reaction at 1585 keV," *Phys. Rev. C*, vol. 111, p. 024 620, 2 Feb. 2025 (cit. on pp. 73, 95).

[140] M. Macías Martínez, "HiSPANoS (HiSPAlis Neutron Source) at CNA: Installation and commissioning of the first neutron time of flight beamline in spain," PhD thesis, Universidad de Sevilla, 2019 (cit. on p. 89).

[141] E. Musacchio González, "Maxwell-boltzmann-like neutron spectrum production for maxwellian averaged cross section measurement," PhD thesis, Università degli Studi di Ferrara, 2020 (cit. on p. 89).

[142] A. Verdera and J. Praena, "Study on novel neutron irradiation without beam shaping assembly in Boron Neutron Capture Therapy," *Scientific Reports*, vol. 14, no. 1, p. 22 434, Sep. 28, 2024 (cit. on p. 97).

[143] International Commission on Radiation Units and Measurements, "Annals of the ICRP: Pulblication 103. The 2007 Recommendations of the International Commission on Radiological Protection," in The International Commission on Radiological Protection by Elservier, 2007 (cit. on p. 102).

[144] J. A. Coderre and G. M. Morris, "The Radiation Biology of Boron Neutron Capture Therapy," *Radiation Research*, vol. 151, no. 1, pp. 1–18, 1999 (cit. on p. 102).

[145] M. Pedrosa-Rivera, J. Praena, I. Porras, *et al.*, "Thermal Neutron Relative Biological Effectiveness Factors for Boron Neutron Capture Therapy from In Vitro Irradiations," *Cells*, vol. 9, no. 10, p. 2144, 2020 (cit. on p. 102).

[146] *Current Status of Neutron Capture Therapy* (TECDOC Series 1223). Vienna: International Atomic Energy Agency, 2001 (cit. on p. 104).

[147] E. Bisceglie, P. Colangelo, N. Colonna, P. Santorelli, and V. Variale, "On the optimal energy of epithermal neutron beams for BNCT," *Physics in Medicine & Biology*, vol. 45, no. 1, p. 49, 2000 (cit. on p. 104).

[148] F. S. Rasouli and S. F. Masoudi, "A study on the optimum fast neutron flux for Boron Neutron Capture Therapy of deep-seated tumors," *Applied Radiation and Isotopes*, vol. 96, pp. 45–51, 2015 (cit. on p. 104).

[149] P. Torres-Sánchez, I. Porras, F. Arias de Saavedra, M. Sabariego, and J. Praena, "On the upper limit for the energy of epithermal neutrons for Boron Neutron Capture Therapy," *Radiation Physics and Chemistry*, vol. 156, pp. 240–244, 2019 (cit. on p. 104).

[150] P. Torres-Sánchez, I. Porras, F. A. de Saavedra, and J. Praena, "Study of the upper energy limit of useful epithermal neutrons for Boron Neutron Capture Therapy in different tissues," *Radiation Physics and Chemistry*, vol. 185, p. 109 490, 2021 (cit. on p. 104).

[151] International Electrotechnical Commission, "Medical electrical equipment – Part 2-64: Particular requirements for the basic safety and essential performance of light ion beam medical electrical equipment," *IEC 60601-2-33 Ed. 3.0*, 2010 (cit. on p. 105).

[152] H. Koivunoro, H. Kumada, H. Tanaka, Y. Sakurai, and Y. Kiyanagi, "Out-of-field leakage in Boron Neutron Capture Therapy," in *Virtual Technical Meeting on Advances in Boron Neutron Capture Therapy, EVT1905174*, IAEA, 2020, pp. 27–31 (cit. on pp. 105, 106).

[153] A. Verdera, P. Torres-Sánchez, J. Praena, and I. Porras, "Study of the out-of-field dose from an accelerator-based neutron source for Boron Neutron Capture Therapy," *Applied Radiation and Isotopes*, p. 111 458, 2024 (cit. on pp. 106, 114, 125).

[154] T. Aihara and N. Morita, "BNCT for Advanced or Recurrent Head and Neck Cancer," in *Neutron Capture Therapy: Principles and Applications*, Springer, 2012, pp. 417–424 (cit. on p. 106).

[155] International Commission on Radiological Protection (ICRP), *Conversion Coefficients for Radiological Protection Quantities for External Radiation Exposures* (ICRP Publication 116, Ann. ICRP 20). ICRP, 2010, vol. 40, pp. 2–5 (cit. on pp. 107, 108).

[156] B. Siebert and H. Schuhmacher, "Quality factors, ambient and personal dose equivalent for neutrons, based on the new ICRU stopping power data for protons and alpha particles," *Radiation Protection Dosimetry*, vol. 58, no. 3, pp. 177–183, 1995 (cit. on p. 107).

[157] A. Ferrari and M. Pelliccioni, "On the conversion coefficients from fluence to ambient dose equivalent," *Radiation Protection Dosimetry*, vol. 51, pp. 251–252, 1994 (cit. on p. 107).

[158] Y.-W. Liu, T. Huang, S. Jiang, and H. Liu, "Renovation of epithermal neutron beam for BNCT at THOR," *Applied radiation and isotopes*, vol. 61, no. 5, pp. 1039–1043, 2004, Topics in Neutron Capture Therapy: Proceedings of the Eleventh World Congress on Neutron Capture Therapy (ISNCT-11) (cit. on pp. 120, 125, 126).

[159] O. Kononov, V. Kononov, M. Bokhovko, *et al.*, "Optimization of an accelerator based epithermal neutron source for neutron capture therapy," *Applied Radiation and Isotopes*, vol. 61, no. 5, pp. 1009–1013, 2004, Topics in Neutron Capture Therapy: Proceedings of the Eleventh World Congress on Neutron Capture Therapy (ISNCT-11) (cit. on pp. 120, 126).

[160] T. Seppälä *et al.*, "FiR 1 epithermal neutron beam model and dose calculation for treatment planning in neutron capture therapy," Ph.D. dissertation, Helsingin yliopisto, 2002 (cit. on p. 125).

[161] H. Koivunoro, "Dosimetry and dose planning in Boron Neutron Capture Therapy: Monte carlo studies," Ph.D. dissertation, University of Helsinki, 2012 (cit. on p. 125).

[162] Y. Sakurai, A. Maruhashi, and K. Ono, "The irradiation system and dose estimation joint-system for NCT wider application in Kyoto University," *Applied Radiation and Isotopes*, vol. 61, no. 5, pp. 829–833, 2004, Topics in Neutron Capture Therapy: Proceedings of the Eleventh World Congress on Neutron Capture Therapy (ISNCT-11) (cit. on p. 125).

[163] H. Tanaka, Y. Sakurai, M. Suzuki, *et al.*, "Characteristics comparison between a cyclotron-based neutron source and KUR-HWNIF for Boron Neutron Capture Therapy," *Nuclear Instruments and Methods in Physics Research Section B: Beam Interactions with Materials and Atoms*, vol. 267, no. 11, pp. 1970–1977, 2009 (cit. on pp. 125, 126).

[164] Y. Sakurai, H. Tanaka, T. Takata, *et al.*, "Advances in Boron Neutron Capture Therapy (BNCT) at Kyoto University- From reactor- based BNCT to accelerator-based BNCT," *Journal of the Korean Physical Society*, vol. 67, pp. 76–81, 2015 (cit. on p. 125).

[165] V. Giusti, P. M. Munck af Rosenschöld, K. Sköld, B. Montagnini, and J. Capala, "Monte Carlo model of the Studsvik BNCT clinical beam: Description and validation," *Medical Physics*, vol. 30, no. 12, pp. 3107–3117, 2003 (cit. on pp. 125, 126).

[166] D. Bleuel, R. Donahue, B. Ludewigt, and J. Vujic, "Designing accelerator-based epithermal neutron beams for Boron Neutron Capture Therapy," *Medical physics*, vol. 25, no. 9, pp. 1725–1734, 1998 (cit. on p. 126).

[167] K.-O. Kim, J. K. Kim, and S. Y. Kim, "Optimized therapeutic neutron beam for accelerator-based BNCT by analyzing the neutron angular distribution from ^{7}Li$(p,n)^{7}$Be reaction," *Applied Radiation and Isotopes*, vol. 67, no. 7, pp. 1173–1179, 2009, 6th International Conference on Isotopes (cit. on p. 126).

[168] H. Koay, M. Fukuda, H. Toki, R. Seki, H. Kanda, and T. Yorita, "Feasibility study of compact accelerator-based neutron generator for multi-port BNCT system," *Nuclear Instruments and Methods in Physics Research Section A: Accelerators, Spectrometers, Detectors and Associated Equipment*, vol. 899, pp. 65–72, 2018 (cit. on p. 126).